



# DESTROYING GALAXIES (OR NOT) WITH AGN FEEDBACK

**Martin Albert Bourne**  
MPhys(Oxon.)

Submitted in fulfilment of the requirements of the degree of  
Doctor of Philosophy

2015

Theoretical Astrophysics Group  
Department of Physics and Astronomy  
University of Leicester

## Destroying galaxies (or not) with AGN feedback

by

**Martin Albert Bourne**

MPhys(Oxon.)

Supermassive black holes (SMBHs) are believed to reside at the centres of most galaxies. Observations suggest that the host galaxies are strongly affected by feedback produced by accreting SMBHs. Feedback in the form of ultra-fast outflows (UFOs), which are expected to interact with the interstellar medium (ISM), have been used to explain scaling relations between SMBHs and their host galaxies. Such relations suggest that the feedback and ISM must couple very weakly, however, it is not clear how this is achieved.

In this thesis I provide observational tests to constrain UFO shock physics. I show that if UFO shocks cool via inverse Compton (IC) scattering, they should be observable in X-rays, but are not actually seen. The likely explanation for this is that the outflow is in a two-temperature, non-radiative regime. This implies that AGN outflows do not lose their kinetic energy to radiation and that an alternative energy loss mechanism is needed to explain the weak coupling required.

I use high-resolution simulations to investigate an UFO impacting upon a turbulent ISM. Complex processes occur in the turbulent medium, such as the detachment of mass and energy flows, which are missed in a homogeneous medium. While the shocked UFO can escape through low density regions, high density clumps are resistant to feedback and can continue to have negative radial velocities. Energy losses in the multiphase ISM may provide an alternative to the IC radiative loss mechanism.

Given the importance placed upon simulations in aiding our understanding of AGN feedback, I present a resolution study using a commonly employed sub-grid feedback prescription. I find that changes in resolution impact upon feedback efficiency, although not necessarily in a systematic way. I therefore suggest caution when analysing simulation results in order to ensure that numerical artefacts are not interpreted as physical phenomena.

---

Significant portions of this thesis have been published separately in:

- Inverse Compton X-ray signature of AGN feedback - **M. A. Bourne**, S. Nayakshin  
Monthly Notices of the Royal Astronomical Society, Volume 436, Issue 3, p.2346-2351 (2013)
- Black hole feedback in a multiphase interstellar medium - **M. A. Bourne**, S. Nayakshin, A. Hobbs  
Monthly Notices of the Royal Astronomical Society, Volume 441, Issue 4, p.3055-3064 (2014)
- The resolution bias: low-resolution feedback simulations are better at destroying galaxies - **M. A. Bourne**, K. Zubovas, S. Nayakshin  
Monthly Notices of the Royal Astronomical Society, Volume 453, Issue 2, p.1829-1842 (2015)

---

# Acknowledgements

There are many people whom I need to thank for their support and guidance throughout my PhD and indeed even before I started. First and foremost I thank my supervisor Sergei Nayakshin who has provided so much insight and encouragement over the last 3 years. He has suggested a number of very interesting and fruitful projects as well as countless discussions and various pieces of invaluable advice. On this front I would also like to thank the other members of staff in the theory group for the Tuesday morning grillings/discussions; Andrew King, Walter Dehnen, Mark Wilkinson, Graham Wynn and Richard Alexander and outside of the theory group I should thank Ken Pounds and Sergey Sazonov for useful feedback and advice. In particular I should thank Mark Wilkinson as my second supervisor and Nial Tanvir as my personal tutor for their guidance and advice during thesis committee meetings.

I have been fortunate enough to collaborate with a number of people on projects both in and beyond this thesis. Those people, whom I now thank are Chris Power, Kastytis Zubovas, Alex Hobbs and Alessia Gualandris. I should also mention the post-docs who have provided varying levels of humour and advice during my time in Leicester; Stuart Muldrew, Stephen Fendyke and Sung-Huon Cha. Of course behind the scenes of Academia is a plethora of bureaucracy that needs to be navigated whether that was to do with my studies, travel or teaching and so I thank Lisa, Kiri, Merry and Joan for all of their help with these issues.

It goes without saying that I am also thankful for the great office mates I have had during the past few years whom have, to some extent, kept me sane and provided many fun and enjoyable experiences as well providing academic advice (especially Hossam). The role of honour includes Alex, Gillian, Hossam, Pete, Hastyar, Tom, Charlie, Clément (I hope I got the accent correct), Claire, Lillian, Mark, Christian and Hasan. I should also thank Christian again for proof reading this thesis, so thank you. With regard to keeping my sanity intact, although not necessarily my wrists (Ben), I would like to thank everyone who has taken part in Monday afternoon football. With regard to the wrists I would also like to thank Leicester Royal Infirmary for successfully putting them back together again!

Much of my research has relied heavily on high performance computing. As such I acknowledge the use of the ALICE High Performance Computing Facility at the University of Leicester and the DiRAC Complexity system, operated by the University of Leicester IT Services, which forms part of the STFC DiRAC HPC Facility ([www.dirac.ac.uk](http://www.dirac.ac.uk)). This equipment is funded by BIS National E-Infrastructure capital grant ST/K000373/1 and STFC DiRAC Operations grant ST/K0003259/1. DiRAC is part of the UK National E-Infrastructure. The use of these machines would have been considerably more difficult if it was not for the IT support team, I am particularly grateful for all of the help provided by Gary Gilchrist, as well as Jon Wakelin, Chris Rudge and Liam Gretton. I also acknowledge the use of GADGET written by Volker Springel, Justin Read for the use of SPHS and

---

Dan Price for the use of `SPLASH`.

Before arriving in Leicester, right back to my school days there are a number of people I should thank, including all of my teachers at Heathcote School and Wisbech Grammar as well as my tutors in Oxford. In particular I also want to thank Davor Krajnovik and James Binney for kindling my interest in astrophysics and everyone I met during my time in Leiden, especially Joop Schaye and Craig Booth who introduced me to `GADGET`!

Outside of academia I want to thank my family, especially my parents for always being there when needed over the last 27 and a bit years and my brother for distracting me with Cricket when necessary. Finally I would like to say a big thank you to Jonathan who has supported me and put up with me through everything and without whom this work would have been far more difficult.

---

# Contents

|  |            |
|--|------------|
| <b>Abstract</b>  | <b>i</b>   |
| <b>Acknowledgements</b>  | <b>iii</b> |
| <b>List of abbreviations</b>   | <b>xi</b>  |
| <b>1 Introduction</b>  | <b>1</b>   |
| 1.1 Finding our place . . . . .  | 2          |
| 1.2 Black holes . . . . .  | 3          |
| 1.2.1 Theoretical developments . . . . .                                 | 3          |
| 1.2.2 The discovery of supermassive black holes . . . . .                | 5          |
| 1.2.3 “Observing” black holes . . . . .                                  | 7          |
| 1.2.3.1 Stellar mass black holes . . . . .                               | 8          |
| 1.2.3.2 Supermassive black holes . . . . .                               | 8          |
| 1.3 Galaxy formation and black hole seeds . . . . .                      | 10         |
| 1.4 Active galaxies (and AGN) . . . . .                                  | 12         |
| 1.5 SMBH - host galaxy co-evolution . . . . .                            | 15         |
| 1.6 Coupling AGN feedback to the host galaxy . . . . .                   | 19         |
| 1.6.1 Ultra-fast outflows (and BAL QSOs) . . . . .                       | 21         |
| 1.6.1.1 To cool or not to cool? . . . . .                                | 23         |
| 1.6.1.2 Driving scaling relations with momentum (and energy) . . . . .   | 26         |
| 1.6.2 The role of AGN feedback in galaxy formation simulations . . . . . | 30         |
| 1.7 This thesis . . . . .  | 31         |
| <b>2 Hydrodynamical simulations</b>                                      | <b>34</b>  |
| 2.1 Astrophysical simulations . . . . .                                  | 35         |
| 2.2 Gravity and the N-body technique . . . . .                           | 36         |
| 2.3 Smooth particle hydrodynamics . . . . .                              | 39         |
| 2.3.1 The SPH(S) equations of motion . . . . .                           | 40         |
| 2.3.2 The kernel . . . . .   | 41         |

|          |   |           |
|----------|---|-----------|
| 2.3.3    | Dissipation . . . . .   | 42        |
| 2.4      | Time integration . . . . .                                    | 44        |
| 2.4.1    | Euler method . . . . .  | 44        |
| 2.4.2    | Leapfrog method . . . . .                                     | 45        |
| 2.4.3    | Timesteps . . . . .   | 46        |
| 2.5      | Radiative cooling . . . . .                                   | 47        |
| 2.6      | Star formation . . . . .                                      | 49        |
| 2.7      | SMBH feedback . . . . .                                       | 51        |
| <b>3</b> | <b>IC signature of AGN feedback</b>                           | <b>53</b> |
| 3.1      | Introduction . . . . .  | 54        |
| 3.2      | Inverse Compton feedback component . . . . .                  | 55        |
| 3.2.1    | General procedure to calculate the X-ray spectrum . . . . .   | 55        |
| 3.2.2    | The electron energy distribution in the 2T regime . . . . .   | 57        |
| 3.2.3    | 1T cooling cascade behind the shock . . . . .                 | 58        |
| 3.3      | Resulting spectra for 1T and 2T shocks . . . . .              | 63        |
| 3.4      | Discussion and conclusions . . . . .                          | 67        |
| <b>4</b> | <b>Black hole feedback in a multi-phase ISM</b>               | <b>71</b> |
| 4.1      | Introduction . . . . .  | 72        |
| 4.2      | Simulation set-up . . . . .                                   | 75        |
| 4.2.1    | Numerical method . . . . .                                    | 75        |
| 4.2.2    | Initial conditions . . . . .                                  | 77        |
| 4.3      | Turbulent vs. homogeneous ISM . . . . .                       | 81        |
| 4.4      | Dynamics of clumpy gas . . . . .                              | 83        |
| 4.4.1    | Gas dynamics as a function of its density . . . . .           | 83        |
| 4.4.2    | The column density perspective . . . . .                      | 86        |
| 4.4.3    | Time evolution of the outflow . . . . .                       | 88        |
| 4.4.4    | Decoupling of energy and mass flow . . . . .                  | 90        |
| 4.5      | Discussion . . . . .  | 94        |
| 4.5.1    | Feedback on a homogeneous versus a multiphase ISM . . . . .   | 94        |
| 4.5.2    | Pertinence to the $M_{\text{BH}} - \sigma$ relation . . . . . | 95        |
| 4.5.3    | Comparison with other work . . . . .                          | 96        |
| 4.5.4    | Implications for cosmological simulations . . . . .           | 97        |
| 4.6      | Conclusion . . . . .  | 98        |

|          |  |            |
|----------|--|------------|
| <b>5</b> | <b>The resolution bias</b>   | <b>99</b>  |
| 5.1      | Introduction . . . . .   | 100        |
| 5.2      | Simulation set-up . . . . .  | 103        |
| 5.2.1    | Numerical method . . . . .   | 103        |
| 5.2.2    | Initial conditions . . . . .   | 105        |
| 5.2.3    | AGN feedback model . . . . .   | 105        |
| 5.2.4    | Summary of simulations . . . . .   | 108        |
| 5.3      | Results . . . . .  | 108        |
| 5.3.1    | Pre-feedback properties of the ISM . . . . .                             | 108        |
| 5.3.2    | Overview of numerical resolution trends . . . . .                        | 111        |
| 5.3.3    | Impact of feedback on the ISM . . . . .                                  | 114        |
| 5.3.3.1  | Resolving the ISM density structure . . . . .                            | 114        |
| 5.3.3.2  | Resolving outflows and inflows . . . . .                                 | 114        |
| 5.3.4    | Efficiency of feedback versus numerics . . . . .                         | 119        |
| 5.3.4.1  | The over-cooling problem . . . . .                                       | 119        |
| 5.3.4.2  | Gas ejection efficiency . . . . .  | 123        |
| 5.4      | Discussion . . . . .   | 127        |
| 5.4.1    | Resolving the multiphase ISM and outflow properties . . . . .            | 127        |
| 5.4.2    | Cooling of the feedback bubble . . . . .                                 | 128        |
| 5.4.3    | Star formation during an AGN outburst . . . . .                          | 129        |
| 5.4.4    | Black hole growth and the $M_{\text{BH}} - \sigma$ relation . . . . .    | 130        |
| 5.4.5    | Comparison with previous work . . . . .                                  | 131        |
| 5.4.6    | Implications for cosmological simulations . . . . .                      | 133        |
| 5.5      | Summary . . . . .  | 135        |
| <b>6</b> | <b>Conclusions</b>   | <b>136</b> |
| 6.1      | Observational signatures of ultra-fast outflows . . . . .                | 138        |
| 6.2      | The role of the ambient ISM in determining feedback efficiency . . . . . | 138        |
| 6.3      | Simulating AGN feedback and the effects of resolution . . . . .          | 139        |
| 6.4      | Future work . . . . .  | 140        |
| 6.5      | Final remarks . . . . .  | 142        |
|          | <b>References</b>  | <b>143</b> |



---

# List of Tables

|     |                                  |     |
|-----|----------------------------------|-----|
| 5.1 | Summary of simulations . . . . . | 106 |
|-----|----------------------------------|-----|

---

# List of Figures

|     |  |     |
|-----|--|-----|
| 1.1 | Stellar orbits around Sagittarius A* . . . . .                                 | 9   |
| 1.2 | AGN unification scheme . . . . .   | 13  |
| 1.3 | Galaxy halo mass and stellar mass functions . . . . .                          | 14  |
| 1.4 | Black hole scaling relations . . . . .   | 16  |
| 1.5 | Large scale outflows of ionised and molecular gas . . . . .                    | 20  |
| 1.6 | Ultra-fast outflow observations and statistics . . . . .                       | 22  |
| 1.7 | Wind shock schematic . . . . .   | 23  |
| 1.8 | Wind shock temperature evolution and cooling times . . . . .                   | 25  |
| 1.9 | Numerical solutions to momentum and energy driven outflows . . . . .           | 28  |
| 2.1 | Barnes and Hut oct tree . . . . .  | 37  |
| 2.2 | Softened gravitational potential and force . . . . .                           | 38  |
| 2.3 | Optically thin radiative cooling function . . . . .                            | 48  |
| 3.1 | The dimensionless electron temperature distribution $G(\theta)$ . . . . .      | 60  |
| 3.2 | Electron energy distribution for 1T cooling cascade. . . . .                   | 61  |
| 3.3 | IC emission from a shocked UFO with $v_w = 0.1c$ . . . . .                     | 62  |
| 3.4 | IC emission for UFO with $v_w = 0.05, 0.1$ and $0.2c$ , 1T case only . . . . . | 63  |
| 3.5 | IC emission assuming whole AGN spectrum as input . . . . .                     | 66  |
| 4.1 | Density and temperature slices for homogeneous ISM . . . . .                   | 80  |
| 4.2 | Density and temperature evolution for turbulent ISM . . . . .                  | 82  |
| 4.3 | Radial gas distribution . . . . .  | 84  |
| 4.4 | Radial velocity distribution . . . . .   | 85  |
| 4.5 | Gas column density seen from the SMBH . . . . .                                | 88  |
| 4.6 | Evolution of gas radial position and velocity . . . . .                        | 89  |
| 4.7 | Radial mass and energy flows . . . . .   | 91  |
| 4.8 | Absolute change in specific energy vs. density . . . . .                       | 92  |
| 5.1 | Gas density distribution after 1 Myr . . . . .                                 | 109 |
| 5.2 | Gas temperature distribution after 1 Myr . . . . .                             | 110 |

|      |  |     |
|------|--|-----|
| 5.3  | Rendered density slices after 1.5 Myr . . . . .        | 112 |
| 5.4  | Rendered temperature slices after 1.5 Myr . . . . .    | 113 |
| 5.5  | FN Density distribution - 1 vs 2 Myr . . . . .         | 115 |
| 5.6  | FM Density distribution - 1 vs 2 Myr . . . . .         | 116 |
| 5.7  | FM radial velocity distribution - 1 vs 2 Myr . . . . . | 117 |
| 5.8  | FN radial velocity distribution - 1 vs 2 Myr . . . . . | 118 |
| 5.9  | Maximum temperature evolution . . . . .                | 120 |
| 5.10 | Gas/AGN energy ratio . . . . .                         | 122 |
| 5.11 | Evolution of fraction mass change in 200pc . . . . .   | 125 |
| 5.12 | Evolution of gas with $v_r > 2\sigma$ . . . . .        | 126 |

---

# List of Abbreviations

|               |   |
|---------------|---|
| <b>1T</b>     | One temperature   |
| <b>1TCC</b>   | One temperature cooling cascade                           |
| <b>1TIC</b>   | One temperature inverse Compton                           |
| <b>2T</b>     | Two temperature   |
| <b>2TIC</b>   | Two temperature inverse Compton                           |
| <b>AGN</b>    | Active galactic nuclei                                    |
| <b>BAL</b>    | Broad absorption line                                     |
| <b>BH</b>     | Black hole  |
| <b>CMB</b>    | Cosmic Microwave Background                               |
| <b>CS</b>     | Cubic spline  |
| <b>DKD</b>    | Drift-Kick-Drift  |
| <b>EAGLE</b>  | Evolution and Assembly of GaLaxies and their Environments |
| <b>EED</b>    | Electron energy distribution                              |
| <b>GADGET</b> | GAxaxies with Dark matter and Gas intERacT                |
| <b>GHMF</b>   | Galaxy halo mass function                                 |
| <b>GR</b>     | General relativity  |
| <b>GSMF</b>   | Galaxy stellar mass function                              |
| <b>HST</b>    | Hubble space telescope                                    |
| <b>IC</b>     | Inverse Compton   |
| <b>ICCC</b>   | Inverse Compton cooling cascade                           |
| <b>IMF</b>    | Initial mass function                                     |
| <b>ISM</b>    | Interstellar medium                                       |
| <b>KDK</b>    | Kick-Drift-Kick   |
| <b>ngb</b>    | Neighbour   |
| <b>NGC</b>    | New general catalogue                                     |
| <b>NR</b>     | Non-relativistic  |
| <b>OWLS</b>   | OverWhelmingly large simulations                          |
| <b>QSO</b>    | Quasi-stellar object                                      |
| <b>RMS</b>    | Root mean square  |

|             |  |
|-------------|--|
| <b>SDSS</b> | Sloan Digital Sky Survey                                 |
| <b>SF</b>   | Star formation   |
| <b>SIS</b>  | Singular isothermal sphere                               |
| <b>SMBH</b> | Supermassive black hole                                  |
| <b>SPH</b>  | Smooth particle hydrodynamics                            |
| <b>SPHS</b> | Smooth particle hydrodynamics with a second order switch |
| <b>UFO</b>  | Ultra-fast outflow                                       |
| <b>UR</b>   | Ultra-relativistic                                       |
| <b>UV</b>   | Ultraviolet  |

---

*Dedicated to my Aunty Wendy (aka Plug)*

---

# 1

## Introduction

*“Black holes are where god divided by zero”*

*Albert Einstein (1939)*

## 1.1 Finding our place

For thousands of years man has looked up to the heavens in wonder and tried to understand the celestial dances. Astronomy is one of the oldest sciences, as far back as the Babylonians, people recorded the motions of the stars and planets (Sachs, 1974), and maybe even Halley’s comet (Stephenson et al., 1985). However, ancient civilisations did not merely observe the positions and movements of the stars, but utilised them. For example, the Ancient Egyptians are believed to have derived their calendar from astronomical observations and used stellar positions to help in building the pyramids and other monuments (e.g., Belmonte, 2009).

As far as our place in the Universe goes, this has been transformed tremendously in the intervening centuries. Evolving from the geocentric model of Aristotle and Ptolemy to the heliocentric models championed by Copernicus, Kepler, Galileo and Newton. However the size of the Universe and our perception of it has never changed more rapidly than during the 20th century. The Universe went from the lonely Milky Way described by Wright (1750) to one in which  $\sim 125$  billion other galaxies existed, akin to the *island Universes* of Emmanuel Kant, thanks to observations placing *nebulae* beyond the realm of the Milky Way (e.g., Curtis, 1917; Hubble, 1925). Not only did we realise that the Universe is full of other galaxies but that they are accelerating away from us in every direction (Hubble, 1929).

Further compelling evidence, such as observations of the Cosmic Microwave Background (CMB, Penzias & Wilson, 1965), which has now been measured to incredible accuracy (Planck Collaboration et al., 2015), big bang nucleosynthesis (Hoyle & Tayler, 1964) and observations of large scale structure (Geller & Huchra, 1989; Colless et al., 2001) suggests that we live in a  $\Lambda$ CDM Universe which formed during the *Big Bang*<sup>1</sup> and has expanded over the last  $\sim 13.8$  billion years to reach the point we are at today. From the confines of our own Solar system we have now observed galaxies and bright Quasars that are billions of light years away. The domain of Astronomy has transformed from one which is largely anthropocentric to one in which we are merely a small piece in a very large puzzle that we are still trying to solve.

---

<sup>1</sup>I note however that the idea of a Big Bang like origin of the Universe was not necessarily a new idea and had been considered during the middle ages (see for example, Bower et al., 2014)



## 1.2 Black holes

### 1.2.1 Theoretical developments

The first recorded use of the term *black hole* is accredited to the journalist Ann Ewing, in her 1964 article “Black holes in space”, however it was not until a lecture given by John Wheeler in 1967 that the term came into more common use within the science community (as detailed in, for example, Ferrarese & Ford, 2005; Graham, 2016). While I point the reader to other texts for a more detailed account of events (e.g., McCormach, 1968; Schaffer, 1979; Montgomery et al., 2009; Anderson, 2015), it is interesting to note, that the concept of a black hole, or at least an object very similar to what we now describe as a black hole, was first envisaged in the 18th century. Almost simultaneously, although separately, the English parson John Michell (Michell, 1784) and the French mathematician Pierre-Simon Laplace (Marquis de Laplace, 1798) argued that if light is made up of particles, as in Newton’s corpuscular theory, it would be decelerated by the gravity of the star. The extent to which the particles are slowed would depend upon the density of the star; leading them to surmise that if a star were both sufficiently massive and compact it would not emit any light. Michell dubbed these theoretical phenomena *dark stars* and stated that there may be many such objects throughout the universe that we simply cannot see.

The size and mass of a *dark star* or *black hole* can be defined using Newtonian gravity. The escape velocity from the surface of an object of mass  $M_{\text{BH}}$  and radius  $R_{\text{S}}$  is equal to

$$v_{\text{esc}} = \sqrt{\frac{2GM_{\text{BH}}}{R_{\text{S}}}}, \quad (1.1)$$

where  $G$  is the gravitational constant. Setting  $v_{\text{esc}} = c$ , where  $c$  is the speed of light, we find that

$$R_{\text{S}} = \frac{2GM_{\text{BH}}}{c^2} = 10^{-5} \left( \frac{M_{\text{BH}}}{10^8 M_{\odot}} \right) \text{pc}, \quad (1.2)$$

which is known as the Schwarzschild radius, named after Karl Schwarzschild, who derived it not from Newtonian arguments but from general relativity (GR). In 1916, a year after Einstein published his GR field equations (Einstein, 1915), Schwarzschild provided the first exact solution (Schwarzschild, 1916). Now known as the Schwarzschild metric, it describes space-time around a non-rotating, spherically symmetric, compact, massive object. Along with a physical singularity at  $r = 0$ , there is a coordinate singularity at  $r = R_{\text{S}}$ , which can be removed with a coordinate transformation (e.g. Eddington, 1924;

Lemaître, 1933; Finkelstein, 1958). An example of such a coordinate system are the Eddington-Finkelstein coordinates as given by Penrose (1965).

A lack of appetite for black holes in the GR community meant that much of the early work on physical black holes concentrated on stellar mass objects. The late 1920s and early 1930s saw a number of works attempting to understand the properties of extremely dense stars supported by the degeneracy pressure of a Fermi-gas. While Chandrasekhar (1931b,a) is synonymous with the topic for his derivation of the maximum stable mass of a white dwarf with a polytropic density profile, as highlighted by Graham (2016), the foundations had already been laid by previous works. Stoner (1929) presented the structure of a white dwarf composed of non-relativistic electrons and later for relativistic electrons (Stoner, 1930, 1932a,b), although not before the less well known works of Frenkel (1928) and Anderson (1929).

Further to this, Landau (1932) was the first to suggest that neutron degeneracy pressure would support stars that had exceeded the Chandrasekhar mass limit<sup>2</sup>. With the limiting mass of a neutron star being derived by Oppenheimer & Volkoff (1939), who later that year also showed that overly massive neutron stars should collapse into stellar mass black holes (Oppenheimer & Snyder, 1939). Such a fate had already been predicted by other authors (Chandrasekhar, 1932; Landau, 1932; Chandrasekhar, 1935). It would, however, take more than three decades before the first neutron stars would be observed with the discovery of pulsars (Hewish et al., 1968; Pilkington et al., 1968).

The intervening decades saw more progress in understanding GR interpretations of black holes. The singularity at the Schwarzschild radius was recognised as an *event horizon* by Finkelstein (1958), who stated “*The Schwarzschild surface  $r=2m^3$  is not a singularity but acts as a perfect unidirectional membrane: causal influences can cross it but only in one direction.*”. In other words, whilst information can pass across the event horizon towards  $r = 0$ , once beyond it information cannot return. Five years later Kerr (1963) derived the more general metric of a spinning black hole, which in the limit of no rotation tended to the Schwarzschild metric. Other solutions for charged black holes also emerged (Newman et al., 1965) whilst the *no hair theorem* was also developed (e.g. Israel, 1967; Carter, 1971; Robinson, 1975), stating that any black hole is fully described by only 3 physical properties: mass, spin and charge.

---

<sup>2</sup>Interestingly Landau actually wrote this work in 1931 (see Yakovlev et al., 2013), a year prior to the discovery of the neutron (Chadwick, 1932b,a).

<sup>3</sup>assuming units such that  $G = c = 1$

### 1.2.2 The discovery of supermassive black holes

Despite the leaps and bounds made in theoretical understanding of black holes, the acceptance of SMBHs in mainstream physics would take a number of additional decades (for more detailed historical overviews see, for example, Shields, 1999; Ferrarese & Ford, 2005; Longair, 2006; Graham, 2016). Seyfert (1943) galaxies, first observed by Fath (1909) and Slipher (1917), with particularly strange nuclei, provided the first indirect evidence for SMBHs. As discussed by Ferrarese & Ford (2005), their broad nuclear emission lines, which indicated gas velocities of  $\sim 8500 \text{ km s}^{-1}$ , set Seyfert galaxies apart from other typical galactic nuclei. However, the field was revolutionised with the emergence of radio astronomy in the early 50's with major groups being set up at Cambridge, Manchester and CSIRO (Shields, 1999). A number of particularly bright radio sources, such as Vir A and Cygnus A, were matched with galaxy counterparts (Baade & Minkowski, 1954). Burbidge (1956) used Synchrotron theory to estimate the energy output of M87, the host of Vir A, to be  $\sim 2 \times 10^{55}$  ergs and later estimated the energy output for a number of other galaxies (Burbidge, 1959), indicating the existence of a number of very high energy sources. By the early 60's a considerable amount of evidence had been accumulated and presented by Burbidge et al. (1963) suggesting extreme processes occurring in galactic nuclei.

The discovery of quasars, extremely bright objects with stellar like optical spectra but which reside at extra-galactic distances (hence quasar from quasi-stellar object) added to the pool of high energy objects. The brightest and potentially one of the most important quasars in the history of the field is 3C 273. First discovered as a bright radio source in the third Cambridge catalogue of radio sources (Edge et al., 1959), 3C 273 was found to have a stellar like optical counterpart (Hazard et al., 1963) but a redshift of  $z=0.158$  (Oke, 1963; Schmidt, 1963), placing it at a substantial distance from the Milky Way. Many more radio sources ( $\sim 1/3$  of all high latitude sources, Ferrarese & Ford, 2005) were also found to be high- $z$  quasars (e.g., Minkowski, 1960; Greenstein, 1963; Matthews & Sandage, 1963; Schmidt & Matthews, 1964; Schmidt, 1965), plus a large population of radio-quiet quasars (Sandage, 1965) along with other active galaxies (Zwicky, 1964; Markarian, 1967) were also found. Although the resolution limit of early observations placed an upper size limit of  $\sim 1''$  (Allen et al., 1962) on some sources, short variability timescales  $\Delta t \sim 1 \text{ yr}$  (e.g., Smith & Hoffleit, 1963; Oke, 1967) reduced this estimate to  $R \sim \Delta t c \sim 1 \text{ pc}$ . X-ray observations have since constrained even shorter variability timescales on the order of minutes (e.g., Mushotzky et al., 1993; Ulrich et al., 1997; Türler et al., 1999), providing tighter upper limits on the size of the central engine.

The immense energies produced in such small volumes posed a number of problems for conventional sources of energy production and resulted in various ideas being proposed. A considerable number of theories invoked stellar sources (e.g. Burbidge, 1961; Burbidge & Burbidge, 1962; Hoyle & Fowler, 1962; Cameron, 1962; Hoyle & Fowler, 1963; Field, 1964; Spitzer & Saslaw, 1966; Bisnovatyi-Kogan et al., 1967; Arons et al., 1975), while others considered galaxy mergers (e.g. Harrower, 1960) and even *white holes* (Novikov, 1965), before (and even after) the idea of a gravitational energy source was suggested. As highlighted by Ferrarese & Ford (2005), a number of authors envisaged the growth of a massive, compact object at the centre of a galaxy (e.g. Salpeter, 1964; Zeldovich & Novikov, 1964; Ne’eman, 1965) while later work explicitly explored the idea that quasars were powered by accretion onto SMBHs (e.g. Lynden-Bell, 1969; Wolfe & Burbidge, 1970; Lynden-Bell & Rees, 1971). Finally, using quasar counts and their luminosity density, Soltan (1982) argued that “*the mass contained in dead quasars in 1 Gpc<sup>3</sup> is  $8 \times 10^{13} M_{\odot}$  assuming 10 per cent efficiency of conversion of mass into radiation*”. From this he calculated that there are approximately  $10^5 - 10^6$  SMBHs of mass  $10^8 - 10^9 M_{\odot}$  within 1 Gpc<sup>3</sup>, meaning that every massive galaxy should contain a SMBH at its centre. This line of reasoning has become commonly known as the Soltan argument.

In the late 1970s a number of techniques were used to ascertain the black hole masses in galaxies such as M87. Sargent et al. (1978) used velocity dispersion measurements to estimate a mass of  $\sim 5 \times 10^9 M_{\odot}$  in the central 110 pc, while Young et al. (1978) used the centrally peaked stellar light distribution to estimate a mass of  $2.6 \times 10^9 M_{\odot}$ . Such estimates relied upon ground based observations for which the seeing makes it difficult to resolve the central region of the host galaxy. Therefore there was sufficient room in the models to have a high mass stellar component opposed to a SMBH (e.g. Dressler & Richstone, 1990). It was not until the arrival of the Hubble Space Telescope (HST) that more definitive dynamical measurements could be made in order to confirm the presence of SMBHs in galaxy centres. In 1994 a pair of papers provided compelling evidence that the central mass in M87 was indeed a SMBH. Ford et al. (1994) presented HST observations of a small disc of ionised gas in the nucleus while Harms et al. (1994) used HST spectra of the disc to find that it followed Keplerian rotations with radial velocities of  $\approx \pm 500 \text{ km s}^{-1}$  relative to the systematic velocity of M87. These results strongly suggested the presence of a  $\sim 2.4 \times 10^9 M_{\odot}$  SMBH.

### 1.2.3 “Observing” black holes

Black holes themselves provide essentially no direct observational signature other than a potential event horizon shadow (Falcke et al., 2000), expected to have a size of  $\sim 10R_S$  which is  $\sim 10^{-6}$  pc for the SMBH at the galactic centre. The *Event Horizon Telescope* project at MIT Haystack is attempting such observations, however they are incredibly challenging and have so far provided no definitive results (e.g., Fish et al., 2011, 2014). Alternatively, the interactions of a black hole with its surroundings are potentially observable. The main two methods of interaction are accretion of material local to the black hole and the gravitational interaction with objects and material within the black hole’s sphere of influence, defined as the radius at which the orbital speed due to the mass of the black hole is equal to the stellar velocity dispersion  $\sigma(r)$  (§4.8.1 Binney & Tremaine, 2008), i.e.

$$|v_{\text{orb}}| = \sqrt{\frac{GM_{\text{BH}}}{r_{\text{BH}}}} = \sigma(r_{\text{BH}}), \quad (1.3)$$

and thus

$$r_{\text{BH}} = \frac{GM_{\text{BH}}}{\sigma^2(r_{\text{BH}})} = 10.8 \text{ pc} \left( \frac{M_{\text{BH}}}{10^8 M_{\odot}} \right) \left( \frac{\sigma(r_{\text{BH}})}{200 \text{ km s}^{-1}} \right)^{-2}, \quad (1.4)$$

which is significantly larger than an event horizon shadow and thus presents a far less formidable task to resolve. Within  $r_{\text{BH}}$ , the black hole dominates the dynamics of the stars and their velocity dispersion can be assumed to be due only to the mass of the black hole. One can also consider the scales on which the black hole influences the gas within the galaxy. In this case the relevant scale is the Bondi (1952) radius which is defined as the radius at which the potential due to the black hole is equal to the specific thermal energy of the gas, i.e.

$$\frac{GM_{\text{BH}}}{r_{\text{B}}} = \frac{1}{2} c_s(r_{\text{B}})^2 \quad (1.5)$$

where  $c_s(r_{\text{B}})$  is the sound speed of the gas at the Bondi radius ( $r_{\text{B}}$ ) and so

$$r_{\text{B}} = \frac{2GM_{\text{BH}}}{c_s(r_{\text{B}})^2}. \quad (1.6)$$

Equations (1.4) and (1.6) provide similar information either for collisionless or collisional components of the galaxy, respectively and which of them is dominant largely depends upon the temperature of the gas component.

Black holes can be split into two main categories; stellar mass and supermassive<sup>4</sup>,

---

<sup>4</sup>A third class of intermediate mass black holes is theorised to exist, although there is currently little definitive observational evidence and I do not discuss this topic further here.

which I discuss separately below.

### 1.2.3.1 Stellar mass black holes

The most compelling evidence for stellar mass black holes comes from observations of binary systems in which there is an *unseen* massive companion of an observable star (e.g., Casares, 2007). From the motion of the observable star one can use Kepler's laws to estimate the mass of the companion object from the mass function

$$f(M_*, M_{\text{BH}}, i) = \frac{(M_{\text{BH}} \sin i)^3}{(M_{\text{BH}} + M_*)^2} = \frac{M_{\text{BH}} (\sin i)^3}{(1 + M_*/M_{\text{BH}})^2} = \frac{P v_*^3}{2\pi G} \quad (1.7)$$

where  $M_*$  is the observable star's mass,  $P$  is the orbital period,  $v_*$  is the radial velocity of the observable star and  $i$  is the inclination angle of the orbit. From equation (1.7) it is found that  $M_{\text{BH}} > f(M_*, M_{\text{BH}}, i)$ , which places a lower limit on the mass of the unseen object. Given that the maximum theoretical mass for a neutron star is  $\sim 3 M_\odot$  (Bombaci, 1996), radial velocity observations in which  $f(M_*, M_{\text{BH}}, i)$  exceeds this value provide strong, although indirect, evidence that the unseen companion must be a black hole. Out of about 40 candidate black holes in X-ray binary systems,  $\sim 20$  have masses above  $\sim 3 M_\odot$  (McClintock & Remillard, 2006). Further limits can be placed upon  $M_{\text{BH}}$  if  $M_*$  is known.

Additional evidence supporting stellar mass black holes also comes from binary systems, in particular X-ray binaries which can emit vast amounts of energy. Luminosities that far exceed levels expected to be produced directly from stars are believed to indicate accretion onto compact objects. The first such candidate black hole was Cygnus X-1, which showed short X-ray timescale variability (Schreier et al., 1971; Webster & Murdin, 1972) and has an estimated black hole mass of  $\sim 14.8 M_\odot$  (Orosz et al., 2011).

### 1.2.3.2 Supermassive black holes

As discussed in the previous section, observations of active galaxies that are emitting vast amounts of energy, combined with variability measurements, confirm that the emission originates from a small volume (e.g., Mushotzky et al., 1993; Ulrich et al., 1997) and provide the first indirect evidence of SMBHs in galaxy centres.

The motions of individual objects within the sphere of influence of the black hole (see equations (1.4) and (1.6)) and thus accelerated by its gravity can indicate the presence of a SMBH. The most compelling evidence comes from observations of our own

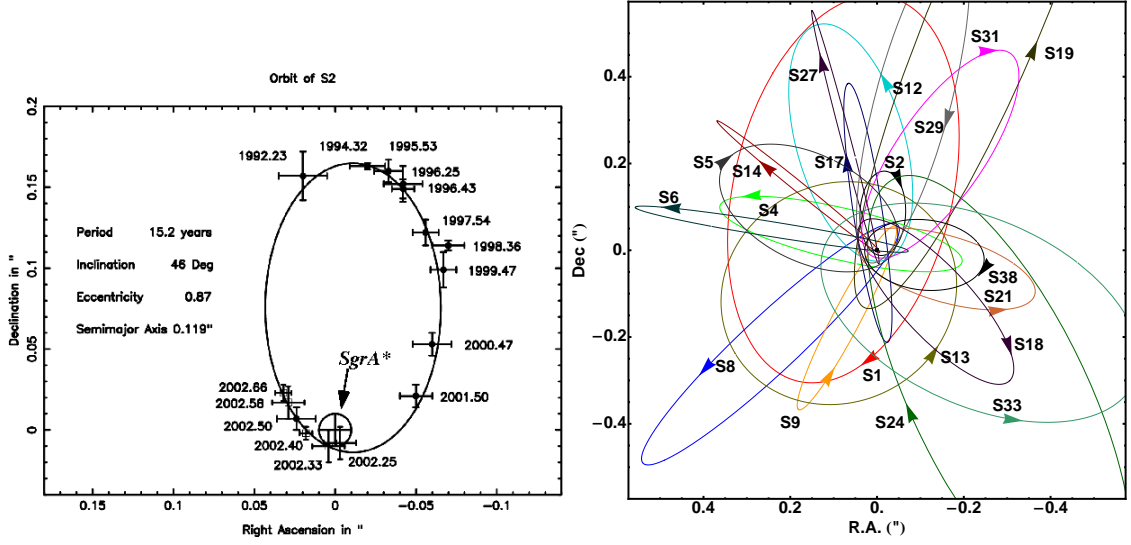


Figure 1.1: Examples of stellar orbits around Sgr A\*. LHS: the positions of the S2 star over a 10 year period between 1992 and 2002, relative to Sgr A\*, (Reprinted by permission from Macmillan Publishers Ltd: Nature, Schödel et al., 2002, copyright 2002) RHS: an illustration of the orbits of 28 S-stars calculated using data from a 16 year period. (Taken from Gillessen et al., 2009, figure 16., © AAS. Reproduced with permission.)

galactic centre. The first indication of a SMBH in the Milky Way was in the form of Synchrotron emission (Balick & Brown, 1974). However, concrete evidence of the existence of the SMBH, associated with the radio source Sagittarius A\* (or Sgr A\* for short), comes from proper motion and radial velocity measurements (e.g., Schödel et al., 2002; Ghez et al., 2005, 2008; Gillessen et al., 2009) of individual stars, which shows that they are orbiting an *invisible* mass of  $\sim 4 \times 10^6 M_{\odot}$  (see e.g., Peterson, 2014, for a review on measuring SMBH masses). Given that the peri-centre radius of the S2 star is  $\sim 124$  AU (Schödel et al., 2002), it is very difficult to reconcile this object with anything other than a SMBH. Figure 1.1 shows a selection of stellar orbits about Sgr A\*. The plot on the LHS is taken from Schödel et al. (2002) and shows the position of the S2 star over a ten year period between 1992 and 2002. This original data suggested that  $M_{\text{BH}} \approx 3.7 \times 10^6 M_{\odot}$ . The plot on the RHS is taken from Gillessen et al. (2009) and shows the orbits of 28 S-stars calculated using 16 years of observations, which suggest that  $M_{\text{BH}} \approx 4.31 \times 10^6 M_{\odot}$ . A further example of such evidence is provided by high angular resolution observations of NGC 4258 in which the motions of individual water masers within a sub-parsec region show the existence of a SMBH with a mass of  $3.6 \times 10^7 M_{\odot}$  (Miyoshi et al., 1995; Herrnstein et al., 2005). These objects provide good black hole mass estimates due to

the ability to resolve motions of objects within the sphere of influence of the black hole (Peterson, 2014). Such large masses within small volumes present compelling evidence for SMBHs.

For many galaxies it is not possible to resolve the motions of individual objects close to the black hole, however, the collective motion of objects can instead be used. Doppler shifts of stellar absorption lines (e.g., Kormendy et al., 1997; Cappellari et al., 2002; Schulze & Gebhardt, 2011; Rusli et al., 2013b,a) and gas emission lines (e.g., Ferrarese et al., 1996; van der Marel & van den Bosch, 1998; Sarzi et al., 2001; de Francesco et al., 2008; Walsh et al., 2010) provide kinematic information for the central regions of galaxies. Such kinematics can be used to constrain the overall underlying mass distribution and hence estimate any required black hole mass (see e.g., Ferrarese & Ford, 2005, for a discussion).

### 1.3 Galaxy formation and black hole seeds

Galaxies, coming from the Greek word “galaxias”, meaning *milky*, are dynamically bound collections of stars, gas, dust and dark matter. These “*Island Universes*”, as Kant described them in the 18th century, exist in a wide variety of shapes and sizes and are strewn throughout our vast universe. The formation of galaxies occurs in dark matter halos, which themselves grow from fluctuations in the dark matter distribution at high redshift. Over-dense regions of dark matter grow as they attract surrounding material and undergo gravitational collapse. Given that dark matter is collisionless, the properties of the collapsed halo are determined by the virial theorem (which also applies to collisional matter) such that  $\sigma_{\text{vir}}^2 \sim GM_{\text{vir}}/R_{\text{vir}}$ , where  $\sigma_{\text{vir}}$ ,  $M_{\text{vir}}$  and  $R_{\text{vir}}$  are halo velocity dispersion, mass and radius respectively. Baryonic material, on the other hand, is collisional (unless it is in the form of stars, in which case it is collisionless). As the halo collapses the gas is shock heated, converting kinetic energy into thermal energy, which in turn can be radiated away allowing the gas to cool and lose energy. The subsequent outcome of this process depends upon the cooling time of the gas,  $t_{\text{cool}}$ . Galaxies are believed to form in the regime where  $t_{\text{cool}}$  is less than both the Hubble time and the dynamical time of the system (Rees & Ostriker, 1977; Silk, 1977). Under such conditions the gas is able to collapse into the centre of the halo on the dynamical timescale and potentially fragment leading to star formation and even the formation of black hole seeds.

SMBHs, with masses of  $\sim 10^6 - 10^{10} M_{\odot}$ , are present in the centres of most local galaxies (Richstone et al., 1998; Ho, 1999a; Ferrarese & Ford, 2005) with recent observations



suggesting that they exist in the centres of dwarf galaxies as well (Reines et al., 2011; Reines & Deller, 2012; Reines et al., 2013). At some point during the galaxies' formation and subsequent evolution it is expected that a black hole will form within the centre of the galaxy. The exact formation mechanism is currently unknown but a number of candidate theories have been proposed. Volonteri (2010) reviews a range of theories such as black hole seeds forming from population III stellar remnants (Madau & Rees, 2001), stellar collisions in high density nuclear clusters (Begelman & Rees, 1978; Ebisuzaki et al., 2001; Portegies Zwart et al., 2004; Freitag et al., 2006; Gürkan et al., 2006) and direct collapse scenarios (Haehnelt & Rees, 1993; Bromm & Loeb, 2003; Koushiappas et al., 2004; Begelman et al., 2006; Lodato & Natarajan, 2006). Whichever method is correct, they all require vast amounts of gas to cool and undergo star formation or direct collapse into a black hole.

Observations of quasars at redshifts of  $z \gtrsim 6$  (Fan et al., 2000, 2001) require the first SMBHs to have formed within  $\sim 10^9$  years after the big bang. Black hole growth is expected to be limited by the Eddington rate

$$\dot{M}_{\text{Edd}} = \frac{L_{\text{Edd}}}{\eta c^2} \quad (1.8)$$

where  $\eta$  is the radiative efficiency of accretion and, depending upon the spin of the black hole, takes a value between 0.057 – 0.42 (Bardeen et al., 1972) and  $L_{\text{Edd}}$  is the Eddington luminosity and defines the luminosity at which the force due to the radiation pressure balances the gravitational force between a black hole of mass  $M_{\text{BH}}$  and a body of gas (or dust) with mass  $m$  and opacity  $\kappa$  a distance  $R$  apart, i.e.,

$$F_{\text{rad}} = \kappa \frac{L_{\text{Edd}} m}{4\pi R^2 c} = F_{\text{grav}} = \frac{GMm}{R^2}. \quad (1.9)$$

Rearranging and setting  $\kappa = \sigma_T/m_p$  to the electron scattering opacity we find that

$$L_{\text{Edd}} = \frac{4\pi GM_{\text{BH}} m_p c}{\sigma_T} = \eta \dot{M}_{\text{Edd}} c^2. \quad (1.10)$$

Combing this limited growth rate with the expected seed mass of a black hole puts further constraints on how long after the big bang the black hole seeds must have formed. The mass of a black hole accreting at the Eddington rate with radiative efficiency  $\eta$  for a time

$t$  is given as (e.g., Volonteri & Rees, 2005)

$$M_t = M_0 \exp\left((1 - \eta) \frac{t}{t_{\text{Salp}}}\right) \quad (1.11)$$

where

$$t_{\text{Salp}} = \frac{M_{\text{BH}}}{\dot{M}_{\text{Edd}}} = 4.5 \times 10^7 \left(\frac{\eta}{0.1}\right) \text{ yrs} \quad (1.12)$$

is the Salpeter (1964) time. At the time of writing the highest redshift quasar known is ULAS J112001.48+064124.3 with  $z = 7.085$  and a black hole mass of  $(2 - 3) \times 10^9 M_{\odot}$  (Mortlock et al., 2011). Such a high redshift means that this black hole has formed and grown to this size within  $\sim 7.5 \times 10^8$  years. Plugging this time and mass into equation (1.11) gives a seed mass of  $\sim (6 - 9) \times 10^2 M_{\odot}$ , allowing one to place further constraints upon formation mechanisms.

## 1.4 Active galaxies (and AGN)

It is expected that SMBHs gain most of their mass through episodes of luminous accretion (Salpeter, 1964; Lynden-Bell, 1969; Shakura & Sunyaev, 1973; Soltan, 1982; Rees, 1984). Such episodes emit vast amounts of radiation from very compact nuclear regions of the host galaxy. As mentioned above, the radiative efficiency of a luminous thin accretion disc (Shakura & Sunyaev, 1973) takes values in the range  $0.057 \lesssim \eta \lesssim 0.42$ , but on average is found to be  $\sim 0.1$  (Davis & Laor, 2011). Therefore setting  $\eta = 0.1$ , the energy liberated during the growth of the SMBH is given as (King & Pounds, 2015)

$$E_{\text{BH}} = \eta M_{\text{BH}} c^2 \sim 2 \times 10^{61} \left(\frac{M_{\text{BH}}}{10^8 M_{\odot}}\right) \text{ erg}. \quad (1.13)$$

To provide some perspective and highlight just how considerable this is, we can compare to the typical binding energy of a galaxy bulge, which can be approximated as (King & Pounds, 2015)

$$E_{\text{b}} \sim M_{\text{b}} \sigma^2 \sim 8 \times 10^{58} \left(\frac{M_{\text{b}}}{10^{11} M_{\odot}}\right) \left(\frac{\sigma}{200 \text{ km s}^{-1}}\right)^2 \text{ erg} \quad (1.14)$$

which is a factor of 250 smaller. Galaxies undergoing such episodes of accretion and energy production are known as active galaxies, while the central region is the Active Galactic Nucleus (AGN, although this term is also commonly used to describe the whole

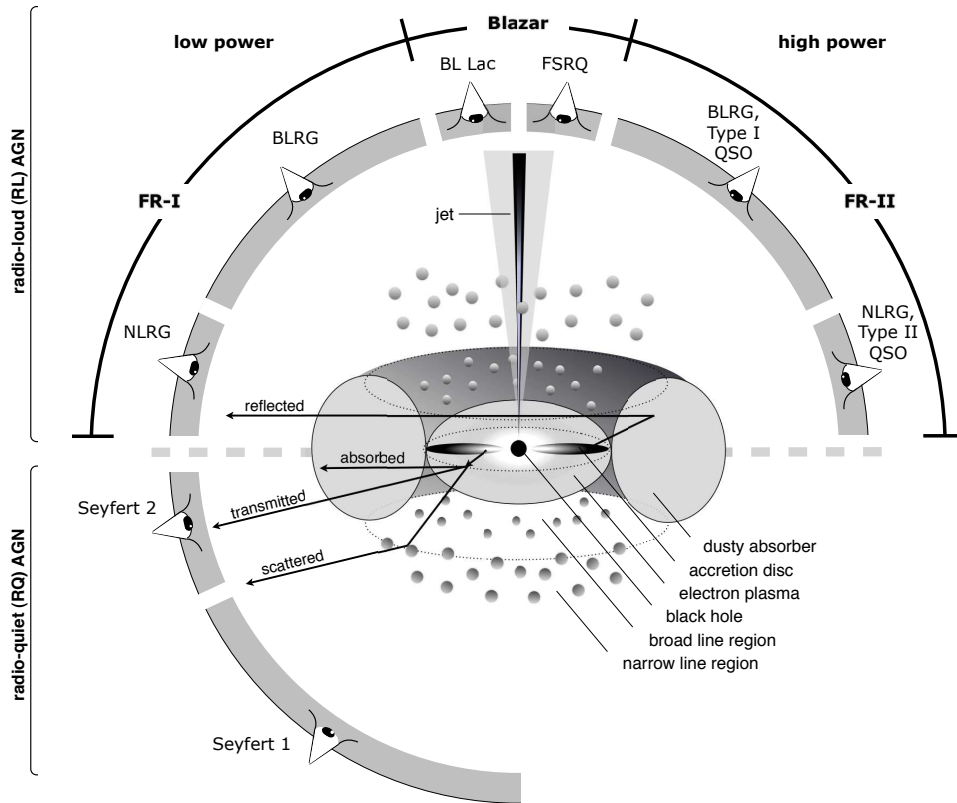


Figure 1.2: Illustration of the AGN unification scheme highlighting how radio loudness and obscuration can affect the observed properties of the central engine. Taken from Beckmann & Shrader (2012, figure 1.)

galaxy). We have already discussed AGN as evidence for the existence of SMBHs, here I briefly discuss some further properties of these objects.

AGN are the sites of some of the most extreme physical processes in the Universe. As mentioned in section 1.2.2, they can be extremely energetic, with luminosities of  $L_{\text{bol}} \sim 10^{41} - 10^{47} \text{ erg s}^{-1}$ , which can outshine the rest of the host galaxy. Strong flux variability (e.g., Mushotzky et al., 1993; Ulrich et al., 1997; Türler et al., 1999), across a range of frequencies, can be used to constrain the source region size, which is typically  $\sim 1 \text{ pc}^3$ .

The range of properties exhibited by AGN can in general be explained by the AGN unification scheme (Barthel, 1989; Antonucci, 1993) as illustrated in Figure 1.2 (taken from Beckmann & Shrader, 2012). The scheme considers the combination of the radio loudness of the central source and the orientation of the object, which in turn can affect the obscuration. The radio loudness of an object depends upon the production of radio jet structures while the orientation and hence obscuration of the central engine can affect

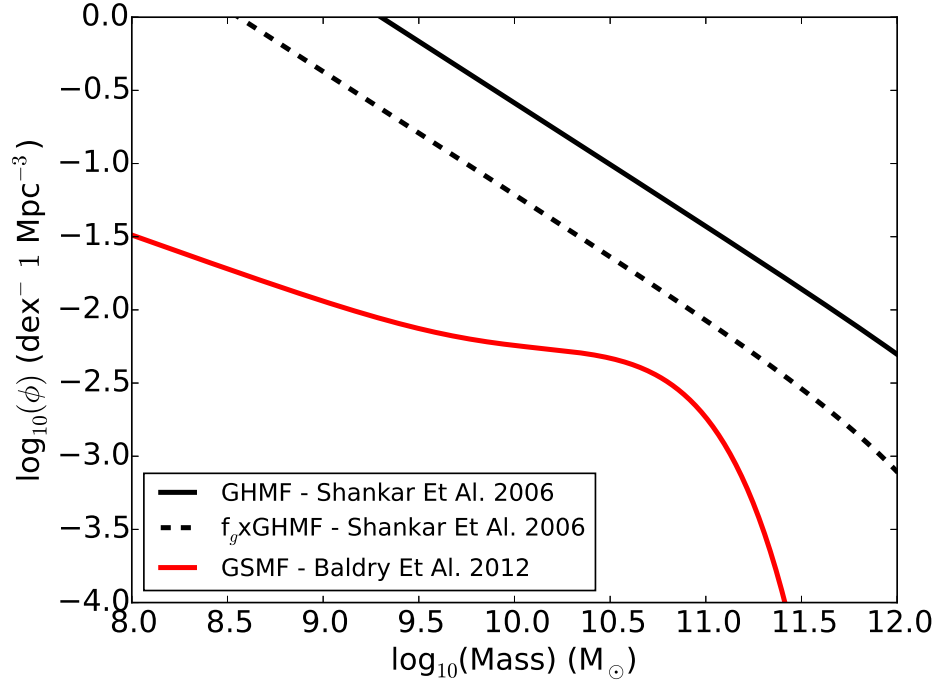


Figure 1.3: Comparisons of the galaxy halo mass function (GHMF) with the galaxy stellar mass function GSMF. The GHMF (solid black line) is plotted using the Schechter (1976) fit of Shankar et al. (2006), also shown is the same function rescaled by the expected baryonic mass fraction of the halos  $f_g = 0.18$  (dashed black line). The GSMF (solid red line) is plotted using the double Schechter (1976) fit of Baldry et al. (2012).

whether or not the broad line region is observable. Within these broad classifications fall other types of AGN which are classified based upon their radiative power and/or the morphological properties of their radio jets (e.g., Fanaroff & Riley, 1974).

AGN feedback occurs due to the production of energy (in the form of radiation, winds and/or jets), during episodes of SMBH accretion, and its interaction with the ISM (Fabian, 2012). It can generally be split into two different modes depending upon the energy generation mechanism near the central source. Quasar mode feedback (also known as the radiative or wind mode) proceeds in radio quiet objects (which make up  $\sim 90\%$  of the AGN population) and takes the form of winds produced when the black hole is accreting close to the Eddington limit. This feedback mode is believed to produce powerful outflows that can expel gas from a host galaxy, quench star formation and ultimately drive observed scaling relations (see section 1.6). On the other hand, the maintenance mode (also known as the kinetic or radio mode) occurs in radio loud sources with pronounced jets that are

typically believed to form at lower accretion rates. Unlike the quasar mode, which is believed to quench star formation, the maintenance mode acts to prevent gas cooling onto the galaxy and forming new stars. For reviews of AGN feedback see, for example, Fabian (2012) and King & Pounds (2015).

A clearer picture of the role of AGN feedback in galaxy evolution can be seen by considering the galaxy stellar and halo mass functions (GSMF and GHMF, respectively) shown in figure 1.3. The solid black line shows a Schechter (1976) fit to the GHMF of Shankar et al. (2006), while the dashed black line shows the same function but with the mass rescaled by the baryon mass fraction  $f_g = 0.18$ . If all of the baryons within a galaxy ended up in stars, this is the expected GSMF. However, as shown by solid red line, a double Schechter (1976) fit of the Baldry et al. (2012) GSMF, this is not the case. Not only is it below the modified GHMF, it also has a very different shape, suggesting that the star formation efficiency is a function of halo mass and peaks in  $\sim 10^{11} M_\odot$  halos. Stellar feedback in the form of supernova leads to the suppression of star formation at the low mass end (e.g., Benson et al., 2003) by clearing gas out of the halo. However, at higher masses, supernova are unable to clear the gas out indefinitely and it can fall back leading to further star formation. Therefore, while being able to reproduce the observed GSMF at low halo masses, stellar feedback alone is unable to produce the dearth of high mass galaxies. Instead the inclusion of AGN feedback is found to be necessary to quench star formation in high mass halos (e.g., Bower et al., 2006; Croton et al., 2006). However, although necessary, AGN are not sufficient to produce the observed GSMF and can only be effective in hydrostatic halos (Binney, 2004; Bower et al., 2006), where the cooling time is longer than the free-fall time. This condition is met for halos with masses  $\gtrsim 10^{11} M_\odot$ , in close coincidence with the knee of the GSMF.

## 1.5 SMBH - host galaxy co-evolution

To date 85 SMBH masses have been measured in galaxies using dynamical modelling of spatially resolved kinematics (Kormendy & Ho, 2013). With this growing number of SMBH observations, relations between the SMBH mass and properties of its host galaxy have been found. Using HST photometry and ground based kinematics for 36 nearby galaxies, Magorrian et al. (1998) found that SMBH mass scales with the bulge mass as  $M_{\text{BH}}/M_b \simeq 0.005$ , confirming previous suggestions (Kormendy, 1993; Kormendy & Richstone, 1995) that  $M_{\text{BH}} \propto M_b$ . Further work has since come to a similar conclusion with slightly lower SMBH-to-bulge mass ratios of  $\sim 0.001 - 0.003$  (e.g.,

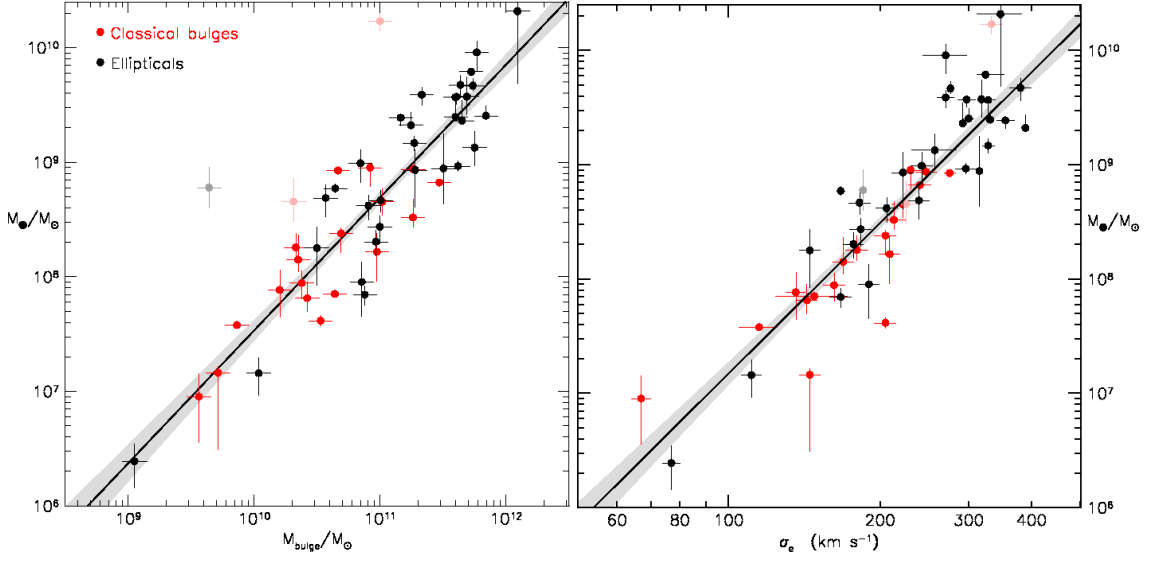


Figure 1.4: Examples of black hole scaling relations taken from Kormendy & Ho (2013). The LHS shows the  $M_{\text{BH}} - M_{\text{b}}$  relation while the RHS shows the  $M_{\text{BH}} - \sigma$  relation. Both plots are for classical bulges (red) and ellipticals (black) only. Least-square fits (black line) and the  $1\sigma$  range of the fits (grey shading) also shown.

Ho, 1999b; Kormendy & Gebhardt, 2001; Merritt & Ferrarese, 2001; McLure & Dunlop, 2002; Marconi & Hunt, 2003; Häring & Rix, 2004; Sani et al., 2011; Beifiori et al., 2012; McConnell & Ma, 2013). These observations did not typically discriminate against galaxy type and it was found that the scatter was reduced by excluding disc galaxies (McLure & Dunlop, 2002; Graham, 2016, for further discussion). More recently the review of Kormendy & Ho (2013) further found that SMBH mass does not correlate with the mass of pseudo-bulges as it does in classical bulges and elliptical galaxies. In essence classical bulges and elliptical galaxies are the same beast and are formed during *rapid* merger events (Toomre, 1977), while pseudo bulges form due to *slow* secular processes within disc galaxies (Kormendy & Kennicutt, 2004). Observationally, pseudo bulges can be distinguished from classical bulges/ellipticals as having a disc like morphology, flatter surface brightness profiles and being more rotationally supported (for an extensive list see Kormendy & Ho, 2013). Eliminating data from galaxies with pseudo-bulges they find a SMBH-bulge mass relation of

$$M_{\text{BH}} = 4.9 \times 10^8 M_{\odot} \left( \frac{M_{\text{b}}}{10^{11} M_{\odot}} \right)^{1.16} \quad (1.15)$$

which gives a mean SMBH-to-bulge mass ratio of  $\sim 0.005$  (similar to Magorrian et al., 1998) and an intrinsic scatter of 0.3 dex. This relationship can be seen in the left hand plot in Figure 1.4 (taken from Kormendy & Ho, 2013).

Perhaps even more remarkable than this relation is the tight correlation between SMBH mass and the host spheroid velocity dispersion,  $\sigma$ , which typically takes the form  $M_{\text{BH}} \propto \sigma^\alpha$ . The correlation was first discovered by Ferrarese & Merritt (2000) and Gebhardt et al. (2000) who found  $\alpha = 4.8$  and 3.75, respectively. The original correlations probed  $\sigma$  in the range of  $\sim 67 - 375 \text{ km s}^{-1}$  while subsequent work has investigated galaxies with velocity dispersions down to  $\sigma \sim 36 \text{ km s}^{-1}$  using a sample of 15 Dwarf Seyfert I galaxies (Barth et al., 2005) and up to  $\sigma \sim 389 \text{ km s}^{-1}$  (Rusli et al., 2013b) using a sample of 10 high mass early-type galaxies. Again the recent review of Kormendy & Ho (2013) have recalculated the relation solely for classical bulges and elliptical galaxies and is shown in the right hand plot of Figure 1.4 (taken from Kormendy & Ho, 2013). They find a relation of

$$M_{\text{BH}} = 3.09 \times 10^8 M_\odot \left( \frac{\sigma}{200 \text{ km s}^{-1}} \right)^{4.38} \quad (1.16)$$

with an intrinsic scatter of 0.29, similar to that of the SMBH-bulge mass relation. This scatter is found to be at most only slightly worse than the observational errors (Ferrarese & Merritt, 2000; Gebhardt et al., 2000; Tremaine et al., 2002; Gültekin et al., 2009), thus providing compelling evidence that there is indeed some form of co-evolution between the SMBH and its host galaxy (Kormendy & Ho, 2013). It should, however, be noted that since most kinematic estimates of SMBH masses do not resolve the sphere of influence, the  $M_{\text{BH}} - \sigma$  relation may be an upper limit for SMBH masses at a given  $\sigma$  (Batcheldor, 2010).

The growing number of SMBH mass measurements allows one to try to understand how the relation behaves in different galaxies and at different red-shifts. The lack of a correlation with pseudo-bulges (Kormendy & Gebhardt, 2001; Kormendy et al., 2011; Kormendy & Ho, 2013) suggests that the processes driving the formation of classical bulges and elliptical galaxies, i.e., mergers, also plays a role in driving SMBH growth and the scaling relations (Di Matteo et al., 2005; Springel et al., 2005; Hopkins et al., 2006; Alexander & Hickox, 2012; Kormendy & Ho, 2013). SMBH properties also seem not to correlate with galaxy disc properties (e.g., Kormendy & Gebhardt, 2001; Kormendy et al., 2011; Kormendy & Ho, 2013), however, whether there is (Ferrarese, 2002; Baes et al., 2003; Volonteri et al., 2011) or is not (Kormendy & Bender, 2011; Kormendy & Ho, 2013) a fundamental correlation with the dark matter halo is up for debate. Although

it is interesting to note that cosmological simulations have shown that, for self-regulated growth of a galaxy, it is the dark matter halo mass and not the bulge stellar mass, which determines  $M_{\text{BH}}$  (Booth & Schaye, 2010).

Furthermore, there have been a number of attempts to understand how the scaling relations evolve (if at all) with redshift. To date only a handful of studies have attempted to ascertain the  $M_{\text{BH}} - \sigma$  relation beyond  $z \sim 0.3$  (Treu et al., 2004; Woo et al., 2006; Shen et al., 2008; Woo et al., 2008; Canalizo et al., 2012; Shen et al., 2015), while the  $M_{\text{BH}} - M_{\text{b}}$  relation has been measured beyond  $z \sim 2$  (Peng et al., 2006b,a; Shields et al., 2006; Decarli et al., 2010; Sarria et al., 2010; Targett et al., 2012; Bongiorno et al., 2014). In both cases there is little consensus on if, let alone how, the scaling relations evolve. On the one hand, some authors find that SMBHs resided in relatively less massive bulges at higher redshift (e.g., Peng et al., 2006b,a; Shields et al., 2006; Woo et al., 2008; Decarli et al., 2010; Sarria et al., 2010; Targett et al., 2012; Bongiorno et al., 2014), while others have found no *physical* evolution and suggest that any changes are due to observational bias (e.g., Volonteri & Stark, 2011; Schulze & Wisotzki, 2011, 2014; Shen et al., 2015). Irrespective of any potential evolution, Kormendy & Ho (2013) point out that scaling relations already seem to be in place at  $z \sim 2 - 6$  (albeit with larger scatter) and any evolution that does occur slows for  $z \lesssim 2$ , when considering observations of the  $M_{\text{BH}} - M_{\text{b}}$  relation across a wide redshift range. This suggests that many of the processes driving co-evolution and the scaling relations happened during this period. They also suggest that the decreased scatter seen in local relations can, at least in part, be attributed to merger averaging. Indeed, at one extreme it has been suggested that the scaling relations are purely driven by merger averaging (Peng, 2007; Hirschmann et al., 2010; Gaskell, 2011; Jahnke & Macciò, 2011)

Finally, it is interesting to consider outliers from the observed relations as they may shed light onto the nature of the co-evolution of the host galaxy and its SMBH. Systems currently undergoing mergers seem to host under-massive SMBHs compared to their bulge masses and luminosities (e.g., Nowak et al., 2008; Gültekin et al., 2011; Kormendy & Ho, 2013), while in the opposite direction there exist a number of monster SMBHs which are over-massive compared to their bulge masses and luminosities (e.g., Kormendy et al., 1997; Cretton & van den Bosch, 1999; Rusli et al., 2011; Bogdán et al., 2012; van den Bosch et al., 2012; Ferré-Mateu et al., 2015; Scharwächter et al., 2015; Trakhtenbrot et al., 2015; van Loon & Sansom, 2015). I note however that both sets of objects are still consistent with the  $M_{\text{BH}} - \sigma$  relation. One potential explanation for such over-massive SMBHs is that they did once sit on the  $M_{\text{BH}} - M_{\text{b}}$  relation but the host



galaxy was tidally stripped. This however would result in not just the stars being stripped, but also the dark matter, which does not seem to be the case (Bogdán et al., 2012). An alternative explanation from Ferré-Mateu et al. (2015) invokes evolving scaling relations whereby the SMBH grows early and the host galaxy catches up. However in the case of the over-massive black holes the galaxies simply stopped growing too early.

## 1.6 Coupling AGN feedback to the host galaxy

In order to drive the observed SMBH scaling relations, it is expected that the SMBH communicates its presence to the host galaxy. We can rule out the source of this communication being gravitational by considering the sphere of influence of the SMBH, which is significantly smaller than the bulge. Considering the energy released during accretion onto a SMBH and the binding energy of the galaxy bulge in equations 1.13 and 1.14 respectively, it is clear that  $E_{\text{BH}} \gg E_{\text{b}}$ . This suggests that energetic feedback from accretion onto a SMBH has the potential to affect the host on large scales. This feedback will only act on the *gas* and so a more appropriate comparison would be with the binding energy of the gas within the bulge  $E_{\text{g}} = f_{\text{g}} E_{\text{b}} \simeq f_{\text{g}} M_{\text{b}} \sigma^2$  (King & Pounds, 2015), where  $f_{\text{g}}$  is the bulge gas mass fraction. Assuming for simplicity a black hole at its  $M - \sigma$  mass and that  $M_{\text{BH}} \sim 0.005 M_{\text{b}}$ , we find an approximate ratio between the black hole energy and gas binding energy of

$$\frac{E_{\text{BH}}}{E_{\text{g}}} \sim 0.005 \frac{\eta}{f_{\text{g}}} \frac{c^2}{\sigma^2} \sim 1125 f_{\text{g}}^{-1}, \quad (1.17)$$

which for a typical gas fraction of  $f_{\text{g}} \sim 0.18$ , is considerable. This suggests two things; firstly accretion onto a SMBH produces more than enough energy to be able to clear the gas from the bulge of a host galaxy and hence is a potential driving force behind the observed scaling relations. Secondly, given the large ratio in equation (1.17), the coupling between the feedback from the black hole and the host galaxy must be very weak. The energy, at least initially, will be emitted as radiation from the accretion disc. Given that we observe it, we know that most of the radiation escapes the galaxy, however, some of it must couple (King & Pounds, 2015).

There is growing evidence for AGN feedback interacting with the host galaxy (Fabian, 2012; King & Pounds, 2015); while observed scaling relations can provide *indirect* evidence, it is the number of large scale outflows observed which perhaps provide the most compelling indication of its existence. Such outflows are seen with velocities in excess of  $1000 \text{ km s}^{-1}$  for neutral and ionised gas (e.g., Feruglio et al., 2010; Sturm et al., 2011a;

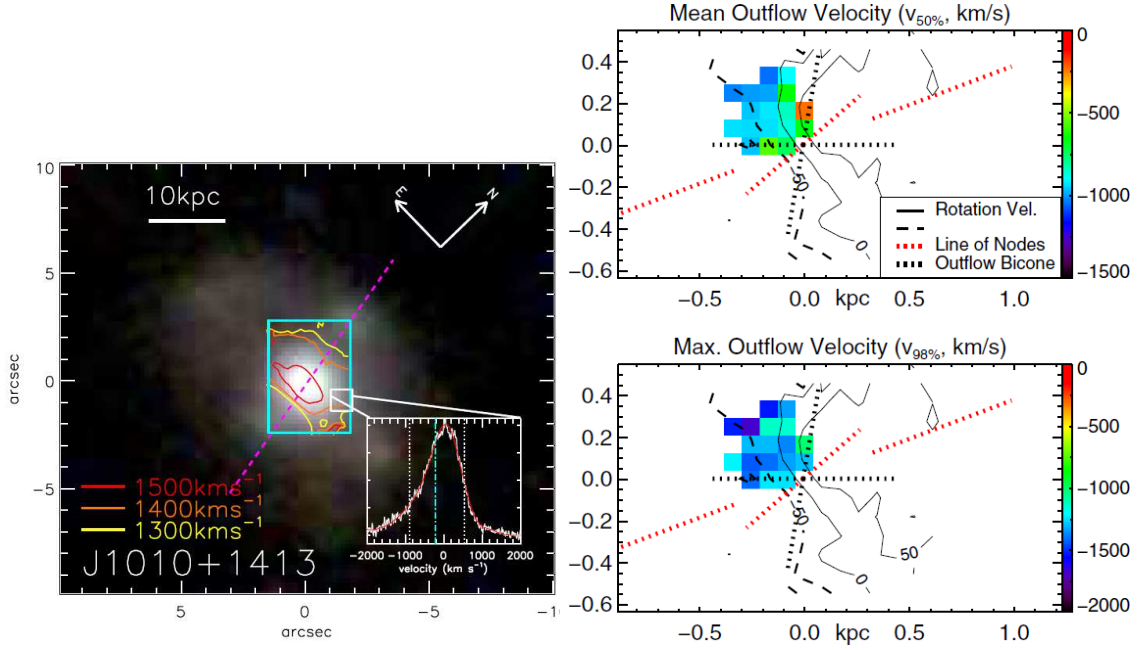


Figure 1.5: Observations of large scale, AGN driven, outflows. LHS: SDSS image with added velocity contours for outflowing OIII (taken from Harrison et al., 2014, figure 6.). RHS: velocity maps of outflowing H<sub>2</sub> (taken from Rupke & Veilleux, 2013a, figure 2., © AAS. Reproduced with permission.)

Arav et al., 2013; Rupke & Veilleux, 2013a,b; Harrison et al., 2014; Maiolino et al., 2012; Cicone et al., 2012, 2014, 2015; Carniani et al., 2015; Tombesi et al., 2015). Figure 1.5 provides a couple of examples of kpc scale outflows. The left hand plot, taken from Harrison et al. (2014, figure 6.), shows an ionised outflow with velocities of  $\sim 1500 \text{ km s}^{-1}$  while the right hand plot, taken from Rupke & Veilleux (2013a), shows a cold molecular outflow with velocities of  $\sim 1000 \text{ km s}^{-1}$ . An interesting feature of a number of these outflows is their high momentum rates, which can be up to  $\sim 30$  times the radiative momentum output of the host AGN (Feruglio et al., 2010; Rupke & Veilleux, 2011a; Sturm et al., 2011a; Faucher-Giguère et al., 2012; Faucher-Giguère & Quataert, 2012; Arav et al., 2013; Cicone et al., 2014; Genzel et al., 2014; Tombesi et al., 2015). This puts constraints on the exact feedback mechanism which communicates the radiation emitted from accretion onto the black hole to the host galaxy. One promising mechanism driving these large scale outflows originates with accretion disc driven winds, which I discuss in the next section.

### 1.6.1 Ultra-fast outflows (and BAL QSOs)

Feedback in the form of a wind produced close to the black hole has been used by a number of authors to explain the observed black hole scaling relations (e.g. Silk & Rees, 1998; Fabian, 1999; King, 2003; Nayakshin, 2014). UV observations of broad absorption line quasars (BAL QSOs) show outflows with velocities of up to  $v_w \sim 0.1c$  (Hazard et al., 1984; Turnshek, 1988; Knigge et al., 2008; Gibson et al., 2009). Furthermore, direct observations of local AGN have found winds, dubbed ultra-fast outflows (UFOs), detected via X-ray observations of blue-shifted iron absorption lines (e.g., Pounds et al., 2003b,a; Pounds & Reeves, 2009; Tombesi et al., 2010a,b, 2015). An example absorption feature from Pounds & Reeves (2009, figure 8.) can be seen in the left hand plot of Figure 1.6, while the right hand plot shows the velocity distribution for a number of observed outflows, which have an average velocity of  $v_w \sim 0.1c$ . These outflows are consistent with those expected from theory (e.g., Shakura & Sunyaev, 1973; King, 2003) for SMBHs accreting gas at close to the Eddington rate, with mass outflow rates  $\dot{M}_w \sim \dot{M}_{\text{Edd}}$ . We also note that the UFOs have a high detection rate of  $\sim 40\%$ , (Tombesi et al., 2010a) suggesting that they are wide angled. In fact it has been suggested that UFOs and BAL QSOs have a common launch mechanism and it is purely the mass inflow rate which determines whether the wind is fast and low mass (UFO) or slow and high mass (BAL QSO) (Zubovas & King, 2013).

Potential processes driving these winds include radiation pressure on free electrons (King & Pounds, 2003) and/or spectral lines (Proga et al., 2000) or possibly hydromagnetic processes (Fukumura et al., 2015). However, when considering the interaction of such winds with the ISM, the exact driving mechanism of the wind on small scales is not important. The wind can be parameterised as having a typical momentum flux of (e.g., Faucher-Giguère & Quataert, 2012)

$$\dot{p}_w = \dot{M}_w v_w = \tau \frac{L_{\text{AGN}}}{c} \quad (1.18)$$

where  $\dot{M}_w$  and  $v_w$  are the wind mass outflow rate and velocity respectively and  $\tau$  is the optical depth of the wind at the launch radius. Assuming that the AGN is at the Eddington limit, i.e.  $L_{\text{AGN}} = L_{\text{Edd}} = \eta \dot{M}_{\text{Edd}} c^2$ , then the outflow velocity is given as

$$v_w = \tau \eta \frac{\dot{M}_{\text{Edd}}}{\dot{M}_w} c \sim 0.1c \quad (1.19)$$

where the value of  $0.1c$  arises self consistently for an outflow with  $\dot{M}_{\text{Edd}}/\dot{M}_w = 1$ ,  $\eta = 0.1$

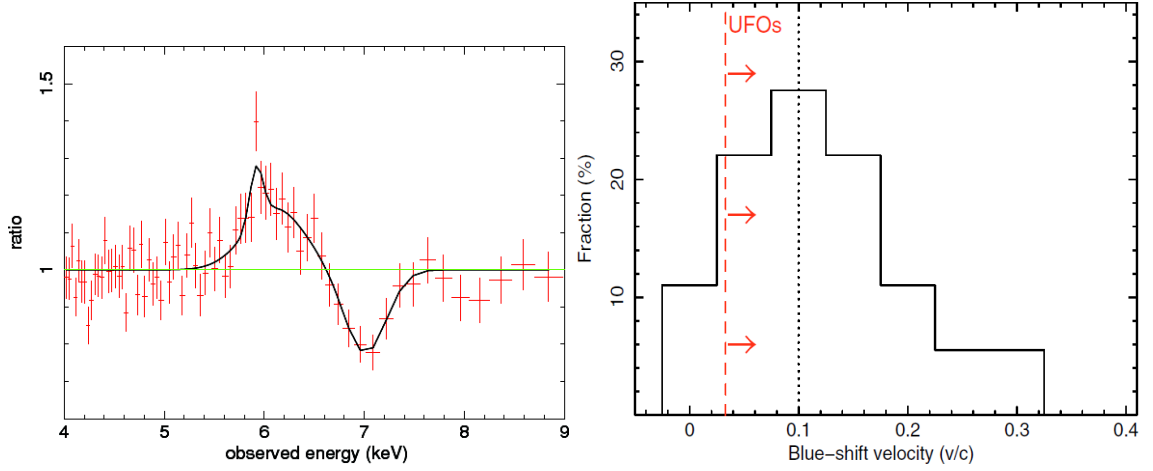


Figure 1.6: LHS: Fe K profile from stacked observations of PG1211+134, along with a fit, taken from Pounds & Reeves (2009, figure 8.). The profile shows a P Cygni like shape comprising of emission and blue-shifted absorption, typical of an outflow. RHS: Histogram of UFO velocities (taken from Tombesi et al., 2010a, A&A, reproduced with permission, © ESO). The vertical red-dashed line shows the velocity cutoff for the absorber to be determined an UFO while the vertical black-dotted line shows the peak and mean velocity of  $\sim 0.1$  c.

and  $\tau = 1$  at the launch radius. In the case of radiative driving of the wind this suggests that every photon scatters once giving up all of its momentum to the outflow, which is consistent with theoretical predictions (King & Pounds, 2003). Combining equations 1.18 and 1.19 we find an energy flux for the wind of

$$\dot{E}_w = \frac{1}{2} \dot{M}_w v_{\text{wind}}^2 = \frac{\tau}{2} \frac{L_{\text{AGN}}}{c} v_w \quad (1.20)$$

which for an Eddington limited outflow is given as (King, 2010)

$$\dot{E}_w = \frac{\eta}{2} L_{\text{Edd}} \sim 0.05 L_{\text{Edd}} \quad (1.21)$$

If such winds are the main way in which the radiation emitted during accretion onto the black hole couples with the bulge gas, then we can see that the useful energy emitted in growing the black hole is reduced by a factor of  $\eta/2$  and so equation (1.17) becomes

$$\frac{E_{\text{BH}}}{E_{\text{bulge}}} \sim 0.005 \frac{\eta^2}{2 f_g} \frac{c^2}{\sigma^2} \sim 56.25 f_g^{-1}. \quad (1.22)$$

While being significantly less than the value in equation (1.17), this is still a significant

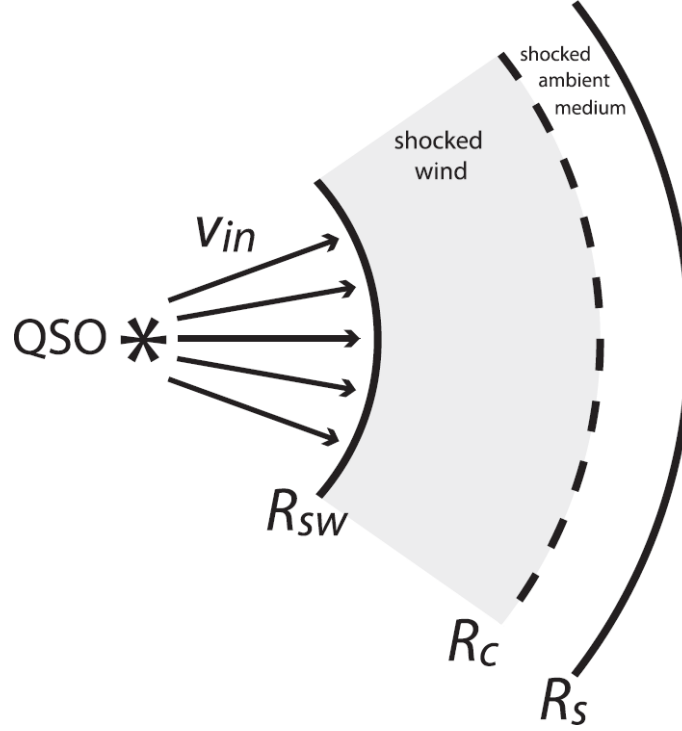


Figure 1.7: A schematic of the expected shock pattern resulting from the wind-ISM interaction taken from Faucher-Giguère & Quataert (2012, figure 1.). The wind collides with the ambient ISM producing a reverse wind shock ( $R_{sw}$ ) and forward shock ( $R_s$ ) into the ISM separated by a contact discontinuity ( $R_c$ ). The cooling of the wind shock is expected to determine the evolution of the outflow.

value, suggesting that not all of the energy within the wind is communicated to the ISM.

#### 1.6.1.1 To cool or not to cool?

The winds interact with the bulge gas through colliding with and shocking against the ambient ISM. This results in the formation of a reverse shock into the wind and a forward shock into the ISM as illustrated in Figure 1.7, taken from Faucher-Giguère & Quataert (2012, figure 1.). The velocity of the reverse shock ( $R_{sw}$  in figure 1.7) is considerable less than the wind velocity (Faucher-Giguère & Quataert, 2012) and, from strong-shock jump conditions, the velocity of the shocked wind directly behind the shock drops by a factor 4 while the density increases by a factor 4 and is given as

$$\rho_{sw} = 4\rho_w = \frac{\dot{M}_w}{\pi R^2 v_w} \quad (1.23)$$

where  $\rho_w$  is the wind density and  $R$  is the shock radius. From conservation of momentum, the pressure directly behind the shock is then given as  $P_{sw} = (3/4)\rho_w v_w^2$ . Combining this with  $Pm_i = \rho k_B T$ , the temperatures of the protons and electrons are given as

$$T_i = \frac{3}{16} \frac{m_i}{k_B} v_w^2 \sim \begin{cases} 2 \times 10^{10} \left( \frac{v_w}{0.1c} \right)^2 & \text{K for protons} \\ 1 \times 10^7 \left( \frac{v_w}{0.1c} \right)^2 & \text{K for electrons.} \end{cases} \quad (1.24)$$

How the shock evolves beyond the initial shock phase and the subsequent evolution of the outflow ultimately depends on whether or not the shocked wind can cool. There are two main regimes for the outflow, which depend on the relative magnitudes of the cooling time,  $t_c$ , and the flow time,  $t_{\text{flow}} = R/v$ , where  $v$  is the outflow velocity of the shock pattern (not to be confused with  $v_w$ ). If  $t_c \ll t_{\text{flow}}$ , then the shocked wind can cool effectively. This results in the post shock gas pressure tending to the pre-shock ram pressure, i.e.  $P_{sw} = \rho_w v_w^2 = L_{\text{Edd}}/(4\pi R^2 c)$ , which goes into driving out the ambient ISM and is known as the momentum driven regime. However, if  $t_c \gg t_{\text{flow}}$ , then the shocked wind cannot cool, retains the thermalised kinetic energy and results in an outflow driven by the thermal pressure within the shocked wind bubble. This is known as the energy driven regime.

Inverse Compton (IC) scattering of soft AGN photons with hot electrons in the shocked wind is expected to be the dominant cooling mechanism for AGN wind shocks (Ciotti & Ostriker, 1997, 2001; King, 2003). The cooling time for this process is given as (King, 2003)

$$t_{\text{IC}} = \frac{3}{8\pi} \frac{m_e c}{\sigma_T U_{\text{rad}}} \frac{m_e c^2}{E} \quad (1.25)$$

where  $E = \gamma m_e c^2$  is the energy of a shocked electron and

$$U_{\text{rad}} = \frac{L_{\text{Edd}}}{4\pi R^2 c} \quad (1.26)$$

is the energy density of the AGN radiation field. IC cooling only acts on electrons, however, most of the energy within the shock is carried by the protons. Therefore one should consider the coupling between the electrons and protons. Assuming that the electrons and protons rapidly reach thermal equilibrium and the shocked wind is in the one-temperature (1T) regime i.e.,  $T_e = T_p$ , King (2003) gives the IC cooling time as

$$t_{\text{IC}} \simeq 10^7 \left( \frac{R}{1 \text{ kpc}} \right)^2 \left( \frac{v_w}{0.1c} \right)^{-2} \left( \frac{M_{\text{BH}}}{10^8 M_\odot} \right)^{-1} \text{ yr.} \quad (1.27)$$

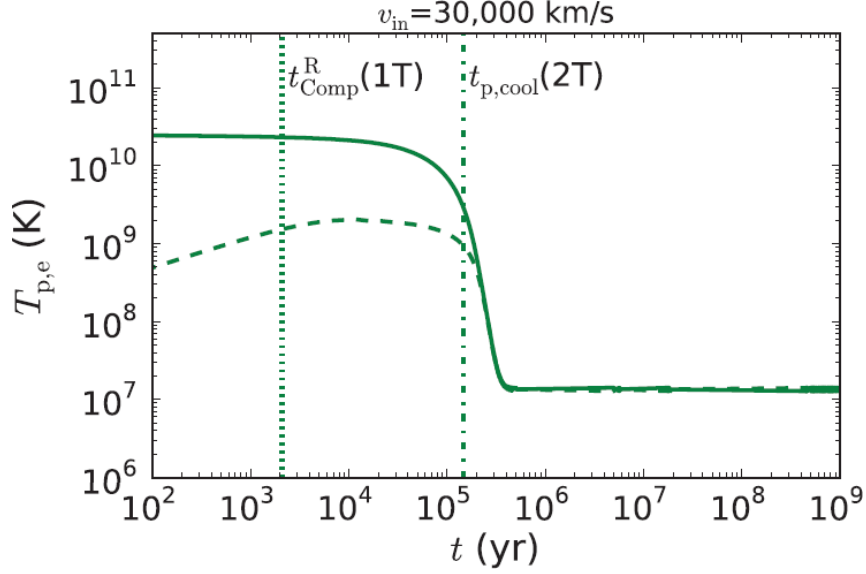


Figure 1.8: Temperature evolution of the protons (solid line) and electrons (dashed line) for an outflow velocity of  $0.1 c$  (typical for an UFO), at a radius of 10 pc. The vertical dotted and dot-dashed lines show the 1 and 2 temperature cooling times respectively. Figure taken from Faucher-Giguère & Quataert (2012, middle panel, figure 2.)

Equating this to the momentum driven flow time (Zubovas & King, 2012b)

$$t_{\text{flow}} = 7 \times 10^6 \left( \frac{R}{1 \text{ kpc}} \right) \left( \frac{\sigma}{200 \text{ kms}^{-1}} \right) \left( \frac{M_{\text{bh}}}{10^8 M_{\odot}} \right)^{-1/2} \left( \frac{f_g}{0.16} \right)^{-1/2} \text{ yr}, \quad (1.28)$$

one can rearrange to define a cooling radius (Zubovas & King, 2012b):

$$R_{\text{IC}} \sim 520 \left( \frac{\sigma}{200 \text{ kms}^{-1}} \right) \left( \frac{M_{\text{bh}}}{10^8 M_{\odot}} \right)^{1/2} \left( \frac{v_w}{c} \right)^2 \left( \frac{f_g}{0.16} \right)^{1/2} \text{ pc}, \quad (1.29)$$

which approximately defines the transition between a momentum or energy driven outflow. Therefore within the central few hundred parsecs of the host galaxy the outflow is expected to be momentum driven, while beyond this it is expected that the outflow becomes energy driven.

However, it is not clear that the 1T assumption is correct and one may need to account for two-temperature (2T) processes. Assuming Coulomb collisions dominate the energy exchange between protons and electrons, the timescale on which they reach equipartition

is given as (Faucher-Giguère & Quataert, 2012)

$$t_{\text{ep}} = \frac{3m_e m_p}{8(2\pi)^{0.5} n_p e^4 \ln \Lambda} \left( \frac{k_B T_e}{m_e} + \frac{k_B T_p}{m_p} \right)^{\frac{3}{2}} \quad (1.30)$$

where

$$\ln \Lambda \approx 39 + \ln \left( \frac{T_e}{10^{10} \text{K}} \right) - \frac{1}{2} \ln \left( \frac{n_e}{1 \text{cm}^{-3}} \right), \quad (1.31)$$

is the Coulomb logarithm and  $n_e$  and  $n_p$  are the electron and proton number density respectively. equation (1.29) is only valid for the regime in which  $t_{\text{ep}} \ll t_c$ . Faucher-Giguère & Quataert (2012) investigated the impact of the Coulomb interaction and found that, depending on the wind properties, the effective cooling time of the gas increases by a factor  $\sim 10 - 100$ . Figure 1.8, taken from their paper (middle panel, figure 2.), shows the temperature evolution of the protons (solid line) and electrons (dashed line) for an outflow velocity of  $0.1 c$  (typical for an UFO) at a radius of  $10 \text{ pc}$ . The vertical dotted and dot-dashed lines show the 1T and 2T cooling times respectively. The increase in cooling time results in the cooling radius, defined in equation (1.29), shrinking by the same factor, essentially resulting in the outflow always being in the energy driven regime. This could have profound effects on how an outflow impacts upon the host galaxy. In light of this, Chapter 3 attempts to establish observational signatures of the shocked wind which can potentially be used to distinguish between the 1T and 2T regimes.

### 1.6.1.2 Driving scaling relations with momentum (and energy)

In this section I consider the critical value for  $M_{\text{BH}}$  needed to clear a host galaxy of its gas in either the momentum or energy driven regimes. This value can then be compared to equation (1.16) to gain physical insight into how the AGN feedback couples to the ISM. Such derivations have already been performed in the literature by a number of authors (e.g., Silk & Rees, 1998; King, 2003, 2005; Murray et al., 2005; Costa et al., 2014) and typically involve solving for the motion of a shell of gas in a background potential. It is expected that as the shock propagates outwards it sweeps up the ambient ISM into such a shell for which the equation of motion is (King, 2005)

$$\frac{d[M_{\text{sh}}(R) \dot{R}]}{dt} = 4\pi R^2 P_{\text{sw}} - \frac{GM_{\text{sh}}(R) [M_{\text{BH}} + M_{\text{tot}}(R)]}{R^2}, \quad (1.32)$$

where  $M_{\text{sh}}(R)$  is the mass of the shell at radius  $R$ ,  $M_{\text{tot}}(R)$  is the total mass of material remaining within  $R$ , including dark matter and stars, and  $P_{\text{sw}}$  describes the pressure driving



the outflow. We note that  $M_{\text{sh}}(R) = M_{\text{gas}}(R)$ , which is the mass of gas originally within  $R$ . For a halo and gas profile following that of a singular isothermal sphere (SIS, e.g., §4.3.3b Binney & Tremaine, 2008), the radial density profile follows as

$$\rho(R) = \frac{f\sigma^2}{2\pi GR^2} \quad (1.33)$$

and the enclosed mass profile follows as

$$M(R) = \frac{2f\sigma^2 R}{G} \quad (1.34)$$

where  $f = 1$  for the properties of the underlying potential (e.g., dark matter, stars and gas) and  $f = f_g = M_g/M_{\text{tot}}$  for the gas component. Far from the black hole we can neglect the contribution of  $M_{\text{BH}}$  in equation (1.32), which can then be written as

$$\frac{d[M_{\text{sh}}(R)\dot{R}]}{dt} = 4\pi R^2 P_{\text{sw}} - \frac{4f_g}{G}\sigma^4 \quad (1.35)$$

First considering the momentum driven limit, we set the post shock pressure to the pre-shock ram pressure and so  $4\pi R^2 P_{\text{sw}} = L_{\text{Edd}}/c$ . Balancing the force of the outflow with the weight of the ambient gas in the galaxy we find that

$$\frac{L_{\text{Edd}}}{c} = \frac{4f_g\sigma^4}{G}. \quad (1.36)$$

Substituting in for  $L_{\text{Edd}}$  and rearranging gives a critical black hole mass of (King, 2005)

$$M_{\sigma,p} = \frac{f_g K}{\pi G^2} \sigma^4 \simeq 4.56 \times 10^8 \left( \frac{\sigma}{200 \text{ kms}^{-1}} \right)^4 \left( \frac{f_g}{0.2} \right) M_{\odot}, \quad (1.37)$$

above which a momentum driven outflow is able to sweep up and clear out the gas within the host galaxy. Further work by McQuillin & McLaughlin (2012) has investigated the effect of alternative background density profiles and found that the result of King (2005) still holds with

$$M_{\sigma,p} \rightarrow \frac{f_g K}{\pi G^2} \frac{V_{\text{c,pk}}^4}{4} \simeq 1.14 \times 10^8 \left( \frac{V_{\text{c,pk}}}{200 \text{ kms}^{-1}} \right)^4 \left( \frac{f_g}{0.2} \right) M_{\odot}, \quad (1.38)$$

where  $V_{\text{c,pk}}$  is the peak circular velocity of the galaxy potential. The solutions match the observed  $M_{\text{BH}} - \sigma$  relation given in equation (1.16) remarkably well, suggesting that it

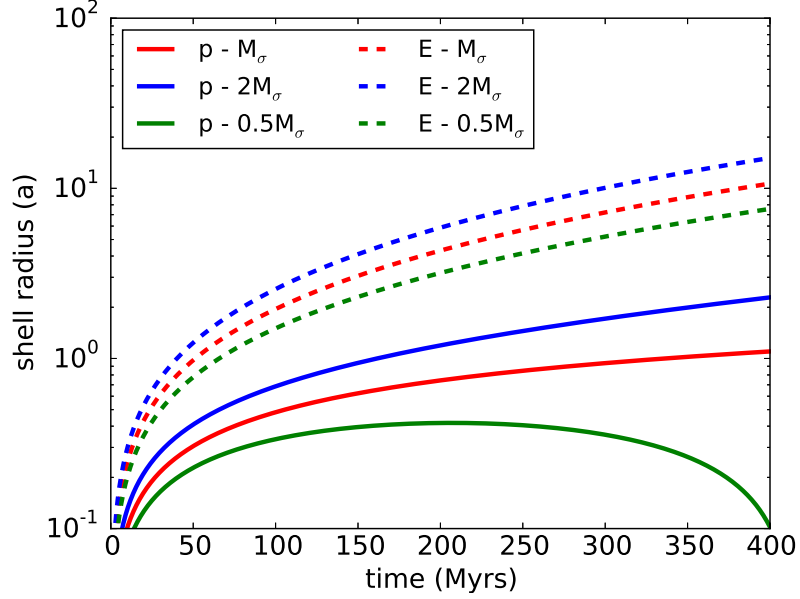


Figure 1.9: Solution to equation (1.32) showing the time evolution of the radius of the swept up shell. The gas and background potential follow a Hernquist (1990) profile with  $f_g = 0.2$ . A momentum driven outflow is shown by the solid lines while the addition of energy driving is shown by the dashed lines. The green, red and blue lines are for black hole masses equal to 0.5, 1 and 2 times the  $M_{\text{BH}} - \sigma$  mass as given by equation (1.38).

is the momentum of the black hole wind that effects the host galaxy. Figure 1.9 shows the evolution of the swept up shell radius, which I calculated by numerically solving equation (1.32) assuming the gas and background potential follow a Hernquist (1990) profile with  $f_g = 0.2$ . The solid lines show the solution for a momentum driven outflow with a black hole mass of 0.5, 1 and 2 times the  $M_{\sigma,p}$  (given by equation (1.38) in green, red and blue respectively. Also shown, by the dashed lines, are solutions for an energy driven outflow with the same black hole masses. We can see that for  $M_{\text{BH}} < M_{\sigma,p}$  (green line) the momentum driven solution stalls and shrinks, however for  $M_{\text{BH}} \gtrsim M_{\sigma,p}$  the shell can escape. However, in the energy driven regime, all of the solutions can clear the gas out of the galaxy potential. This highlights that the  $M_{\text{BH}} - \sigma$  relation is likely driven by the momentum of the feedback. Despite this, a purely momentum driven outflow cannot explain the high momentum fluxes observed for large scale outflows and so we now consider the energy-driven limit. Following Zubovas & King (2012a), from conservation of energy we see that

$$\frac{1}{2} \dot{M}_w v_w^2 \simeq \frac{1}{2} \dot{M}_{\text{out}} v_{\text{out}}^2 \quad (1.39)$$

where  $\dot{M}_{\text{out}}$  and  $v_{\text{out}}$  are, respectively, the mass flux and velocity of the large-scale outflow. This can be rewritten as

$$\frac{\dot{p}_{\text{w}}^2}{2\dot{M}_{\text{w}}} \simeq \frac{\dot{p}_{\text{out}}^2}{2\dot{M}_{\text{out}}} \quad (1.40)$$

where  $\dot{p}_{\text{out}}$  is the momentum flux of the large-scale outflow which is found to be

$$\dot{p}_{\text{out}} \simeq \dot{p}_{\text{w}} \left( \frac{\dot{M}_{\text{out}}}{\dot{M}_{\text{w}}} \right)^{1/2} \simeq \frac{L_{\text{Edd}}}{c} \left( \frac{\dot{M}_{\text{out}}}{\dot{M}_{\text{w}}} \right)^{1/2} \quad (1.41)$$

where we have used  $\dot{p}_{\text{w}} = L_{\text{Edd}}/c$ . For an SIS potential and setting  $f_{\text{g}} = 0.16$ , the expanding bubble sweeps up ambient material such that  $\dot{M}_{\text{out}} \sim 420\dot{M}_{\text{w}}$  (Zubovas & King, 2012a). This therefore provides an explanation for the observed momentum fluxes for large scale outflows of  $\dot{p}_{\text{out}} \sim 20L_{\text{Edd}}/c$ . Nonetheless, as shown in Figure 1.9, an energy driven outflow cannot be reconciled with the  $M_{\text{BH}} - \sigma$  relation, as I now show analytically.

In the energy driven limit it is the thermal pressure of the bubble that drives out material and so we need to solve the energy equation of the hot bubble (Zubovas & Nayakshin, 2014, equation 5, neglecting their final term)

$$\frac{d[2\pi R^3 P_{\text{sw}}]}{dt} = \frac{\eta}{2} L_{\text{Edd}} - P_{\text{sw}} \frac{dV}{dt} - \frac{4f_{\text{g}}\sigma^4}{G} \frac{dR}{dt} \quad (1.42)$$

where we have assumed an SIS potential and the terms on the RHS are the rate of energy injection into the bubble, adiabatic expansion loss rate and work done against gravity in moving the gas shell in the background potential. Assuming a constant shell velocity, i.e.  $v = R/t$ , equation (1.35) can be written as (Zubovas & Nayakshin, 2014)

$$4\pi R^2 P_{\text{sw}} = \frac{2f_{\text{g}}\sigma^2}{G} (v^2 + 2\sigma^2). \quad (1.43)$$

By substituting this into equation (1.42), the LHS becomes

$$\frac{d}{dt} \left[ \frac{f_{\text{g}}\sigma^2}{G} (v^2 + 2\sigma^2) R \right] = \frac{f_{\text{g}}\sigma^2}{G} (v^2 + 2\sigma^2) \frac{dR}{dt} = \frac{f_{\text{g}}\sigma^2}{G} (v^3 + 2\sigma^2 v), \quad (1.44)$$

while the RHS becomes

$$\frac{\eta}{2} L_{\text{Edd}} - \frac{f_{\text{g}}\sigma^2}{2\pi R^2 G} (v^2 + 2\sigma^2) \frac{dV}{dt} - \frac{4f_{\text{g}}\sigma^4}{G} \frac{dR}{dt} = \frac{\eta}{2} L_{\text{Edd}} - \frac{2f_{\text{g}}\sigma^2}{G} (v^3 + 2\sigma^2 v) - \frac{4f_{\text{g}}\sigma^4}{G} v, \quad (1.45)$$

where I have used

$$\frac{dV}{dt} = 4\pi R^2 v. \quad (1.46)$$

Equating equations 1.44 and 1.45 and rearranging I find that

$$\frac{\eta G L_{\text{Edd}}}{2 f_g \sigma^2} = 3v^3 + 10\sigma^2 v. \quad (1.47)$$

Finally, assuming, as in Costa et al. (2014), that the necessary velocity to escape the halo is  $v = 2\sigma$ , substituting in for  $L_{\text{Edd}}$  and rearranging gives a critical black hole mass of

$$M_{\sigma,E} = \frac{22 f_g \kappa}{\eta c \pi G^2} \sigma^5 = \frac{22}{\eta} \frac{\sigma}{c} M_{\sigma,p} \quad (1.48)$$

which sits significantly below the observed  $M_{\text{BH}} - \sigma$  relation. This suggests that we require momentum driving to set the  $M_{\text{BH}} - \sigma$  relation, but energy driving to explain the momentum fluxes of large scale outflows. The models in which IC cooling is effective within a radius of  $\sim 500$  pc (e.g., King, 2003, 2005, 2010; Zubovas & King, 2012a,b) provide a natural explanation to this scenario. However, if correct, the findings of Faucher-Giguère & Quataert (2012), that 2T effects can seriously inhibit cooling beyond a few parsecs, pose problems to these models and an alternative method of energy loss may be needed. Nayakshin (2014) has proposed such an alternative in the form of energy losses through low density channels in a multiphase ISM. In this model high density clumps, which carry most of the mass, only feel the ram pressure of the outflow, which itself can escape through low density channels in the energy driven regime. This model provides the motivation for Chapter 4 in this thesis.

## 1.6.2 The role of AGN feedback in galaxy formation simulations

As we have seen in the previous sections, analytical models have invoked AGN feedback in order to explain the observed scaling relations (Silk & Rees, 1998; Fabian, 1999; King, 2003, 2005; Murray et al., 2005; Nayakshin, 2014) and observational properties (Faucher-Giguère & Quataert, 2012; Zubovas & King, 2012a) of SMBHs and their host galaxies. AGN feedback is also an important ingredient in cosmological simulations (e.g., Springel et al., 2005; Schaye et al., 2010; Dubois et al., 2012; Schaye et al., 2015) in order to quench star formation and produce *red and dead*<sup>5</sup> galaxies at the high mass end.

---

<sup>5</sup>By red and dead I refer to galaxies, typically ellipticals, which consist only of old stellar populations that are *red* in colour and are not undergoing any new episodes of star formation and hence are *dead*.

This is a necessity if simulations are to match observations such as the galaxy luminosity function and  $M_{\text{BH}} - \sigma$  relation. The important ingredient in simulations is self-regulation (Schaye et al., 2015). The analytical models discussed previously simply assume an Edington limited feedback episode that is not linked to accretion onto the black hole. However, in cosmological simulations the rate at which energy is injected into the ISM,  $\dot{E}$  is linked to the accretion rate such that

$$\dot{E} = \epsilon_{\text{BH}} \dot{m}_{\text{accr}} c^2 \quad (1.49)$$

where  $\dot{m}_{\text{accr}}$  is the rate at which the SMBH accretes gas,  $c$  is the speed of light and  $\epsilon_{\text{BH}}$  is an efficiency parameter. In such a scenario the feedback and accretion regulate each other such that an  $\dot{E}$  is reached whereby feedback driven outflows balance gas inflow. The black hole mass for which this occurs will be determined by the chosen value of  $\epsilon_{\text{BH}}$  such that  $M_{\text{BH}} \propto \epsilon_{\text{BH}}^{-1}$  (Booth & Schaye, 2010). As long as the chosen value for  $\epsilon_{\text{BH}}$  is non-zero, the equilibrium value of  $\dot{E}$  is always the same. This means that self-regulation renders the feedback efficiency irrelevant when determining AGN outflow rates (Schaye et al., 2015) and hence also has no impact upon the global properties of the galaxy such as the stellar mass (e.g. Di Matteo et al., 2005; Springel et al., 2005; Sijacki et al., 2007; Booth & Schaye, 2009, 2010).

Given that  $\epsilon_{\text{BH}}$  purely determines  $M_{\text{BH}}$ , simulators are able to tune it to a value such that they are able to match, for example, the  $M_{\text{BH}} - \sigma$  relation. However,  $\epsilon_{\text{BH}}$  cannot be considered a prediction of the simulations as there are numerical artefacts that can affect the overall efficiency of AGN feedback. These may include radiative cooling in the ISM (which may be over-predicted due to poor resolution), which is a further external energy loss mechanism in addition to  $\epsilon_{\text{BH}}$ . Potential numerical influences in determining feedback efficiency are the focus of Chapter 3.

## 1.7 This thesis

This thesis consists of six chapters; a scientific introduction, an introduction to hydrodynamical simulations with GADGET, three science chapters and a conclusion. Here I summarise the science chapters, each of which focus on an aspect of AGN feedback and its interaction with the host galaxy. Such feedback is thought to play a key role in regulating the growth of galaxies and in driving the observed scaling relations. Indeed galaxy formation modellers often have to invoke AGN feedback, especially at the high mass end,

to quench star formation.

A potential source of such AGN feedback are the UFOs introduced in section 1.6.1. Chapter 3 presents calculations of the observational signatures of the wind shock. In particular I calculate the IC spectrum emitted and find stark differences between the spectral shape when the shock is in the 1T and 2T regime. I find a broad feature in mid-to-high energy X-rays in the 1T case but a narrower feature only in the soft X-rays for the 2T regime. While the 1T component should be observable, current data do not seem to show evidence for such a component. The 2T component is likely much more difficult to observe and in fact it is possible that the observed soft X-ray excess of AGN is partially or fully due to the 2T shock emission. The lack of evidence for the 1T component may suggest that UFOs are in the energy-driven regime outside of the central few pc. This means that they inject considerable amounts of energy into the host ISM. I suggest that additional X-ray observations are necessary in order to constrain AGN feedback models further.

Given the results of Faucher-Giguère & Quataert (2012) and Chapter 3 (Bourne & Nayakshin, 2013), it is evident that other channels for energy loss, beyond IC cooling, may be necessary to ensure that AGN feedback does not completely destroy its host galaxy. One potential solution is to consider feedback acting on an inhomogeneous ambient gas distribution. To this end, Chapter 4 presents high-resolution simulations of a thermalised UFO impacting the host ISM. Inhomogeneity of the ambient gas strongly effects the evolution and efficiency of the feedback. Similar to the analytical models of an energy driven outflow discussed in section 1.6.1.2, all of the ambient gas is driven outward rapidly for a homogeneous and spherically symmetric gas distribution. However, if the ambient gas is clumpy and inhomogeneous, the mass and energy flows can decouple. The shocked UFO is able to escape the system through low density channels whilst high density clumps and filaments are only weakly affected. In fact the clumps should only feel the ram-pressure of the outflow. Such energy leakage could therefore provide an alternative explanation as to why feedback only weakly couples with the host galaxy's ISM.

Finally, Chapter 5 is concerned with the numerical modelling of AGN feedback. Cosmological and galaxy formation simulations using the SPH technique have been performed across a wide range of resolutions and yet the same sub-grid AGN feedback prescription is often employed. Therefore I carry out a resolution study to understand how the simulated AGN feedback changes when only the SPH particle mass changes. The simulations explored in this chapter model an energy driven outflow and how it interacts

with a turbulent and clumpy interstellar medium (ISM). I test a standard feedback method (e.g., Di Matteo et al., 2005) at 4 different resolutions which span four orders of magnitude. I find that at lower resolution feedback becomes more efficient at clearing out all gas in its path. The difference in the mass of the gas ejected by the feedback can vary by more than an order of magnitude between the highest and lowest resolution simulations. While high density clumps and low density channels can be resolved at high resolution, they are washed out at low resolutions, which as we saw in Chapter 2, can affect the efficiency of the feedback. I also investigate the role of IC cooling, finding, as expected, that if included it only has an impact at high resolution when the feedback bubble can reach sufficiently high temperatures.

---

# 2

## Hydrodynamic simulations (with GADGET)

*“Everyone knows that debugging is twice as hard as writing a program in the first place. So if you’re as clever as you can be when you write it, how will you ever debug it?”*

*Kernighan & Plauger (1978)*



## 2.1 Astrophysical simulations

While many significant works and much progress has been made using simple analytical models to understand astrophysical processes, some problems become so complicated and mathematically involved that it is necessary to utilise computers to help simulate and understand various processes. One of the earliest “*simulations*”, carried out by Holmberg (1941), modelled the close gravitational interaction of two *nebulae*, each of which were modelled by 37 light bulbs. The power of each light bulb represented mass while measurements of the light intensity represented gravity. However the first N-body (see Section 2.2) simulations performed using a computer are attributed to von Hoerner (1960), who used up to  $N = 16$  particles. Despite such simple beginnings, thanks to vast improvements in computational power the largest N-body simulations can now employ hundreds of billions of particles, such as the Millennium-XXL simulations (Angulo et al., 2012), which simulated a 4.1 Gpc cosmological box with 303 billion particles. I point the interested reader to the review of Dehnen & Read (2011) for more information on N-body simulations.

Such simulations purely model the gravity of astrophysical systems, much of the interesting physics in galaxy formation also requires simulation of the baryonic component and one therefore has to employ hydrodynamical simulations. Such simulations can typically be split into two types; Eulerian, which discretise space and Lagrangian, which discretise mass. Such techniques have been used to simulate a number of astrophysical systems from proto-planetary discs (Rice et al., 2003, 2004; Alexander et al., 2008) to large cosmological volumes (Springel et al., 2005; Di Matteo et al., 2008; Schaye et al., 2010; Dubois et al., 2012; Schaye et al., 2015; Vogelsberger et al., 2014). Similar to the N-body simulations in the previous paragraph, the scale of hydrodynamical simulations has also improved vastly. While the original smooth particle hydrodynamics (SPH, see Section 2.3) simulations of Gingold & Monaghan (1977) used only 80 particles, modern SPH simulations can employ billions of particles, for example the recent EAGLE simulation (Schaye et al., 2015) used up to  $3.4 \times 10^9$  SPH particles as well as another  $3.4 \times 10^9$  N-body particles to model dark matter.

In this thesis I make use of the hybrid N-body/hydrodynamical SPH code GADGET-3, a modified version of GADGET-2 presented in Springel (2005). This code solves for gravitational interactions using the collisionless N-body approach and solves the hydrodynamics of the gas using the SPH technique. I discuss these methods, as well as other processes and modifications implemented in the code, in this chapter.

## 2.2 Gravity and the N-body technique

GADGET makes use of the N-body technique to solve for gravity. In this approach the gravitational force acting on a single particle is calculated from the underlying gravitational potential of the body of particles. This is a key point with regard to the collisionless n-body approach, as it is the gravity due to a *smooth* mass distribution that is calculated. The gravitational potential  $\Phi$  is then given by Poisson's equation:

$$\nabla^2 \Phi = 4\pi G \rho, \quad (2.1)$$

where  $\rho$  is the *smooth* density distribution of the particles. If we consider the exact solution for the gravitational force acting upon a single particle due to the other  $N - 1$  bodies within an N-body system, it is given as

$$m_i \ddot{\mathbf{x}}_i = -G \sum_{j \neq i}^N m_i m_j \frac{\mathbf{x}_i - \mathbf{x}_j}{|\mathbf{x}_i - \mathbf{x}_j|^3}, \quad (2.2)$$

where  $m$  is the mass of a particle,  $\ddot{\mathbf{x}}$  is the particle acceleration and  $\mathbf{x}$  is the particle position. This approach requires a loop over  $N$  particles to calculate the force acting on a single particle and so to calculate the force acting on all  $N$  particles requires another loop over  $N$ . Therefore the time it takes to carryout this calculation scales as  $N^2$ , which can be prohibitively long for very large  $N$  simulations. It is therefore necessary to use algorithms that make suitable approximations in order to calculate the gravitational force quickly and efficiently while still providing robust results.

A commonly used method is the Tree algorithm which makes use of the fact that the gravitational force follows an inverse square law. This means that the forces calculated over large distances can be approximated whilst still providing an accurate result. The tree algorithm works by splitting up space into a tree structure, starting with a root node (containing all of the particles), which is then repeatedly divided into cells containing successively fewer particles, until the leaves of the tree are reached. Tree leaves do not necessarily contain single particles but rather present the case whereby if the gravitational force estimated using a leaf cell is not accurate enough then the gravitational force is calculated by direct summation over all of the particles in the leaf cell (Dehnen & Read, 2011). A popular method for the exact division of space is the Barnes and Hut oct tree (Barnes & Hut, 1986), which splits each parent node into 8 cubic child nodes, (see Figure 2.1, taken from Springel et al., 2001). The contribution to the gravitational potential

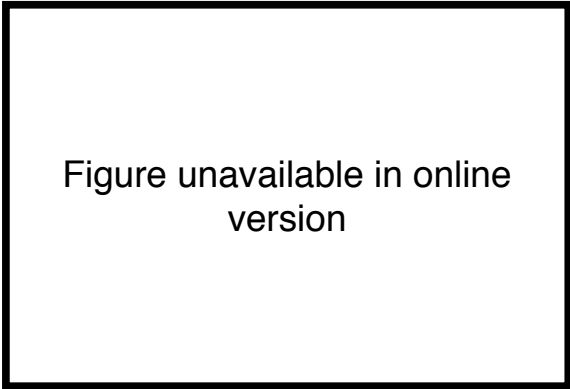


Figure unavailable in online  
version

Figure 2.1: Two dimensional illustration of the Barnes and Hut oct tree. Here the root node is split into 4 daughter nodes, which are then again divided until each cell contains only 1 particle, these represent the leaves of the tree. Reprinted from New Astronomy, Springel et al. (2001), copyright (2001), with permission from Elsevier.

at a point of interest by a group of particles within a cell a distance  $\mathbf{r}$  away, can be approximated by grouping those particles together and assessing the gravity due to their combined mass assuming it is all at the centre of mass of the cell. This means that the gravitational force acting on a particle can be calculated without looping over all of the other  $N - 1$  particles and as such the time to carry out the calculation scales as  $N \ln N$ , opposed to  $N^2$  in the direct summation case.

When calculating the gravitational potential, it is clear from equation (2.2) that it diverges as particles approach one another. While such a divergence is physical when each particle represents a single body, in the collisionless limit this is not the case. Instead the entire population of particles (whose individual masses can exceed the mass of physical objects within the system by many orders of magnitude) is used to represent the underlying mass distribution of the system and as such any close encounters between the particles and the possible formation of binaries is entirely unphysical. In order to suppress this behaviour the gravitational force is softened when two particles get close to one another, which as well as inhibiting undesired two-body effects, also allows more efficient use of computational resources by preventing tight binaries, which require accurate integration and tiny timesteps, from forming (Dehnen & Read, 2011).

Following Springel et al. (2001), the potential at the point  $\mathbf{r}$  due to a group of particles with positions  $\mathbf{x}_k$  is given by

$$\Phi_{\text{node}}(\mathbf{r}) = -G \sum_k m_k g(|\mathbf{x}_k - \mathbf{r}|) \quad (2.3)$$

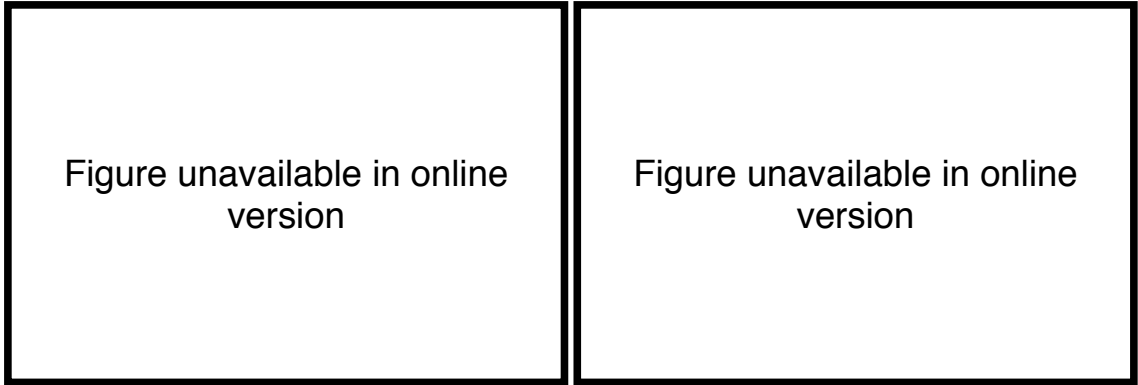


Figure 2.2: The spline softened (solid) and Plummer softened (dotted) potential (LHS) and force (RHS) of a point mass with  $h = 1$  and  $\epsilon = h/2.8$  respectively. For comparison the dashed line which shows the Newtonian solution. Reprinted from New Astronomy, Springel et al. (2001), copyright (2001), with permission from Elsevier.

where  $g(r)$  defines the softened force law, which in the Newtonian limit is  $g(r) = 1/r$ . GADGET makes use of spline softening such that within the smoothing length  $h_i$  of a particle of mass  $m_i$ , the gravitational force is assumed to be due to a density distribution  $\rho(\mathbf{r}) = mW(\mathbf{r}, h)$ , where  $W(\mathbf{r}, h)$  is the normalised cubic spline kernel (see equation (2.15)). The spline softened gravity is therefore given as (Springel et al., 2001)

$$g(r) = -\frac{1}{h}W_2\left(\frac{r}{h}\right), \quad (2.4)$$

where  $W_2(r/h)$  is calculated from  $W(\mathbf{r}, h)$  such that  $\nabla^2 [W_2(r/h)/h] = 4\pi W(\mathbf{r}, h)$ , which arises from substituting  $\rho(\mathbf{r}) = mW(\mathbf{r}, h)$  into equation (2.1) and solving for  $\Phi$ . A feature of this approach, when compared to the Plummer softening method, is that the force is exactly Newtonian for  $r/h > 1$ . Figure 2.2, taken from Springel et al. (2001), compares these methods and shows the kernel softened (solid), Plummer softened (dotted) and exact Newtonian (dashed) potential (LHS) and force (RHS) due to a point mass. For the kernel method  $h = 1$  whilst the Plummer equivalent softening length is  $\epsilon = h/2.8$  which ensures the minimum of the potential is equal.

As in Springel et al. (2001), we can define the vector  $\mathbf{y} = \mathbf{r} - \mathbf{s}$  where  $\mathbf{s}$  is the center-of-mass of the group of particles with total mass  $M$ . Assuming  $|\mathbf{y}| \gg |\mathbf{x}_k - \mathbf{s}|$ , the potential at the point  $\mathbf{r}$  can be expanded as a multi-pole series, however from GADGET-2 onwards the potential is estimated using only the monopole term (Springel, 2005) and so

$$\Phi(\mathbf{r}) = -GMg(y). \quad (2.5)$$

Once the tree has been constructed it is *walked* for each particle starting from the root node. Whether or not the code proceeds to and opens up the next cell is decided by using a cell opening criterion, which in the case of GADGET-2 attempts to compare the truncation error with the total expected force on the particle. As mentioned, GADGET-2 only uses the monopole term when calculating the gravitational force, which results in an error due to the truncation of the multipole expansion. The error is estimated to be equal to the largest higher order term not considered in the force calculation, which is the quadrupole moment (as the dipole moment is zero) and is estimated as  $GM/y^2(l/y)^2$ , where  $l$  is the size of the node. The total force acting on the particle is then estimated from acceleration  $|\mathbf{a}|$  of the particle during the previous timestep and so by requiring the truncation error to be smaller than some fraction,  $\alpha$ , of the total force, one arrives at the cell opening criteria (Springel, 2005)

$$\frac{GM}{y^2} \left( \frac{l}{y} \right)^2 \leq \alpha |\mathbf{a}|. \quad (2.6)$$

If this condition is met then no further cells are opened and the current calculated gravitational force is used for the contribution of the particles in the assessed cell. If, however, this condition is not met the cell is opened further and the process is repeated for each of the sub-cells, potentially until the leaves of the tree are reached.

## 2.3 Smooth particle hydrodynamics

While gravity plays a major role in determining the large scale structure of the Universe as the force through which dark matter interacts, it is the baryons that we can directly see and interact with on a daily basis. Therefore to understand the gas, stars and galaxies that we observe we need an understanding of how the baryonic component of the Universe evolves and interacts beyond just gravity, therefore we additionally need to model the hydrodynamics. GADGET makes use of the SPH technique, which is a Lagrangian approach developed by Lucy (1977) and Gingold & Monaghan (1977) (for recent reviews see e.g., Springel, 2010; Monaghan, 2012; Price, 2012). In particular the version of GADGET-3 used here solves the Euler equations in the *entropy* form (Springel & Hernquist, 2002) and are given as (adapted from Read & Hayfield, 2012):

$$\frac{d\rho}{dt} = -\rho \nabla \cdot \mathbf{v}, \quad (2.7)$$

$$\frac{d\mathbf{v}}{dt} = -\frac{\nabla P}{\rho} + \left. \frac{d\mathbf{v}}{dt} \right|_{\text{visc}} - \nabla\Phi, \quad (2.8)$$

$$\frac{dA}{dt} = \left. \frac{dA}{dt} \right|_{\text{visc}} + \left. \frac{dA}{dt} \right|_{\text{diss}}, \quad (2.9)$$

where  $\rho$ ,  $\mathbf{v}$  and  $P$  are the gas density, velocity and pressure, respectively,  $A(s)$  is the entropy function (defined in equation (2.14) below),  $s$  is the specific entropy of the gas and  $-\nabla\Phi$  is the acceleration due to the (self-)gravity of the gas, where  $\Phi$  is the gravitational potential of the gas. Furthermore *visc* and *diss* terms encompass viscous and dissipative processes, respectively and are defined in section 2.3.3 below. In the absence of these extra-terms, equations 2.7, 2.8 and 2.9 present the conservation of mass, momentum and entropy, respectively. In the SPH approach the fluid is represented by a number of particles that move with the flow and act as interpolation points for the properties of the fluid at the particle locations. In GADGET-2 the self-gravity of the gas is accounted for using the tree-method described above in section 2.2 and therefore the  $-\nabla\Phi$  term is not included in the description below.

### 2.3.1 The SPH(S) equations of motion

The discretised form of equation (2.8) leads to the equation of motion for a single particle, which in the general form (neglecting viscous and dissipative terms) is given as (Read et al., 2010):

$$\frac{d\mathbf{v}_i}{dt} = - \sum_j^N m_j \left[ \frac{P_i \phi_i}{\rho_i^2 \phi_j} + \frac{P_j \phi_j}{\rho_j^2 \phi_i} \right] \nabla_i \bar{W}_{ij} \quad (2.10)$$

where  $m_j$ ,  $P_j$  and  $\rho_j$  are the mass, Pressure and density of particle  $j$ ,  $\phi_i$  is a free function,  $\bar{W}_{ij} = \frac{1}{2} [W_{ij}(h_i) + W_{ij}(h_j)]$  and  $W$  is a symmetric kernel, (see equations 2.15 and 2.16) and  $h_i$  is the smoothing length of the particle  $i$ , defining the length over which fluid properties are calculated. There is some freedom with regard to the values chosen for  $\phi$ . In *standard* SPH these are just set to 1, however, I use a modified version of SPH based on Read et al. (2010) and Read & Hayfield (2012) dubbed SPHS<sup>1</sup>. In SPHS  $\phi = \rho$ , which results in a reduction in the  $|\mathbf{E}_0|$  error, which arises in the SPH force calculation and is a result of truncating the pressure estimate used in the momentum equation (Read et al., 2010).

---

<sup>1</sup>Smoothed Particle Hydrodynamics with a higher order Switch

Equation (2.10) therefore becomes

$$\frac{d\mathbf{v}_i}{dt} = - \sum_j^N m_j \frac{m_j}{\rho_i \rho_j} [P_i + P_j] \nabla_i \bar{W}_{ij}. \quad (2.11)$$

A fundamental aspect of the SPH technique is the density estimate at the position of a particle  $i$ , which is given by

$$\rho_i = \sum_{j=1}^N m_j W(|\mathbf{r}_{ij}|, h_i), \quad (2.12)$$

where  $|\mathbf{r}_{ij}| = |\mathbf{r}_i - \mathbf{r}_j|$  is the distance between particles  $i$  and  $j$ . This solution automatically satisfies equation (2.7). The smoothing length  $h_i$  is adaptive and defined such that  $h_i$  and  $\rho_i$  obey the equation

$$\frac{4\pi}{3} h_i^3 \rho_i = N_{\text{SPH}} m_{\text{SPH}}, \quad (2.13)$$

where  $N_{\text{SPH}}$  is the typical number of neighbours and  $m_{\text{SPH}}$  is the particle mass. Finally the pressure of a particle with specific internal energy  $u_i$  and density  $\rho_i$  can be calculated using the equation of state

$$P_i = (\gamma - 1) \rho_i u_i = A(s_i) \rho_i^\gamma, \quad (2.14)$$

where, as mentioned previously,  $A(s)$  is a monotonic function of  $s_i$ , which is the specific entropy of the particle  $i$ . Provided there is no dissipation or heating,  $A(s)$  is constant and implicitly solves the energy equation (see Read et al., 2010; Read & Hayfield, 2012). However, in astrophysically interesting scenarios this will not be the case, as is discussed in section 2.3.3.

## 2.3.2 The kernel

The choice of kernel also has an effect on the performance and accuracy of the SPH code. While the modification to the equation of motion (Eq. 2.11) helps to reduce the  $|\mathbf{E}_0|$  error, it is still present. Formally we require  $|\mathbf{E}_0|$  to shrink faster than  $h$  with increasing resolution (Read & Hayfield, 2012), which can be achieved by using a high neighbour

number. Standard SPH typically uses the cubic spline (CS, Monaghan & Lattanzio, 1985)

$$W(r, h) = \frac{8}{\pi h^3} \begin{cases} 1 - 6\left(\frac{r}{h}\right)^2 + 6\left(\frac{r}{h}\right)^3, & 0 \leq \frac{r}{h} \leq \frac{1}{2}, \\ 2\left(1 - \frac{r}{h}\right)^3, & \frac{1}{2} < \frac{r}{h} \leq 1, \\ 0, & \frac{r}{h} > 1. \end{cases} \quad (2.15)$$

However, this kernel suffers from a particle pairing instability for high neighbour numbers (Dehnen & Aly, 2012; Price, 2012). This is a problem because if the particles clump, increasing the neighbour number will not lead to improved sampling of the kernel and the  $|\mathbf{E}_0|$  error will remain large (Read et al., 2010; Read & Hayfield, 2012). The pairing instability is avoided by using a kernel for which the Fourier transform is non-negative (Dehnen & Aly, 2012). We have therefore chosen to use a Wendland kernel (Wendland, 1995; Dehnen & Aly, 2012), in particular the  $C^2$  kernel

$$W(r, h) = \frac{21}{2\pi h^3} \begin{cases} \left(1 - \frac{r}{h}\right)^4 \left(1 + 4\frac{r}{h}\right), & 0 \leq \frac{r}{h} \leq 1 \\ 0, & \frac{r}{h} > 1 \end{cases} \quad (2.16)$$

which does not suffer from the pairing instability for all neighbour numbers. Further, it can be noted that it is less computationally expensive to calculate.

### 2.3.3 Dissipation

The above description outlines fully reversible fluid dynamics for a dissipationless ideal gas. However, in realistic astrophysical systems it is common for discontinuities, such as shocks and contact discontinuities, to form. In such shocks, heat is generated and the entropy increases as the kinetic energy of the flow is converted into thermal energy. In SPH an artificial viscosity is used to increase the entropy of shocked gas and dissipate local velocity differences. This prevents particle penetration and a multi-valued momentum in the flow (Cullen & Dehnen, 2010). In SPHS the artificial viscosity is included as an additional acceleration in the equation of motion (Monaghan, 1997; Springel, 2005; Read & Hayfield, 2012):

$$\left. \frac{d\mathbf{v}_i}{dt} \right|_{\text{visc}} = - \sum_j^N m_j \Pi_{ij} \nabla_i \bar{W}_{ij} \quad (2.17)$$



where

$$\Pi_{ij} = \begin{cases} -\frac{\bar{\alpha}_{ij}}{2} \frac{v_{\text{sig},ij} w_{ij}}{\bar{\rho}_{ij}} & \text{if } \mathbf{v}_{ij} \cdot \mathbf{r}_{ij} < 0 \\ 0 & \text{otherwise,} \end{cases} \quad (2.18)$$

$\bar{\alpha}_{ij} = (1/2)[\alpha_i + \alpha_j]$ ,  $\alpha_i$  is a viscosity parameter,  $w_{ij} = (\mathbf{v}_{ij} \cdot \mathbf{r}_{ij})/|\mathbf{r}_{ij}|$ ,  $v_{\text{sig},ij} = c_i + c_j - 3w_{ij}$  and  $c_i$  is the sound speed at the location of particle  $i$ . Further, entropy is generated at the shock front in order to conserve energy and is produced at a rate (Read & Hayfield, 2012):

$$\left. \frac{dA_i}{dt} \right|_{\text{visc}} = -\frac{1}{2} \frac{\gamma - 1}{\rho_i^{\gamma-1}} \sum_j^N m_j \bar{\alpha}_{ij} \Pi_{ij} \mathbf{v}_{ij} \cdot \nabla_i \bar{W}_{ij}. \quad (2.19)$$

Finally, given that the aim of artificial viscosity is to generate entropy at shocks, only bulk viscosity is required. Therefore the SPHS formalism makes use of a Balsara (1989) like switch in order to reduce any shear viscosity, where  $\alpha_i$  is multiplied by a factor

$$f_{\text{Balsara},i} = \frac{|\nabla \cdot \mathbf{v}|_i}{|\nabla \cdot \mathbf{v}|_i + |\nabla \times \mathbf{v}|_i + 0.0001 c_i / h_i}. \quad (2.20)$$

Artificial viscosity prevents multi-valued momentum as particles converge. However, momentum is not the only property that should be considered, in fact any un-smoothed property that is advected with the particles could become multivalued. For example, density is smoothed over a kernel and so is not multivalued but the entropy can be multivalued if particles with very different entropy approach each other. This in turn can lead to multivalued pressure. Similar to the artificial conduction proposed by Price (2008), this is resolved by an additional entropy dissipation term (Read & Hayfield, 2012)

$$\left. \frac{dA_i}{dt} \right|_{\text{diss}} = \sum_j^N \frac{m_j}{\bar{\rho}_{ij}} \bar{\alpha}_{ij} v_{\text{sig},ij}^p L_{ij} \left[ A_i - A_j \left( \frac{\rho_j}{\rho_i} \right)^{\gamma-1} \right] K_{ij}, \quad (2.21)$$

where  $\bar{\rho}_{ij} = [\rho_i + \rho_j]/2$ ,  $K_{ij} = \hat{r}_{ij} \dot{\nabla}_i W_{ij}$ ,  $L_{ij}$  is a pressure limiter (see below) and in an attempt to promote dissipation in approaching opposed to receding pairs of particles, the signal velocity is given as (Read & Hayfield, 2012)

$$v_{\text{sig},ij}^p = \begin{cases} c_i + c_j - 3w_{ij}, & \text{if } 3w_{ij} < (c_i + c_j) \\ 0 & \text{otherwise.} \end{cases} \quad (2.22)$$

If, however, the entropy dissipation is excessive, pressure waves can be driven, resulting in poorer modelling of the system than when there is no dissipation. Therefore, a pressure

limiter is employed where

$$L_{ij} = \frac{|P_i - P_j|}{P_i + P_j}. \quad (2.23)$$

The viscosity parameter  $\alpha_{ij}$  describes the amount of dissipation between particles. Such dissipation is only necessary for converging flows with the value of  $\alpha$  depending on the strength of the flow convergence. Formally a local flow is converging when the velocity divergence is negative i.e.  $\nabla \cdot \mathbf{v}_i < 0$ . If the magnitude of  $\alpha_{ij}$  is also set using  $\nabla \cdot \mathbf{v}$  then it will only come into effect when the flow is already converging, by which time it may be too late. Therefore, the viscosity magnitude is set by the spatial derivative of  $\nabla \cdot \mathbf{v}_i$ , resulting in the viscosity of a particle being set by (Read & Hayfield, 2012):

$$\alpha_{\text{loc},i} = \begin{cases} \frac{h_i^2 |\nabla(\nabla \cdot \mathbf{v}_i)|}{h_i^2 |\nabla(\nabla \cdot \mathbf{v}_i)| + h_i |\nabla \cdot \mathbf{v}_i| + n_s c_s} \alpha_{\text{max}} & \nabla \cdot \mathbf{v}_i < 0 \\ 0 & \text{otherwise} \end{cases} \quad (2.24)$$

where  $\alpha_{\text{max}} = 1$  is the maximum allowed value for  $\alpha_i$  and  $n_s = 0.05$  is a ‘noise’ parameter. If  $\alpha_{\text{loc},i}$  is greater than the current viscosity,  $\alpha_i$ , of the particle then we set  $\alpha_i = \alpha_{\text{loc},i}$  (as in Cullen & Dehnen, 2010). Otherwise a particle’s viscosity is allowed to decay over a timescale  $\tau_i = h_i/v_{\text{max},i}$ , such that

$$\dot{\alpha}_i = (\alpha_{\text{loc},i} - \alpha_i)/\tau_i, \quad \alpha_{\text{min}} < \alpha_{\text{loc},i} < \alpha_i \quad (2.25)$$

$$\dot{\alpha}_i = (\alpha_{\text{min}} - \alpha_i)/\tau_i, \quad \alpha_{\text{min}} > \alpha_{\text{loc},i} \quad (2.26)$$

where  $\alpha_{\text{min}} = 0.2$  ensures that the viscosity decays back to zero in the post shock region. Note that in some other treatments,  $\alpha_{ij}$  only decays to  $\alpha_{\text{min}}$ , not 0.

Due to the higher order nature of the viscosity switch in equation (2.24), a good estimate of the first and second derivatives of the velocity field are required to ensure that there is no unnecessary dissipation. This is achieved by fitting a second order polynomial to the fluid quantities as in Maron & Howes (2003). The coefficients of the fit provide the first and second order derivatives (see Read & Hayfield, 2012, for details).

## 2.4 Time integration

### 2.4.1 Euler method

From the force, as calculated above, comes the accelerations of the particles, which allows one to calculate the motion of individual particles. The simplest method of integrating

this motion with time is Euler integration. Here the evolution of particle positions and velocities are calculated as

$$\mathbf{x}_i(t + \Delta t_i) = \mathbf{x}_i(t) + \dot{\mathbf{x}}_i(t)\Delta t_i \quad (2.27)$$

and

$$\dot{\mathbf{x}}_i(t + \Delta t_i) = \dot{\mathbf{x}}_i(t) + \ddot{\mathbf{x}}_i(t)\Delta t_i, \quad (2.28)$$

where  $\Delta t_i$  is the particle timestep. While simple to implement, this is essentially just a first order Taylor expansion and thus has an error  $\propto \Delta t^2$ . By using a higher order integrator one can reduce this error, however, this would require the computation of the coefficients of the higher order terms, e.g., jerk ( $\dddot{\mathbf{x}}_i$ ), snap ( $\ddddot{\mathbf{x}}_i$ ) etc. Alternatively one can use a symplectic integrator that precisely solves an approximate Hamiltonian, meaning that the time averaged energy is conserved and hence energy errors will not grow over long periods (see e.g., Dehnen & Read, 2011).

### 2.4.2 Leapfrog method

GADGET uses what is known as the leapfrog integrator in which the force at time  $t$  is used to *kick* the particles half a timestep

$$\dot{\mathbf{x}}_i(t + \Delta t_i/2) = \dot{\mathbf{x}}_i(t) + \ddot{\mathbf{x}}_i(t)\Delta t_i/2, \quad (2.29)$$

the particle is then *drifted* a whole timestep using  $\dot{\mathbf{x}}_i(t + \Delta t_i/2)$  such that

$$\mathbf{x}_i(t + \Delta t_i) = \mathbf{x}_i(t) + \dot{\mathbf{x}}_i(t + \Delta t_i/2)\Delta t_i \quad (2.30)$$

and finally the acceleration at this new position is used to *kick* the particle half a timestep to give an updated velocity of

$$\dot{\mathbf{x}}_i(t + \Delta t_i) = \dot{\mathbf{x}}_i(t + \Delta t_i/2) + \ddot{\mathbf{x}}_i(t + \Delta t_i)\Delta t_i/2. \quad (2.31)$$

As such this is known as a *kick-drift-kick* (KDK) operation. Alternatively one may *drift-kick-drift* (DKD), however it is found that the energy error grows  $\sim 4$  times faster compared to the KDK scheme (Springel, 2005). Combining equations 2.29, 2.30 and 2.31 we find that over a whole timestep the position and velocity of a particle evolve as

$$\mathbf{x}_i(t + \Delta t_i) = \mathbf{x}_i(t) + \dot{\mathbf{x}}_i(t)\Delta t_i + \ddot{\mathbf{x}}_i(t)\Delta t_i^2/2 \quad (2.32)$$

and

$$\dot{\mathbf{x}}_i = \dot{\mathbf{x}}_i(t) + (\ddot{\mathbf{x}}_i(t) + \ddot{\mathbf{x}}_i(t + \Delta t_i))\Delta t_i/2, \quad (2.33)$$

respectively. In practise, a *drift* step occurs between times  $t$  and  $t + \Delta t$  and requires  $\mathbf{x}(t)$  and  $\dot{\mathbf{x}}(t + \Delta t/2)$  while a *kick* step occurs between times  $t - \Delta t/2$  and  $t + \Delta t/2$  and requires  $\dot{\mathbf{x}}(t - \Delta t/2)$  and  $\ddot{\mathbf{x}}(t)$ . The acceleration due to gravity only depends upon particle positions and so can easily be calculated using the drifted positions. However acceleration due to hydrodynamical processes are not simple functions of position and may depend upon quantities that are normally advanced on the kick step. In this case GADGET predicts the values that such quantities are expected to have at time  $t$  and uses these estimates when calculating accelerations.

### 2.4.3 Timesteps

Finally GADGET allows particles to have individual timesteps. which are organised into rungs, each of which differ by a factor of two. This allows particles that require a particularly accurate time integration, for instance if they are on short orbits, to have small timesteps while not slowing down the whole computation by letting other particles have longer timesteps. All particles are subjected to a timestep criterion of

$$\Delta t_i = \min \left[ \Delta t_{\max}, \sqrt{\frac{2\eta\epsilon}{|\mathbf{a}_i|}} \right], \quad (2.34)$$

where  $\Delta t_{\max}$  is a maximum potential timestep set by the user and  $\sqrt{2\eta\epsilon/|\mathbf{a}_i|}$  is the gravitational timestep estimate and makes use the particle's gravitational softening length  $\epsilon$ , acceleration  $|\mathbf{a}_i|$  and the parameter  $\eta$  used to set the accuracy. This timestep is convenient as all of the parameters are already available, meaning that the calculation of further quantities is not necessary, plus the timestep is Gallilean invariant. However, its construction is purely based upon dimensional arguments and better alternatives may be available. For example using the orbital time such that  $\Delta t \propto \sqrt{r^3/GM}$ , has the advantage of being sufficiently short on small orbits but more efficient (allowing longer timesteps) on larger orbits when compared to the timestep criterion I employ. Despite these apparent drawbacks, the timestepping used here has been extensively tested and shown to be robust in galaxy evolution simulations (Power et al., 2003).

In addition, the timestep of an SPH particle is limited such that

$$\Delta t_i < \frac{Ch_i}{\max(v_{ij}^{\text{sig}})}, \quad (2.35)$$

where  $C$  is a Courant et al. (1928) like factor,  $h_i$  is the particle smoothing length and  $v_{ij}^{\text{sig}}$  is the (non-zero) signal velocity as defined in the previous section. For pure N-body particles the hydrodynamical timestep is neglected.

However, if every particle had its own individual timestep, then a situation could easily arise where only one particle is updated during each timestep. In order to avoid this scenario, particle timesteps are organised into rungs, which in the case of GADGET follow a power of two hierarchy, such that multiple particles can be evolved simultaneously (Makino, 1991). Particles are placed on the highest timestep rung such that the particles timestep will be less than or equal to the  $\Delta t_i$  calculated in equations 2.34 and 2.35. This ensures that particles are advanced coherently and that at the end of a timestep of length  $\Delta t_{\text{max}}$ , all particles will be synchronised. Finally, to ensure the proper treatment of explosions and shock front propagation, a constraint is applied such that the timesteps of neighbouring particles differ at most by a factor of four (Read & Hayfield, 2012). This value is chosen as a balance between computational expense and sufficient accuracy for capturing blast waves (Saitoh & Makino, 2009) and ensures that particles, which may initially be on long timesteps are “awoken” in order to respond to the new conditions.

## 2.5 Radiative cooling

Radiative cooling processes occur on scales significantly below the resolution limit of astronomical simulations and so cooling rates are typically estimated using various techniques. A common technique for galaxy scale simulations is to use an optically thin radiative cooling function  $\Lambda(\rho, u)$ , which is a function of the gas internal energy  $u$  (or temperature  $T$ ) and gas density  $\rho$ . From this the cooling rate of an SPH particle can be estimated given its temperature and density. These cooling functions typically incorporate a number of cooling processes, for example Figure 2.3 taken from (Wiersma et al., 2009, figure 6.) shows a sample cooling function (solid black line) for solar abundances along with the contribution from hydrogen and helium (black dashed curve) and individual metal contributions (solid coloured curves). At high temperatures the function is dominated by Bremsstrahlung with  $\Lambda \propto T^{1/2}$ , while at lower temperatures, as the gas becomes less ionised, the dominant cooling processes are collisional excitation and radiative

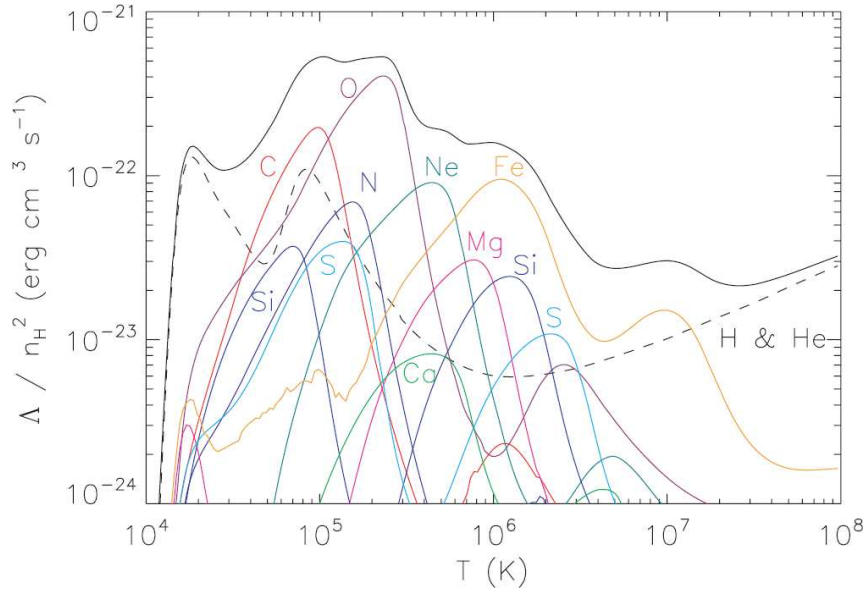


Figure 2.3: Sample optically thin radiative cooling curve taken from Wiersma et al. (2009, figure 6.). The black solid curve shows the overall cooling rate assuming solar abundances while the black dashed curve shows the cooling rate due to hydrogen and helium only and the other coloured curves show the contributions from different *metals*.

de-excitation. Below  $10^4$  K the cooling rate drops rapidly due to most of the electrons having recombined. Cooling in this regime is only possible if the gas is enriched with cooling being facilitated by fine structure and metastable lines of metals and collisional excitation of rotational and/or vibrational levels of molecules (see §8.1.3 Mo et al., 2010, and references therein for more details).

For the simulations presented in Chapters 4 and 5 I make use of two optically thin cooling functions, one taken from Sazonov et al. (2005), which includes Bremsstrahlung cooling, photoionisation heating, line and recombination continuum cooling and Compton heating and cooling due to interaction with radiation emitted by an AGN and is valid for  $T \gtrsim 10^4$  K. Below  $10^4$  K we employ the function described by Mashchenko et al. (2008), whereby fine structure and metastable lines of C, N, O, Fe, S and Si are employed for cooling. This function is valid down to temperatures of 20 K and both functions assume solar metallicity for the gas.

The timescale on which cooling occurs can be very much shorter than the typical hydrodynamical or gravitational timestep within a simulation. So much so that to include a cooling timestep limit becomes infeasible. Therefore, one has to iterate on the cooling rate over a timestep. In GADGET-2 the internal energy is advanced with the *kick* step and at

the end of such a timestep is found by iteration such that (Springel et al., 2001)

$$u_i(t + \Delta t_i/2) = u_i(t - \Delta t_i/2) + \dot{u}^{ad}(t)\Delta t - \frac{\Lambda [\rho_i(t), u_i(t + \Delta t_i/2)] \Delta t_i}{\rho_i(t)}, \quad (2.36)$$

where  $u_i(t - \Delta t_i/2)$  and  $u_i(t + \Delta t_i/2)$  are the specific internal energy at the beginning and end of a *kick* step respectively and  $\dot{u}^{ad}(t)$  is the rate of change for the specific internal energy due to adiabatic gas processes at time  $t$ , i.e, in the middle of the *kick* step. This leads to a cooling rate of

$$\dot{u}_i = [u_i(t + \Delta t/2) - u_i(t - \Delta t/2)] / \Delta t. \quad (2.37)$$

However, even with this scheme there still may be situations in which the cooling time becomes incredibly short leading to a particle losing a significant fraction of its internal energy in a single timestep. Therefore, methods are used to damp the cooling rate in extreme cases (e.g., Katz & Gunn, 1991; Springel et al., 2001). In *GADGET* the cooling rate is restricted such that a particle can lose at most half of its internal energy during a single timestep.

## 2.6 Star formation

The exact physical processes governing the formation of individual stars often occur below the resolution limit of simulations. As such many of the complications (a number of which are still unknown) of star formation are neglected by simply introducing a “*star*” particle when the properties of a gas particle exceed some critical values. The star particle is typically a N-body particle, which may also act as a sink particle allowing it to merge with other sink particles and/or accrete SPH particles that come within the star particle’s “*accretion radius*”. The interpretation of the star particle that forms depends entirely on the nature and resolution of the simulation. For example, in high resolution simulations of single molecular clouds (e.g., Bate et al., 2003; Bate, 2009a, 2012), sink particles represent individual stars allowing one to derive an initial mass function (IMF) from the simulation. However, on the scale of a whole galaxy, star particle masses become very large and are interpreted as stellar populations (e.g., Katz, 1992; Schaye & Dalla Vecchia, 2008). Various conditions are used in the literature for star formation, I discuss a few key ideas below.

Conceptually the most straight forward condition for star formation would be when

the gravity of a gas clump exceeds any pressure support and hence the gas undergoes gravitational collapse. This occurs when the sound crossing time for the clump exceeds the free-fall time. From this condition one can define a critical mass for the clump, known as the Jeans mass, above which the clump will undergo collapse. If the clump can collapse to high enough densities it would be expected to undergo star formation. The finite resolution of simulations places a limit on the densities to which one can follow the collapse of a gas cloud before short timesteps become an issue. Further to this, Bate & Burkert (1997) have shown that fragmentation can be artificially suppressed if the minimum resolvable mass exceeds the local Jeans mass, i.e.,  $M_{\text{res}} \approx N_{\text{ngb}} m_{\text{SPH}} > M_{\text{J}}$  (see also Whitworth, 1998). This leads naturally to a Jeans density threshold for the conversion of SPH particles into star particles

$$\rho_{\text{J}} = \left( \frac{\pi k_{\text{B}} T}{\mu m_{\text{p}} G} \right)^3 \left( N_{\text{ngb}} m_{\text{SPH}} \right)^{-2}, \quad (2.38)$$

where  $T$  is the gas temperature,  $\mu$  is the mean molecular weight,  $m_{\text{p}}$  is the proton mass,  $N_{\text{ngb}}$  is the typical SPH neighbour number and  $m_{\text{SPH}}$  is the SPH particle mass (for a derivation see section 4.2.1). In its simplest form, if the density of an SPH particle exceeds  $\rho_{\text{J}}$  it is converted into a star particle (e.g., Zubovas & Nayakshin, 2014; Zubovas, 2015).

Further to this, many galaxy formation simulations (e.g., Gnedin, 1996; Katz et al., 1996; Springel, 2000; Kravtsov, 2003; Springel & Hernquist, 2003) impose the empirically derived Schmidt (1959) law,  $\dot{\rho}_* \propto \rho_{\text{gas}}^{3/2}$ , to govern star formation in addition to or instead of a Jeans criteria. This can be implemented by attaching a probability to converting a SPH particle into a star particle (e.g., Katz, 1992) of the form<sup>2</sup>

$$P = 1 - \exp\left(-\epsilon_{\text{SF}} \frac{\Delta t}{\tau_{\text{ff}}}\right) \quad (2.39)$$

where  $\epsilon_{\text{SF}}$  is an assumed star formation efficiency ranging from 0.01 – 1 (and can be tuned to match observations),  $\Delta t$  is the SPH particle's timestep and  $\tau_{\text{ff}} \sim \sqrt{3\pi/32G\rho}$  is the local free fall time of the gas. This approach is usually combined with other conditions, the simplest of which takes the form of density and temperature thresholds for star formation.

The Schmidt law approach can also be combined with a Jeans collapse condition by including a density dependant temperature floor such as the one used in Chapter 5 (see also Robertson & Kravtsov, 2008; Hobbs et al., 2013). The temperature floor prevents gas of a given temperature collapsing to densities above  $\rho_{\text{J}}$ . This ensures that  $M_{\text{res}} > M_{\text{J}}$  and

---

<sup>2</sup>Note that Schaye & Dalla Vecchia (2008) also employ a similar method, however they take the probability to be  $P = \min[\Delta t/t_{\text{ff}}, 1]$ .



hence fragmentation is not suppressed by numerical artefacts. Further, by only allowing gas that has reached the temperature floor to be star forming means that only gas undergoing Jeans collapse can be converted into star particles. The temperature floor essentially manifests itself as a polytropic equation of state of the form  $P \propto \rho^{4/3}$ . In fact it is not uncommon, particularly in low resolution simulations, for gas above some critical density to be forced onto an effective equation of state of this form (e.g., Springel & Hernquist, 2003; Schaye & Dalla Vecchia, 2008). Gas that follows the equation of state is considered star forming with SPH particles being converted into star particles in accordance with equation (2.39).

## 2.7 SMBH feedback

Accretion onto a SMBH can release vast amounts of energy as radiation, which can potentially drive powerful outflows, winds and jets (e.g., Fabian, 2012; King & Pounds, 2015). I have already discussed at length the properties of AGN driven winds and their interaction with the host ISM in section 1.6. One problem which is immediately apparent in trying to simulate such winds is the minuscule mass that they carry compared to the mass of the host galaxy. It therefore makes it very difficult, at least with SPH simulations, to directly simulate the wind itself when modelling a galaxy on kpc scales, as the wind mass becomes comparable to only a handful (at best) of particles.

However, we can model the effects of the wind interaction with the host ISM by considering the momentum and energy input from the wind. Traditionally this is done using a kernel weighted scheme, which distributes the expected energy and/or momentum output from the AGN to neighbouring gas particles (e.g., Di Matteo et al., 2005; Costa et al., 2014). The fraction of energy or momentum given to an individual gas particle is

$$f_{\text{inj},k} = \frac{m_{\text{SPH}} W(r_k - r_{\text{BH}}, h_{\text{BH}})}{\rho_g(r_{\text{BH}})}, \quad (2.40)$$

where  $m_{\text{SPH}}$  is the mass of an SPH particle,  $W(r_k - r_{\text{BH}}, h_{\text{BH}})$  is the kernel weight of the SPH particle relative to the black hole,  $h_{\text{BH}}$  is the black hole *smoothing* length (typically  $O(10-100)$  pc for the simulations presented here), calculated over a set number of neighbours and  $\rho_g(r_{\text{bh}})$  is the gas density at the location of the black hole. This process is simple to implement as it can use the existing neighbour list and density calculation to normalise feedback across particles local to the black hole and it is relatively fast. However, it preferentially distributes the feedback to high density material as this is where most of the

SPH particles reside (see Chapter 5 or Zubovas et al., 2015). Therefore, the feedback can become non-isotropic and radiative losses can become large.

An alternative method developed by Nayakshin et al. (2009a) and subsequently modified by Nayakshin & Power (2010) implements a Monte-Carlo scheme, which models the transfer of the outflow momentum to the host ISM. This model has further been modified to include the transfer of energy to the ISM also (Zubovas & Nayakshin, 2012). This model gives a good approximation for the momentum driven regime and mimics the energy driven regime by heating pre-existing SPH particles to high temperatures which can form a hot feedback bubble. Unlike the kernel weighted scheme, this method can be truly isotropic and has better energy retention due to this (Zubovas et al., 2015). The drawbacks of this method, however, are that like the kernel weighted scheme, there is not a separate hydrodynamical wind component and it can be very computationally expensive compared to kernel weighted schemes.

---

# 3

## Inverse Compton X-ray signature of AGN feedback

*“The Universe is under no obligation to make  
sense to you.”*

*Neil deGrasse Tyson*

### 3.1 Introduction

SMBHs produce powerful winds (Shakura & Sunyaev, 1973; King, 2003) when accreting gas at rates comparable to the Eddington accretion rate. Such winds are consistent with the UFOs introduced in section 1.6.1, which have velocities of  $v_w \sim 0.1c$ , detected via X-ray line absorption (e.g., Pounds et al., 2003a,b; Pounds & Reeves, 2009; Tombesi et al., 2010a,b). The winds must be wide-angle to explain their  $\sim 40\%$  detection frequency (Tombesi et al., 2010a,b). UFOs may carry enough energy to clear out significant fractions of *all* gas from the parent galaxy (e.g., King, 2010; Zubovas & King, 2012a) when they shock and pass their momentum and perhaps energy to kpc-scale neutral and ionised outflows (see section 1.6) with outflow velocities of  $\sim 1000 \text{ km s}^{-1}$  and mass outflow rates of hundreds to thousands of  $M_\odot \text{ yr}^{-1}$  (e.g., Feruglio et al., 2010; Sturm et al., 2011b; Rupke & Veilleux, 2011b; Liu et al., 2013; Rupke & Veilleux, 2013a,b; Harrison et al., 2014; Maiolino et al., 2012; Ciccone et al., 2012, 2014, 2015; Carniani et al., 2015; Tombesi et al., 2015).

As discussed in section 1.6.1.1, most previous models of UFO shocks assumed that they are in a 1T regime where the electron and ion temperatures in the flow are equal to each other at all times including after the shock. Faucher-Giguère & Quataert (2012) showed that shocked UFOs are sufficiently hot and yet diffuse that electrons may be much cooler than ions and hence actually be in the 2T regime. They found that for a wind velocity of  $0.1 c$  and energy of  $L_{Edd} = 10^{46} \text{ erg s}^{-1}$ , the ion temperature is  $\sim 2.4 \times 10^{10} \text{ K}$ , but the electron temperature reaches a maximum of only  $T_e \sim 3 \times 10^9 \text{ K}$  in the post-shock region. The 1T regime may, however, still be appropriate if there are collective plasma physics effects that couple the plasma species more tightly (e.g., Quataert, 1998; Riquelme & Spitkovsky, 2011). There is thus a significant uncertainty in how UFOs affect their hosts, e.g., with energy or momentum (King, 2010).

Here I propose a direct observational test of the 1T and 2T UFO shock scenarios. AGN spectra are dominated by thermal disc emission coming out in the optical/UV spectral region. The shocked electron temperature in both scenarios is rather high, e.g.,  $T_e \sim 10^9 \text{ K}$  (2T) to  $T_e \gtrsim 10^{10} \text{ K}$  (1T). IC scattering of the AGN disc photons against these electrons produces either soft X-ray (2T Inverse Compton; 2TIC) or medium to hard X-ray energy (1TIC) radiation. Provided that the shock occurs within the IC cooling radius defined in section 1.6.1.1,  $R_{IC} \sim 500 \text{ pc } M_8^{1/2} \sigma_{200}$  (where  $M_8$  is the SMBH mass in units of  $10^8 M_\odot$  and  $\sigma_{200}$  is the velocity dispersion in the host in units of  $200 \text{ km s}^{-1}$ , Zubovas & King, 2012b), essentially *all* of the kinetic energy of the wind, which is  $L_k = (v_w/2c)L_{Edd} \sim$

$0.05L_{\text{Edd}}$  for  $v_{\text{out}} = 0.1c$ , should be radiated away. I calculate this IC spectral component and find it somewhat below, but comparable to, the observed X-ray emission for a typical AGN. Significantly, the IC emission is likely to be steady-state and unobscured by a cold “molecular torus”, which, for the 1T case, is in contrast to typical AGN X-ray spectra. I therefore make a tentative conclusion that current X-ray observations of AGN are more consistent with the 2T picture. In view of the crucial significance of this issue to models of SMBH - host galaxy co-evolution, I urge X-ray observers to search for the 1TIC and 2TIC emission components in AGN spectra in order to constrain the models of AGN feedback further.

## 3.2 Inverse Compton feedback component

### 3.2.1 General procedure to calculate the X-ray spectrum

In what follows I assume that the UFO velocity is  $v_w$  (as in section 1.6.1), the total mass loss rate is given by  $\dot{M} = L_{\text{Edd}}/(cv_w)$  and that the gas is pure hydrogen in the reverse shock such that  $n_e = n_p$ . Assuming the strong shock jump conditions, the shocked UFO temperature immediately past the shock is given by

$$k_B T_{\text{sh}} = \frac{3}{16} m_p v_w^2, \quad (3.1)$$

while the density of the shocked gas is

$$\rho_{\text{sh}} = 4 \times \rho_w = 4 \times \frac{\dot{M}_w}{4\pi R^2 v_w} = \frac{L_{\text{Edd}}}{\pi R^2 c v_w^2}, \quad (3.2)$$

where  $\rho_w$  is the pre-shocked wind density and  $\dot{M}_w$  is the mass outflow rate in the wind. The factor of 4 in the density above comes from the density jump in the strong shock limit (King, 2010; Faucher-Giguère & Quataert, 2012). The shock is optically thin for radii  $R \gtrsim 4GM_{\text{BH}}/v_w^2 = 2 \times 10^{-3} \text{ pc } M_8$ .

The dominant cooling mechanism of the shocked wind is IC Scattering<sup>1</sup> (Ciotti & Ostriker, 1997, 2001; King, 2003). Soft photons produced by the AGN are up-scattered by the hot electrons of the shocked wind to higher energies (X-rays for the problem considered here). Given the input spectrum of the soft photons and the electron energy distribution (EED,  $F(\gamma)$  below, where  $\gamma = E/m_e c^2$  is the dimensionless electron

---

<sup>1</sup>Note that at low gas temperatures,  $T < 10^7 \text{ K}$ , Compton processes instead heat the gas up (Ciotti & Ostriker, 2007).

energy) of the hot electrons in the shock, one can calculate the spectrum of the IC up-scattered photons.

First let us consider the case when the electron energy losses due to the IC process are negligible compared with the adiabatic expansion energy losses of the shocked gas. In the zeroth approximation, I have a monochromatic population of photons with energy  $E_0$  and total luminosity  $L_0$  being up-scattered by a population of electrons with a fixed Lorentz factor  $\gamma$ . The typical energy of the up-scattered photons is given as  $E_f \approx \gamma^2 E_0$ . Therefore the emitted luminosity of the up-scattered photons is given by

$$L_{\text{IC}} = L_0 \left( \frac{E_f}{E_0} \right) \tau, \quad (3.3)$$

where  $\tau = \kappa_{\text{es}} \rho \Delta R$ , is the Thompson optical depth of the shell,  $\kappa_{\text{es}}$  is the electron Thompson scattering opacity,  $\rho$  is the shocked gas density and  $\Delta R$  is the shell's thickness. The optical depth of the shell,  $\tau$ , determines the average number of times a photon will scatter before escaping and so to arrive at the total luminosity of the IC emission one needs to calculate  $\tau$  as a function of time for the expanding shell. In any event, since I assumed that IC losses are small, the luminosity due to IC scattering is much less than the kinetic luminosity of the UFO, i.e.  $L_{\text{IC}} \ll L_k = (v_w/2c)L_{\text{Edd}}$ . This regime corresponds to the shock extending well beyond the cooling radius such that  $R_C \gg R_{\text{IC}}$ , where  $R_C$  is the contact discontinuity radius shown in figure 1.7 and  $R_{\text{IC}}$  is defined in equation (1.29).

Here I am interested in the opposite limit, e.g., when the contact discontinuity radius is  $R < R_{\text{IC}}$ , so that IC energy losses are rapid for the shocked electrons. In this case the luminosity of the IC emission is set by the total kinetic energy input in the shock so that

$$L_{\text{IC}} = L_k = \frac{1}{2} \frac{v_w}{c} L_{\text{Edd}}. \quad (3.4)$$

On the other hand one cannot assume that the energy distribution of the shocked electrons is constant.

Below I calculate the cooling electron energy distribution and the resulting IC spectrum in both the 1T and 2T regimes. I take into account the fact that the input soft photon spectrum is not monochromatic but rather covers a range of energies and that the electron population also has a distribution in  $\gamma$ . The spectral luminosity density,  $L_{E_f}$ , of the up-scattered photons, assumed to be completely dominated by the first scattering<sup>2</sup> is given

---

<sup>2</sup>Since the wind shock is optically thin each photon should scatter no more than once before escaping the system.

by,

$$\frac{dL}{dE_f} = cE_f \int_1^\infty d\gamma \frac{dF(\gamma)}{d\gamma} \int_0^\infty dE_0 \frac{dn_0}{dE_0} \frac{d\sigma(E_f, E_0, \gamma)}{dE_f} \quad (3.5)$$

where  $dn_0/dE_0 = (1/4\pi R^2 c E_0)(dL_{E_0}/dE_0)$  is the differential input photon number density at the location of the shock radius ( $R$ ), and  $d\sigma(E_f, E_0, \gamma)/dE_f$  is the angle-averaged IC scattering cross-section for a photon of energy  $E_0$  to scatter to energy  $E_f$  by interacting with an electron of energy  $\gamma$  (as calculated by Nagirner & Poutanen, 1994).

The overall process to calculate the IC spectrum is as follows; in sections 3.2.2 and 3.2.3 the EED of the shocked electrons,  $F(\gamma)$ , is calculated. This part of the calculation is independent of the soft input spectrum, as long as the up-scattered photons are much less energetic than the electrons that they interact with. In order to calculate the output spectrum, however, I need to introduce the soft photon spectrum explicitly. These are model dependent since the precise physics, geometry and emission mechanism of the AGN accretion flows remains a work in progress. I therefore try three different models for the soft photon continuum: a black-body spectrum with  $k_B T = 3\text{eV}$ , the UV region (1-100eV) of a typical AGN spectrum taken from Sazonov et al. (2004) and the entire (1 –  $10^6\text{eV}$ ) AGN spectrum taken from Sazonov et al. (2004). Finally, the integrals in equation (3.5) are calculated numerically and the total IC luminosity is normalised using equation (3.4).

### 3.2.2 The electron energy distribution in the 2T regime

In the 2T wind shock regime, Faucher-Giguère & Quataert (2012) show that while cooling behind the shock the electrons spend a considerable amount of time in a “temporary equilibrium” state with temperature  $T_{\text{eq}} \sim 2 \times 10^9 \text{ K}$  for  $v_w = 0.1c$  (see Figure 2 in Faucher-Giguère & Quataert, 2012). Here I therefore make the approximation that in the 2T regime the electrons have a thermal EED at temperature  $T = T_{\text{eq}}$ , described by the Maxwell-Jüttner distribution (Jüttner, 1911), which when normalised to a single electron is given as

$$\frac{dF(\gamma)}{d\gamma} = f_{\text{MJ}}(\gamma, \theta) = \frac{\beta \gamma^2}{\theta K_2\left(\frac{1}{\theta}\right)} e^{-\frac{\gamma}{\theta}}, \quad (3.6)$$

where  $\theta = k_B T/(m_e c^2)$  is the dimensionless electron temperature,  $\beta = v/c$  and  $K_2$  is the modified Bessel function of the second kind. The Maxwell-Jüttner distribution takes into account relativistic effects expected for high  $\gamma$  electrons but in the non-relativistic regime is identical to the Maxwell-Boltzmann distribution (Maxwell, 1860).

### 3.2.3 1T cooling cascade behind the shock

Now I turn to the 1T case assuming that the electron and ion temperatures in the shocked UFOs are equal to one another at all times. In this case there is no “temporary equilibrium” state; behind the shock the electron temperature drops with time from  $T = T_{\text{sh}}$  according to the IC cooling rate. The absolute minimum temperature to which the electrons will cool is given by the Compton temperature of the AGN radiation field, which is found to be  $T_{\text{IC}} = 2 \times 10^7$  K by Sazonov et al. (2004). The cooling of the electrons leads to an electron temperature distribution being set up behind the shock (King, 2010), which I calculate here.

The electron-electron thermalisation timescale is  $\sim m_e/m_p$  times shorter than the energy exchange timescale with protons (Stepney, 1983). One can also show that IC electron losses, even in the 1T regime, are not sufficiently large compared with the electron self-thermalisation rate to lead to strong deviations from a thermal distribution for the electrons (cf. equation 5 in Nayakshin & Melia, 1998). I therefore assume that the electrons maintain a thermal distribution behind the shock at all times as they cool from the shock temperature  $T_{\text{sh}}$  to  $T_{\text{IC}}$ . The goal should thus be to calculate how much time electrons spend at different temperatures as they cool; this will determine  $F(\gamma)$  and the resulting IC spectrum.

The rate of cooling of a population of electrons, which in this case are described by the Maxwell-Jüttner distribution, due to IC scattering against a radiation field with an energy density  $U_{\text{rad}}$  is given by<sup>3</sup>

$$\left(\frac{du}{dt}\right)_{\text{IC}} = -\frac{4}{3}\sigma_{\text{T}}cU_{\text{rad}} \int_1^\infty (\gamma^2 - 1) f_{\text{MJ}}(\gamma, \theta) d\gamma. \quad (3.7)$$

The internal energy per ion-electron pair,  $u$ , is the sum of the ion contribution,  $(3/2)k_{\text{B}}T$ , and that for the electron. For convenience of notations I define  $u = a_e(\theta)\theta m_e c^2$ , where

$$a_e(\theta) = \frac{3}{2} + \frac{\langle\gamma\rangle - 1}{\theta} \quad (3.8)$$

and  $\langle\gamma\rangle = \int_1^\infty \gamma f_{\text{MJ}}(\gamma, \theta) d\gamma$  is the average electron  $\gamma$ -factor. Clearly,  $a_e = 3$  and  $a_e = 9/2$  in the non-relativistic and extreme relativistic electron regimes, respectively (assuming that the protons are always non-relativistic). Finally,  $U_{\text{rad}} = L_{\text{Edd}}/(4\pi R^2 c)$  is the energy density of the AGN radiation field. I neglect the contribution of stars to  $U_{\text{rad}}$ .

---

<sup>3</sup>For a derivation of this equation see, for example, Rybicki & Lightman (1986).



I also need to include the compressional heating behind the shock front, so that

$$\frac{du}{dt} = \left( \frac{du}{dt} \right)_{\text{IC}} - P \frac{dV}{dt}, \quad (3.9)$$

where  $P = (\Gamma - 1)n_{e,i}u$  is the pressure of the gas,  $\Gamma$  is the adiabatic index and  $V = 1/n_{e,i}$  is the inverse of the electron-ion pair number density. Assuming that the flow velocity is much smaller than the sound speed behind the shock, the region can be considered almost isobaric<sup>4</sup>. and so one finds  $-PdV/dt = (1 - \Gamma)du/dt$ . Using this result and combining equations 3.7, 3.8 and 3.9, the electron temperature evolution can be solved from

$$m_e c^2 \frac{d}{dt} (a_e(\theta)\theta) = \frac{1}{\Gamma} \left( \frac{du}{dt} \right)_{\text{IC}}. \quad (3.10)$$

This equation is solved numerically in order to determine  $\dot{\theta} = d\theta/dt$ . One can define the dimensionless function  $G(\theta)$  as

$$G(\theta) = \frac{1}{t_c} \frac{\theta}{|\dot{\theta}|}, \quad (3.11)$$

where  $t_c = m_e c^2 / (\sigma_T c U_{\text{rad}})$ , is a timescale factor which happens to be the order of magnitude of the IC cooling time for non-relativistic electrons.

I call  $G(\theta)$  the Inverse Compton 1T cooling cascade (1TCC) distribution, and plot it in Figure 3.1. Note that the function is independent of the outflow rate,  $\dot{M}_w$ , the energy density of the AGN radiation field,  $U_{\text{rad}}$ , and the soft photon spectrum as long as the up-scattered photons are much less energetic than the electrons themselves. The function  $G(\theta)$  is thus a basic property of the IC process itself.

$G(\theta)$  is calculated numerically and plotted in Figure 3.1 below, but one can easily obtain the general form of the function in the two opposite regimes analytically. Rybicki & Lightman (1986) show that in the non-relativistic (NR,  $\theta \ll 1$ ) and ultra-relativistic (UR,  $\theta \gg 1$ ) limits the IC rate of cooling for a thermal distribution of electrons is given by

$$\frac{du}{dt} = -c\sigma_T U_{\text{rad}} \begin{cases} 4\theta & \text{non-relativistic} \\ 16\theta^2 & \text{ultra-relativistic} \end{cases} \quad (3.12)$$

---

<sup>4</sup>The time it takes a sound wave to travel across the shocked wind is much less than the time it takes the shock pattern to propagate the same distance and so any fluctuations in the pressure will very quickly be washed out, see Weaver et al. (1977)

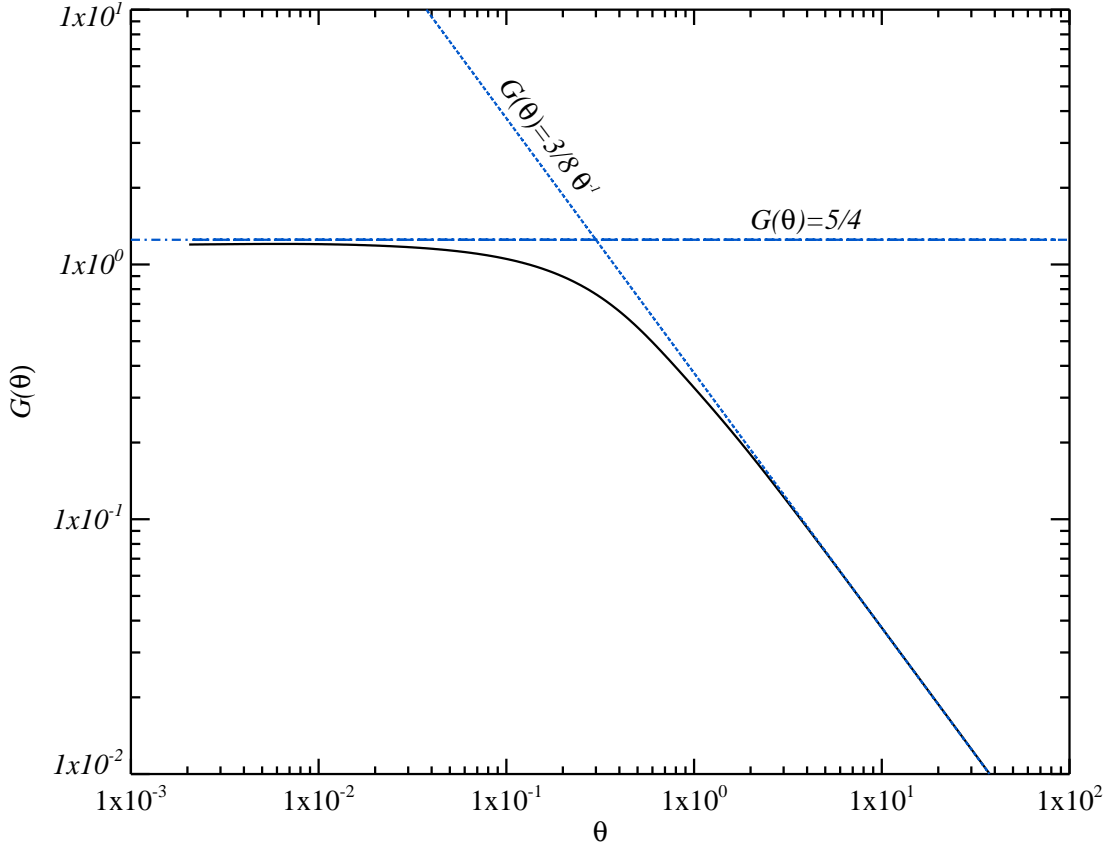


Figure 3.1: The dimensionless electron temperature distribution  $G(\theta) = \theta/(\dot{\theta}t_c)$ . The dashed and dotted lines are labelled to show how the distribution behaves in the non-relativistic and ultra-relativistic regimes respectively. i.e.  $G(\theta) = 5/4$  and  $(3/8)\theta^{-1}$ .

Using these one can solve equation (3.10) analytically in the NR and UR limits to find:

$$\frac{d\theta}{dt} = -\frac{c\sigma_T U_{rad}}{m_e c^2} \begin{cases} \frac{4}{3}\theta & \text{non-relativistic} \\ \frac{32}{9}\theta^2 & \text{ultra-relativistic} \end{cases} \quad (3.13)$$

and so  $G(\theta) = 5/4$  and  $(3/8)\theta^{-1}$  in the NR and UR regimes respectively.

The blue dashed and dotted lines in Figure 3.1 show these limits highlighting that my solution for  $G(\theta)$  behaves correctly in the limiting regimes. The physical interpretation of the limiting forms of  $G(\theta)$  is quite clear. At high  $\theta$ , electrons are relativistic and thus their IC cooling time is inversely proportional to  $\theta$ . Thus, the hotter the electrons, the faster they cool. This yields the  $G(\theta) \propto \theta^{-1}$  behaviour at  $\theta \gg 1$ . In the opposite, non-relativistic limit, the IC cooling time is independent of electron temperature and this results in the

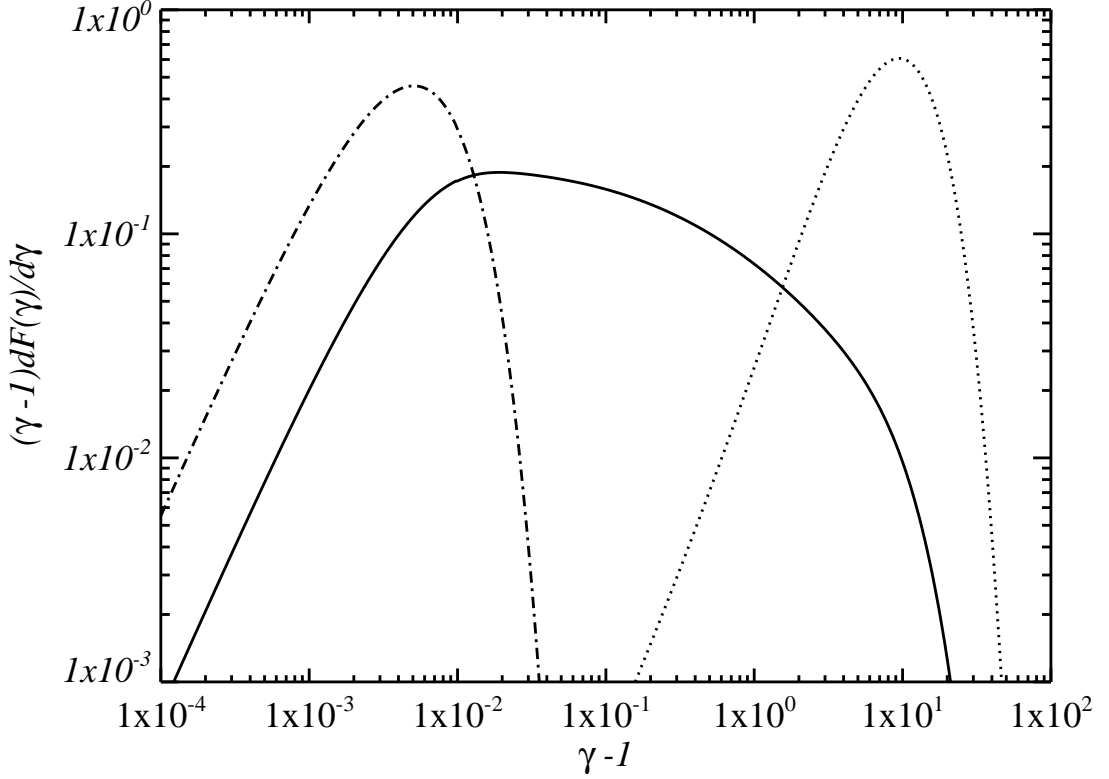


Figure 3.2: Electron energy distribution for 1T cooling cascade with  $v_w = 0.1c$  and  $T_{\text{sh}} = 2 \times 10^{10}\text{K}$  (solid curve). For comparison, a single temperature thermal electron distributions are also shown for  $T = T_{\text{sh}}$  and  $T = T_{\text{IC}} = 2 \times 10^7\text{K}$  with the dotted and dash-dotted curves, respectively.

$G(\theta) = 5/4$  limit.

$G(\theta)$  can be used to calculate the “integrated” EED as seen by the soft AGN photons passing through the shocked shell. The number of electrons with a temperature between  $\theta$  and  $\theta + d\theta$  is given by  $dN = (dN/d\theta)d\theta = \dot{N}dt$ , where  $dt = d\theta/\dot{\theta}$  is the time that it takes electrons to cool from temperature  $\theta + d\theta$  to  $\theta$ , and  $\dot{N} = \dot{M}_w/m_p$  is the rate of hot electron “production”. Clearly,

$$\frac{dN}{d\theta} = \frac{\dot{N}}{\dot{\theta}} = \frac{\dot{N}t_c}{\theta} G(\theta). \quad (3.14)$$

As electrons at each  $\theta$  are distributed in the energy space according to equation (3.6), the number of electrons with  $\gamma$ -factor between  $\gamma$  and  $\gamma + d\gamma$ ,  $(dF(\gamma)/d\gamma)d\gamma$ , is given by a convolution of the thermal distribution  $f_{\text{MJ}}(\gamma, \theta)$  with the electron cooling history

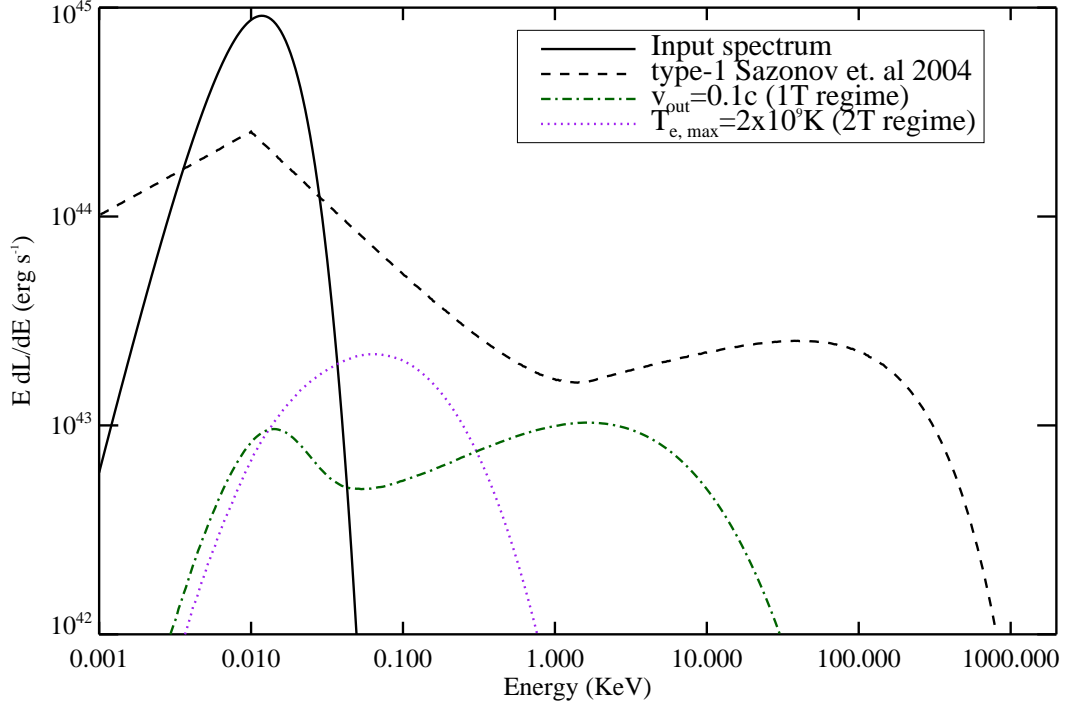


Figure 3.3: The Inverse Compton emission from shocked UFOs with  $v_w = 0.1c$  in the 1T and 2T regimes (green dashed and purple dotted lines respectively). The primary soft photon spectrum from AGN, modelled as a simple black-body at  $k_B T = 3\text{eV}$ , is also shown with a solid curve at low energies. The dashed curve shows a synthetic type 1 AGN spectrum from Figure 4 of Sazonov et al. (2004).

(function  $dN/d\theta$ ):

$$\frac{dF(\gamma)}{d\gamma} = \int_{\theta_{\text{IC}}}^{\theta_{\text{sh}}} f_{\text{MJ}}(\gamma, \theta) \frac{dN}{d\theta} d\theta, \quad (3.15)$$

where  $\theta_{\text{sh}} = k_B T_{\text{sh}}/(m_e c^2)$ , and  $\theta_{\text{IC}} = k_B T_{\text{IC}}/(m_e c^2)$ .

The cooling-convolved electron distribution function,  $dF/d\gamma$ , normalised per electron in the flow, is shown in Figure 3.2. I assumed  $v_w = 0.1c$  and hence,  $T_{\text{sh}} \simeq 2 \times 10^{10} \text{ K}$  (from equation (3.1)). For comparison I also plot the single temperature EEDs,  $f_{\text{MJ}}(\gamma, \theta_{\text{sh}})$ , and  $f_{\text{MJ}}(\gamma, \theta_{\text{IC}})$ . This figure shows that in terms of the number of electrons, the distribution is strongly dominated by the lower-energy region,  $\theta = \theta_{\text{IC}}$ . This is because high energy electrons cool rapidly and then “hang around” at  $T \approx T_{\text{IC}}$ . On the other hand, electron energy losses are dominated by the  $\theta \approx \theta_{\text{sh}}$  end of the distribution since these are weighted by the additional factor  $\sim (\gamma^2 - 1)$  (cf. equation (3.7)). Since the EED is power-law like in a broad energy range, I expect the resulting IC spectra to be power-law like in a broad range as well.

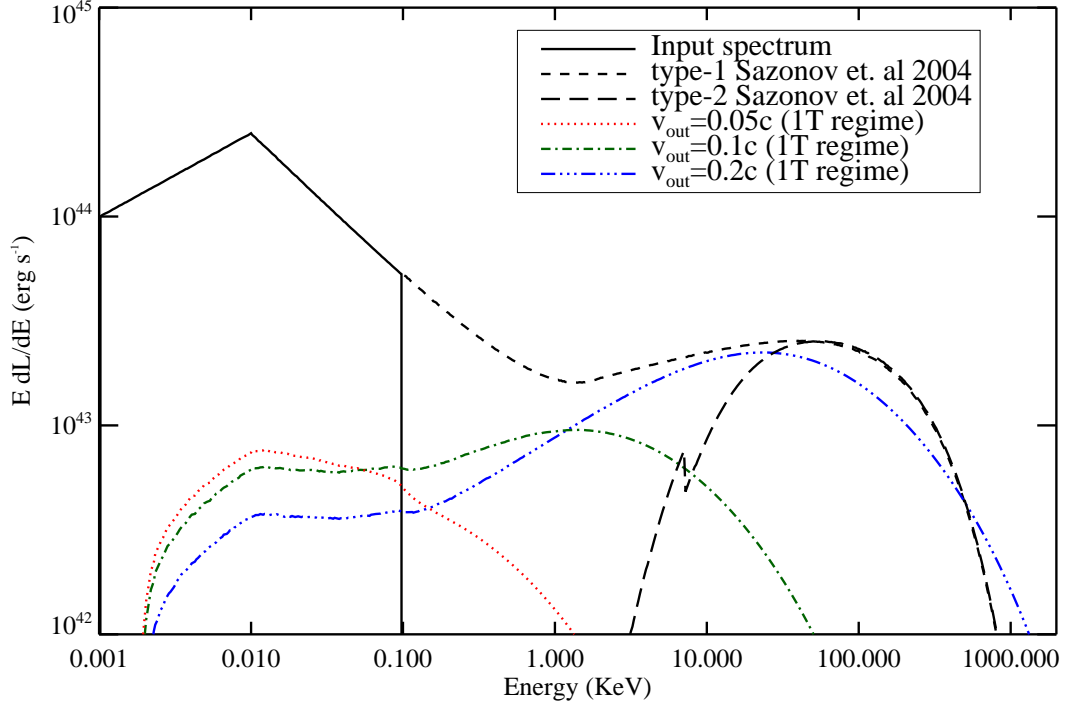


Figure 3.4: The Inverse Compton emission from shocked UFOs with  $v_w = 0.05, 0.1$  and  $0.2c$  (red dotted, green dash-dotted and blue dash-double dotted respectively) in the 1T regime only. In contrast with fig. 3.3 the primary soft photon spectrum from the AGN is modelled by the the 1 – 100eV region of the type 1 AGN spectrum from Figure 4 Sazonov et al. (2004). The black dashed and long-dashed curves shows synthetic type 1 and type 2 AGN spectra from Figure 4 of Sazonov et al. (2004) respectively.

### 3.3 Resulting spectra for 1T and 2T shocks

Figure 3.3 shows the IC spectra in both the 2T and 1T regimes, as labelled in the Figure. I assumed a SMBH with  $M_{\text{BH}} = 10^7 M_\odot$  and an outflow velocity of  $v_w = 0.1 c$ . The input spectrum is modelled by a black-body of single temperature  $k_B T = 3 \text{ eV}$  and bolometric luminosity  $L = L_{\text{bol}} = L_{\text{Edd}}$ . This simple model assumes that the UV luminosity of the innermost accretion disc is absorbed and reprocessed into a cooler black-body spectrum (I remind the reader that I assume that the UFO shocks at “large” distances from the AGN, e.g.,  $R \sim 0.1 - 100 \text{ pc}$ ). Also shown on the plots, for comparison, is a synthetic spectrum of a type 1 AGN, as computed by Sazonov et al. (2004), normalised to the same bolometric luminosity. This last spectral component demonstrates that both the 1T and 2T spectral components are actually comparable to the overall theoretical AGN spectra without UFOs; the 1T in the  $\sim 2 - 10 \text{ keV}$  photon energy spectral window, whereas the

2T shock could be detectable in softer X-rays.

To explore the sensitivity of the results to model parameters, in Figure 3.4 I use an observationally-motivated soft photon spectrum from Sazonov et al. (2004) for energies below 0.1 keV, and I also consider two additional values for the outflow velocity,  $v_w/c = 0.05$  and  $0.2$ . This figure also shows a synthetic type 2 (obscured) AGN spectrum from Sazonov et al. (2004), shown by the long-dash line.

The figure demonstrates that at high enough outflow velocities,  $v_w \sim 0.2c$ , the shocked UFOs produce power-law like spectra similar in their general appearance to that of a typical AGN. In fact, I made no attempt to fine tune any of the parameters of the King (2003, 2005) model in order to produce these spectra, so it is quite surprising that they are at all similar to the observed type 1 AGN spectra. In view of this fortuitous similarity of some of the IC spectra to the typical AGN X-ray spectra, one can enquire whether IC emission from  $\sim$ parsec scale shocks do actually contribute to the observed spectra.

Let us therefore compare the model predictions and X-ray AGN observations in some more detail:

1. *Bolometric luminosity.* Figures 3.3 and 3.4 are computed assuming 100% conversion of the UFO's kinetic power into radiative luminosity, i.e.,  $L_{IC} = L_k$  (cf. equation (3.4)) which is a fair assumption within the cooling radius,  $R_{IC}$ , for the reverse shock (which is  $\sim$  hundreds of pc for the 1T and just a few pc for the 2T models respectively, see Zubovas & King, 2012b; Faucher-Giguère & Quataert, 2012). The ratio between the X-rays and the soft photon radiation in the model is thus  $\sim (v_w/2c)$ , e.g.,  $0.05$  for  $v_w = 0.1c$ , which is just a factor of a few smaller than it is in the typical observed AGN spectra. In terms of shear bolometric luminosity 1TIC and 2TIC are thus definitely observable.

When the shock front propagates further than  $R_{IC}$ , the overall luminosity of the shock decreases. In the limit of extremely large  $R_{cd}$ , where  $R_{cd}$  is the contact discontinuity radius, the primary outflow shocks at the radius  $R_{sw} \sim (1/5)R_{cd}$  (see the text below equation 6 in Faucher-Giguère & Quataert, 2012). When  $R_{sw} \gtrsim R_{IC}$ , the outflow is in the energy-conserving mode. I estimate that the IC luminosity would scale as  $\propto R_{IC}/R_{sw}$  in this regime. In the intermediate regime,  $R_{sw} < R_{IC} < R_{cd}$ ,  $L_{IC} < L_k$ . A more detailed calculation is required in this regime to determine  $L_{IC}$  than has been performed in this chapter.

In the model of King (2003), while the SMBH mass is below its critical  $M_{BH} - \sigma$  mass, the outflow stalls in the inner galaxy,  $R \lesssim R_{ic}$ . Once  $M_{BH} > M_{\sigma,p}$  (given by

equation (1.38)), however, the outflow quickly reaches  $R \sim R_{\text{IC}}$  and then switches over to the energy-conserving mode, which is far more efficient. Therefore I would expect that the 1TIC shock emission should be a relatively widespread and relatively easily detectable feature in this scenario. But in the 2TIC case  $R_{\text{IC}}$  is just a few pc. Furthermore, since the outflow is much more likely to be in the energy conserving mode, even SMBHs below their  $M_{\text{BH}} - \sigma$  mass may clear galaxies. I would expect that shocks in this model spend most of the time in the regime  $R_{\text{cd}} \gg R_{\text{IC}}$  and are thus much dimmer than shown in Figures 3.3 and 3.4. The 2TIC component is therefore harder to detect for these reasons.

2. *Variability.* The IC shocks are very optically thin, so that the observer sees an integrated emission from the whole spherical shocked shell. Accordingly, the IC shell emission cannot vary faster than on a time scale of  $R_{\text{cd}}/c \sim 30 \text{ years } R_{\text{cd}}/(10 \text{ pc})$ . The shock travel time is even longer by the factor  $c/v_w \sim 10$ . This therefore predicts that IC shock emission must essentially be a steady-state component in X-ray spectra of AGN. In contrast, observed X-ray spectra of AGN vary strongly on all sorts of timescales, from the duration of human history of X-ray observations, e.g., tens of years, to days, hours and minutes (e.g., Mushotzky et al., 1993; Türler et al., 1999; Vaughan et al., 2003). This rapid variability is taken to be direct evidence that observed X-rays must be emitted from very close in to the last stable orbit around SMBHs and, as discussed in section 1.2.2, provided early evidence for the existence of SMBHs in galaxy centers.
3. *No molecular torus obscuration in X-rays.* Nuclear emission of AGN, from optical/UV to X-rays, is partially absorbed in “molecular torii” (Antonucci, 1993) of  $\sim \text{pc}$  scale (Tristram et al., 2009). This obscuration produces the very steep absorption trough in soft X-rays seen in type 2 AGN as compared with the type 1 sources (cf. long-dashed versus dashed curves in Figure 3.4). If a sizeable fraction of X-ray continuum from AGN were arising from the IC shocks on larger scales then that emission would not show any signatures of nuclear X-ray absorption. While Gallo et al. (2013) reports one such “strange” AGN, it is also a very rapidly varying one (cf. their figs. 9 and 10), which again rules out the 1TIC model. There are also examples where soft X-ray absorption has varied strongly on short timescales (e.g., Puccetti et al., 2007), indicating that the X-ray emission region is as small as  $10^{-4} \text{ pc}$ .
4. *No reflection component.* Compton down scattering and soft X-ray absorption by

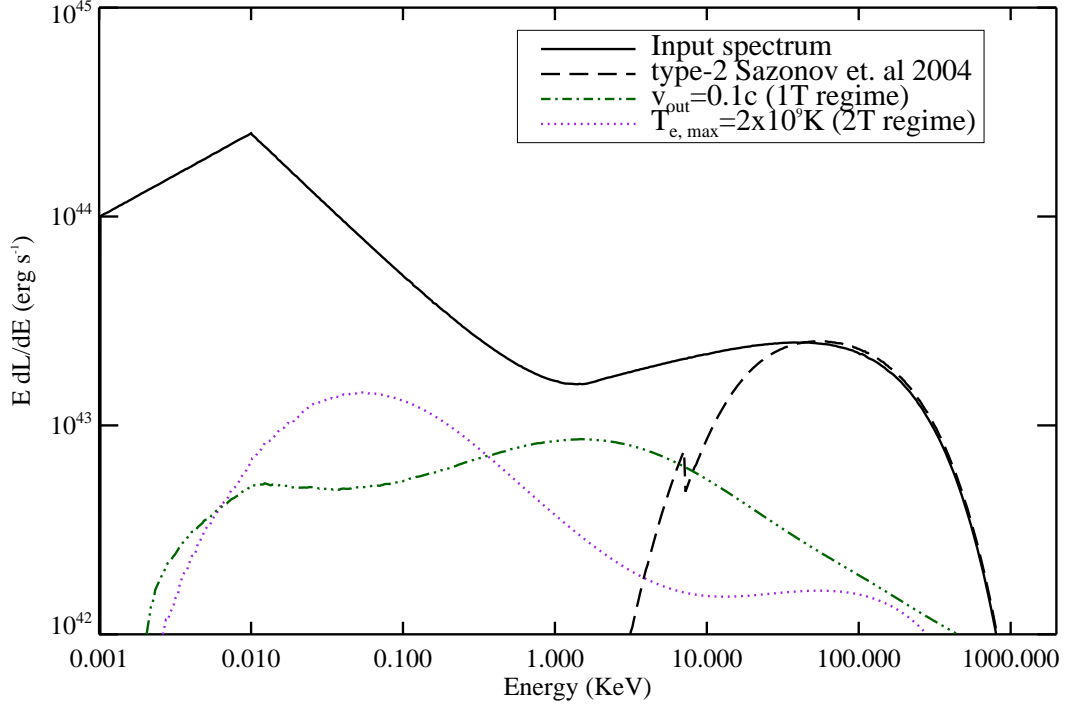


Figure 3.5: Same as Figure 3.3, but now assuming that the AGN spectrum is exactly equal to the model of Sazonov et al. (2004). Again I show the case where  $v_w = 0.1c$  in the 1T and 2T regimes (green dashed and purple dotted lines respectively).

circum-nuclear gas produces the reflection component or “Compton hump” observed in many AGN at  $\sim 30$  keV (Guilbert & Rees, 1988; Pounds et al., 1990). In addition, the fluorescent Fe K- $\alpha$  line emission is associated with the same process and is frequently detected in X-ray spectra of AGN (Nandra & Pounds, 1994). Since the shocks that I study occur on large scales, the IC emission would likely impact optically thin cold gas and thus result in much weaker X-ray reflection and Fe K- $\alpha$  line emission than is actually observed.

Given these points, I can completely rule out the most extreme assumption that the X-ray emission of AGN is due to UFO shocks alone. The next question to ask is whether having the 1TIC or 2TIC emission from the UFOs in *addition* to the “nuclear” X-ray corona emission of AGN (Haardt & Maraschi, 1993) would be consistent with the present data. To address this, I calculate the 1TIC and 2TIC emission as for Figure 3.4, but now include the part of the Sazonov et al. (2004) spectrum above 0.1 keV, which means that I now also include IC scattering of the higher energy radiation from AGN in the UFO shocks (rather than only the disc emission). The resulting spectra are shown in Figure



3.5.

I see that the 1TIC spectra would be ruled out in deeply absorbed type 2 AGN spectra, because the 1TIC component would be very obvious in these sources below a few keV. The 2TIC component, on the other hand, would not be so prominent except in very soft X-rays where interstellar absorption is significant. I therefore preliminarily suggest that X-ray emission from 1T UFO shocks may contradict the data for type II AGN, whereas 2TIC spectra would probably be comfortably within the observational limits.

### 3.4 Discussion and conclusions

I have calculated X-ray spectra of 1T and 2T IC shocks resulting from UFOs in AGN colliding with the ambient medium of the host galaxy. I conclude that 1TIC spectra could be detectable in AGN and distinguishable from “typical” AGN spectra actually observed by the absence of rapid variability, Compton reflection and Fe K- $\alpha$  lines. This disfavours 1T models for AGN feedback in my opinion. I must nevertheless caution that the quoted typical observed AGN spectra and properties may be dominated by local objects that are simply not bright enough to produce a significant kinetic power in outflows, which the model here assumed. I therefore urge X-ray observers to search for the un-absorbed and quasi-steady emission components presented in this chapter in order to clarify the situation further.

It is interesting to note that the 2TIC comes out mainly in the soft X-rays where it is far less conspicuous as this region is usually strongly absorbed by a cold intervening absorber. In fact it is possible that the 2TIC emission component calculated here does contribute to the observed “soft X-ray excess” feature found at softer X-ray energies ( $< 1$  keV) but not yet understood (Gierliński & Done, 2004; Ross & Fabian, 2005; Crummy et al., 2006; Scott et al., 2012). The 2T spectral component in Figure 3.3 would provide a soft excess that matches the observed shape and that is independent of the X-ray continuum, a requirement suggested by e.g. Rivers et al. (2012). The observed soft excess does not vary in spectral position over a large range of AGN luminosities (Walter & Fink, 1993; Gierliński & Done, 2004; Porquet et al., 2004). The 2TIC model may account for this as well since Figure 2. of Faucher-Giguère & Quataert (2012) shows that  $T_{\text{eq}}$  is quite insensitive to the exact value of the outflow velocity. Finally, the 2TIC emission would exhibit little time variability. Uttley et al. (2003) and Pounds & Vaughan (2011) report a quasi-constant soft X-ray component in NGC 4051 which can only be seen during periods of low (medium energy) X-ray flux. The feature is qualitatively consistent with the 2TIC

shock scenario. Therefore, I conclude that general facts from present X-ray observations of AGN not only disfavour a 1TIC component over a 2TIC component, but may actually hint to the presence of a 2TIC one in the observed spectra.

Whether or not the electrons thermally decouple from hot protons is vitally important for the problem of the impact of AGN feedback on their host galaxies. Because of their far larger mass, the ions carry virtually all of the kinetic energy of the outflow. At the same time, however, the ions are very inefficient at radiating their energy away compared with the electrons. In the 1T model the electrons are able to sap away most of the shocked ions energy and therefore the AGN feedback is radiative, that is, momentum-driven, inside the cooling radius (King, 2003). In this scenario only the momentum of the outflow affects the host galaxy's gas. In the 2T scenario, the outflow is non-radiative, so that the ions retain most of their energy. The AGN feedback is thus even more important for their host galaxies in this energy-driven regime (Zubovas & King, 2012a; Faucher-Giguère & Quataert, 2012). Further, given that the ions carry most of the energy of the shocked wind, they are expected to dominate the thermal pressure. Therefore the pressure of the hot bubble can still be calculated using the equation of state for an ideal gas (i.e. equation (2.14)), an assumption that is used when modelling feedback in the simulations run in Chapters 4 and 5.

If the outflows are indeed in the 2T mode then one immediate implication concerns the recently discovered *positive* AGN feedback on their host galaxies. Well resolved numerical simulations of Nayakshin & Zubovas (2012); Zubovas et al. (2013b) show that ambient gas, when compressed in the forward shock (to clarify, the shock I studied here is the reverse one driven in the primary UFO), can cool rapidly in the gas-rich host galaxies. The nearly isothermal outer shock is gravitationally unstable and can form stars. In addition Zubovas et al. (2013a) argue that galactic gas discs can also be pressurised very strongly by the AGN-driven bubble. In these cases AGN actually have a positive – accelerating – influence on the star formation rate in the host galaxy. Within the 1T formalism, the AGN-triggered starbursts occur outside  $R_{IC} \sim$  hundreds of pc only (Zubovas et al., 2013a). If outflows are 2T then AGN could potentially accelerate or trigger star bursts even in the nuclear regions ( $O(10)$  pc) of their hosts.

Finally, given the expected difficulty in observing shocked outflows especially in the 2T regime, alternative *direct* sources of evidence may be necessary to confirm that UFOs shock with and couple to the host ISM. To this end Nims et al. (2015) have calculated the observational signature for the forward (ISM) shock (see figure 1.7) produced when a wind collides with the ambient gas. They find that a thermal component in the 1 –

10 keV region should be produced with a luminosity of  $10^{41} - 10^{44}$  erg s<sup>-1</sup> through IC and Bremsstrahlung processes within the forward shock. They also propose that shock accelerated electrons should produce a non-thermal radio signal indicating that even radio quiet galaxies should produce a significant radio luminosity.



---

# 4

## Black hole feedback in a multi-phase inter-stellar medium

*“Twinkle, twinkle, quasi-star  
Biggest puzzle from afar  
How unlike the other ones  
Brighter than a billion suns  
Twinkle, twinkle, quasi-star  
How I wonder what you are.”*

*George Gamow*

## 4.1 Introduction

Observational correlations between the mass of SMBHs and their host galaxies, such as those detailed in section 1.4 e.g., the  $M_{\text{BH}} - \sigma$  relation (Ferrarese & Merritt, 2000; Gebhardt et al., 2000; Tremaine et al., 2002; Kormendy & Ho, 2013) and the  $M_{\text{BH}} - M_{\text{b}}$  relation (Magorrian et al., 1998; Ho, 1999b; Kormendy & Gebhardt, 2001; Merritt & Ferrarese, 2001; McLure & Dunlop, 2002; Marconi & Hunt, 2003; Häring & Rix, 2004; Sani et al., 2011; Beifiori et al., 2012; McConnell & Ma, 2013; Kormendy & Ho, 2013) link the evolution of the SMBH and their host bulge. As discussed in section 1.6.1, feedback (e.g., Silk & Rees, 1998; King, 2003, 2005) in the form of UFOs, has been invoked to explain and derive the  $M_{\text{BH}} - \sigma$  relation from analytical arguments (King, 2003, 2005; Nayakshin, 2014). The model is very attractive due to its simplicity, reliance on common sense physics (Eddington limit, escape velocity and radiation momentum outflow rate arguments), observational analogy to outflows from massive stars (that are also near their Eddington limits), and finally direct observations of UFOs in nearby bright AGN (Pounds et al., 2003b; King & Pounds, 2003; Tombesi et al., 2010a,b; Pounds & Vaughan, 2011; Tombesi et al., 2015).

As outlined in section 1.6.1.2, assuming a homogeneous gas distribution following a SIS potential (e.g., §4.3.3b in Binney & Tremaine, 2008), King (2003) shows that within the IC cooling radius,  $R_{\text{IC}} \sim 500 M_8^{1/2} \sigma_{200} \text{ kpc}$  (defined in section 1.6.1.1 and taken from Zubovas & King, 2012b), the wind shock, which develops when the UFO collides with the ISM, can cool effectively via IC scattering. Most of the thermalised wind kinetic energy is lost to this radiation, and only the pre-shock ram pressure impacts the ISM. By considering the equation of motion of the swept up ISM shell, King (2003) derived the mass that the SMBH had to attain in order to clear the host galaxy's gas and I point the reader to section 1.6.1.2 and in particular equation (1.37) for more details. Beyond the cooling radius,  $R_{\text{IC}}$ , the wind shock cannot cool effectively and retains the wind's kinetic energy in the form of thermal energy and the outflow becomes energy driven. This regime is much more effective at clearing gas from the host galaxy.

The model of King (2003) assumes that the electrons and ions in the shock share a single temperature at all times, initially the shock temperature  $T_{\text{sh}} \sim 10^{10} \text{ K}$ . However, Faucher-Giguère & Quataert (2012) have shown that, due to the high temperature and low density of the shocked wind, the electron-ion energy equilibration time-scale is long compared with the Compton time-scale. This would imply that the electron temperature is much lower than the ion temperature, i.e.  $T_{\text{e}} \ll T_{\text{ion}}$ , as shown in Figure 1.8

(taken from Faucher-Giguère & Quataert, 2012) for a  $v_w = 0.1 c$  UFO. In chapter 3 (see also Bourne & Nayakshin, 2013) I point out an observational test to distinguish between outflows with a 1T ( $T_e = T_i$ ) or 2T structure, and conclude preliminarily that X-ray observations broadly support the findings of Faucher-Giguère & Quataert (2012). This would, however, lead to significant implications for AGN feedback on host galaxies: most of the UFO's kinetic energy carried by the ions is then conserved rather than radiated away. The cooling radius,  $R_{IC}$ , becomes negligibly small on the scale of the host galaxy and the outflow is essentially always in the energy conserving phase. Based on spherically symmetric analytical models (e.g., King, 2005), as shown in section 1.6.1.2, even black holes  $\sim 100$  times below the  $M_{BH} - \sigma$  could clear a galaxy of its gas. It is then not clear (i) how black holes manage to grow so massive and (ii) why momentum-conserving flows provide such a tight fit to the observed  $M_{BH} - \sigma$  relation (King, 2003).

Several recent additional numerical and analytical results, however, call the spherically symmetric models of AGN feedback into question. In the context of the physically related problem of stellar feedback, Harper-Clark & Murray (2009) modelled the structure of a hot bubble inflated by a cluster of young stars in Carina Nebula and have shown that the models assuming spherical symmetry do not explain the observational data. At the same time a model in which the ambient ISM is clumpy accounts for observations much better. Harper-Clark & Murray (2009) build a toy analytical model in which a significant fraction of the energy inside of the hot bubble is lost via advection, e.g., adiabatic expansion energy losses rather than radiative energy losses (which can be directly observed in X-rays in the case of Carina Nebula and are much lower than expected in the spherically symmetric models). Physically, the authors argue that the compressed shell of a multiphase ISM has pores through which the hot gas escapes. This deflates the bubble and allows a much better explanation of the bubble size, age and luminosity.

Rogers & Pittard (2013) have recently performed 3D numerical simulations of a supernova exploding inside an inhomogeneous giant molecular cloud and found results consistent with that of Harper-Clark & Murray (2009): the densest molecular regions turned out to be surprisingly resistant to ablation by the hot gas which was mainly escaping from the region via low density channels.

For the AGN feedback problem that I study here, Wagner et al. (2012) have found very similar results when studying the interaction of an AGN jet with the multiphase ISM. Furthermore, Wagner et al. (2013) studied the interaction of a wide-angle outflow with an inhomogeneous ambient medium finding again that the hot gas mainly streams away through channels between the cold clouds; the latter are impacted by the momentum of

the UFO only. These authors also concluded that the opening angle of the UFO at launch appears secondary, since interactions of the UFO with the intervening clouds isotropise the hot bubble so that the result of a jet or an UFO running into the inhomogeneous ISM may actually be much more similar than often assumed.

In an analytical study, Nayakshin (2014) has also argued that most of the UFO energy leaks out of the porous bulge via the low-density voids and that the cold gas is affected only by the ram pressure. He argued that the densest cold clouds may continue to feed the AGN via the ‘chaotic accretion mode’ (King & Pringle, 2006; Hobbs et al., 2011) despite the AGN blowing an energy-driven bubble into the host galaxy and that the balance between the ram pressure of the UFO on the clouds and cloud self-gravity leads to an  $M_{\text{BH}} - \sigma$  correlation very similar in functional form to that of King (2003, 2005).

Furthermore, Zubovas & Nayakshin (2014) have presented numerical simulations of AGN feedback impacting elliptical, initially homogeneous ambient gas distributions and showed that the UFO energy escapes via directions of least resistance (along the minor axis of the ellipsoid). They additionally presented a toy analytical model similar in spirit to that of Harper-Clark & Murray (2009), which showed that the SMBH growth stops when the SMBH reaches a mass of the order of the King (2003) result. In this chapter I investigate these ideas further numerically. I set up a hot bubble of shocked UFO gas bounded by either one- or two-phase ambient gas and then study the resulting interaction. The multiphase gas is produced by evolving a Gaussian random velocity field as is frequently done in numerical models of star formation inside turbulent molecular clouds (e.g., Bate, 2009b), similar to earlier work by Hobbs et al. (2011).

The numerical methods and initial conditions differ substantially from that of Wagner et al. (2012, 2013) and Zubovas & Nayakshin (2014), but the results are qualitatively similar. I also find that most of the UFO energy is carried away by hot low density gas escaping the innermost regions of the host via paths of least resistance, which exists in the clumpy ISM in abundance (e.g., McKee & Ostriker, 1977). Most of the gaseous mass in the models is in the high-density cold phase of the ISM that occupies a small fraction of the host’s volume and for this reason host galaxies turn out to be much less vulnerable to AGN feedback than could be thought based on energy budget arguments alone.



## 4.2 Simulation set-up

### 4.2.1 Numerical method

The simulations presented here make use of a modified version of the N-body/hydrodynamical code GADGET-3, an updated version of the code presented in Springel (2005), which I described extensively in Chapter 2. I implement the SPHS<sup>1</sup> formalism as described in Read et al. (2010) and Read & Hayfield (2012) in order to correctly treat mixing within multiphase gas together with a second-order Wendland kernel (see equation (2.16), Wendland, 1995; Dehnen & Aly, 2012) with 100 neighbours. The SPHS algorithm was developed for the express purpose of capturing instabilities such as Kelvin-Helmholtz and Rayleigh-Taylor, and has been demonstrated as robust in many test problems (Read & Hayfield, 2012) and full galaxy formation simulations (Hobbs et al., 2013). Details of the SPHS technique have also been discussed in section 2.3 of this thesis.

The simulations are run in a SIS potential with the total mass of the potential within radius  $R$  following:

$$M_{\text{pot}}(R) = \frac{M_a}{a} R = \frac{2\sigma_{\text{pot}}^2}{G} R, \quad (4.1)$$

where  $M_a = 5 \times 10^{10} M_\odot$  and  $a = 4 \text{ kpc}$ . The potential is softened at small radii in order to avoid divergence in the gravitational force as  $R$  tends to zero. The one dimensional velocity dispersion of the potential is  $\sigma_{\text{pot}} = (GM_a/2a)^{1/2} \simeq 164 \text{ km s}^{-1}$ .

I assume an ideal gas with the equation of state given by equation (2.14), with  $\gamma = 5/3$ . The temperature of the gas is subsequently calculated as  $T = (\gamma - 1)\mu u/k_B$ , where  $u$  is the specific internal energy of the gas,  $k_B$  is the Boltzmann constant, and  $\mu$  is the mean molecular weight, which is calculated self-consistently (although I assume  $\mu = 0.63$  when plotting  $T$ ). I use the optically thin radiative cooling function of Sazonov et al. (2005) described in section 2.5, for gas ionised, cooled and heated in the presence of an AGN radiation field (assuming a fixed black hole luminosity of  $L_{\text{Edd}} = 2.5 \times 10^{46} \text{ erg s}^{-1}$ ) for  $T > 10^4 \text{ K}$ . Below  $10^4 \text{ K}$ , cooling is modelled as in Mashchenko et al. (2008, also described in section 2.5), which proceeds through fine structure and metastable lines of C, N, O, Fe, S and Si. For simplicity, I fix metal abundances at solar metallicity. I impose a temperature floor of 100 K.

As discussed in section 2.6, many prescriptions are used to model star formation in simulations. I use an approach similar to Zubovas & Nayakshin (2014) and Zubovas

---

<sup>1</sup>Smooth particle hydrodynamics with a high-order dissipations switch.

(2015) in which SPH particles are converted into star particles according to a Jeans instability condition. SPH particles with density above a critical density of

$$\rho_{crit} = \rho_{thresh} + \rho_J \quad (4.2)$$

are turned into star particles, where  $\rho_{thresh} = 10^{-20} \text{ g cm}^{-3}$  and  $\rho_J$  is the local Jeans density, which can be derived as follows. A gas cloud is in virial equilibrium when

$$E_{pot} = -2E_{kin}, \quad (4.3)$$

where  $E_{pot}$  and  $E_{kin}$  are the gravitational potential and kinetic energy of the cloud respectively. Assuming a spherical cloud of constant density  $\rho$ , mass  $M$ , radius  $R$  and temperature  $T$ , this can be rewritten as

$$\frac{3}{5} \frac{GM^2}{R} = 3 \frac{Mk_B T}{\mu m_p}. \quad (4.4)$$

Substituting in

$$R = \left( \frac{3}{4\pi} \frac{M}{\rho} \right)^{1/3}, \quad (4.5)$$

and rearranging we find a critical density of

$$\rho = \left( \frac{4\pi}{3} \right)^2 \left( \frac{15}{4\pi} \right)^3 \left( \frac{k_B T}{G \mu m_p} \right)^3 M^{-2}, \quad (4.6)$$

which defines the density threshold above which a gas cloud of a given mass and temperature will undergo gravitational collapse. As discussed in section 2.6, I require the mass of a resolution element to not exceed the local Jeans mass, i.e.  $M \simeq N_{ngb} m_{SPH} < M_J$ , which is achieved provided the density of the resolution element does not exceed a value of<sup>2</sup>

$$\rho_J = \left( \frac{\pi k_B T}{\mu m_p G} \right)^3 (N_{ngb} m_{SPH})^{-2} \simeq 1.17 \times 10^{-18} \left( \frac{T}{10^4 \text{ K}} \right)^3 \text{ g cm}^{-3} \quad (4.7)$$

where  $N_{ngb} = 100$  is the typical number of neighbours of an SPH particle and  $m_{SPH}$  is the SPH particle mass. The  $\rho_{thresh}$  term ensures that only high-density gas is converted into star particles whilst the second term is the local Jeans density (see section 2.6) and ensures that stars only form in gas that is unstable towards gravitational collapse<sup>3</sup>. Removing

<sup>2</sup>The numerical value of  $\left( \frac{4\pi}{3} \right)^2 \left( \frac{15}{4\pi} \right)^3 \simeq \pi^3$ .

<sup>3</sup>Strictly speaking in order to properly follow the collapse of gas one should be able to resolve the local

high-density gas aids in reducing the computation time by removing particles that would otherwise have prohibitively short time-steps. Each newly formed star particle has the same mass as the original SPH particle and only interacts with other particles through gravity. The exact star formation prescription employed is largely unimportant for the simulations presented in this chapter because the length of the simulation is significantly shorter than the timescale on which star formation occurs. Similarly it is not necessary to include sources of turbulent driving such as stellar feedback because the timescale on which the ISM alters significantly is also much shorter than the length of the simulation.

### 4.2.2 Initial conditions

Simulation of isolated galaxies by definition does not model gas inflows into galaxies from larger scales and therefore idealised initial conditions for the ISM of the host must be used. There is a considerable freedom in choosing these initial conditions. In Wagner et al. (2012, 2013), cold, high-density clumps in hydrostatic equilibrium with the hot, low-density phase are introduced at the beginning of the simulation. The initial velocity of the gas is zero everywhere.

In the current chapter, however, since the epoch I am interested in is one of rapid SMBH growth and star formation in the host galaxy, the ambient gas may be in a very dynamical non-equilibrium state, which I model with an imposed turbulent velocity flow. In doing so I am inspired by numerical studies of star formation in molecular clouds (e.g., Bate et al., 2003). In practice, the method for generating two-phase initial conditions is based on earlier work by Hobbs et al. (2011), where the importance of high-density gas clumps for SMBH *feeding rather than feedback* was studied.

I seed a sphere of gas (cut from a relaxed, glass-like configuration) with a turbulent velocity field following Dubinski et al. (1995), as described in Hobbs et al. (2011). Here I provide a brief summary of the process and I point the reader to the aforementioned articles for more detailed explanations. The Kolmogorov turbulence power spectrum,  $P_v(k) \sim k^{-11/3}$ , is assumed for the velocity field, where  $k$  is the wavenumber. The gas velocity  $\mathbf{v}$  is defined as  $\mathbf{v} = \nabla \times \mathbf{A}$ , where  $\mathbf{A}$  is a vector potential whose power spectrum is also described by a power-law with a cutoff at  $k_{\min} = 2\pi/\lambda_{\max}$ . This defines the largest physical scale,  $\lambda_{\max} = 2\pi/k_{\min}$ , on which turbulence can be driven. Here I set

---

Jeans mass,  $M_J$ , i.e.  $n_{\text{ngb}} m_{\text{sph}} < M_J$  (Bate & Burkert, 1997; Whitworth, 1998). Gas with  $T = T_{\text{floor}} = 100$  K has  $\rho_J \simeq 10^{-24}$  g cm $^{-3}$  leading to some gas having  $\rho > \rho_J$  but not being converted into stars and hence I am not resolving the Jeans mass of this gas. However for the purpose of these simulations I am not particularly interested in studying star formation in detail and the number of particles for which the above condition is true is negligibly small.

---

$k_{\min} \simeq 1/R_{\text{out}}$ , as the shell becomes distorted for larger  $\lambda_{\max}$ . In defining  $\mathbf{v}$  as the curl of a vector potential, I assume that the velocity field is divergence free, i.e.,  $\nabla \cdot \mathbf{v} = 0$ . This means that the turbulence is produced by solenoidal, opposed to compressive, forcing (for comparisons see, e.g., Federrath et al., 2008, 2009, 2010). In reality a combination of solenoidal and compressive forcing is expected. However, for the purpose of this chapter, in which the primary goal of the turbulence is to produce an inhomogeneous medium, purely solenoidal forcing will suffice. Following Hobbs et al. (2011), the statistical realisation of the velocity field is produced by sampling the vector potential  $\mathbf{A}$  at each point  $(k_x, k_y, k_z)$  in Fourier space. The components of  $\mathbf{A}_{\mathbf{k}}$  are complex and can therefore be described by an amplitude, which is drawn from a Rayleigh distribution with standard deviation  $\langle |\mathbf{A}_{\mathbf{k}}| \rangle$ , and a phase angle, which takes a random value between 0 and  $2\pi$ . Finally in order to recover the velocity field in real space I take the Fourier transform of  $\mathbf{v}_{\mathbf{k}} = i\mathbf{k} \times \mathbf{A}_{\mathbf{k}}$  and interpolate the velocity onto the particle positions.

The gas initially follows the SIS potential (meaning that  $\rho(R) \propto R^{-2}$ ) from  $R_{\text{in}} = 0.1$  kpc to  $R_{\text{out}} = 1$  kpc with a gas mass fraction  $f_g = M_g/(M_g + M_{\text{pot}}) = 0.5$ , where  $M_g$  and  $M_{\text{pot}}$  are the gas and potential mass within the shell  $0.1 \leq R \leq 1$  kpc respectively. In order to avoid particles at small radii with prohibitively small time steps I add a sink particle at the centre of the simulation domain with  $M_{\text{sink}} = 2 \times 10^8 M_{\odot}$  ( $\sim M_{\sigma,p}/2$ , see equation (1.16), taken from Kormendy & Ho, 2013). The turbulent velocity is normalised such that the root-mean-square velocity,  $v_{\text{turb}} \simeq \sigma \simeq 232 \text{ km s}^{-1}$ , where  $\sigma \simeq (GM_a/2a(1 - f_g))^{1/2}$  is the velocity dispersion of the background potential plus gas component. The initial gas temperature is set to  $T \simeq 1 \times 10^6 \text{ K}$ , such that the shell is marginally virialised, i.e;  $(E_{\text{turb}} + E_{\text{therm}})/|E_{\text{grav}}| \sim 1/2$ , where  $E_{\text{turb}}$  and  $E_{\text{therm}}$  are the total turbulent kinetic energy and total thermal energy of the gas respectively and  $E_{\text{grav}}$  is the gravitational potential energy of the system.

The system is allowed to evolve under the action of the turbulent velocity field for time  $\sim \tau_{\text{dyn}}/3 = R_{\text{out}}/3\sigma$ , allowing the density inhomogeneities to grow. The resulting gas shell is then re-cut to have an inner radius  $R_{\text{in}} = 0.3$  kpc and outer radius  $R_{\text{out}} = 1$  kpc. The total gas mass is  $M_g \simeq 5.9 \times 10^9 M_{\odot}$ , corresponding to a gas fraction of  $f_g \simeq 0.4$  and giving a velocity dispersion for the system (gas + potential within the shell) of  $\sigma \simeq 212 \text{ km s}^{-1}$ . The total number of particles in the gas shell is  $N_{\text{SPH}} \simeq 2.6 \times 10^6$  with a particle mass  $m_{\text{SPH}} \simeq 2250 M_{\odot}$ .

As already outlined in section 1.6.1, typical parameters for an UFO give a velocity  $v_{\text{out}} \sim 0.1 c$ , mass outflow rate  $\dot{M}_{\text{out}} \sim 0.1 M_{\odot} \text{ yr}^{-1}$  and kinetic energy flux  $\dot{M}_{\text{out}} v^2/2 \simeq 0.05 L_{\text{Edd}}$ . It has been highlighted in section 2.7 that modelling a continuous injection

of fast wind particles by SPH is not currently feasible: at our present mass resolution (which is much higher than a typical cosmological simulation), a single SPH particle accounts for all of the UFO mass over  $\sim 22.5$  kyr. Fortunately it is the total energy budget of the hot shocked wind bubble and not its minuscule mass that determines the strength of the bubble's impact on the ambient medium (the mass of the UFO is so small compared to the host galaxy that it does not even enter in the analytic theory; King, 2010). Therefore, I rescale the properties of the UFO particles, keeping the hot bubble's energy at a desirable value but increasing the outflow's mass, to be able to model the thermalised UFO hydrodynamically and with a reasonable numerical resolution. In particular the UFO thermalised in the reverse shock is introduced in the initial condition as a hot spherical bubble of radius  $R_{\text{bub}} = 0.3$  kpc centred on the sink particle. I have tested different bubble masses and find that, qualitatively, the main conclusions of this chapter remain unchanged. I note here that in chapter 5 I present an AGN feedback resolution study using a common subgrid feedback prescription.

The initial gas density and temperature are assumed constant throughout the bubble as expected (Faucher-Giguère & Quataert, 2012). The temperature and mass of the bubble are determined based upon the desired energy ratio between the hot bubble ( $\sim M_{\text{H}}c_s^2$ ) and the ambient gas ( $\sim M_{\text{a}}\sigma^2$ ) components:

$$E_r = \frac{E_{\text{H}}}{E_{\text{a}}} = \frac{M_{\text{H}}c_s^2}{M_{\text{a}}\sigma^2} \quad (4.8)$$

where  $E_{\text{H}}$  and  $E_{\text{a}}$  are approximations of the energy in the hot bubble and the ambient gas, respectively,  $M_{\text{H}}$  and  $M_{\text{a}}$  are the total mass in the hot and cold component, respectively,  $c_s$  is the sound speed in the hot bubble and  $\sigma \simeq 212 \text{ km s}^{-1}$  is the velocity dispersion. All simulations presented in this chapter use  $c_s \simeq 3000 \text{ km s}^{-1}$  and  $E_r = 5$ ; the main conclusions of this chapter are independent of  $E_r$  as long as  $E_r \gg 1$ , as expected for AGN-inflated feedback bubbles (King, 2010). The left-most panels in Figure 4.2 show the initial density and temperature structure of the system.

As well as the runs with a turbulent medium, I have a control simulation that has not been seeded with turbulence to contrast the outcomes. The radial gas distribution of the control run follows the same profile as the turbulent shell *before* relaxation (i.e., SIS), so that the gas is homogeneous, but has a mass equal to that of the turbulent shell *after* relaxation (i.e.,  $M = 5.9 \times 10^9 M_{\odot}$ ). The initial radially binned gas distribution is hence identical for the homogeneous and turbulent runs save for a slight evolution during relaxation of the latter runs as described above (compare the dashed red and blue curves

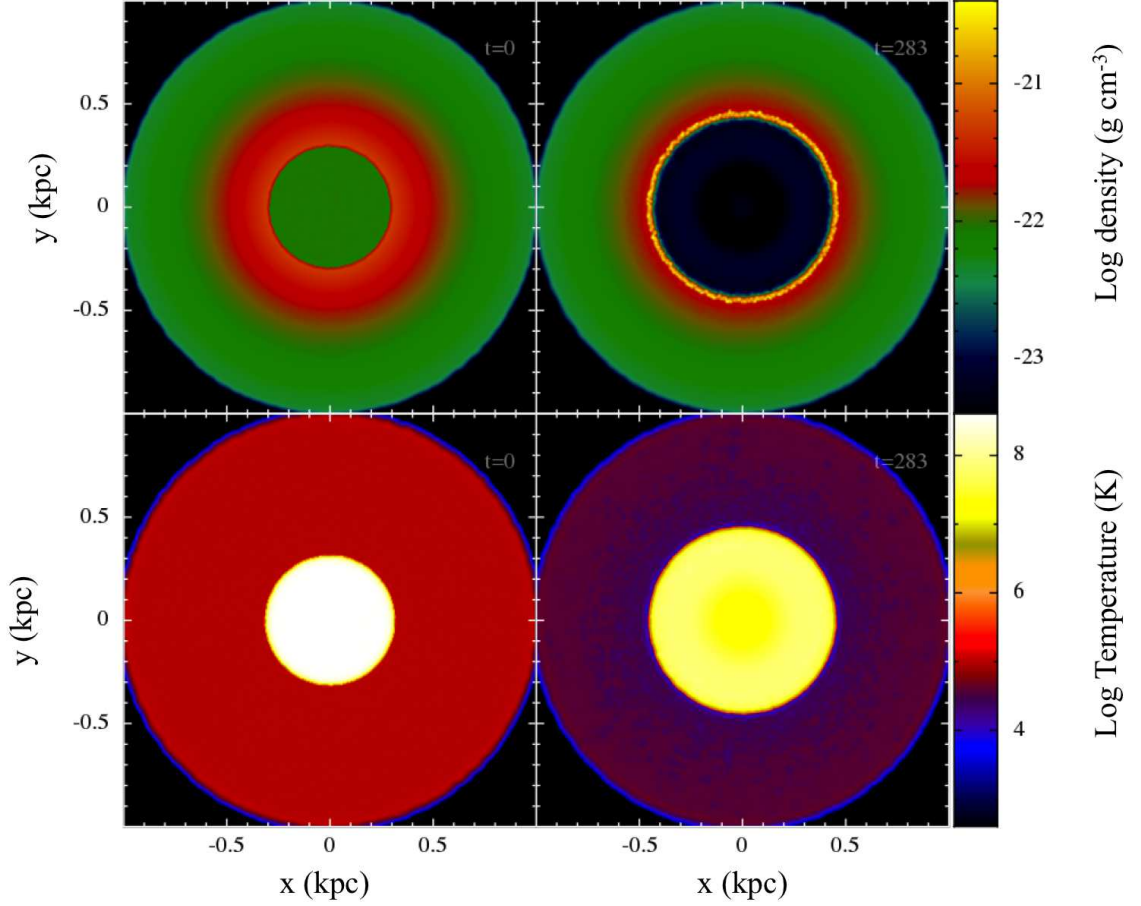


Figure 4.1: Density (top panel) and temperature (bottom) slices through  $z=0$  plane at time  $t=0$  and  $t \approx 282$  kyr for homogeneous initial condition simulation H1.

in Figure 4.3).

It should also be noted that the control run has a low initial temperature  $T \approx 10^5$  K, which is sub-virial in order to ensure that the gas remains homogeneous during the simulation, which is the regime I wish to study here. Further, since there is no imposed turbulent velocity field that would develop into the turbulent multiphase ISM, there is no need to relax this initial condition before applying the hot bubble. For this reason, the gas has a zero initial velocity in the homogeneous control run, unlike the turbulent run. This difference in initial conditions has a minor effect on the final outcome of the simulations because the radial velocity gained by the gas in the homogeneous run is much larger than the difference in the initial velocities in the two runs. I also note that the static nature of the gas distribution in the homogeneous run is similar to the gas properties assumed for a number of analytical models (e.g., King, 2003, 2005).

In what follows I refer to the simulations as the turbulent (T1) and control (homoge-

neous, H1) runs. In order to study the direct impact of the hot bubble on the ambient gas and/or to avoid confusion due to the dense gas phase shielding lower density gas behind it (at larger radii), a number of figures only include the SPH particles that were within the radial range  $0.3 \leq R \leq 0.35$  kpc at  $t = 0$  kyr. Behaviour of gas initially at larger radii will nevertheless be discussed in some of the figures below.

### 4.3 Feedback on turbulent versus homogeneous medium

Figure 4.1 shows density (top) and temperature (bottom) slices at time  $t = 0$  (left) and  $t \simeq 283$  kyr (right) for the homogeneous density run, H1. Figure 4.2 shows the same quantities at four different times for the turbulent initial condition simulation T1. The times of the first and the last snapshots are the same as those for Figure 4.1.

It is immediately obvious that the homogeneous ambient density case, H1, produces a “boring” spherically symmetric, dense, shell that is expanding under the pressure of the hot bubble in the middle. The bubble also remains spherically symmetric.<sup>4</sup> Importantly, the bubble drives *all* of the ambient gas encountered outward at a high velocity, in line with the analytical models discussed in section 1.6.1.2.

This is in stark contrast to the turbulent run as can be seen in Figure 4.2. The expansion of the hot bubble into the ambient phase occurs along the paths of least resistance. The low-density ambient phase is swept up and pushed out, while the high-density gas suffers a much smaller positive radial acceleration and little (if any) gain in temperature. Some compression and ablation of the cold dense medium does occur, but most of it survives the bubble’s passage intact.

Figure 4.3 highlights the differences in the results of simulation H1 and T1 in a more compact way by presenting the distribution of gas in radial bins. The blue and red dashed curves show the initial ambient gas mass within concentric spherical shells of 10 pc width for the turbulent and the homogeneous (control) runs respectively. The solid curves of the same colour show how these gas distributions evolve by time  $t \simeq 283$  kyr. Note that the bubble swept up *all* of the ambient gas within a radius of  $\sim 0.45$  kpc into a dense shell in the control run, but is obviously having great difficulties in removing the gas in the turbulent simulation. The density of the gas in the inner regions actually increases in the latter simulation as some of the cold dense gas falls in while the hot bubble fizzles out

---

<sup>4</sup>There may be small scale Vishniac (1983) instabilities developing on the surface of the bubble (Nayakshin & Zubovas, 2012), but these instabilities grow slower than the shell is driven outward in this energy-conserving situation.

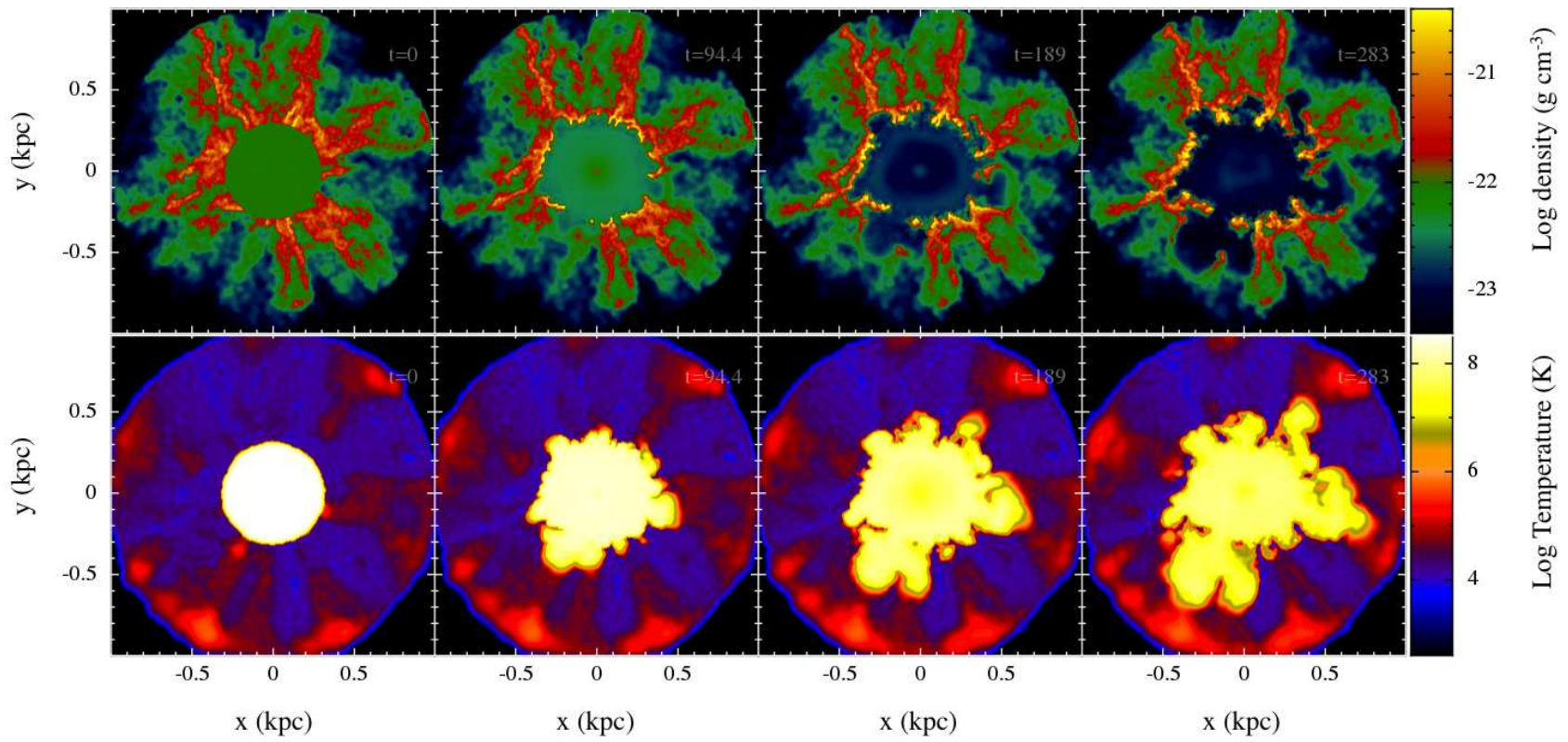


Figure 4.2: Same as Figure 4.1 but for the turbulent initial condition simulation T1. Density (top panel) and temperature (bottom panel) slices through  $z=0$  plane evolving in time from  $t=0$  to  $t \simeq 282$  kyr in steps of  $\sim 94$  kyr, from left to right, respectively.



through the pores in the ambient gas.

These results illustrate clearly the main thesis of this chapter: *the impact of an UFO on the inhomogeneous multiphase medium is much less efficient than expected based on spherically symmetric modelling.*

## 4.4 Dynamics of clumpy gas

### 4.4.1 Gas dynamics as a function of its density

I shall now analyse the response of the ambient gas to the presence of the hot bubble in the turbulent simulation T1 in greater detail. This response is a strong function of the properties of the ambient gas. Figure 4.4 shows the distribution of gas over radial velocity at time  $t \simeq 70.8$  kyr, for three different initial density ranges (i.e. particles are grouped based upon their density at  $t = 0$ ). To avoid confusion due to the dense gas phase shielding lower density gas behind it, that is therefore unaffected by the feedback flow yet, I include only the SPH particles that were within  $0.3 \leq R \leq 0.35$  kpc at  $t = 0$  kyr. The red and blue histograms show particles that originally have the highest and lowest densities whilst the grey curve shows particles around the logarithmic mean density. Each of the histograms accounts for  $\sim 10\%$  of the total number of particles within  $0.3 \leq R \leq 0.35$  kpc at  $t = 0$  kyr. Figure 4.4 demonstrates that the lowest density gas is accelerated to high radial velocities, with a mean of  $\langle v_r \rangle \simeq 661 \text{ km s}^{-1}$ . In contrast, the highest density gas is, on average, continuing to infall with a mean  $\langle v_r \rangle \simeq -145 \text{ km s}^{-1}$ . The logarithmic mean density gas shows a variety of behaviours from an infall with velocity of a few hundred  $\text{km s}^{-1}$  to an outflow with a similar range in velocities.

Also plotted are lines indicating the mean radial velocity of all of the gas originally in the  $0.3 \leq R \leq 0.35$  kpc region in the turbulent simulation ( $\langle v_r \rangle \simeq 125 \text{ km s}^{-1}$ ) and in the homogeneous control run. In the later case the gas is accelerated to high velocities on average ( $\langle v_r \rangle \simeq 563 \text{ km s}^{-1}$ ), in a single spherical shell of swept up material whilst in the turbulent simulation the hot bubble can escape through the porous medium and so much of the material does not get accelerated outwards. For the turbulent simulation, not only does the outflow fail to clear out the high-density material, but a large fraction of the low-density material is also left behind due to shielding by high-density material in front of it.

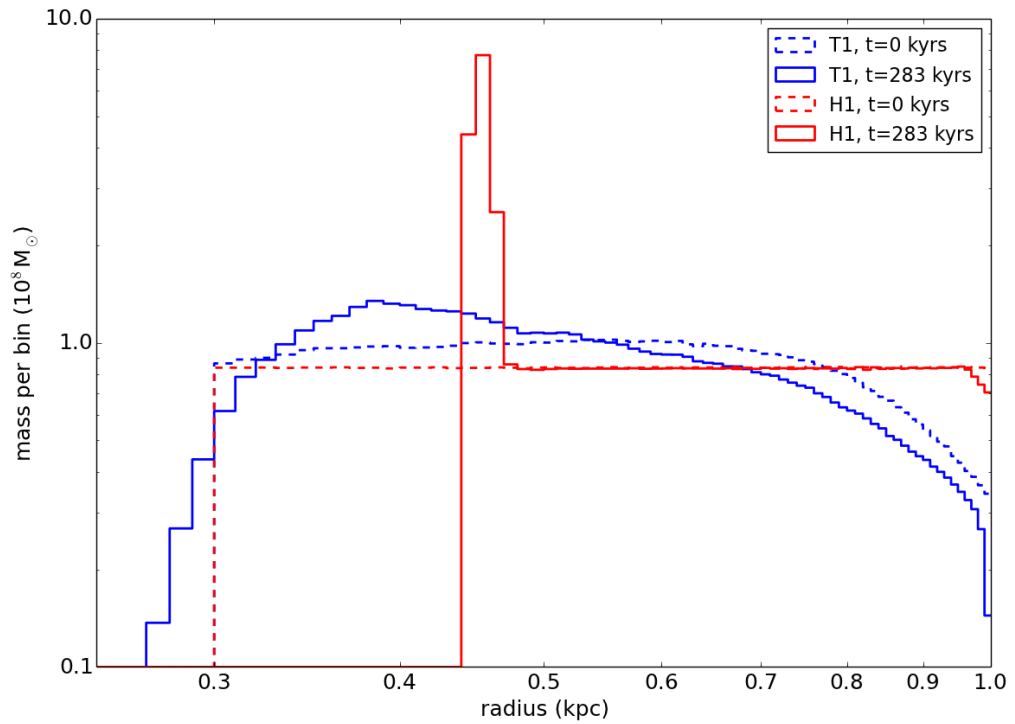


Figure 4.3: Histogram of the gas mass in radial bins. The blue and red lines are for the turbulent clumpy (T1) and homogeneous (H1) gas distributions, respectively. The dashed and solid lines correspond to times  $t = 0$  kyr and  $t \approx 283$  kyr, respectively. Note how little the clumpy distribution evolves: if anything, gas continues to accumulate in the innermost region, whereas it is completely blown away in the H1 run.

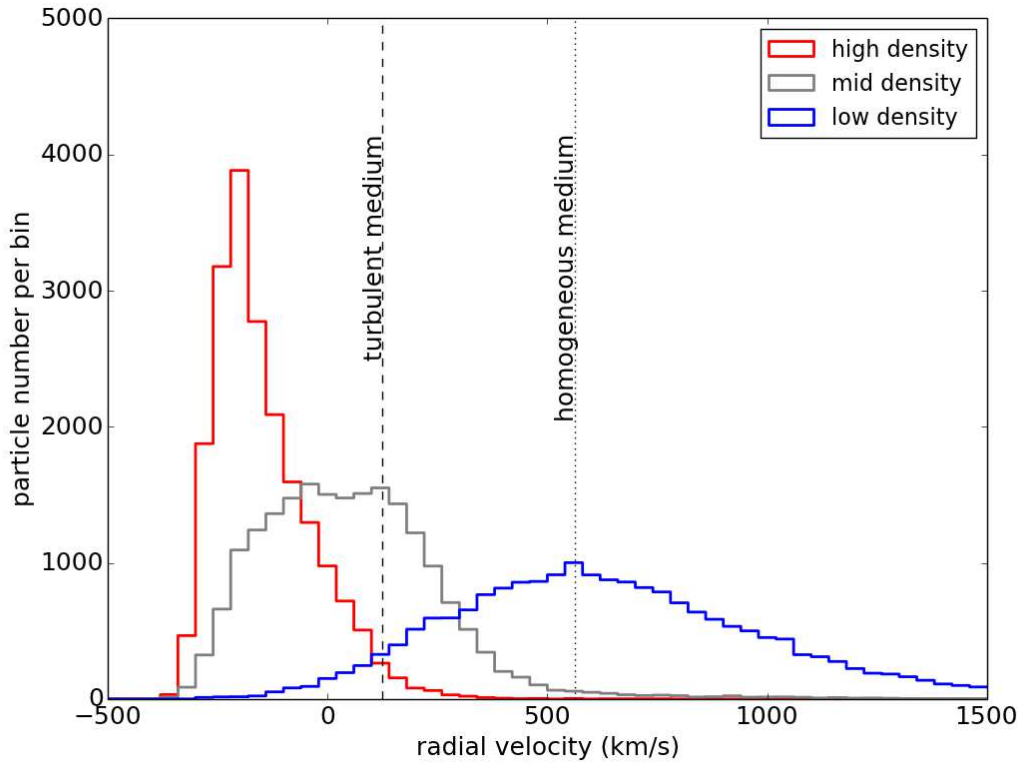


Figure 4.4: Histogram of the radial velocity distributions  $t = 70.8$  kyr for SPH particles that belong to one of the three representative density groups, i.e., the highest 10%, around the logarithmic mean and the lowest 10% of SPH particle densities, as labelled in the inset. Particles selected were within  $R \leq 0.35$  kpc at  $t = 0$  kyr, as explained in the text

#### 4.4.2 The column density perspective

Whilst Figure 4.4 highlights that gas of different densities is affected by the outflow differently, it also shows that there is an overlap in their radial velocities: some low-density gas is infalling whilst some high-density gas is outflowing. This behaviour may partially be due to gas at larger radii being shielded from the feedback by dense gas at smaller radii. To remove this self-shielding effect in the analysis somewhat, I consider the column density of the gas calculated as the integral

$$\Sigma = \int_0^R dr \rho(r, \Theta, \phi), \quad (4.9)$$

along the lines of sight (defined by the spherical coordinate angles  $\Theta$  and  $\phi$ ) from the centre of the galaxy.

Figure 4.5 shows the column density map as a function of the position on the sky as viewed from  $R = 0$ . Only ambient gas located inside  $R \leq 0.35$  kpc at  $t = 70.8$  kyr is taken into account in this analysis. The column density of the ambient gas,  $\Sigma$ , calculated in this way, varies by a factor of about 1000 in Figure 4.5.

Figure 4.5 also presents gas radial velocity information by showing contours for zero velocity gas (red). The mean gas radial velocity along a line of sight,  $\langle v_r \rangle$ , is calculated as

$$\langle v_r \rangle = \frac{\int_0^R dr \rho(r, \Theta, \phi) v_r(r, \Theta, \phi)}{\Sigma}, \quad (4.10)$$

where  $\Sigma$  is given by equation (4.9). Material inside of these contours has a negative radial velocity at this time. I can see that it is the gas with the highest  $\Sigma$  that remains infalling, whilst gas with a low  $\Sigma$  generally has positive radial velocities.

The complex nature of gas dynamics in the turbulent simulation makes defining and analysing the exact dynamics of individual gas clouds difficult, if not impossible, since gas density changes during the simulation. Some of the gas may even switch phases when it cools or heats up. However, I can carry out an approximate analysis by considering the momentum equation for a gas clump,

$$\frac{d}{dt}(m_{cl} v_{cl}) = \pi r_{cl}^2 P_{\text{ram}} - \frac{G m_{cl} M(R)}{R^2}, \quad (4.11)$$

where  $r_{cl}$ ,  $m_{cl}$  and  $v_{cl}$  are the clump's radius, mass and radial velocity, respectively,  $P_{\text{ram}}$  is the hot bubble's ram pressure acting on the clump,  $R$  is the radial position of the clump and  $M(R)$  is the mass of material within  $R$ . Making the assumption that  $m_{cl}$  and  $r_{cl}$  remain

approximately constant I can divide through by  $m_{cl}$ , and re-write equation (4.11) as

$$a_{cl} = \frac{P_{ram}}{\Sigma_{cl}} - a_{grav}, \quad (4.12)$$

where  $a_{cl}$  and  $a_{grav}$  are the clump's acceleration and the acceleration due to gravity, respectively, and  $\Sigma_{cl} = m_{cl}/\pi r_{cl}^2$  is the column density of the clump. The ram pressure of the hot gas cannot be predicted exactly by the analytical model, but I assume that hot gas streams out of its initial spherical configuration at approximately the sound speed through numerous “holes” in the cold ambient gas distribution. This argument suggest that by the order of magnitude  $P_{ram}$  should be comparable to the initial isotropic pressure of the hot gas,  $P$ .

When  $\Sigma_{cl} \ll P/a_{grav}$ , the driving force of the bubble dominates over gravity and I can neglect the  $a_{grav}$  term in equation (4.12), integrating then gives an estimate for a clump's velocity at time  $t$  as

$$v(t) = \frac{P_{ram}}{\Sigma_{cl}}t + v(0). \quad (4.13)$$

Setting  $v(t) = 0$  I can define a critical column density,

$$\Sigma_{crit}(t) = \frac{P_{ram}}{|v(0)|}t, \quad (4.14)$$

such that only material with  $\Sigma > \Sigma_{crit}$  should still be infalling at time  $t$ , whereas lines of sight with  $\Sigma < \Sigma_{crit}$  may be launched in an outflow.

Using the mean radial velocity of SPH particles at  $t = 0$  for  $v_0$ , I find  $\Sigma_{crit} \simeq 0.36 \text{ g cm}^{-2}$  at  $t \sim 70.8 \text{ kyr}$ . Black contours in Figure 4.5 show the lines of sight where  $\Sigma = \Sigma_{crit}$ . We see that there is a close agreement between the red (zero velocity contours) and the black contour lines, suggesting that the approximate analysis based on equation (4.12) does have a certain merit to it. This could be expected from theoretical studies of how a single dense gas cloud is affected by a hot bubble (e.g., McKee & Cowie, 1975; Nayakshin, 2014). The column density of the cloud,  $\Sigma$ , is roughly the product of the mean cloud density,  $\rho_{cl}$ , and the physical size of the cloud,  $r_{cl}$ . Therefore, a dense but physically small (small  $r_{cl}$ ) cloud may have a smallish  $\Sigma$ , and is accelerated to a significant radial velocity by the UFO, and hence may be completely destroyed, despite being dense. A dense and large (large  $r_{cl}$  and  $\Sigma$ ) cloud, on the other hand, may both withstand the onslaught from the hot bubble and also continue to infall.

There are a few caveats to this approach for comparing  $\Sigma$  and the expected radial velocity. The high  $\Sigma$  regions shown in the plot can only be considered an estimate for

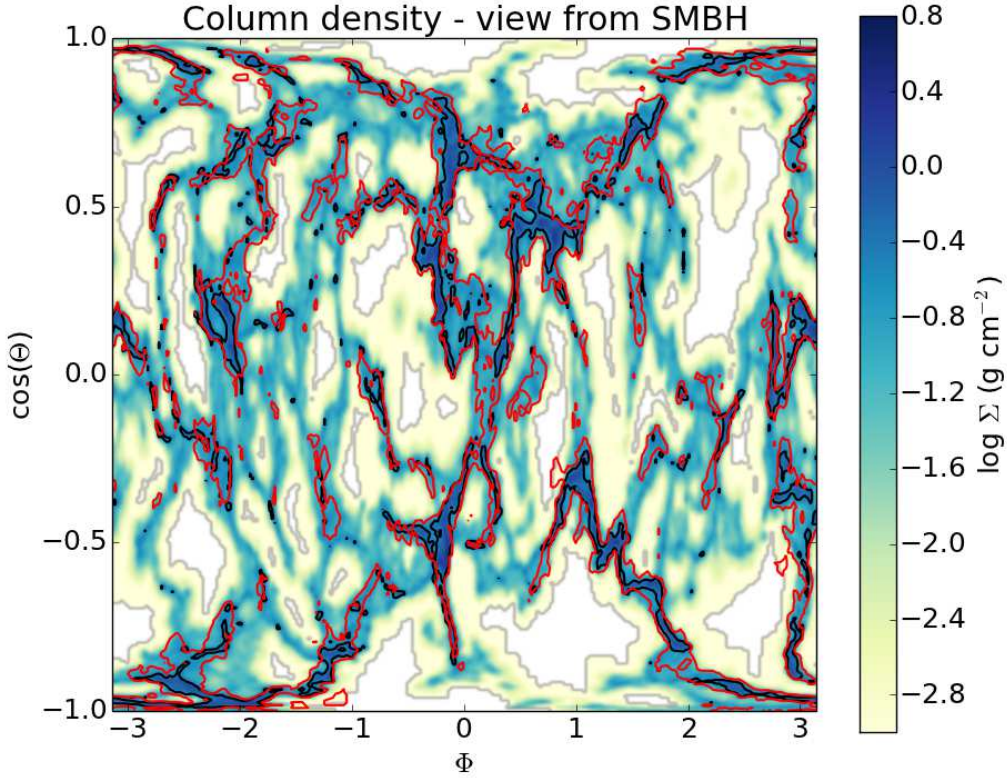


Figure 4.5: Column density of ambient gas at  $R \leq 0.35$  kpc at  $t = 70.8$  kyr, as viewed from the position of the sink particle. Also plotted are contour lines for zero velocity gas (red) and gas with  $\Sigma_{\text{crit}} = 0.36 \text{ g cm}^{-2}$ , which is analytically predicted to have zero velocity at this time. Note that the two contour lines coincide over most of the plot.

the high-density material as they are calculated based upon the entire contribution of material along a particular line of sight out to  $R \leq 0.35$  kpc. This leads to potentially over(under)estimating  $\Sigma$  if the clump extends to radii that are less (greater) than 0.35 kpc. Further, I use an average value for  $v_0$  and assume that the column density of the clump remains approximately constant over the time period considered. Therefore, the estimate here should only be considered as a rough illustration of the interaction of the high-density clumps with the expanding bubble and not an exact solution, which would require a far more detailed analysis than is necessary for the purposes of this chapter.

#### 4.4.3 Time evolution of the outflow

So far I have only shown properties of the system at specific moments in time, however, a consideration of the time evolution of the system is also important. Figure 4.6 shows the

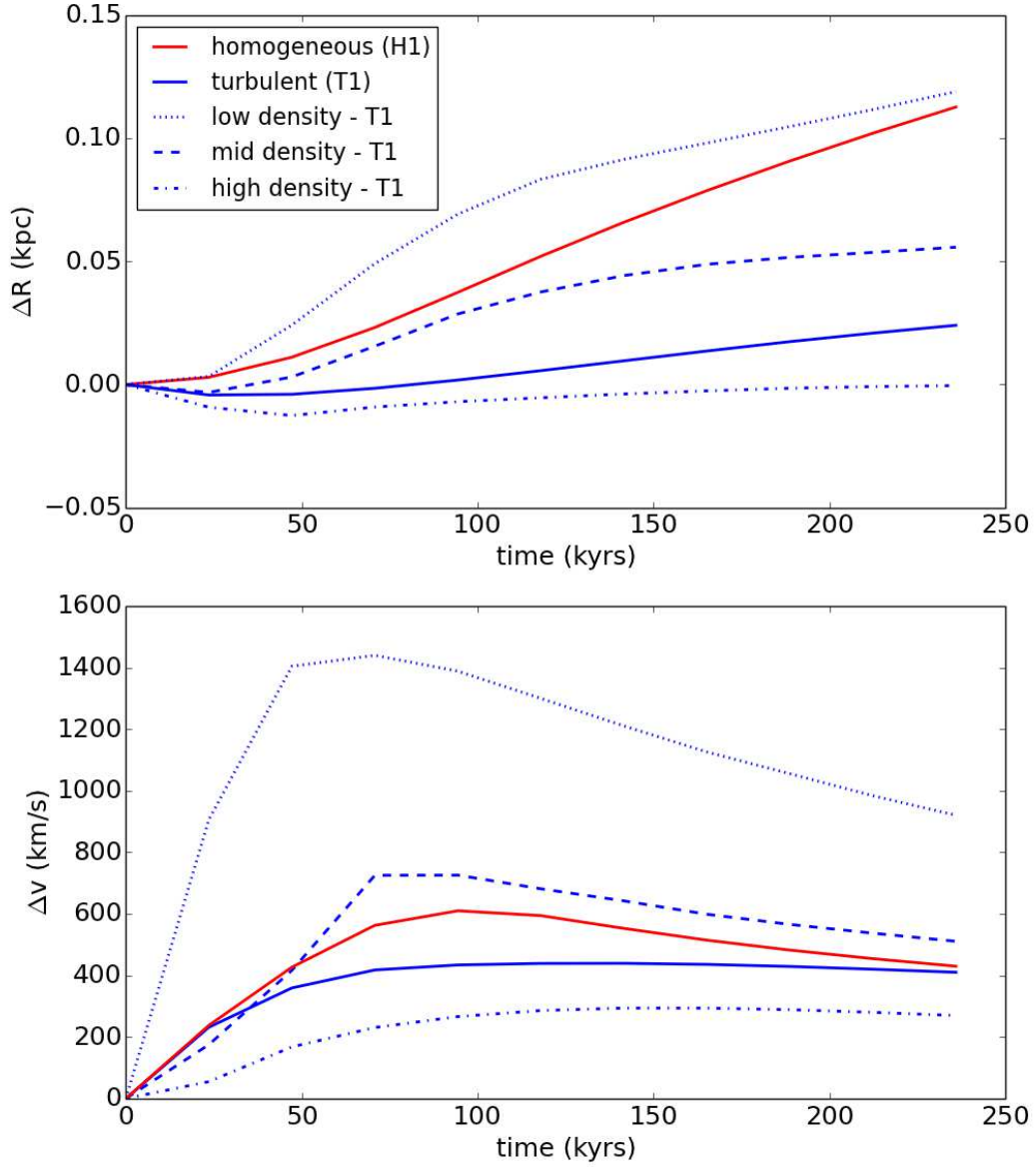


Figure 4.6: Time evolution of the change in mean radial position (top) and change in mean radial velocity (bottom) of gas in the homogeneous (H1, red) and turbulent (T1, blue) runs. In the latter case the gas is further divided into low (dotted), intermediate (dashed) and high (dash-dot) density material.

time evolution of the change in mean radial position,  $\Delta R = \bar{R}(t) - \bar{R}(0)$  (top) and change in mean radial velocity  $\Delta v = \bar{v}(t) - \bar{v}(0)$  (bottom) for ambient SPH particles initially at  $R \leq 0.35$  (these particles are chosen to avoid other complicating factors such as shielding of low density gas). The solid red and blue lines on these figures are taken from the homogenous simulation H1 and turbulent simulation T1 respectively. Also shown on each of the panels in Figure 4.6 is three blue lines calculated from the data of the turbulent simulation T1, showing the change in mean radial position (top) and mean radial velocity (bottom) for low (dotted), intermediate (dashed) and high (dot-dashed) density gas. I apply fixed density thresholds set at the values used in Figure 4.4 earlier. However in that analysis the particles were grouped based upon their original density, here the particles are instead grouped based upon their density at time  $t$ . Both the change in mean radial position and mean radial velocity plots demonstrate again that the low-density gas is affected by the hot bubble much more strongly than the high density gas. However both panels of Figure 4.6 show a certain reduction in the difference between the three density groups as time goes on which is due to (a) mixing between the two phases with time, and (b) the fact that the bubble energy is not replenished in the simulation. I note that the next chapter considers a continuous, 1 Myr long, Eddington limited outburst in an attempt to negate point (b).

#### 4.4.4 Decoupling of energy and mass flow

In the homogeneous control simulation H1, both mass and energy are flowing outward as the bubble expands. The situation is bound to be far more interesting in the case of the turbulent simulation T1, since we saw in Section 4.4.1 that there is both an inflow and an outflow at the same time. Furthermore, since the different phases have widely different radial velocities and temperatures, the overall direction of the flow of mass and energy is not obvious.

To analyse these flows I define the rates of radial mass and energy transfer in a given radial bin of width  $\Delta r_{bin}$ , respectively, as

$$\frac{\partial M}{\partial t} = \sum \frac{m_{sph} v_r}{\Delta r_{bin}} \quad (4.15)$$

$$\frac{\partial E}{\partial t} = \sum \left[ \frac{1}{2} v^2 + \frac{3}{2} \frac{k_B T}{\mu m_p} \right] \frac{m_{sph} v_r}{\Delta r_{bin}}. \quad (4.16)$$

The SPH particles in this sum are selected based on criteria placing them in one or another phase or group (see below). In a steady state spherically symmetric flow these definitions



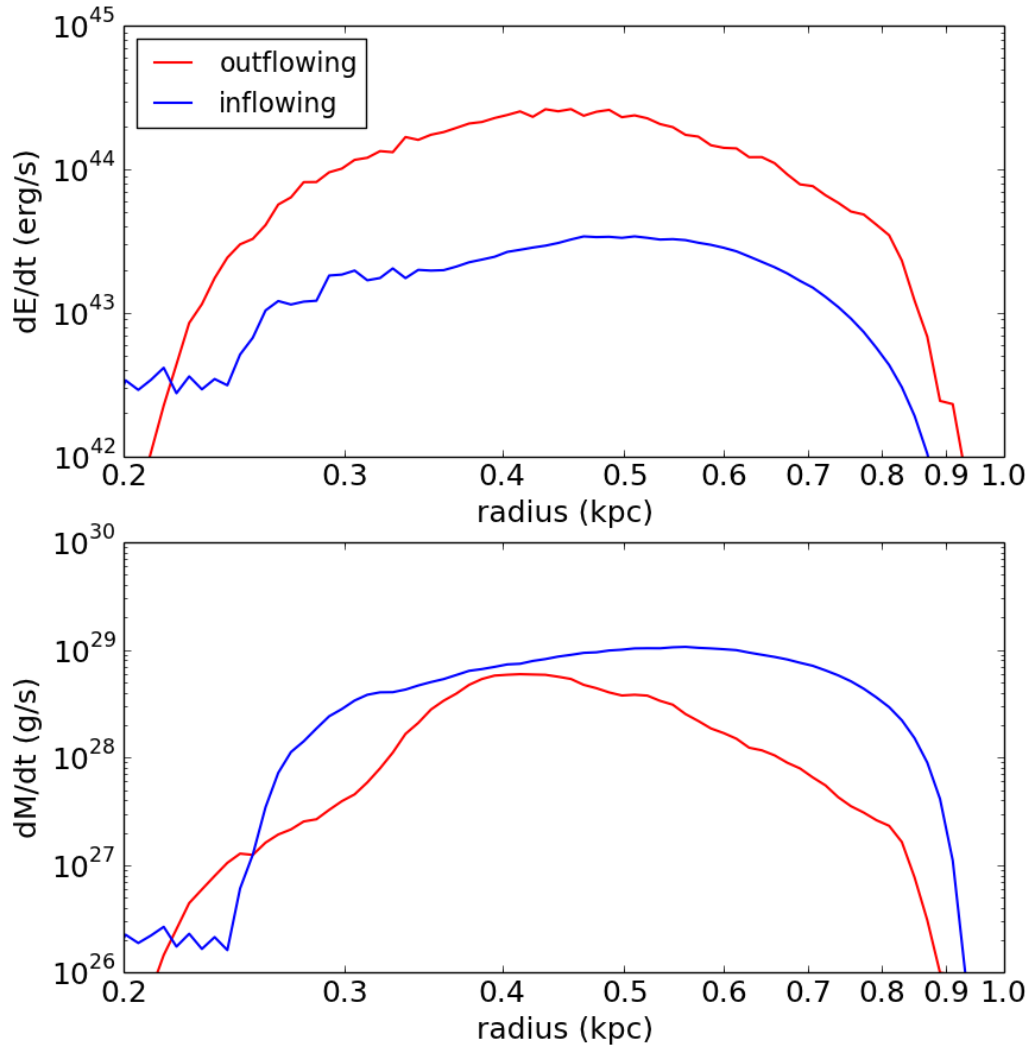


Figure 4.7: Radial flows of energy,  $\dot{E}$  (top panel), and mass,  $\dot{M}$  (bottom panel), for gas that is either in-flowing (blue) or outflowing (red) at time  $t = 283$  kyr in the simulation T1.

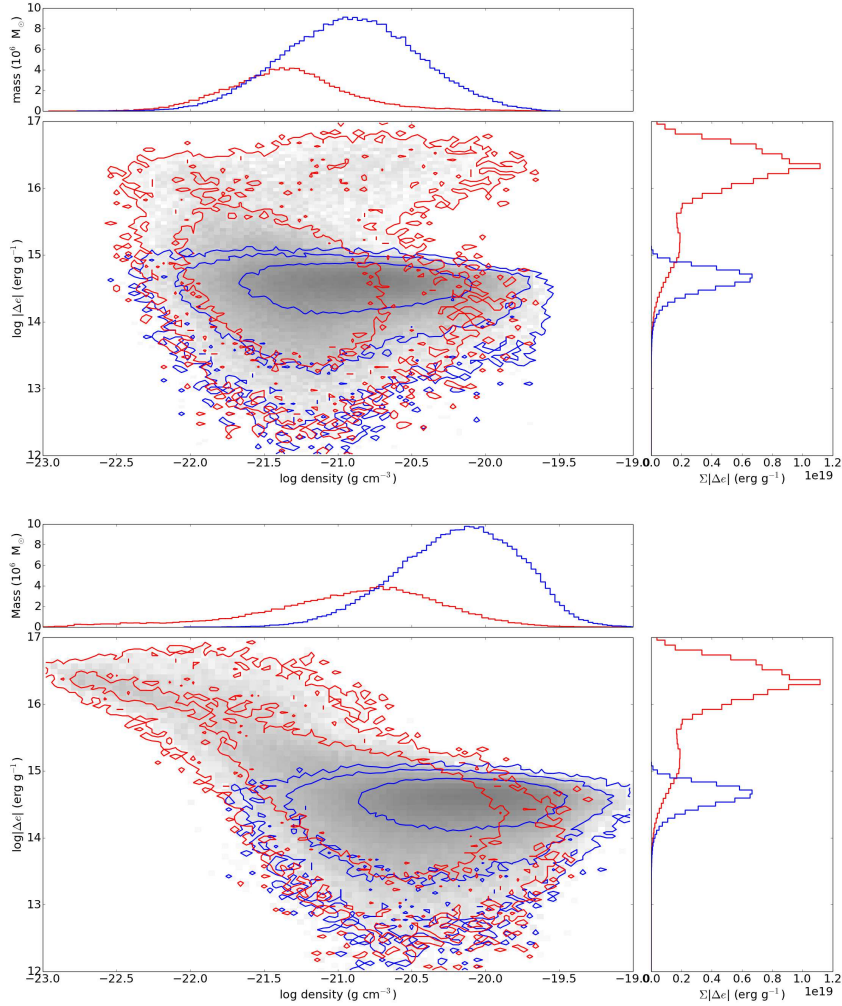


Figure 4.8: Particle distribution plot of absolute change in specific energy between  $t = 0$  and 189 kyr ( $\Delta e$ ) against original gas density (top) and current gas density (bottom). Contours indicate gas that has lost energy (blue) or gained energy (red). The density axis have been collapsed into one-dimensional mass histograms above each panel whilst the energy axis has been collapsed into one-dimensional histograms weighted by  $\Delta e$  to the right of each panel.

would include all of the SPH particles in a bin and would then give the total mass and energy flux rate as a function of position in the flow.

In the homogeneous control run, the energy and mass flows are both dominated by outflowing material but only within the radius of the swept up shell. Beyond this there is no outward  $\partial E/\partial t$  and  $\partial M/\partial t$ , while the inward values are negligibly small.

Figure 4.7 shows  $\partial E/\partial t$  (top) and  $\partial M/\partial t$  (bottom) for in-flowing ( $v_r \leq -\sigma/2$ , blue) and outflowing ( $v_r \geq \sigma/2$ , red) material in the turbulent simulation T1, binned radially at  $t = 283$  kyr. Both panels show that, unlike the spherically symmetric situation (simulation H1), there are outflows and inflows of mass and energy for all radii in the clumpy simulation T1. Interestingly the energy flow is dominated by the material streaming outward, which I identify with the hot low-density gas based on our earlier analysis, whereas the mass flow is mainly inward and is dominated by the high density gas. This shows that *energy and mass flows separate from one another in turbulent flows*. Unlike the spherically symmetric homogeneous case, energy does not necessarily flow with most of the mass. This is in stark contrast to the assumptions made in the analytical models discussed in section 1.6.1.2.

To analyse this energy-mass decoupling further, I define the absolute change in specific energy of SPH particles as

$$|\Delta e| = \left| \frac{1}{2} (v^2 - v_0^2) + \frac{3}{2} \frac{k_B}{\mu m_p} (T - T_0) + G \frac{M_a}{a} \ln \left( \frac{R}{R_0} \right) \right|, \quad (4.17)$$

where the terms on the right hand side are the change in specific kinetic, internal and gravitational potential energy, respectively (note I only include the gravity due to the underlying background potential).  $v$ ,  $T$  and  $R$  are the velocity, temperature and radial positions of each particle, respectively, with the subscript 0 indicating the initial value of each of these parameters.

Figure 4.8 shows the absolute change in SPH particle specific energy ( $|\Delta e|$ ) between  $t = 0$  and 189 kyr versus the gas density at the initial time (the top panel), and, alternatively, versus the gas density at  $t = 189$  kyr (the bottom panel). Contours indicate gas that has lost energy (blue) or gained energy (red). The density axis has been collapsed into one-dimensional mass histograms located at the top of each plot, whilst the energy axis has been collapsed into one-dimensional histograms weighted by  $\Delta e$ , located to the right of each plot. As before (e.g., Figure 4.4), only particles within  $R = 0.35$  kpc at  $t = 0$  are selected for this analysis to minimise complications due to gas self-shielding.

Since gas in simulation T1 is initially infalling due to the initial conditions, so that

radial velocity  $v_r < 0$ , particles that loose specific energy (blue colour in fig. 4.8) correspond to particles that are, in general, only moderately affected by the hot bubble. The radial velocity of such particles is either still negative but less so than initially or has a small positive value. On the other hand particles with a positive energy change (red), as a rule, are particles that are now outflowing with a larger positive  $v_r$ .

Focusing on the 1D mass distributions, above the corresponding panels, we observe from the figure that most of the mass is in the blue gas that is on average denser than the red (outflowing) gas. At the same time the 1D energy distributions to the right of each panel, show that most energy is in the red SPH particles, so that, consistent with Figure 4.7, energy is mainly in the low-density outflowing particles. The low-density tail of the distribution of the red particles in the bottom panel shows that the energy gained by the outflowing particles may be about two orders of magnitude higher than the energy change of the blue dense particles.

Further, comparing the top and the bottom panels, we see that the low-density outflowing gas tail in the bottom panel had on average higher density at time  $t = 0$ . This gas is initially moderately dense but has been ablated from the surface of the clouds and launched in the outflow by the hot bubble. The SPH particles in the blue part of the distribution had their density increased by a factor of several. The hot bubble thus compresses most of the dense gas by a factor of at least a few. This is consistent with earlier results of Nayakshin & Zubovas (2012) (see also Silk & Norman (2009)) showing that AGN outflows may in fact trigger star formation in dense cold gas by compressing it to very high densities.

## 4.5 Discussion

### 4.5.1 Feedback on a homogeneous versus a multiphase ISM

I have studied the impact of a thermalised UFO (modelled as a hot bubble) launched by a rapidly accreting SMBH on the ambient gas of the host galaxy in two contrasting limits. In the first, the ambient gas is initially homogeneous and spherically symmetric, whereas in the second limit it is highly inhomogeneous due to an initially imposed turbulent velocity field. In broad agreement with previous work (Wagner et al., 2012, 2013; Nayakshin, 2014; Zubovas & Nayakshin, 2014), I find marked differences in the outcome of this interaction.

The homogeneous spherically symmetric ambient gas is driven outward by the

hot bubble much in the same way as described by the energy-conserving analytical models of AGN feedback described in section 1.6.1.2 (e.g., King, 2003, 2005, 2010; Zubovas & King, 2012a; Faucher-Giguère & Quataert, 2012). In such models the ambient gas is only driven away if the feedback is sufficiently strong and the weight of the medium sufficiently small. In a stark contrast to this, the turbulent clumpy ISM cannot easily be described in a 1D language. Because of a large density contrast between the different phases in the ISM, there is simultaneously inflowing and outflowing gas streaming throughout the host galaxy.

The cold dense medium is affected by the UFO significantly less than analytic models, quoted above, assume because the medium is overtaken by the UFO rather than being pushed in front of it. I find that some high-density clumps continue to move inward while the hot bubble fizzles out through low-density ‘pores’ and accelerates the low-density phase of the ISM to high outward velocities. Analysis of this behaviour shows that the cold dense phase gets an initial kick from the pressure of the bubble before it is overtaken, after which the driving force acting on the clump diminishes.

Another important result found here is a divergence in the directions of where most of the mass and energy flow in a turbulent ISM. While most of the mass is flowing inward, carried by the cold dense clouds which continue to infall despite AGN feedback, most of the UFO energy manages to percolate through the ambient ISM and flow outward through the bulge.

#### 4.5.2 Pertinence to the $M_{\text{BH}} - \sigma$ relation

Overall, these results suggest that the establishment of the  $M_{\text{BH}} - \sigma$  relation is much more complicated a process than in spherically symmetric models (e.g., Silk & Rees, 1998; Fabian, 1999; King, 2003). In such models, the  $M_{\text{BH}} - \sigma$  mass divides two very different regimes. SMBHs below the  $M_{\text{BH}} - \sigma$  mass are unable to drive the gas outward beyond a small radius (tens to a few hundred pc, depending on the BH mass and the host velocity dispersion). It is only once the SMBH exceeds the  $M_{\text{BH}} - \sigma$  mass that the outflow is able to overcome the weight of the ambient gas in the galaxy and clear *all of the host* of its gas. This paints an all or nothing picture of AGN feedback (above or below the  $M_{\text{BH}} - \sigma$  mass, respectively).

The picture of AGN feedback changes radically if the ISM in the host is multiphase. There is no longer the two different regimes with a sharp boundary, the  $M_{\text{BH}} - \sigma$  mass, between them: at any SMBH mass there may be an inflow and an outflow of gas at the same location in the host and at the same time.

This must dilute the meaning of the  $M_{\text{BH}} - \sigma$  mass, because, on the one hand, “underweight” SMBHs, i.e., those below the  $M_{\text{BH}} - \sigma$  mass, do have an influence on the host galaxy even on large scales. Since the hot gas propagates outward by finding and following the paths of least resistance, the low-density phase at all radii in the host is vulnerable to AGN feedback. On the other hand, the high-density medium is more resilient to SMBH feedback than could be thought based on spherically symmetric models because the medium is over-taken by the UFO rather than being pushed in front of it. Nayakshin (2014) and Zubovas & Nayakshin (2014) proposed that this unexpected resilience of the host gas to AGN feedback explains how SMBH manage to grow to the momentum-limited  $M_\sigma$  masses (King, 2003) rather than the energy-limited ( $\sim 100$  times lower) masses given by equation (1.48), in section 1.6.1.2.

One speculation arising from these results is that a tight  $M_{\text{BH}} - \sigma$  relation could actually never be established in an ensemble of *isolated* galaxies and that mergers of galaxies are crucial to the emergence of the observed relations. On the basis of results presented here and in Zubovas & Nayakshin (2014), I argue that there are simply too many factors determining the SMBH interaction with the host galaxy (the ISM structure, angular momentum of the gas, etc.), and that therefore one should expect a very significant spread in any SMBH-host relation based on *a single episode* of galaxy and SMBH growth. It is likely that averaging occurring during mergers of galaxies (the central limit theorem applied to mergers, see e.g., Jahnke & Macciò, 2011) largely erases this significant spread, leading to a tight  $M_{\text{BH}} - \sigma$  relation at low redshift (Kormendy & Ho, 2013). This view is consistent with the fact that the observed SMBH-host scaling relations are only tight for classical bulges and ellipticals, that the scatter in such relations decreases towards higher masses and that SMBH-host relations have larger scatter at large redshifts (Kormendy & Ho, 2013).

### 4.5.3 Comparison with other work

Out of previous literature, this work is most similar in spirit to Wagner et al. (2012, 2013), with a number of similar conclusions. One difference, however, is that Wagner et al. (2013) finds that the dense clouds are heated strongly and accelerated outwards as a result of the feedback (albeit slower than the hot phase). In this work inflows occur *despite* the feedback.

The response of the cold phase to the UFO is strongly dependent on the initial conditions of the phase and the physics included in the simulation. In Wagner et al. (2013), radiative cooling below a temperature of  $10^4$  K is turned off, which clearly limits the high-

est densities that could be reached by the cold phase under the external compression by the hot medium. In these simulations self-gravity of the clouds is an important factor in ensuring the integrity of the clouds when they are hit by the UFO. Wagner et al. (2012, 2013), on the other hand, do not include self-gravity of the gas and the initial densities of the clouds appear to be comparable to the tidal densities at the clouds' locations. In my opinion, cold clouds in Wagner et al. (2012, 2013) are both susceptible and defenceless to shear from the gravitational potential and hydrodynamic forces by the UFO.

In any event, I believe that neither this study nor the previous work gives complete and *quantitatively* definitive answers on the interaction of an UFO and a clumpy turbulent medium of the host galaxy. Future simulations should focus on modelling the physical properties of the ISM with a greater realism, in particular including star formation and its feedback (which I did not include here).

#### 4.5.4 Implications for cosmological simulations

Cosmological simulations (e.g., Springel et al., 2005; Di Matteo et al., 2008; Schaye et al., 2010; Dubois et al., 2012; Schaye et al., 2015; Vogelsberger et al., 2014) often invoke AGN feedback in order to reproduce observed relationships such as the galaxy luminosity function. In this sense AGN provide a source of negative feedback and therefore the mechanism of the sub-grid prescription employed acts to inhibit star formation and eject gas from a galaxy. This is normally achieved through heating or “kicking” gas local to the black hole. Such simulations, which by necessity, balance on the edge of what is numerically achievable, are unable to resolve the multiphase ISM. It is likely that any feedback would be acting on a single phase medium. The heterogeneous effects that feedback has on the different phases of a multiphase ISM illustrated in these simulations are then lost due to numerical limitations, as we illustrate in Chapter 5.

The extent to which this poses a problem depends upon the exact nature of the multi-phase ISM (Wagner et al., 2012) and upon the problem that one wishes to investigate with the cosmological simulations. With regards to meeting large-scale observational trends, such as the galaxy luminosity function or  $M_{\text{BH}} - \sigma$  relation, the subgrid models employed by cosmological simulations may be sufficient. However, as shown in this chapter, the exact nature of the ISM does impact how AGN feedback couples with the ambient gas in a galaxy. In these simulations the cold dense phase is mainly affected by the ram pressure (momentum) of the UFO, whereas the low-density phase bears the brunt of the UFO's energy content. In contrast, widely used AGN feedback models (e.g., Di Matteo et al., 2008; Dubois et al., 2012) tend to neglect the physical state of the gas and instead focus

on the proximity of the gas to the SMBH. Even though cosmological simulations are currently unable to resolve the ISM, there may still exist material with a range of physical properties close to black hole. It is therefore likely that the robustness of cosmological simulations could be improved by a set of prescriptions that incorporate the physics highlighted by these simulations. Similarly, semi-analytical models (e.g., Bower et al., 2006) may benefit from including an energy-leaking prescription for the hot bubble (see Zubovas & Nayakshin, 2014).

## 4.6 Conclusion

This chapter has presented the outcome of a thermalised UFO impacting upon either a homogeneous or inhomogeneous (and turbulent) gas distribution. The results presented here largely agree with a body of existing work (Wagner et al., 2012, 2013; Nayakshin, 2014; Zubovas & Nayakshin, 2014). In particular, most of the UFO’s energy escapes via low-density channels in the clumpy ISM, which drastically reduces the impact of the UFO on the dense cold phase that contains most of the ambient gas in the host galaxy. I conclude that the state of the ISM in a galaxy is just as important as the AGN feedback model invoked in determining how AGN feedback interacts with the ambient medium.

Given the complexity of these processes, the meaning of the  $M_{\text{BH}} - \sigma$  mass becomes much less well defined than in the spherically symmetric analytic models discussed in section 1.6.1.2 (e.g., Silk & Rees, 1998; Fabian, 1999; King, 2003). In the latter, SMBHs below the  $M_{\text{BH}} - \sigma$  mass are unable to ‘clear’ their host galaxies of gas and hence continue to grow, whereas SMBHs above this mass terminate their and their host’s growth by expelling all of the gas. In a turbulent ISM there may be outflows – of the low density phase – at  $M_{\text{BH}} \ll M_{\sigma,p}$ , but there could also be inflows – of the high-density phase – at  $M_{\text{BH}} \gg M_{\sigma,p}$ . I therefore concluded in Section 4.5.2 that it is hard to see how tight SMBH-host galaxy correlations could occur in an ensemble of *isolated* galaxies, and that mergers of galaxies must be crucial to the emergence of the observed relations. The interesting question arising from this is to what extent can the observed correlations be attributed to AGN feedback physics and to what extent be due to the central limit theorem (Jahnke & Macciò, 2011)?



---

# 5

The resolution bias: low-resolution  
feedback simulations are better at  
destroying galaxies.

*“Galaxy formation is highly nonlinear and  
sensitive to subgrid recipes, to numerical  
implementations and to cosmology”*

*Simon White, Mind the Gap, Cambridge (2013)*

## 5.1 Introduction

As discussed in Section 1.6.2, feedback from AGN is often invoked in galaxy formation and cosmological simulations (e.g., Springel et al., 2005; Schaye et al., 2010, 2015; Dubois et al., 2012; Vogelsberger et al., 2014) as well as in semi-analytical models (e.g., Bower et al., 2006; Croton et al., 2006; Fanidakis et al., 2012) in order to quench star formation in galaxies at the high-mass end of the mass function and reproduce a number of observational correlations such as the  $M_{\text{BH}} - \sigma$  relation (Ferrarese & Merritt, 2000; Gebhardt et al., 2000; Tremaine et al., 2002; Kormendy & Ho, 2013). The general premise in such models is that the AGN provide a source of negative feedback, clearing gas from the host galaxy and inhibiting further star formation and AGN activity.

Outflows on kpc scales with velocities  $\gtrsim 1000 \text{ km s}^{-1}$  (e.g., Cano-Díaz et al., 2012; Maiolino et al., 2012; Cicone et al., 2014, 2015; Tombesi et al., 2015) and momentum fluxes exceeding the radiative output of the AGN,  $\dot{P}_{\text{AGN}} = L_{\text{AGN}}/c$ , by factors of up to  $\sim 30$  (Bautista et al., 2010; Dunn et al., 2010; Feruglio et al., 2010; Rupke & Veilleux, 2011a; Sturm et al., 2011c; Faucher-Giguère et al., 2012; Faucher-Giguère & Quataert, 2012; Genzel et al., 2014; Tombesi et al., 2015) have been observed and are believed to be driven by AGN. Such observations provide compelling evidence that AGN can indeed have an impact on the host galaxy, playing an important role in establishing observed correlations and thus vindicating the use of AGN feedback in simulations and semi-analytic models (see also McNamara & Nulsen, 2007; Fabian, 2012; King & Pounds, 2015).

In Section 1.6.1 I also pointed out that observations of local ( $z \lesssim 0.1$ ) AGN have found that  $\sim 40\%$  of systems host UFOs, with velocities of  $v \sim 0.1 c$  (Tombesi et al., 2010a,b) at small radii. Typically such outflows have mass outflow rates  $\dot{M}_{\text{out}} \sim 0.1 M_{\odot} \text{ yr}^{-1}$  and kinetic energy fluxes  $\dot{M}_{\text{out}} v^2/2 \simeq 0.05 L_{\text{Edd}}$ . Models (King, 2003, 2005) show that when these outflows impact upon the ISM, the wind shock can reach temperatures of order  $\sim 10^{10} - 10^{11} \text{ K}$  (see equation (1.24)). As outlined in Section 1.6.1.2, when radiative cooling of the wind is inefficient, it expands adiabatically and has the potential to drive the high velocity outflows discussed above and clear out significant fractions of gas from the host galaxy (Faucher-Giguère & Quataert, 2012; Zubovas & King, 2012a).

Despite the success of cosmological simulations in reproducing large scale observations (e.g., Schaye et al., 2010; McCarthy et al., 2010; Fabjan et al., 2010; Planelles et al., 2013; Vogelsberger et al., 2014; Schaye et al., 2015), they are unable to resolve scales small enough to probe the “AGN-engine” and thus provide limited insight into the exact processes driving AGN feedback, see Schaye et al. (2015) and Crain et al. (2015) for a

detailed discussion. Therefore, simulations only model the effects of the feedback on the ISM, as opposed to the feedback mechanism itself. Typically such models have to be *tuned*, that is, free parameters of the feedback and other prescriptions have to be varied until a reasonable fit to a set of calibrating observations is found.

This unfortunate situation is unlikely to be drastically improved any time soon because the numerical and physical modelling challenges in AGN and star formation feedback in cosmological simulations are so great (see Sections 1.6.2, 2.6 and 2.7 for more details). Nevertheless, in the interests of the field, it is only fair to ask the question: does this approach create numerical artefacts that may influence predictions of the simulations *in a systematic way*?

To give an example consider how the SMBH mass,  $M_{\text{BH}}$  can be limited by a feedback argument. Suppose that our model for SMBH feedback contains a parameter  $\epsilon_{\text{BH}} = \epsilon_{\text{r}}\epsilon_{\text{f}}$  that defines the fraction of SMBH rest mass energy that goes into the AGN outflow,  $\epsilon_{\text{BH}}M_{\text{BH}}c^2$ , where  $\epsilon_{\text{r}}$  is the radiative efficiency of the black hole and  $\epsilon_{\text{f}}$  is the efficiency with which the radiation couples to the surrounding gas. Some of this energy may be lost in the outflow-ISM interaction, for example to radiation in cooling shocks or by escaping the galaxy through low density voids (see below or above: chapter 4), so effectively only a fraction,  $\epsilon_{\text{ISM}}$ , of the feedback energy impacts the host galaxy gas. In this scenario the maximum SMBH mass is then limited by

$$\epsilon_{\text{ISM}}\epsilon_{\text{BH}}M_{\text{BH}}c^2 = M_{\text{gas}}\sigma^2, \quad (5.1)$$

where  $M_{\text{gas}}$  is the mass of the gas in the host galaxy that AGN feedback needs to remove from the galaxy and  $\sigma$  is the 1D velocity dispersion. From this simple analytical argument the black holes mass should be determined by the efficiency parameters such that  $M_{\text{BH}} \propto (\epsilon_{\text{ISM}}\epsilon_{\text{BH}})^{-1}$ . A similar conclusion is found by Booth & Schaye (2010) who show that  $M_{\text{BH}} \propto (\epsilon_{\text{BH}})^{-1}$ , where  $\epsilon_{\text{BH}}$  is a free parameter of their feedback model.

AGN feedback is often implemented in galaxy formation simulations as a sub-grid model for which the black hole efficiency parameter,  $\epsilon_{\text{BH}}$ , is set by hand.  $\epsilon_{\text{BH}}$  is often calibrated in order to reproduce the observed local black hole scaling relations (e.g. Di Matteo et al., 2005; Springel et al., 2005; Sijacki et al., 2007; Booth & Schaye, 2009), with typical values of  $\epsilon_{\text{r}} = 0.1$  and  $\epsilon_{\text{f}} = 0.05 - 0.15$ . However,  $\epsilon_{\text{ISM}}$ , which cannot be directly set by the simulator, is governed by the ISM modelling i.e. details of the hydrodynamics, radiative cooling and any other sub-grid ISM routines used in the simulation. This provides an explanation as to why values for  $\epsilon_{\text{f}}$  can differ between simulations. As noted in Booth & Schaye (2009) their value of  $\epsilon_{\text{f}} = 0.15$  differs from the value of  $\epsilon_{\text{f}} = 0.05$

used by Springel et al. (2005) due to compensating for differences between sub-grid ISM modelling. This suggests that the effective  $\epsilon_{\text{ISM}}$  is smaller in Booth & Schaye (2009) compared to Springel et al. (2005).

From the arguments above, when a simulation is compared to observations, a constraint is obtained not on  $\epsilon_{\text{BH}}$  directly but on the product  $\epsilon_{\text{ISM}}\epsilon_{\text{BH}}$ . The danger here is that  $\epsilon_{\text{ISM}}$  is dependent on the numerics and hence the value obtained for  $\epsilon_{\text{BH}}$  when calibrating simulations against observed black hole scaling relations does not actually directly tell us about the AGN physics (as already discussed by Schaye et al., 2015). I note that  $\epsilon_f$  is *never* considered a prediction of the subgrid AGN feedback models and that the only requirement for self-regulation of the SMBH growth to occur is that  $\epsilon_f$  is non-zero. Further, it is interesting to note that both the OWLS (Schaye et al., 2010) and EAGLE (Schaye et al., 2015) cosmological simulations had large differences in resolution and subgrid physics, but used the same value of  $\epsilon_f = 0.15$ . This choice did, however, require an increase in the temperature increment of particles heated by AGN feedback in higher resolution simulations (Schaye et al., 2015; Crain et al., 2015). This parameter is set by hand and effectively controls the value of  $\epsilon_{\text{ISM}}$ . The intimate relationship between  $\epsilon_f$  and  $\epsilon_{\text{ISM}}$ , evidenced by these large-scale simulations, shows that it is important to understand any potential numerical trends in  $\epsilon_{\text{ISM}}$ , for example with resolution, before drawing conclusions about AGN feedback mechanisms. Investigation of these mechanisms is a logical next step in galaxy evolution simulations.

In this chapter I perform a resolution study in order to better understand how numerical resolution can affect the coupling between the SMBH feedback and the ISM. As in chapter 4 (Bourne et al., 2014), to achieve a certain degree of realism in modelling the clumpy ISM of real galaxies, I impose a turbulent velocity field upon the initial smooth gas distribution and allow clumpy structures to develop before they are hit with the SMBH outflow. I vary SPH mass resolution over four orders of magnitude and I also vary the SMBH feedback implementation and the cooling prescription used in order to minimise numerical artefacts. Our numerical simulations allow us to test whether there are numerical trends in  $\epsilon_{\text{ISM}}$  for a single SMBH feedback event. Briefly, our main conclusion is that, in the scenario studied, feedback in low resolution simulations is far more effective at destroying galaxies than it is in higher resolution simulations. This indicates, at least qualitatively, that  $\epsilon_{\text{ISM}}$  is resolution dependent.

The chapter is structured as follows; Section 5.2 outlines the numerical method and how the simulations are set up, Section 5.3 highlights the results of the simulations, Section 5.4 discusses the implications of these results, both physical and computational, and

finally in Section 5.5 I summarise the outcome of this work.

## 5.2 Simulation set-up

### 5.2.1 Numerical method

Similar to the simulations presented in chapter 4, I implement the SPHS<sup>1</sup> formalism as described in Read et al. (2010) and Read & Hayfield (2012). This is employed within a modified version of the N-body/hydrodynamical code GADGET-3, an updated version of the code presented in Springel (2005), which I discuss in detail in chapter 2. The second-order Wendland kernel (Wendland, 1995; Dehnen & Aly, 2012), giving in equation (2.16) is employed for both SPH calculations (using 100 neighbours) and weighting of the AGN feedback. The simulations are run in a static isothermal potential with a mass profile given by equation (4.1) with  $M_a = 9.35 \times 10^9 M_\odot$ ,  $a = 1$  kpc and  $\sigma_{\text{pot}} = \sqrt{GM_a/2a} \simeq 142 \text{ km s}^{-1}$ . In order to prevent gravitational forces diverging at small radii I apply a softening length of 0.1 pc to the background potential.

As in chapter 4 (Bourne et al., 2014), an ideal gas is used for all simulations. I set  $\gamma = 5/3$  and the mean molecular weight,  $\mu$ , is calculated self-consistently. However, I again set  $\mu = 0.63$  when plotting temperature. In our fiducial runs, for gas temperatures above  $T = 10^4$  K, I use a modified version of the optically thin radiative cooling function of Sazonov et al. (2005) described in Section 2.5, which includes Bremsstrahlung losses, photoionisation heating, line and recombination continuum cooling and Compton heating and cooling in the presence of an AGN radiation field. For comparison I also carry out runs using the same prescription but neglect the effect of IC cooling against the AGN radiation field. This is in light of recent theoretical predictions (Faucher-Giguère & Quataert, 2012) and observational constraints (Bourne & Nayakshin, 2013, presented in Chapter 3) that suggest UFOs are always energy conserving and do not cool via IC processes as was previously believed (King, 2003). Below  $T = 10^4$  K cooling is modelled as in Mashchenko et al. (2008), proceeding through fine structure and metastable lines of C, N, O, Fe, S and Si. For simplicity solar metallicity is assumed for all cooling functions.

In contrast to chapter 4, where I employed a constant temperature floor of 100 K, here

---

<sup>1</sup>Smooth Particle Hydrodynamics with a high-order dissipation Switch.

I impose a ‘dynamic’ temperature floor such that gas cannot cool below a temperature of

$$T_{\text{floor}} = \rho^{1/3} \frac{\mu m_p G}{\pi k_B} (N_{\text{ngb}} m_{\text{SPH}})^{2/3} \quad (5.2)$$

$$\simeq 350 \left( \frac{\rho}{10^{-22} \text{g cm}^{-3}} \right)^{1/3} \left( \frac{\mu}{0.63} \right) \left( \frac{m_{\text{SPH}}}{1600 M_{\odot}} \right)^{2/3} K$$

where  $\rho$  and  $m_{\text{SPH}}$  are the density and mass of an SPH particle, respectively, and  $N_{\text{ngb}} = 100$  is the typical number of neighbours. Such a temperature floor manifests itself as a polytropic equation of state<sup>2</sup> with an effective polytropic index of  $\Gamma = 4/3$ . This approach is used for purely numerical reasons to guarantee that the Jeans mass is independent of density and Jeans length scales with the SPH kernel smoothing length. As discussed in section 2.6 this ensures that gas clouds are able to collapse while avoiding spurious fragmentation due to resolution (Robertson & Kravtsov, 2008; Schaye & Dalla Vecchia, 2008). This method or variants upon it are widely used in galaxy formation and cosmological simulations alike (e.g., Schaye & Dalla Vecchia, 2008; Hobbs et al., 2013) and thus, despite not being physically motivated, is an important ingredient in our study if I am to compare to resolutions similar to those achieved in cosmological simulations.

SPH particles that have reached the temperature floor and have a density above  $\rho = 10^{-22} \text{ g cm}^{-3}$  are considered star forming. The properties of the temperature floor ensures star formation follows a Jeans instability criterion (see Section 2.6). I employ a probabilistic approach to convert a fraction of this gas into stars. Similar in fashion to Katz (1992), the probability of a SPH particle being converted into a star particle in a given time step  $\Delta t$  is given by

$$P = 1 - \exp\left(-\epsilon_{\text{SF}} \frac{\Delta t}{\tau_{\text{ff}}}\right) \quad (5.3)$$

where  $\epsilon_{\text{SF}} = 0.1$  is the assumed star formation efficiency and  $\tau_{\text{ff}} \sim \sqrt{3\pi/32G\rho}$  is the local free-fall time of the gas. As outlined in section 2.6 this probabilistic approach ensures that the empirical Schmidt (1959) law is followed and is widely used in the literature (e.g., Gnedin, 1996; Katz et al., 1996; Springel, 2000; Kravtsov, 2003; Springel & Hernquist, 2003).

---

<sup>2</sup>For an ideal gas  $P \propto \rho T$  while gas that has reached the temperature floor is forced to behave such that  $T \propto \rho^{1/3}$  and so  $P \propto \rho^{4/3}$ .

### 5.2.2 Initial conditions

The simulations presented here follow a similar setup to those presented in Chapter 4 (Bourne et al., 2014). I wish to investigate the impact of AGN outflows on ambient gas in the host galaxy under realistic conditions, which should certainly include the fact that the ISM is very non-homogeneous, that is, clumpy. To achieve that condition in the controlled environment of an isolated simulation, similar to Hobbs et al. (2011), a turbulent velocity field is imposed upon the gas. I follow the same method as in Chapter 4, in which a sphere of gas is seeded with a turbulent velocity field using the method of Dubinski et al. (1995), as described in Hobbs et al. (2011) and section 4.2.2.

The desired set up for the gas distribution that the AGN feedback acts on, consists of a clumpy gaseous shell with a radial range from 0.1 to 1 kpc and a  $10^8 M_\odot$  black hole at the centre. This is achieved by first setting up a gas distribution, which initially follows a singular isothermal sphere potential from  $R_{\text{in}} = 0.1$  kpc to  $R_{\text{out}} = 1$  kpc. The gas mass fraction within this shell is  $f_g = M_g/M_{\text{total}} = 0.16$ , giving a total initial gas mass  $M_g \simeq 1.6 \times 10^9 M_\odot$ . The system, which initially only consists of SPH particles and the central sink particle, is then allowed to evolve under the action of a turbulent velocity field for 1 Myr resulting in a clumpy gas distribution. The turbulent velocity is normalised such that the root-mean-square velocity,  $v_{\text{turb}} \simeq \sigma \simeq 154 \text{ km s}^{-1}$  and the gas temperature is initially set to  $T \simeq 5.6 \times 10^5 \text{ K}$  such that the shell is virialised.

The black hole is modelled as a  $10^8 M_\odot$  sink particle. During the relaxation period gas is added to the sink particle if it falls within our desired inner boundary for the initial condition of 100 pc (i.e. the accretion radius is 100 pc for the first Myr of the simulations). At the end of the relaxation period the sink particle mass is reset to our desired black hole mass of  $10^8 M_\odot$  and the accretion radius is set to 10 pc. This results in particles at small radii with prohibitively small time steps being removed whilst allowing us to still be able to follow the inflow of dense filaments to small radii during and after the AGN outburst. However, to prevent the removal of gas directly heated by the AGN feedback, SPH particles that are not bound to the collective mass of the sink particle and background potential (within the SPH particles radial position) are not accreted. Here I present simulations that initially have  $N_{\text{SPH}} = 10^3, 10^4, 10^5$  and  $10^6$  SPH particles.

### 5.2.3 AGN feedback model

Even at the resolutions presented in this chapter I am unable to directly model the feedback mechanism of the AGN, however, I can model the effect of the feedback on

| Run  | $N_{\text{SPH}}$ | $m_{\text{SPH}} (M_{\odot})$ | $f_{\text{BH}} N_{\text{ngb}}$ | cooling                                   |
|------|------------------|------------------------------|--------------------------------|---|
| FN3c | $10^3$           | $1.6 \times 10^6$            | $10^2$                         | Sazonov et al. (2005)                     |
| FN4c | $10^4$           | $1.6 \times 10^5$            | $10^2$                         | Sazonov et al. (2005)                     |
| FN5c | $10^5$           | $1.6 \times 10^4$            | $10^2$                         | Sazonov et al. (2005)                     |
| FN6c | $10^6$           | $1.6 \times 10^3$            | $10^2$                         | Sazonov et al. (2005)                     |
| FN3h | $10^3$           | $1.6 \times 10^6$            | $10^2$                         | Sazonov et al. (2005), no Compton cooling |
| FN4h | $10^4$           | $1.6 \times 10^5$            | $10^2$                         | Sazonov et al. (2005), no Compton cooling |
| FN5h | $10^5$           | $1.6 \times 10^4$            | $10^2$                         | Sazonov et al. (2005), no Compton cooling |
| FN6h | $10^6$           | $1.6 \times 10^3$            | $10^2$                         | Sazonov et al. (2005), no Compton cooling |
| FM3c | $10^3$           | $1.6 \times 10^6$            | 10                             | Sazonov et al. (2005)                     |
| FM4c | $10^4$           | $1.6 \times 10^5$            | $10^2$                         | Sazonov et al. (2005)                     |
| FM5c | $10^5$           | $1.6 \times 10^4$            | $10^3$                         | Sazonov et al. (2005)                     |
| FM6c | $10^6$           | $1.6 \times 10^3$            | $10^4$                         | Sazonov et al. (2005)                     |
| FM3h | $10^3$           | $1.6 \times 10^6$            | 10                             | Sazonov et al. (2005), no Compton cooling |
| FM4h | $10^4$           | $1.6 \times 10^5$            | $10^2$                         | Sazonov et al. (2005), no Compton cooling |
| FM5h | $10^5$           | $1.6 \times 10^4$            | $10^3$                         | Sazonov et al. (2005), no Compton cooling |
| FM6h | $10^6$           | $1.6 \times 10^3$            | $10^4$                         | Sazonov et al. (2005), no Compton cooling |

Table 5.1: Summary of simulations showing (l-r) run name, initial number of SPH particles ( $N_{\text{SPH}}$ ), mass of a single SPH particle ( $m_{\text{SPH}}$ ), number of black hole neighbours heated during feedback ( $f_{\text{BH}} N_{\text{ngb}}$ ) and the cooling prescription used. Run nomenclature takes the form FXYZ where  $X$  defines whether the thermal energy of the AGN feedback is deposited into a fixed number of neighbours ( $N$ ) or a fixed mass ( $M$ ) at all resolutions,  $Y = \log_{10}(N_{\text{SPH}})$  and  $Z$  defines runs in which cooling due to IC processes is (c) and is not (h) included.



the ISM. Models of UFOs colliding with the ISM have been particularly successful in explaining observational correlations (e.g., King, 2003, 2005; Zubovas & King, 2012a; Faucher-Giguère & Quataert, 2012). In these models the UFO, with a velocity  $v \sim 0.1c$ , shocks against the ISM driving a reverse wind shock and a forward shock in the ISM. The wind shock can reach temperatures of  $\sim 10^{10} - 10^{11}$  K and expand through thermal pressure, driving out material of the ISM. As in Costa et al. (2014), it is the effect of the reverse wind shock, shown in figure 1.7, that I attempt to mimic in our feedback method. I have discussed some AGN prescriptions in section 2.7. In order to draw comparisons with other galaxy formation and cosmological simulations I choose a fairly standard approach, which is similar to that presented in Di Matteo et al. (2005), where the feedback is thermally coupled to neighbouring gas particles in a kernel-weighted fashion. During a time step of length  $\Delta t$ , the energy released by the AGN is given by

$$E_{\text{therm}} = \epsilon_f L_{\text{AGN}} \Delta t \quad (5.4)$$

where  $\epsilon_f = 0.05$  is the efficiency with which the AGN luminosity couples to the ambient gas, as defined in the introduction and  $L_{\text{AGN}}$  is the AGN luminosity. Our chosen value for  $\epsilon_f$  is physically motivated by models of UFOs, which are expected to have a kinetic luminosity given by equation (1.21);  $\dot{E}_{\text{kin}, \text{UFO}} = (\epsilon_f/2) L_{\text{AGN}} \simeq 0.05 L_{\text{AGN}}$  (e.g., King, 2005; Zubovas & King, 2012a). For simplicity I set the AGN duration to 1 Myr and  $L_{\text{AGN}}$  to the Eddington luminosity,

$$L_{\text{Edd}} = \frac{4\pi G M_{\text{BH}} c}{\kappa} \quad (5.5)$$

where  $M_{\text{BH}} = 10^8 M_{\odot}$  is the black hole mass and  $\kappa = \sigma_T/m_p$  is the electron scattering opacity (where  $\sigma_T$  is the Thompson cross-section and  $m_p$  is the proton rest mass) and  $G$  is the gravitational constant. The energy given to an SPH particle,  $E_{\text{inj}}$ , is then given by

$$E_{\text{inj},k} = E_{\text{therm}} \frac{m_{\text{SPH}} W(r_k - r_{\text{BH}}, h_{\text{BH}})}{\rho_g(r_{\text{BH}})}, \quad (5.6)$$

where  $m_{\text{SPH}}$  is the mass of an SPH particle,  $W(r_k - r_{\text{BH}}, h_{\text{BH}})$  is the kernel weight of the SPH particle relative to the black hole,  $h_{\text{BH}}$  is the black hole *smoothing* length ( $O(10 - 100)$  pc) calculated over  $f_{\text{BH}} N_{\text{ngb}}$  neighbours (see table 5.1) and  $\rho_g(r_{\text{bh}})$  is the gas density at the location of the black hole. This approach ensures that gas closer to the black hole is heated to a higher temperature than gas further away. The total mass heated per time step is given by

$$M_{\text{heat}} \simeq f_{\text{BH}} N_{\text{ngb}} m_{\text{SPH}}, \quad (5.7)$$

where  $f_{\text{BH}}$  is the ratio of the number of black hole neighbours being heated. I consider two main scenarios; one in which  $f_{\text{BH}} = 1$  at all resolutions and one in which I approximately heat a fixed mass at each resolution and hence set  $f_{\text{BH}} = N_{\text{SPH}}/10^4$ . This choice of  $f_{\text{BH}}$  is a balance between heating a sufficient number of particles in the lowest resolution simulations and not heating an excessive number of particles at high resolution.

## 5.2.4 Summary of simulations

A summary of the simulations is given in table 5.1. I use a nomenclature of the form FNYZ or FMYZ, where “FN” signifies that a fixed number of SMBH SPH particle neighbours are heated by the feedback independently of the SPH particle number used in the simulation. This means that  $f_{\text{BH}} = 1$  for such simulations. “FM”, on the other hand, stands for a fixed mass of SMBH neighbour particles being heated. In these runs the number of SPH particle neighbours over which the SMBH feedback is spread depends on the numerical resolution of the simulation, and I set  $f_{\text{BH}} = N_{\text{SPH}}/10^4$ , at all resolutions. The number  $Y = \log_{10}(N_{\text{SPH}})$  encodes the total number of SPH particles used. Finally,  $Z$  is either “h” or “c”, and marks runs in which cooling<sup>3</sup> due to IC processes is included (c) or not (h).

## 5.3 Results

### 5.3.1 Pre-feedback properties of the ISM

Before investigating how the feedback interacts with the ISM I compare the properties of the ISM itself at different resolutions. Figure 5.1 shows the density distribution for the gas, at different resolutions, after 1 Myr i.e. just before the feedback turns on. At this point in the simulation the gas distribution is identical for all of the runs at the same resolution, e.g. the blue curve in the figure is the same for the runs FN6c, FN6h, FM6c and FM6h. Figure 5.1 shows that the lowest resolution runs, with  $10^3$  particles, probe a much narrower density range than the runs in which  $10^6$  particles are used. The highest resolution runs thus resolve the density distribution tails at both the low and high density ends. This means that with improved resolution I am able to better distinguish the high and low density phases of the ISM, which, as I show below, can have a large impact on the efficiency of AGN feedback.

---

<sup>3</sup>Compton heating due to the AGN radiation field is included for gas with  $T \leq 1.9 \times 10^7$  K in all simulations.

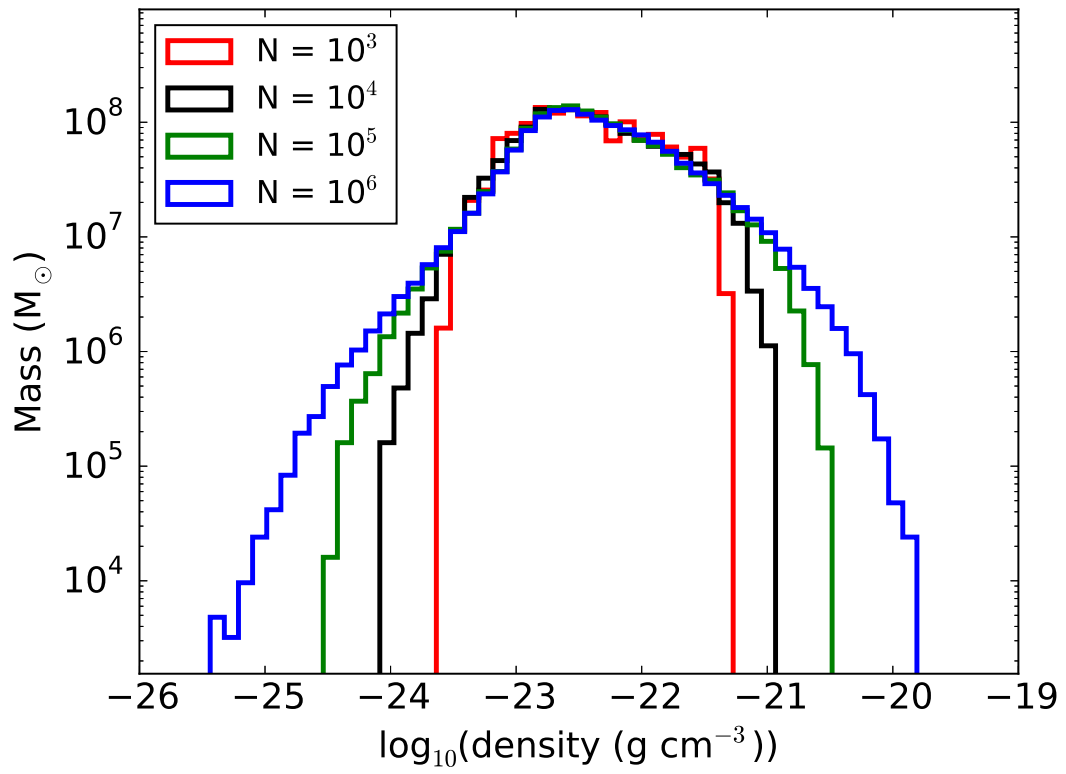


Figure 5.1: Gas density distribution at 1 Myr for simulations with  $10^3$  (red),  $10^4$  (black),  $10^5$  (green) and  $10^6$  (blue) particles. Both the high and the low density tails of the gas density distribution are better resolved as the mass resolution of the simulation is improved.

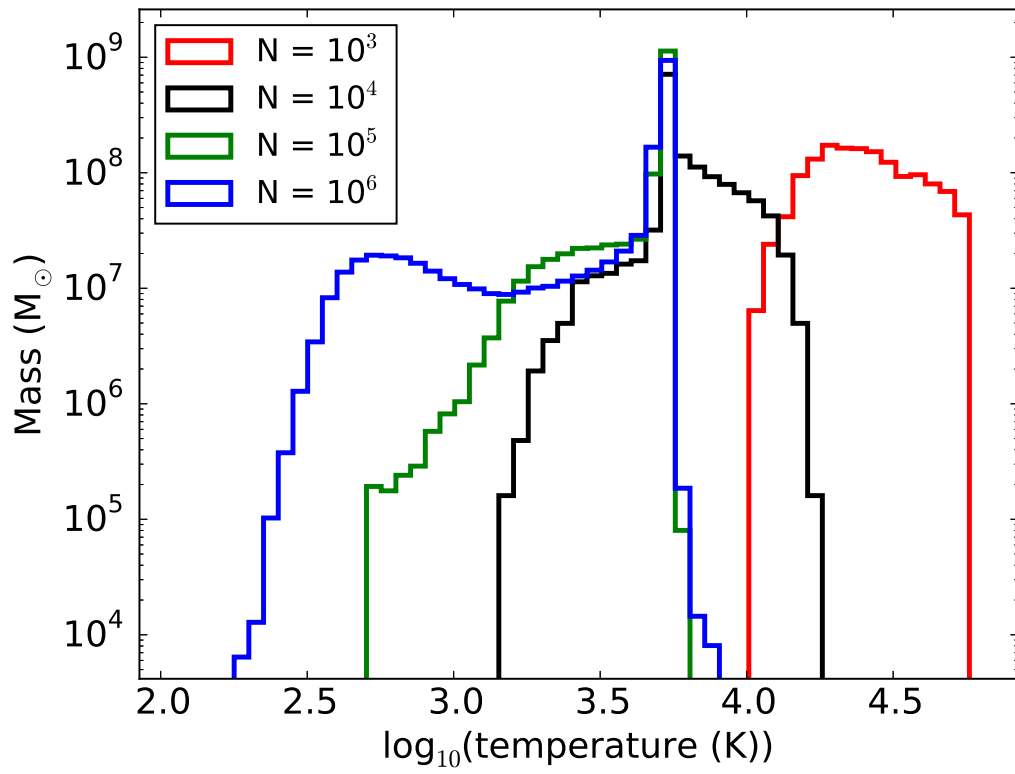


Figure 5.2: Gas temperature distribution at 1 Myr for simulations with  $10^3$  (red),  $10^4$  (black),  $10^5$  (green) and  $10^6$  (blue) particles. The low-temperature (dense) gas is completely unresolved in the low resolution simulations.

Figure 5.2 shows the temperature distribution for the gas, at different resolutions, after 1 Myr. In this figure we can see that in the lowest resolution simulations ( $10^3$  particles) the gas remains warm ( $T > 10^4$  K). This is due to the dynamical temperature floor that I employ (which is a common approach in cosmological and galaxy formation simulations, see text after equation (5.2)). As the mass resolution is increased the gas can cool to progressively lower temperatures. It can also be seen that in simulations with  $10^5$  and  $10^6$  particles the maximum temperature of the gas (before any AGN feedback is initiated) converges to  $T \sim 10^{3.7}$  K. The reason for this is that at lower temperatures ( $T \lesssim 10^4$  K) the gas cools much slower, so that there tends to be a lot of gas “piling up” at  $T \sim 10^4$  K.

### 5.3.2 Overview of numerical resolution trends

Figure 5.3 shows rendered images of gas density slices through the simulation domain at  $y = 0$  after 1.5 Myr. The top row shows the FM3h, FM4h, FM5h and FM6h runs from left to right respectively while the bottom row shows the FN3h, FN4h, FN5h and FN6h runs from left to right respectively. The figure clearly illustrates the increasing complexity of structure that can be resolved with improved resolution. In the low resolution runs (left panels) there is a fairly symmetrical swept-up shell of high density gas, while the high resolution runs (right panels) consist of compressed high density filaments and cleared low density channels through which hot gas can escape.

Figure 5.4 shows the respective temperature slices. At low resolution (left panels) the feedback outflow sweeps up essentially everything in its path, with no cold gas left at small radii, whilst the hot gas is contained in the central regions only. In contrast in the higher resolution runs (right panels) the cold gas is still present in clumps and filaments at small radii, whereas the heated gas escapes through low density channels and is now more spatially extended. Since it is likely that the cold gas is the source of efficient SMBH growth, these results show that not only SMBH feedback but also SMBH growth is affected by the numerical resolution artefacts i.e. at low resolution there is a lack of high density cold gas clumps.

The simulations also show stark differences in gas thermodynamical properties between the runs in which the feedback is coupled to a fixed mass (the FM series of runs) versus those with a fixed neighbour number (the FN series of simulations). For instance, due to the differences in the feedback implementation, in FN6h (bottom right panels of figures 5.3 and 5.4) a factor  $\sim 100$  times less mass is heated than in FM6h (top right panels of figures 5.3 and 5.4) and hence the gas is heated to much higher temperatures in FN6h than in FM6h. This results in the feedback in FN6h being more effective at clearing

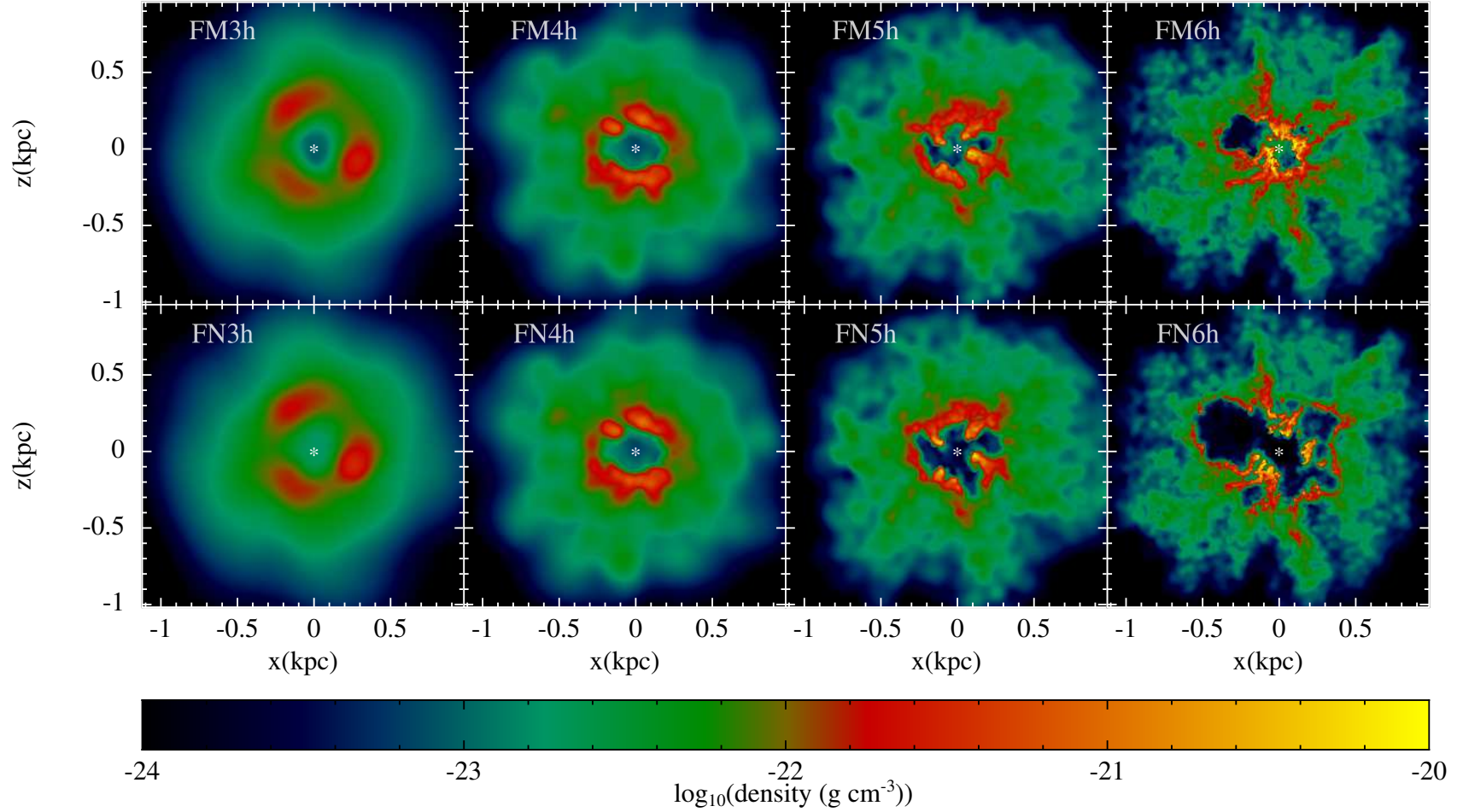


Figure 5.3: Density slices at  $y = 0$  through simulation domains at 1.5 Myr. The top row shows runs FM3h, FM4h, FM5h and FM6h from left to right respectively while the FN3h, FN4h, FN5h and FN6h runs are shown from left to right respectively on the bottom row. The white \* symbol represents the location of the SMBH.

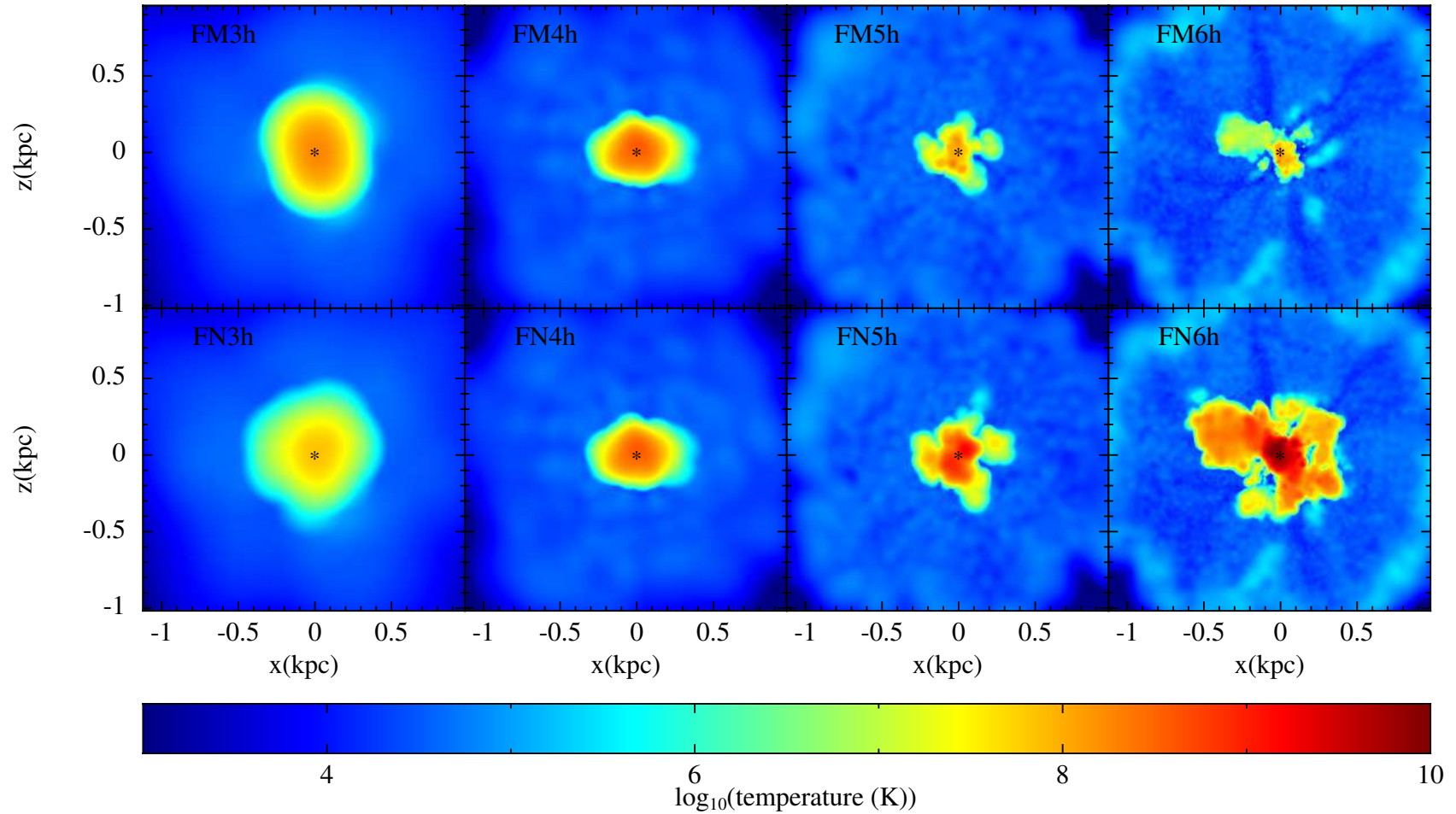


Figure 5.4: Temperature slices at  $y = 0$  through simulation domain showing gas temperature at 1.5 Myr. The top row shows runs FM3h, FM4h, FM5h and FM6h from left to right respectively while the FN3h, FN4h, FN5h and FN6h runs are shown from left to right respectively on the bottom row. The black \* symbol represents the location of the SMBH.

gas from the central region. However, there is still cold, dense, in-flowing gas present at small radii.

### 5.3.3 Impact of feedback on the ISM

#### 5.3.3.1 Resolving the ISM density structure

Figure 5.5 compares the density distribution at 1Myr (filled) and 2Myr (not filled) (i.e. before and after the AGN outburst) for the FN6 (blue) and FN3 (red) runs. In the FN3 runs there is very little evolution in the density distribution with time. However, in the FN6 runs the highest value of gas density reached in the simulation increases by approximately two orders of magnitude, especially when IC cooling is included (compare the dotted and solid lines).

Similar behaviour is seen when comparing the FM3 and FM6 runs in Figure 5.6. The FM6c run exhibits a particularly high density feature not seen in other runs. While the mass in this feature corresponds to only  $\sim$  one resolution element, it is interesting to note its existence. The likely cause of this clump is two-fold. Compared with the FM6h run, the gas in the FM6c run can cool via IC processes allowing it to collapse to higher densities. Furthermore, comparing with the FN6 runs, the gas heated directly by the AGN feedback does not reach such high temperatures in the FM6 runs, potentially resulting in cooler clumps that can reach higher densities.

In the higher resolution runs the AGN feedback is able to compress gas to much higher densities, which could result in triggered star formation (e.g. Elbaz et al., 2009; Gaibler et al., 2012; Nayakshin & Zubovas, 2012; Silk, 2013; Zubovas et al., 2013a; Cresci et al., 2015). The figure demonstrates that compression of the ISM into high density features is largely missed in the low resolution runs probably because the ISM structure is under-resolved.

#### 5.3.3.2 Resolving outflows and inflows

The radial velocity of gas in the simulations is also affected by numerical resolution. Contrasting the FM3 and FM6 runs, Figure 5.7 shows that whilst both high and low resolution runs produce gas out-flowing with velocities of order  $1000 \text{ km s}^{-1}$ , the same cannot be said about the in-flowing gas: the high resolution runs (FM6) show far stronger gas inflows than the low resolution runs (FM3). The same behaviour is found when comparing the FN3 and FN6 runs in Figure 5.8. It is interesting to note that for this implementation of feedback, the out-flowing gas can reach much higher velocities in the



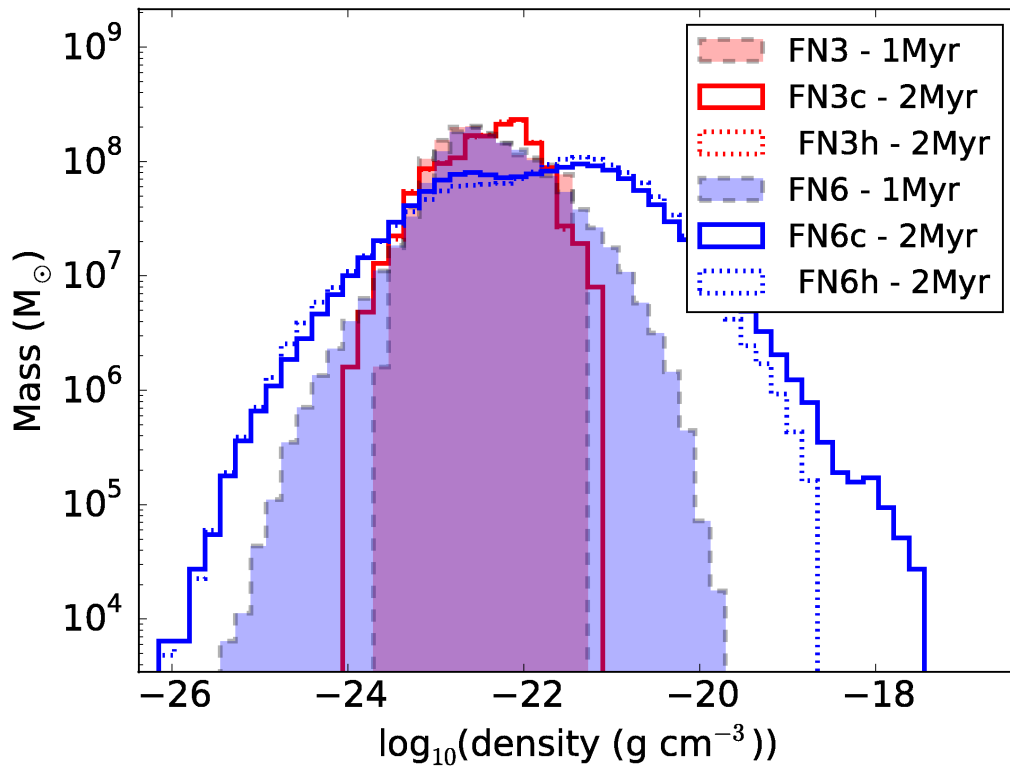


Figure 5.5: Comparison of gas density distributions at 1 Myr (filled) and 2 Myr (not filled) for FN3 (red) and FN6 (blue) runs with and without IC cooling (solid and dotted respectively). It is clear to see that in the FN3 runs the density distribution changes very little, while in the FN6 runs the gas can be compressed to considerably higher densities.

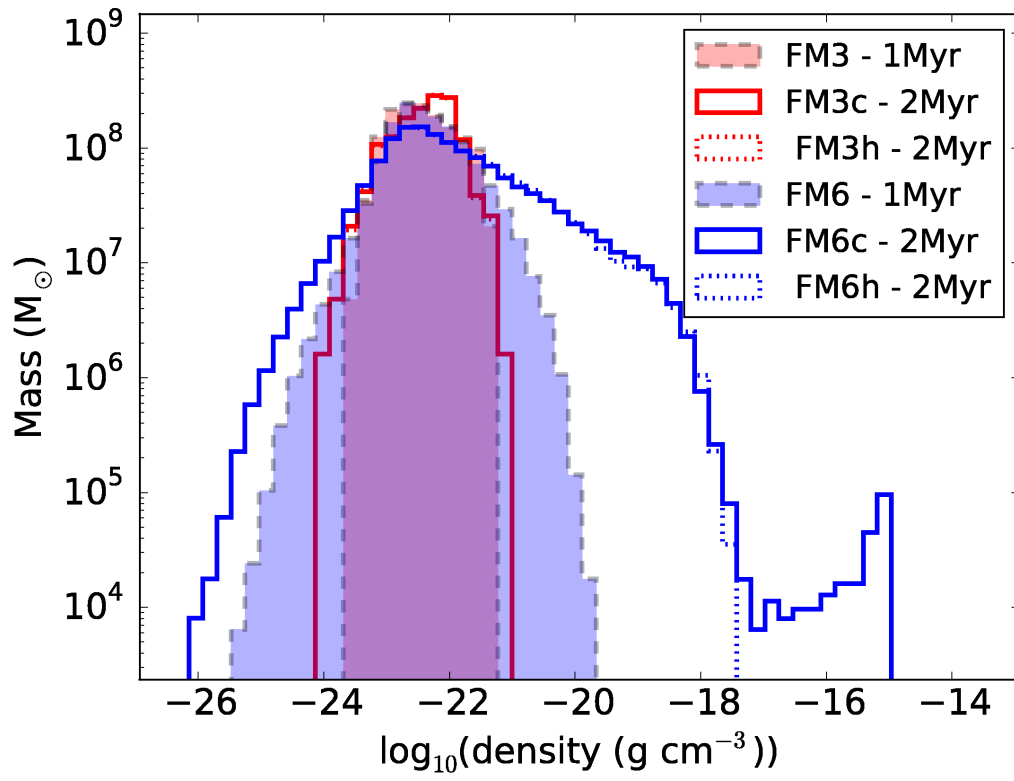


Figure 5.6: As in figure 5.5 except for the FM3 and FM6 runs. However, the FM6c run exhibits a particularly high density feature not seen in other runs.

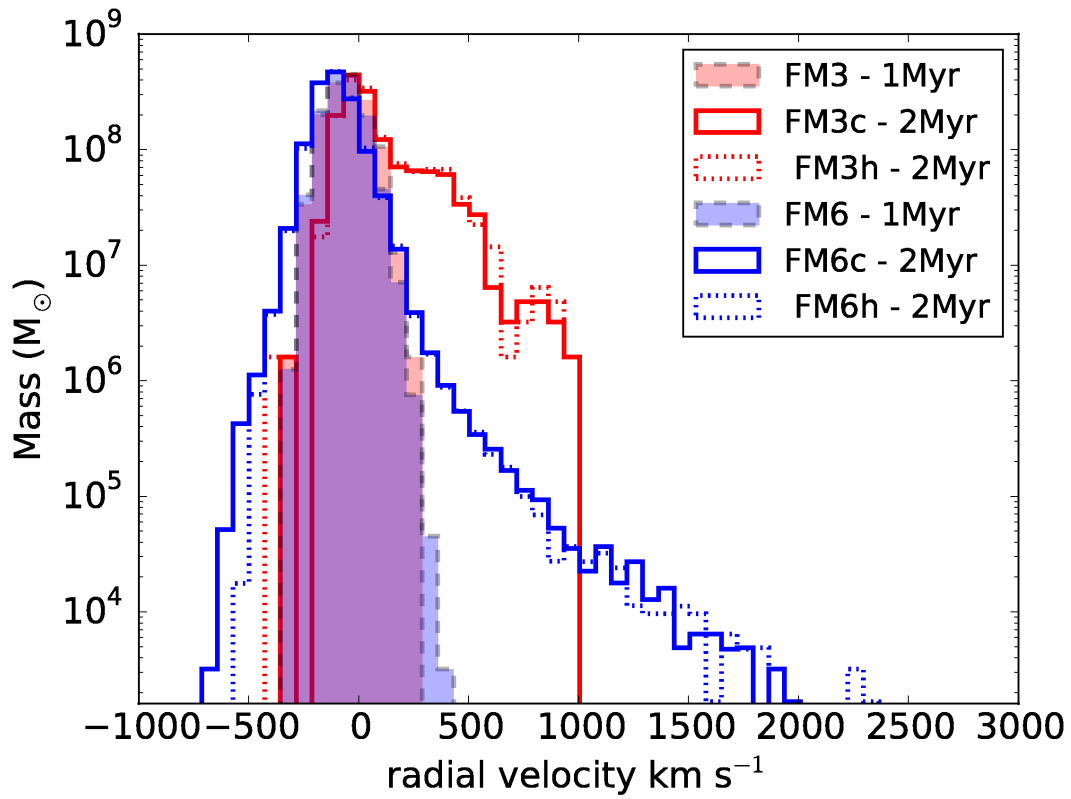


Figure 5.7: Comparison of radial velocity distributions at 1 Myr (filled) and 2 Myr (not filled) for FM3 (red) and FM6 (blue) runs with and without IC cooling (solid and dotted respectively). Both high and low resolution runs produce gas out-flowing with velocities of order  $1000 \text{ km s}^{-1}$ , however, the high resolution runs (FM6) show far stronger gas inflows than the low resolution runs (FM3).

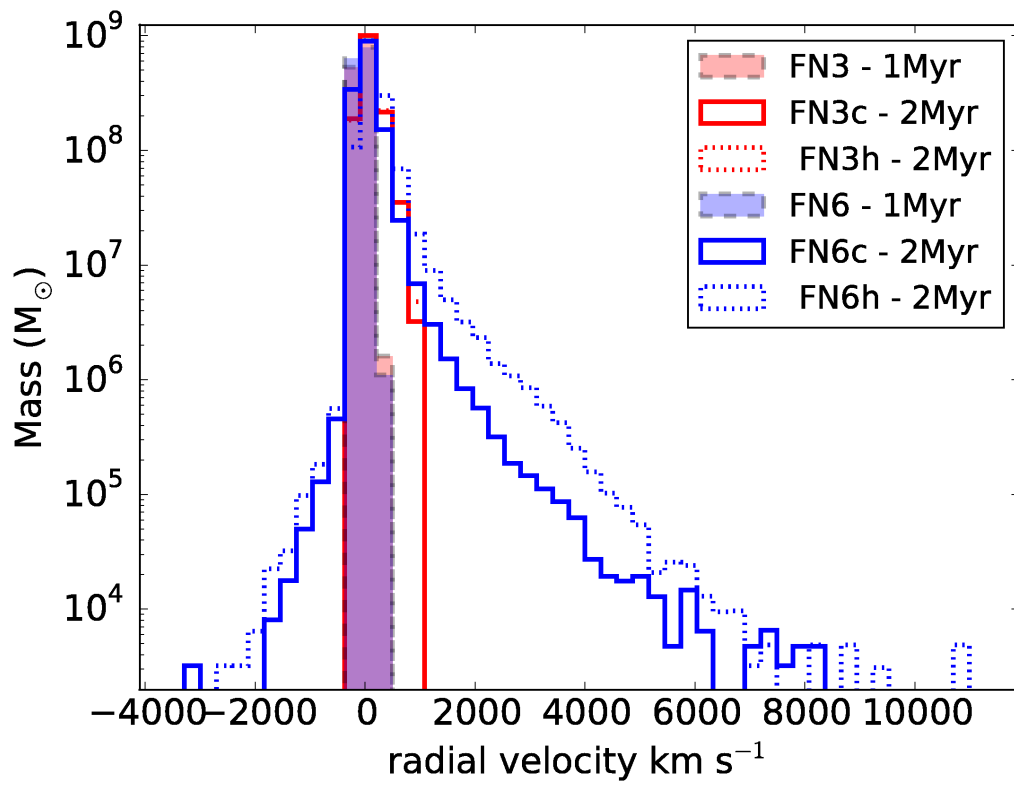


Figure 5.8: As in Figure 5.7 except for the FN3 and FN6 runs. Due to the significantly higher temperatures reached in the FN6 runs, compared to the FM6 runs, the gas outflows can reach much higher velocities.

FN6 run than in the FN3 run (by a factor of  $\sim 10$ ). This can be attributed to the much higher temperatures achieved in the FN6 run. The physical reason for the in-flowing gas present only in the high resolution runs is the previously emphasised inability of the low resolution simulations to model the high density features properly. The high density clumps and filaments present at high resolution are artificially smoothed in lower resolution runs. This results in the high density gas being far less resilient to feedback in the low resolution runs and hence being blown away with the rest of the gas. Needless to say, this is a serious artefact as the SMBH may be fed by exactly this high density gas falling into the centre of the galaxy despite the SMBH feedback (e.g., Nayakshin, 2014).

### 5.3.4 Efficiency of feedback versus numerics

#### 5.3.4.1 The over-cooling problem

Supernova feedback simulations show a well known “over-cooling problem”, which affects simulation results and is discussed at length in Dalla Vecchia & Schaye (2012). This, like other studies (e.g. Booth & Schaye, 2009; McCarthy et al., 2010, 2011; Le Brun et al., 2014; Schaye et al., 2015; Crain et al., 2015), find that a similar problem also exists in AGN feedback simulations. The maximum temperature of the gas directly heated by the feedback, that is the SPH neighbours of the SMBH particle in which the feedback energy is directly deposited, is inversely proportional to the total mass of the gas heated. The radiative cooling rate of the gas is a strong function of temperature in certain temperature ranges. Therefore, the impact of radiative cooling on the thermal evolution of this gas depends in a complicated fashion on the number or total mass of SPH particles in which the feedback energy is injected. In low resolution simulations it is likely that the injected energy is spread over an unrealistically large mass of ambient gas. This typically means that this feedback-heated gas cools on timescales much shorter than one would physically expect.

Figure 5.9 shows the time evolution of the instantaneous maximum gas temperature for simulations in which the feedback energy is injected into a fixed number of SPH particles ( $\sim 100$ ) during each time step (FN3 (red), FN4 (black), FN5 (green) and FN6 (blue)) in the top panel (a) and for simulations in which the feedback energy is injected into a fixed mass ( $\sim 1.6 \times 10^7 M_\odot$ ) of gas during each time step (FM3 (red), FM4 (black), FM5 (green) and FM6 (blue)) in the bottom panel (b). The solid and dotted lines show runs with and without IC cooling respectively. Considering first the fixed number of neighbours (FN) runs in the top panel (a), it roughly follows that each order of magnitude

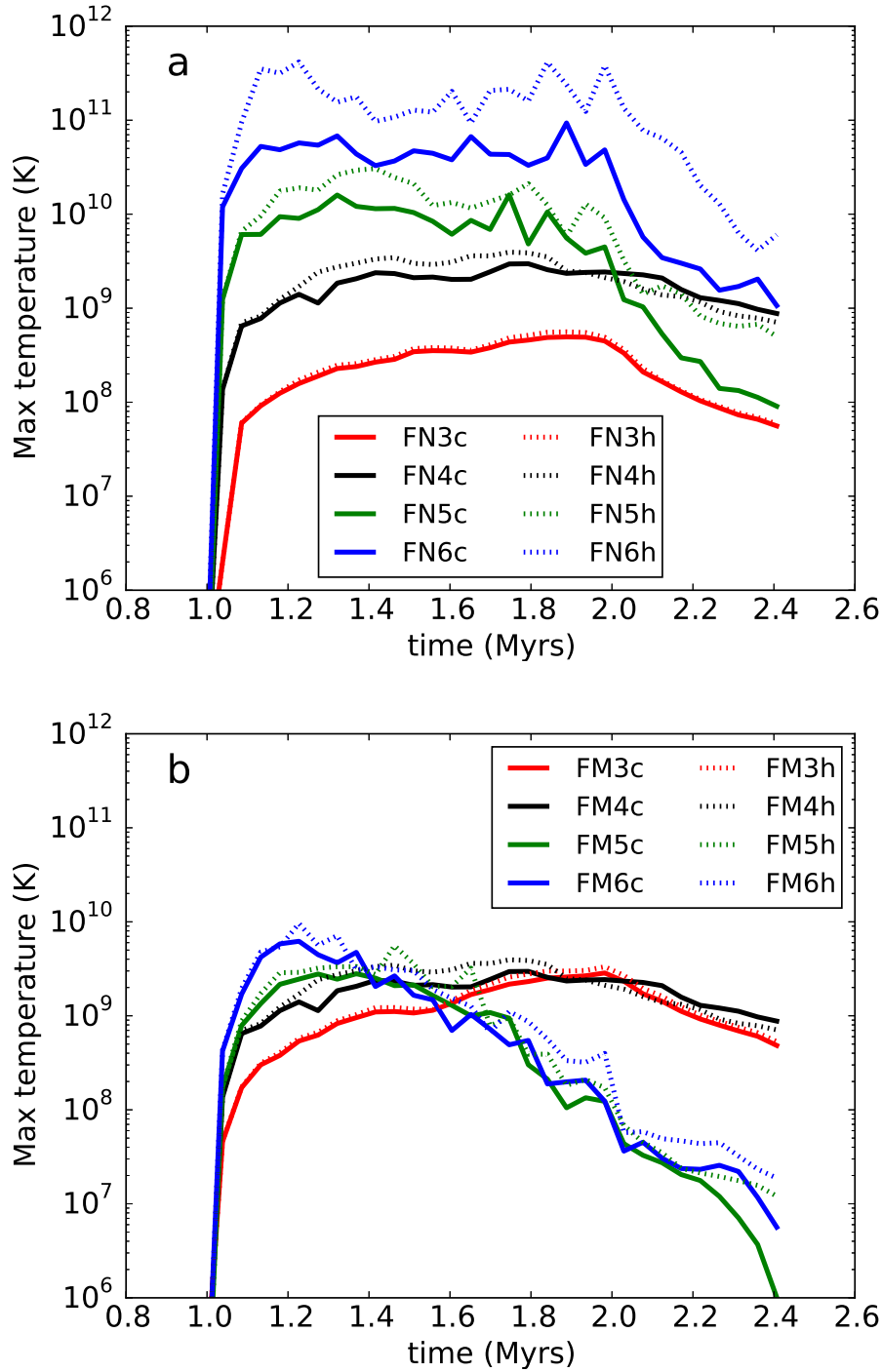


Figure 5.9: Time evolution of the maximum gas temperature. The top panel (a) shows the FN3 (red), FN4 (black), FN5 (green) and FN6 (blue) runs whilst the bottom panel (b) shows the FM3 (red), FM4 (black), FM5 (green) and FM6 (blue) runs. Solid and dotted lines indicate runs with and without IC cooling. This figure shows that the temperature to which gas is heated to is strongly dependent on the mass of gas heated.

improvement in resolution results in an order of magnitude increase in temperature. This is because the feedback energy is injected into a factor  $\sim 10$  times less gas mass for each factor 10 increase in mass resolution.

The fixed mass (FM) runs in the bottom panel (b) lead to more consistent results in that the maximum temperature of gas varies much less between the different resolution simulations, as is expected. However, at later times the higher resolution runs FM5 and FM6 do differ significantly from the lower resolution curves. I believe this is caused by differences in gas properties beyond the immediate feedback deposition region. As shown in Figure 5.3, there is more dense gas near the black hole in the better resolved simulations. This denser gas is hence better at radiating the feedback energy away than in the lower resolution runs.

Finally I note that, if included, IC cooling dominates the cooling function at high temperatures for gas close to the SMBH. This explains why the dotted and dashed curves in Figure 5.9 only exhibit differences when gas is heated to high temperatures.

The mode of feedback energy delivery to the ambient gas strongly affects the subsequent evolution of the system. This can be seen in Figure 5.10, which shows the time evolution of the ratio of the change in gas internal and kinetic energy to the energy injected by the AGN as a function of time. As in Figure 5.9, in the top panel (a) the feedback energy is injected into a fixed number of SPH particles ( $\sim 100$ ) during each time step whereas in the bottom panel (b) the feedback energy is injected into a fixed mass ( $\sim 1.6 \times 10^7 M_\odot$ ) of gas during each time step. The change in total gas kinetic<sup>4</sup> energy (thermal plus mean motion) at time  $t$ ,  $\Delta E_{\text{gas}}(t)$ , is given as

$$\Delta E_{\text{gas}}(t) = E_{\text{gas}}(t) - E_{\text{gas}}(1\text{Myr}) \quad (5.8)$$

where

$$E_{\text{gas}}(t) = \sum_i \left( \frac{1}{2} m_i v_i^2 + \frac{3}{2} \frac{k_B T_i}{\mu m_p} m_i \right) \quad (5.9)$$

is the sum of the kinetic and internal energy of all of the SPH particles at time  $t$ . The total AGN input energy,  $E_{\text{AGN}}$  is given by

$$E_{\text{AGN}} = \epsilon_f L_{\text{AGN}} t_{\text{act}} \quad (5.10)$$

---

<sup>4</sup>Note that the gravitational potential energy is neglected here because I am primarily interested in the ability of the simulations to retain the *feedback* energy. This is dominated by the effectiveness of the radiative cooling of the gas and hence the energy contributions that are most relevant are the energy that is directly injected into the simulation (thermal) and the resulting outflows (mean motion) due to this thermal energy.

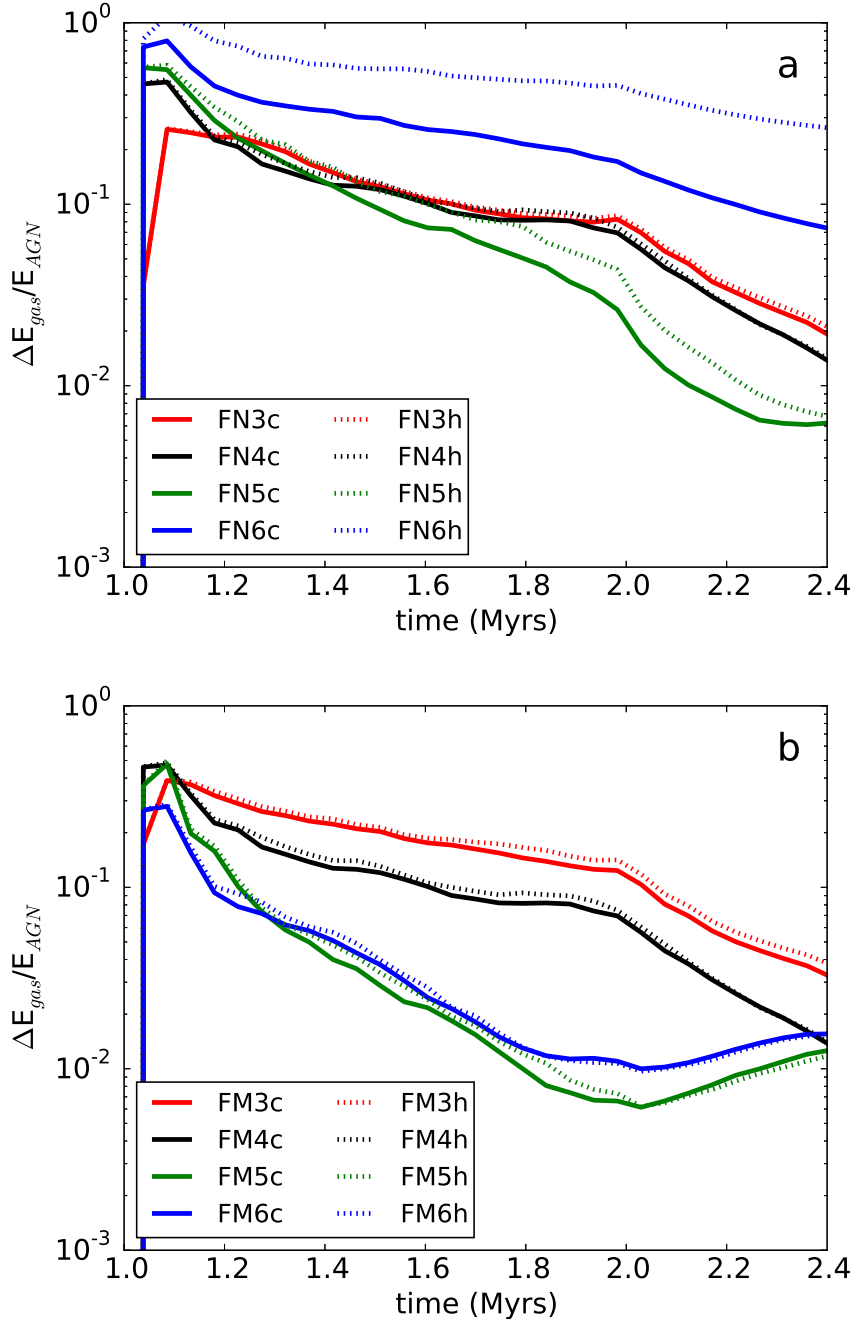


Figure 5.10: Evolution of the ratio of total gas energy,  $E_{\text{gas}}$ , to total AGN input energy,  $E_{\text{AGN}}$ , from the beginning of the AGN outburst between 1 Myr and 2 Myr. The top panel (a) shows the FN3 (red), FN4 (black), FN5 (green) and FN6 (blue) runs. In this panel there is no apparent trend with resolution. In both panels the solid and dotted lines correspond to runs with and without IC cooling respectively. The bottom panel (b) shows the FM3 (red), FM4 (black), FM5 (green) and FM6 (blue) runs. There is an evident trend that lower resolution runs retain more energy than high resolution runs.



where  $t_{\text{act}}$  is the time for which the AGN has been active. Focusing on the FN series of runs first (top panel, a), I find no clear trend in how much feedback energy is retained by the gas. The two low resolution cases, FN3 and FN4, are rather similar; then the higher resolution case, FN5, retains less energy than that, but the highest resolution case, FN6, retains *much more* energy than the low resolution cases. I believe that this is due to competition between two somewhat oppositely directed numerical artefacts; one due to the over cooling problem close to the AGN and the other due to poor sampling of the ambient gas farther out. As the resolution is improved one is able to heat a lower mass of gas and hence heat the gas to higher temperatures resulting in longer cooling times. However, at higher resolution one can resolve high density material, which has a shorter cooling time than the lower density material found in the vicinity of the SMBH in lower resolution simulations. Given the competition between the processes contributing to the gas cooling rate, there is not necessarily a clear trend in feedback energy conservation with resolution.

The fixed mass runs (FM, the bottom panel, b, of the figure) give a more consistent picture, with FM5 and FM6 yielding very similar results, perhaps indicating that a degree of numerical convergence is taking place. Here I see that at higher resolution less feedback energy is retained in the ambient gas of the galaxy, presumably because higher density clumps are better resolved at higher resolutions and they lead to more energy being lost to radiation. These results show that simulations in which feedback is spread around a fixed mass of ambient gas should be preferred for numerical reasons to those where the number of AGN neighbours is fixed instead. However, it should be noted that although injecting feedback energy into a fixed mass of particles provides a degree of numerical convergence, it is not necessarily convergence towards the physically correct result. A further potentially confounding factor is the energy imparted by the momentum of the AGN wind. This is not included in the models presented in this chapter, however, a purely momentum-driven wind should have a kinetic energy rate  $\dot{E}_{\text{mom}} \simeq 2\sigma/(\eta c)\dot{E}_{\text{wind}} \simeq 0.01\dot{E}_{\text{wind}}$ . In the high-resolution models this energy is comparable to the energy retained by the gas and may further complicate gas behaviour. However, a more detailed investigation of the effects of different AGN feedback prescriptions is beyond the scope of this chapter.

#### 5.3.4.2 Gas ejection efficiency

It is believed that the most important effect of AGN feedback onto their host galaxies is to remove gas from the host galaxy and thus quench star formation. In this section I show that the ability of a simulated AGN to clear the gas out of the host is greatly affected by

numerical resolution at least for the initial conditions and parameter space investigated in this chapter.

To quantify the AGN feedback impact on the host, I first consider the evolution of the total baryonic mass enclosed within 200pc of the host's centre. I define the fractional change in baryonic mass as

$$\frac{\Delta M_{<200\text{pc}}(t)}{M_{<200\text{pc}}(1\text{Myr})} = \frac{M_{<200\text{pc}}(t) - M_{<200\text{pc}}(1\text{Myr})}{M_{<200\text{pc}}(1\text{Myr})} \quad (5.11)$$

where  $M_{<200\text{pc}}(t)$  is the total baryonic mass within 200 pc, including gas accreted onto the black hole but not the initial black hole mass ( $10^8 M_\odot$ ) itself. Figure 5.11 shows the time evolution of  $\Delta M_{<200\text{pc}}(t)/M_{<200\text{pc}}(1\text{Myr})$  for simulations with  $10^3$ ,  $10^4$ ,  $10^5$  and  $10^6$  particles shown in black, blue, red and green, respectively. The fixed mass (FM, bottom panel, b) runs show a trend with resolution such that feedback becomes less effective at clearing gas out with improved resolution. The FM3 run, which retains the largest fraction of energy, is the most effective at clearing gas out, whilst the FM5 and FM6 runs, which lose the most energy, cannot prevent the continual infall of gas. However, if I consider the FN runs (top panel, a) there is no clear trend. Even though the FN6 run retains substantially more energy than the FN3 run, it is far less effective at clearing gas out. This can be attributed to being able to resolve structure in the ISM. As I improve resolution, the hot gas can escape through paths of least resistance leaving higher density clumps behind.

Finally I attempt to further quantify the ability of an AGN to clear gas out by calculating the fraction of gas with radial velocity greater than  $2\sigma$ . This is shown in Figure 5.12, with the same colour scheme as previous plots. For the FM runs (bottom panel, b) there is a clear trend that as the resolution is improved the fraction of gas out-flowing at a high velocity becomes smaller. However, for the FN runs (top panel, a) this trend breaks down for the highest resolution run, FN6. This suggests that the cooling as well as the ability to resolve structure plays an important role in determining how effectively gas can be blown out of the galaxy. As discussed when considering Figures 5.4 and 5.9 with respect to the FN5 and FN6 runs, the gas in the FN6 runs is heated to higher temperatures than that in the FN5 runs. The cooling in the FN6 runs is less efficient and thus the hot feedback bubble conserves more energy than in the FN5 runs and is able to drive more powerful outflows.

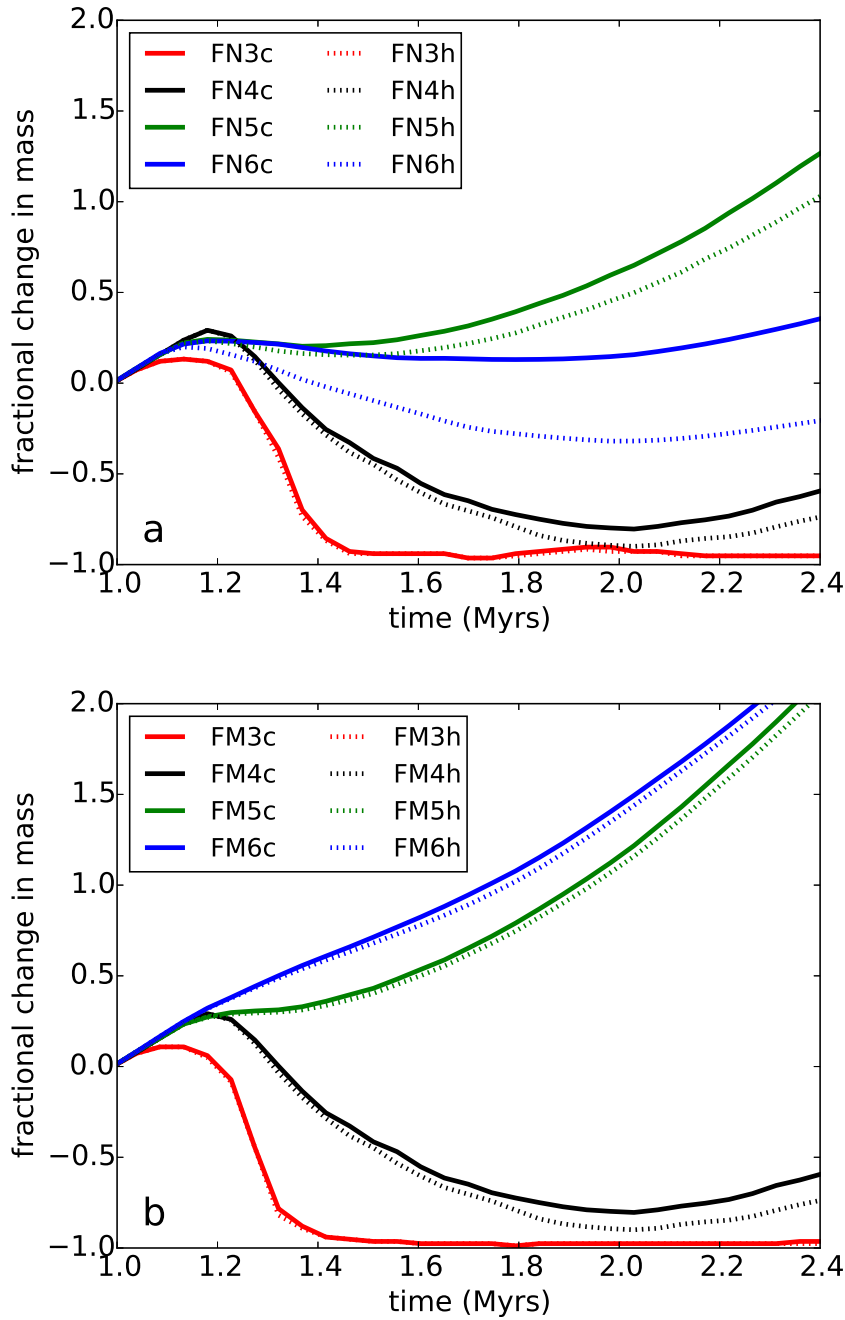


Figure 5.11: Time evolution of the fractional mass change within the central 200 pc of the system. The top panel (a) shows the FN3 (red), FN4 (black), FN5 (green) and FN6 (blue) runs. As in Figure 5.10 there is no apparent trend with resolution, however, like in the FM runs, the FN3 and FN4 runs are the most efficient at removing gas. The bottom panel (b) shows the FM3 (red), FM4 (black), FM5 (green) and FM6 (blue) runs. As the resolution is degraded the feedback becomes more efficient at clearing gas from the central regions. In both panels the solid and dotted lines correspond to runs with and without IC cooling respectively.

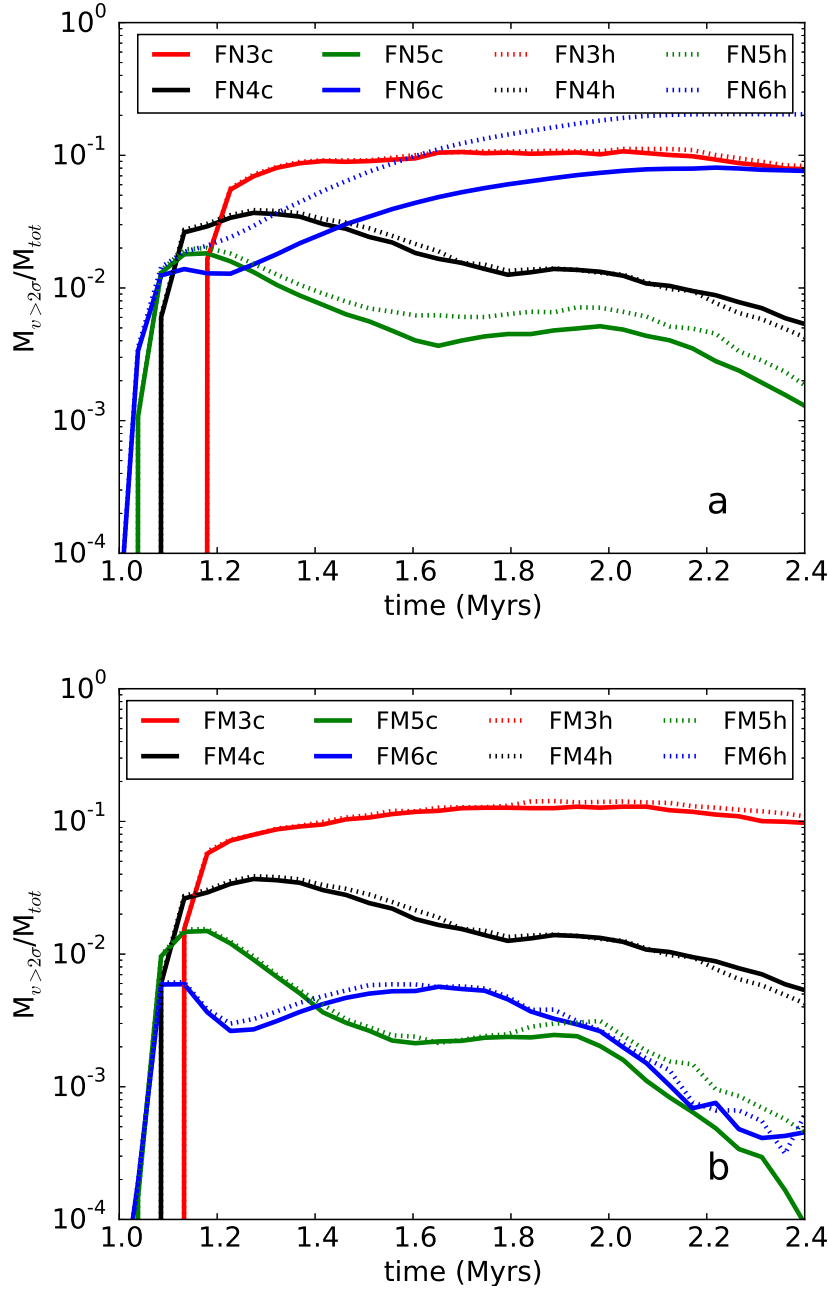


Figure 5.12: Time evolution of the fraction of gas with radial velocity greater than  $2\sigma$ . The top panel (a) shows the FN3 (red), FN4 (black), FN5 (green) and FN6 (blue) runs. Again, as in previous figures there is no apparent trend with resolution with both the FN3 and FN6 runs producing outflows containing similar fractions of gas. The bottom panel (b) shows the FM3 (red), FM4 (black), FM5 (green) and FM6 (blue) runs. As in Figure 5.11 there is an apparent trend with resolution, with a greater fraction of gas being out-flowing at a high velocity in the lower resolution runs than in the high resolution runs. In both panels the solid and dotted lines correspond to runs with and without IC cooling respectively.

## 5.4 Discussion

I have studied the effect of AGN feedback on a multiphase interstellar medium and how such feedback is affected by numerical resolution. The resolution has two competing effects on the results. Unsurprisingly, the density structure is better resolved at higher resolutions, so that there is more hot low-density and also cold high-density gas than in low resolution simulations. Low resolution simulations thus tend to expel all the gas from the centres of host galaxies, whereas higher resolution simulations do not; they also show dense clumps that are more resilient to feedback and may continue to fall inward while most of the gas is driven out. On the other hand, the over-cooling problem may affect the gas in the immediate vicinity of the SMBH, actually reducing feedback efficiency in low resolution simulations. I now discuss these opposing effects in detail.

### 5.4.1 Resolving the multiphase ISM and outflow properties

The inferred properties of outflows in our simulations strongly depend upon the resolution and how the feedback energy is coupled to the ISM. At low resolution the feedback sweeps up *all* the material in SMBH vicinity into an outflow with a modest velocity ( $\sim 1000 \text{ km s}^{-1}$ ). In contrast, at high resolutions only some of the neighbouring gas is launched into the outflow. The outflows can reach higher radial velocities (up to  $\sim 5000 \text{ km s}^{-1}$ ); however, cold dense filaments may continue to fall in and feed the SMBH. Higher resolution SPH simulations thus lead to a much more varied outcome for the gas in the galaxy in every measurable quantity, e.g., density, temperature and velocity. This is potentially very important for SMBH growth since even a tiny mass of ambient gas is sufficient to increase the SMBH mass significantly.

In the same vein, cosmological simulations often have to invoke high *stellar* feedback efficiencies in order to produce observed galactic winds (Schaye et al., 2015). One possible reason for this, in addition to the over-cooling problem, is that low resolution inhibits low density channels through which outflows can escape to reach galactic scales. Alternatively, in some cosmological and galaxy-scale simulations, such winds are hydrodynamically decoupled from the ISM so that they can freely stream to galactic scales (Springel & Hernquist, 2003; Oppenheimer & Davé, 2006; Oppenheimer et al., 2010; Puchwein & Springel, 2013). While such *ad-hoc* prescriptions allow one to produce realistic outflows at large radii, one loses any information regarding the direct interaction of feedback with the ISM. It is therefore clear that cosmological simulations are unable to provide detailed insights into the feedback mechanisms themselves and the best

that one can hope for is that their effects on resolvable scales are modelled correctly.

### 5.4.2 Cooling of the feedback bubble

It is evident that the ability of the feedback bubble to conserve its energy has a significant impact on how efficient it is in destroying the host galaxy. This can depend intimately both on the temperature to which gas is heated directly by the AGN and the processes through which the feedback heated bubble cools. Considering the first point, I have shown that there are stark differences in the properties of the feedback depending upon the mass of the gas heated by AGN feedback. This leads us to the question what temperature is correct? Analytical theory suggests that wind shocks have temperatures of  $10^{10} - 10^{11}$  K, however, as illustrated by Figure 5.9, in order to reach such high gas temperatures in a cosmological simulation, a gas mass of  $\lesssim 1$  SPH particle would need to be heated. Therefore, in such simulations, gas is typically heated to lower temperatures, which could potentially result in incorrect energy conservation in the hot bubble. Such problems may be mitigated to some degree by *tuning* the efficiency of the feedback or artificially turning off radiative cooling in order to match observations. Whilst such procedures can lead to correct large scale properties of the galaxies, e.g. correct stellar masses and the  $M_{\text{BH}} - \sigma$  relation, one clearly loses predictive power if observations need to be used to calibrate the models.

With regard to our second point, i.e. the relevance of different cooling mechanisms, the inclusion or absence of IC processes can have a big effect. Comparing the FN6c and FN6h runs, it is clear from Figures 5.10, 5.11 and 5.12 that the hot bubble retains more energy and clears out more gas when IC cooling is neglected. It is therefore important to understand which scenario is more physically motivated. Faucher-Giguère & Quataert (2012) have shown that given the high temperature and low density properties of shocked outflows, the electrons and ions are thermally decoupled. The electron cooling timescale is shorter than the electron-ion energy exchange timescale (see equation (1.30)) and therefore it is the latter that determines the cooling rate of the gas with IC cooling becoming ineffective. This suggests that the runs in which IC cooling is neglected are more physically motivated. However, because the feedback energy is injected into ISM gas, it is likely to have higher densities than the physically motivated shocked wind bubbles discussed in section 1.6.1.1. This results in the rate of cooling of the hot bubble being over predicted and the subsequent interaction with the host ISM may still be incorrectly modelled. Thus I conclude that direct, physically self-consistent modelling of AGN feedback heating and cooling on small scales is still beyond the reach of modern numerical capabilities.

### 5.4.3 Star formation during an AGN outburst

Figures 5.5 and 5.6 clearly show that gas can be compressed to high densities by an AGN outflow. The presence of dense gas can result in additional star formation, which both quantitatively and qualitatively changes the properties of the AGN host galaxy. Similar aspects of AGN-triggered star formation have already been explored by Nayakshin & Zubovas (2012) and Zubovas et al. (2013a), who found that significant star formation can occur both in the cooling out-flowing medium and in the compressed disc of the host galaxy. Our results show that any density contrasts can be enhanced by AGN outflows.

It is important that one needs simulations with sufficient resolution to recover the compression effect in numerical simulations (Figures 5.5 and 5.6). Large-scale simulations with low numerical resolution typically miss this effect and hence over-predict the negative (gas removal) effect of AGN feedback. Even in high-resolution simulations, star formation in dense clumps is difficult to track during the AGN outflow if one employs a heating-cooling prescription such as that of Sazonov et al. (2005), which includes Compton heating. This prescription assumes that gas is optically thin, which is a good approximation for the low density ISM, but not for the dense clumps. As a result, the clump temperature, in general, stays too high (i.e. above the temperature set by equation (5.2) and fragmentation is slower than it would be with a proper radiative transfer treatment.

The lack of AGN-triggered star formation in low-resolution simulations of galaxy evolution presents two challenges: quantitative and qualitative. The quantitative challenge is the issue of reconciling the star formation histories of simulated and observed galaxies. If one channel of triggered star formation is missed in simulations, the other star formation channels have to be proportionately enhanced (for example, by adopting higher star formation efficiencies or lower density thresholds) in order to reproduce the galaxy stellar mass functions of present-day galaxies. The qualitative challenge is arguably more important: AGN outflows create dense star-forming gas where there was none, i.e. affect the location of star-forming regions in the galaxy. This process directly affects the morphology of the starburst and the dynamics of new-born stars (Nayakshin & Zubovas, 2012; Zubovas et al., 2013b). Both of these effects are missed in low-resolution simulations; however, they can be used as strong indicators of positive AGN feedback.

One region where AGN-induced star formation may be particularly important is galaxy centres. These regions typically contain dense gas discs or rings (e.g. Böker et al., 2008), which often show clumpy structures and embedded young star clusters. It is generally accepted that star formation in these regions is induced by shocks caused by matter

in-falling via galactic bars from larger radii. However, the presence of young clusters and the lack of azimuthal age gradient in some of these systems complicate this picture (Böker et al., 2008). Another trigger of star formation in these systems could be AGN outflows. As these outflows expand perpendicularly to the disc plane due to lower density (Zubovas & Nayakshin, 2014), they significantly compress the gas in the midplane; in addition, ram pressure of the AGN wind pushes the disc gas into a narrower ring, which is more prone to gravitational instability (Zubovas, 2015). In this way, the density contrast between the disc and its surroundings is also enhanced, much like the density contrast between different regions in the simulations presented in this chapter.

#### 5.4.4 Black hole growth and the $M_{\text{BH}} - \sigma$ relation

The general trend in the simulations I present is that at higher resolution less gas is cleared out than at lower resolutions. In low resolution runs the outflow sweeps up everything in its path, creating a sharp cut-off radius between out-flowing material and in-flowing material. However, in high resolution runs the outflow only sweeps up low density material, whilst high density material can continue to flow inward. This could lead to very different feeding cycles for the black hole. The supply of material to the black hole is completely cut off and cleared to large radii in the low resolution runs, whereas in the high resolution runs clumps and filaments can remain in-flowing at small radii and thus continuously feed the black hole. This sets up a scenario in which feedback is “*all or nothing*” at low resolution but more diluted at high resolution, with feeding becoming interminable up to the point that the gas can form stars.

As shown in chapter 4, in the high resolution scenario, the high density clumps will only be acted upon by the momentum of the AGN wind (Bourne et al., 2014; Nayakshin, 2014) with the energy escaping through low density channels. By requiring the ram pressure of the AGN outflow to exceed the gravitational force of the bulge acting on all of the clumps along the line of sight from a SMBH and setting a maximum threshold density for the clumps (assumed to be the density at which they undergo star formation) Nayakshin (2014) finds a critical black hole mass in order to clear out the cold gas of

$$M_{\text{crit}} \sim 2.2 \times 10^8 M_{\odot} \sigma_{200}^4 \quad (5.12)$$

comparable to the observed  $M_{\text{BH}} - \sigma$  relations (e.g., Kormendy & Ho, 2013).



### 5.4.5 Comparison with previous work

Recent work (Wagner et al., 2013; Bourne et al., 2014, see chapter 4) has shown that the structure of the ISM can impact upon the ability of an AGN to clear out gas and hence quench star formation. In Chapter 4 (Bourne et al., 2014) I presented high-resolution simulations of an UFO impacting upon an inhomogeneous, turbulent medium and found new processes such as energy leakage and separation of energy and mass flows within the ISM. The shocked outflows escape via paths of least resistance, leaving the high density gas, which is difficult to expel, largely intact. Such processes have previously been missed in analytical models and cosmological simulations mainly because the multiphase nature of the ISM is not resolved and has to be implemented as a sub-resolution model. For example Springel & Hernquist (2003) include a sub-grid multiphase model for star formation while Murante et al. (2010) include a non-equilibrium model that includes the three ISM phases for each SPH particle. Unfortunately such methods mean that the intricate structure one expects is washed out due to low resolution.

This work builds on that presented in Chapter 4 (Bourne et al., 2014) by implementing a continuous, Eddington limited feedback outburst rather than a single hot bubble. Furthermore, we have explored the role of IC cooling against the AGN radiation field, which has been highlighted in the literature as a key feature in understanding the impact of UFOs (Faucher-Giguère & Quataert, 2012). This work adds to the growing body of work (Wagner et al., 2012, 2013; Bourne et al., 2014; Costa et al., 2014; Gabor & Bournaud, 2014; Zubovas & Nayakshin, 2014, e.g.) highlighting that the AGN *environment* can be just as important as the AGN feedback mechanism itself when modelling galaxy evolution. In Chapter 4 (Bourne et al., 2014), the main aim was to understand the physics of the interaction of an outflow with the multiphase ISM, however, in this work I have focused more on how resolution can affect this interaction.

The role of the ISM and its impact on AGN feedback has been studied by a number of authors both for feedback in the form of jets (e.g. Wagner et al., 2012) and UFOs (Wagner et al., 2013; Bourne et al., 2014, e.g.). Wagner et al. (2012) present high resolution simulations of jet feedback in a clumpy ISM. They found that if the volume filling factor of the clouds is less than 0.1 then the hot feedback bubble can expand as in the energy driven limit. Clouds smaller than  $\sim 25$  pc are destroyed and dispersed, leading them to argue that feedback prescriptions in cosmological simulations should provide a good description of this regime as a source of negative feedback. However, if clouds are larger than  $\sim 25$  pc they are more resilient to the feedback. In agreement with this work they find that the clouds can be compressed, potentially triggering star formation. Such

behaviour is missed in cosmological simulations. Whilst Wagner et al. (2012) suggest a physical setup in which feedback prescriptions in cosmological simulations may produce correct results, I provide a direct comparison of the nature of feedback when simulated at low resolution (similar to cosmological simulations) and up to three orders of magnitude higher resolution. I have found that across such a resolution range there are marked differences in the evolution of the feedback, caused by a combination of effects including the ability to resolve structure and the thermal and physical properties of the hot feedback bubble.

Further work on scales simulating whole galaxies has shown that large scale structure such as a disk (Gabor & Bournaud, 2014) or filaments (Costa et al., 2014) can also reduce the ability of AGN feedback to remove gas from the galaxy. Such structure should be resolved in cosmological simulations, however, resolution effects can still impact upon the properties of the feedback. As I have shown, the temperature to which gas is directly heated by feedback as well as its density can affect the cooling and thus the efficiency of the feedback. Given such large differences between the physical properties of hot feedback bubbles in cosmological simulations and those expected in reality, we should pose the question when, if ever, such processes can be included in these simulations. Following a Moore’s law approach the number of particles used in cosmological N-body simulations approximately doubles every 16 months. This would suggest that an increase in the mass resolution by 3 orders of magnitude could be achieved in  $\sim 13$  years. However, given the fact that algorithms typically scale worse than  $O(N)$  and also considering that the silicon chip capacity is limited, this is an extremely optimistic estimate. It is therefore likely that such an improvement in resolution would take much longer to achieve and depends upon the efficiency with which simulators and programmers can harness the power of parallel processing and other technological advances.

The approach taken to modelling the AGN feedback in this chapter is based on a feedback technique commonly used in galaxy formation simulations (e.g., Di Matteo et al., 2005; Springel et al., 2005; Vogelsberger et al., 2013; Costa et al., 2014; Sijacki et al., 2015a) in which a fraction of the feedback is injected directly into the ambient ISM as thermal energy during every timestep. Alternative approaches have been used in the literature, with a popular choice being to store the feedback energy until it is able to heat neighbouring gas to some minimum critical temperature (e.g., Booth & Schaye, 2009; Schaye et al., 2010; Dubois et al., 2012; Schaye et al., 2015) in an attempt to negate the *over-cooling* problem discussed in section 5.3.4.1. However, despite this advantage, the method still requires re-tuning when the resolution is changed, as discussed in sections 5.1

and 5.4.6 with regard to comparing the OWLS and EAGLE simulations. An additional ingredient in my simulations is gas heating/cooling due to the AGN radiation field, which is often neglected in galaxy formation simulations, although similar processes have been included in recent cosmological simulations (Vogelsberger et al., 2013, 2014; Sijacki et al., 2015a) and could play an important role, particularly in heating gas local to the AGN during episodes of quasar mode feedback. Finally my treatment of the ISM equation of state follows the approach of Hobbs et al. (2013) in which gas only follows the polytropic equation of state once it has reached the temperature floor in equation (5.2). As illustrated in figure 5.2 this leads to very different temperature distributions at different resolutions, with most of the gas sitting on the temperature floor in the lowest resolution run but only a small fraction of the gas reaching the temperature floor in the highest resolution run. A common approach to avoid such disparate temperature distributions is to force all gas above some critical density (usually the star formation threshold) to follow a fixed effective equation of state (e.g., Springel & Hernquist, 2003; Schaye & Dalla Vecchia, 2008), which can ensure that the temperature distribution of the gas is consistent (although not necessarily physically correct) at different resolutions and thus aid in convergence.

### 5.4.6 Implications for cosmological simulations

A caveat to the results presented in this chapter is that our simulations do not include self-regulation of the AGN feedback, which plays an important role in galaxy evolution. Instead our simulations only model a single, 1 Myr long, Eddington limited AGN feedback event that is not linked to the gas content of the host galaxy. It may therefore be argued that our results on the numerical artefacts in AGN feedback efficiency do not have direct implications for cosmological simulations. In such simulations the system will undergo multiple feedback events over cosmological timescales. The rate at which a black hole injects energy into the host galaxy ISM is coupled to the gas accretion rate  $\dot{m}_{\text{accr}}$  through the equation

$$\dot{E} = \epsilon_{\text{BH}}(M_{\text{BH}}, \dot{m}_{\text{accr}}) \dot{m}_{\text{accr}} c^2 \quad (5.13)$$

where  $\epsilon_{\text{BH}}(M_{\text{BH}}, \dot{m}_{\text{accr}})$  is as defined in the introduction and can be a function of  $M_{\text{BH}}$  and  $\dot{m}_{\text{accr}}$ . For example Davis & Laor (2011) determined  $\epsilon_r$  in 80 quasars by using their bolometric luminosities and absolute accretion rates, calculated using thin accretion disk model spectral fits, finding a scaling with  $M_{\text{BH}}$  such that  $\epsilon_r = 0.089 M_8^{0.52}$ , where  $M_8$  is  $M_{\text{BH}}$  in units of  $10^8 M_{\odot}$ . Often, however,  $\epsilon_{\text{BH}}(M_{\text{BH}}, \dot{m}_{\text{accr}})$  is set to be a constant for simplicity.

The coupling of the AGN feedback to the gas content of the galaxy through equation (5.13) leads to self-regulation of the SMBH growth and feedback resulting in the *correct*  $\dot{E}$  such that the feedback driven outflows balance mass inflow. This, therefore, does not uniquely establish  $M_{\text{BH}}$  but rather the product  $\epsilon_{\text{BH}} M_{\text{BH}}$  (because  $\dot{m}_{\text{accr}}$  is usually limited to the Eddington accretion rate). To reproduce the observed black hole correlations, one *fixes* the value of  $\epsilon_{\text{BH}}$  (e.g., Booth & Schaye, 2009, 2010; Schaye et al., 2015). Further, provided that  $\epsilon_{\text{BH}}$  is set to a value within a suitable range, the observed SMBH scaling relations can be reproduced despite large differences in resolution and sub-grid prescriptions (e.g., Di Matteo et al., 2005; Springel et al., 2005; Sijacki et al., 2007; Booth & Schaye, 2009; Schaye et al., 2010, 2015), although some fine tuning may be required (see discussion in the introduction). A key element of self-regulation is that the physical properties of the galaxies such as the stellar mass (e.g. Di Matteo et al., 2005; Springel et al., 2005; Sijacki et al., 2007; Booth & Schaye, 2009, 2010) or AGN driven outflow rates (Schaye et al., 2015) do *not* depend upon the chosen value of  $\epsilon_{\text{BH}}$ . The result of this is that any dependencies that  $\epsilon_{\text{BH}}$  has on resolution would not effect the global properties of the galaxy due to self-regulation, although may lead to changes in the SMBH mass.

As an alternative to tuning efficiencies, a number of authors have attempted a more physically constrained approach to AGN feedback in which  $\epsilon_{\text{BH}}(M_{\text{BH}}, \dot{m}_{\text{accr}})$  is not a free parameter. For example, here I have followed the model of King (2005) in setting  $\epsilon_{\text{f}} = 0.05$ . Additionally, there is growing evidence that AGN should undergo separate *quasar* and *radio* modes of feedback (e.g., Churazov et al., 2005; Heinz et al., 2005; Croton et al., 2006; Ishibashi et al., 2014) depending on the Eddington ratio,  $\dot{m}_{\text{accr}}/\dot{M}_{\text{Edd}}$ , each with differing values for  $\epsilon_{\text{f}}$ . It has also been suggested that  $\epsilon_{\text{f}}$  depends upon  $\dot{m}_{\text{accr}}$  (e.g., Narayan & Yi, 1995; Mahadevan, 1997; Ciotti & Ostriker, 2001; Ciotti et al., 2009), with some cosmological simulations already attempting to include this additional physics (e.g., Sijacki et al., 2007, 2015b; Vogelsberger et al., 2014). Further, an effect that is not typically taken into account in galaxy formation simulations is that of the black hole spin, which can lead to variations in the radiative efficiency in the range of  $0.055 < \epsilon_{\text{f}} < 0.42$ .

I believe that the future of the field is in these more physically motivated approaches that would hopefully provide predictions constraining the physics of black hole growth and feedback. Despite our simulations lacking self-regulated AGN feedback our results are still important for such an approach. As discussed in the introduction some fine tuning of sub-grid feedback parameters can still be necessary when changing resolution (e.g., Schaye et al., 2015; Crain et al., 2015), sub-grid ISM models (e.g., Booth & Schaye, 2009) or cooling prescriptions (e.g., Sijacki et al., 2015b). When comparing results of

simulations with different AGN feedback physics to the observations, one must be acutely aware of numerical artefacts that may skew the interpretation of such comparisons.

Further, I note the potential dependence that  $\epsilon_{\text{BH}}$  has with the spatial resolution of the SMBH surroundings. If a simulation probes this parameter on sub-pc scales then the factor will determine the efficiency of BH wind production; on pc scales, the factor tells us something about the coupling between the wind and the surrounding ISM (perhaps about the clumpiness of the ISM); on scales of tens or hundreds of pc, the factor also encompasses the thermal effects (mostly cooling, but perhaps also heating by the AGN radiation field) of the gas surrounding the AGN. Therefore, simulations with different spatial resolution might be probing different processes that contribute to AGN feedback efficiency. This is an important point to consider when interpreting constrained values of  $\epsilon_{\text{BH}}$ .

## 5.5 Summary

In this chapter I have studied the effect of an Eddington-limited AGN outburst on a multiphase turbulent ISM, with particular focus on the effects of numerical resolution. In general, at higher numerical resolution, more dense clumps and also voids through which the feedback can escape are found. This reduces the efficiency with which AGN feedback clears out the host's gas. At low resolution this behaviour is lost as the feedback sweeps up essentially all the gas in its path. Additionally, depending on uncertain physical detail of the radiative cooling function for the gas heated by AGN feedback, numerical resolution also affects the amount of AGN feedback energy lost to radiation, and it is not possible to say whether it will increase or decrease the feedback efficiency in a general case. It is therefore plausible that resolution dependent effects alter the efficiency of AGN feedback in such a way that it is difficult to attach solid physical meaning to constrained values of  $\epsilon_{\text{BH}} = \epsilon_f \epsilon_r$ . I also note that although over cosmological timescales self-regulation results in consistent galaxy properties and outflow rates irrespective of the chosen feedback efficiency, our simulations illustrate certain physical processes, such as energy leakage through a clumpy ISM, that can only be modelled at sufficiently high resolution. Finally, in agreement with Schaye et al. (2015), I therefore suggest caution when trying to “invert” the results of cosmological simulations (usually tuned to fit observations) to learn about certain physical aspects of AGN feeding and feedback.

---

# 6

## Conclusions

*“Astronomy taught us our insignificance in  
Nature.”*

*Ralph Waldo Emerson*

The work presented in this thesis is largely concerned with trying to better understand how outflows from AGN interact with the ISM of the host galaxy. Given the potentially critical role feedback from SMBHs plays in shaping galaxy evolution, as deduced from the observed SMBH scaling relations (Kormendy & Ho, 2013), the details of this interaction are vitally important. As discussed in section 1.6.1.2, the  $M_{\text{BH}} - \sigma$  relation strongly suggests that it is the **momentum** of the AGN feedback which drives the observed correlation. However, in order to explain large scale outflows (e.g., Maiolino et al., 2012; Cicone et al., 2012, 2014, 2015; Carniani et al., 2015; Tombesi et al., 2015), it is also necessary to communicate the feedback **energy** to the ISM. This suggests that one requires a mechanism through which only the momentum is transferred to the bulk of the ISM, at least at small radii, and yet allows the energy to act at large radii, in order to explain large momentum boosts with factors of upto  $\sim 30$  (Faucher-Giguère et al., 2012; Faucher-Giguère & Quataert, 2012; Zubovas & King, 2012a).

Radially dependent cooling, such as IC scattering against the AGN radiation field, could provide an explanation, as has been suggested in the literature by King (2003, 2005) and Zubovas & King (2012a) and discussed in section 1.6.1.1. Although the effectiveness of such a cooling mechanism can depend sensitively upon the properties of the shocked outflow and the coupling of the protons and electrons within it (Faucher-Giguère & Quataert, 2012).

Chapter 3 attempts to constrain observational signatures for the wind shock when it is in either the momentum or energy driven phase. The hope is that observations of such features will inform us about the shock physics discussed in section 1.6.1.1 and thus aid us in understanding how the black hole scaling relations discussed in section 1.4 arise.

Given the uncertainty in the wind shock cooling, it may be that the outflow is essentially always in the energy driven regime. However, simple analytical arguments, such as those outlined in section 1.6.1.2, make it difficult to reconcile this with the observed  $M_{\text{BH}} - \sigma$  relation. Chapter 4 investigates the effect of an outflow impacting upon an inhomogeneous ISM (which can provide an alternative energy loss mechanism) opposed to a smooth gas distribution.

Finally, given the importance placed on simulations in trying to understand AGN feedback and, conversely, the importance placed upon AGN feedback in simulations, it is important to understand any limitations in the currently employed feedback prescriptions. To this end Chapter 5 presents an AGN feedback resolution study using the SPH technique.

## 6.1 Observational signatures of ultra-fast outflows

UFOs, launched due to accretion onto a SMBH, are expected to shock violently against the ambient ISM of the host galaxy. The subsequent evolution of the shock depends sensitively upon whether or not the wind shock is able to cool. In the 1T regime the dominant cooling mechanism is expected to be IC scattering of the AGN radiation field (King, 2003, 2005). However, it has been suggested that the wind properties are so extreme that weak coupling between the electrons and protons leads to a 2T plasma which renders IC processes ineffective (Faucher-Giguère & Quataert, 2012). In Chapter 3 I calculated the expected IC spectrum for each case, showing that they are distinguishable from each other and in the case of the 1T regime potentially observable.

Given the large light crossing time at the shock radius, I expect the timescale on which the IC component varies to be long compared to nuclear radiation variability. Further, the IC component should not suffer from obscuration by optically thick nuclear material (commonly associated with a torus). This means that the 1T IC component should be readily observable in type 2 AGN and yet has not been identified. On the other hand, the low luminosity of the 2T component and its location in the soft X-ray band make it potentially difficult to observe. Observations so far seem to rule out the 1T model, however, this is a tentative conclusion, which if correct, has significant implications for AGN feedback models as the cooling rate of the shocked wind plays a role in determining whether it is energy or just momentum which is communicated to the host ISM.

## 6.2 The role of the ambient ISM in determining feedback efficiency

Chapter 4 showed that the properties of the ISM can play an important role in determining how effective an AGN outflow can be at clearing out gas from a galaxy. As discussed in section 1.6.1.2, analytical models (e.g., Silk & Rees, 1998; King, 2003, 2005) often make the simplifying assumption of neglecting the multiphase and inhomogeneous nature of the ISM. It was found, from the simulations presented in Chapter 4, that there can be considerable differences between feedback in a homogeneous versus inhomogeneous gas distribution. In the case of a uniform gas distribution, *all* of the ambient gas is swept up into an outflowing shell. However, for the clumpy medium it was found that the gas flow becomes more sophisticated. High density material, which is resilient to the onslaught of the feedback, can continue to flow inwards while the low density gas can be swept up and



cleared out at high velocities. This results in a decoupling of mass and energy flows, with most of the mass flowing inwards in high density clumps while the energy escapes the system carried by the outflowing, low density phase.

The results of this section have a number of implications. In order to explain the high masses reached by SMBHs it is expected that most of the energy in AGN feedback needs to be lost from the system and not interact with the host ISM. The models of King (2003, 2005) invoke IC cooling in order to achieve this, however, Chapter 4 provides an alternative channel for energy loss, through the low density voids in the multiphase ISM. This result can potentially relieve any tension between the findings of Faucher-Giguère & Quataert (2012) and the implications discussed in section 1.6.1.2 that only the momentum of the outflow can be communicated to the (bulk of) the host ISM in order to be consistent with the  $M_{\text{BH}} - \sigma$  relation.

### 6.3 Simulating AGN feedback and the effects of resolution

AGN feedback is an important ingredient in cosmological and galaxy formation simulations, however, the same subgrid prescription is often used across a wide range in resolution. In Chapter 5 I therefore test the validity of this and investigate any numerical effects that arise due to changes in resolution.

The study highlighted two competing processes that affect the efficiency of AGN feedback. The first is radiative cooling, which is modelled with an optically thin cooling curve in the simulations presented. The cooling rate is sensitive to the gas temperature and density, both of which can be affected by resolution. The second process is that of being able to resolve structure in the ambient ISM, which is also a function of resolution. I found that the behaviour of and interplay between these processes can be quite complex and dependant upon how the feedback energy is distributed to the SPH particles. When injecting energy into a fixed gas mass, some general trends with resolution were observed. This is largely because fixing the mass essentially fixes the feedback temperature ( $\sim 10^9$  K) and so it is only the ability to resolve structure which affects the results. In general feedback became less effective at high resolution because high density gas is better resolved and hence the radiative cooling rate is increased. On the other hand, in the fixed neighbour runs there is no clear trend, with both the highest and lowest resolution runs retaining significant amounts of energy. Despite this, the properties of the outflows (and inflows)

where quite different.

I suggest that resolution impacts the efficiency of the AGN feedback and as such it can be difficult to disentangle physical efficiency from numerical efficiency in such simulations. However, I also highlight that the saving grace for cosmological simulations is the role of self-regulation. Linking the AGN feedback to the accretion rate leads to regulation of the black hole growth such that the final black hole mass will be proportional to  $\epsilon_{\text{BH}}^{-1}$  (Booth & Schaye, 2009, 2010). Further, other large scale properties of the galaxy are independent of the value of  $\epsilon_{\text{BH}}$ .

Finally I found that the structure of the ISM, which in itself can be dictated by the resolution, can affect the sites of star formation. In particular, AGN triggered star formation could potentially occur in high density clumps, which when enveloped in the hot expanding feedback bubble, are pressurised.

## 6.4 Future work

A very important question that remains unanswered is whether or not the AGN driven outflows are in the momentum or energy conserving regime or some combination of the two. This requires further observational studies of active galaxies to see if any of the reverse wind-shock features discussed in Chapter 3 or forward shock features presented by Nims et al. (2015) exist. Observations of large scale AGN driven outflows in conjunction with SMBH mass measurements could also shed light on how the feedback interacts with the host ISM. In the multiphase ISM picture presented in Chapters 4 and 5, I propose that the SMBH can affect the host bulge on large scales even if it is below its  $M_{\text{BH}} - \sigma$  mass. This could be confirmed if one observes large scale outflows in a galaxy sitting below the  $M_{\text{BH}} - \sigma$  relation.

With regard to improving the simulations presented in this thesis, there are a number of further processes that can be included. Star formation and SMBH growth are intricately linked, however, it is not completely clear how these processes interact and so the inclusion of star formation and stellar feedback in my future simulations is potentially important. It has been proposed that competition for cold gas between star formation and black hole growth can be determined by the properties of the host galaxy (Nayakshin et al., 2009b) and so feedback from the dominant component may quench the growth of the other. As discussed by Nayakshin (2014) and in Section 5.4.4, the density threshold for star formation could play a crucial role in establishing the  $M_{\text{BH}} - \sigma$  relation in a multiphase medium. In setting an upper limit for the density of gas clouds to exist, one also sets the

necessary limit at which the feedback from a SMBH is able to clear out such clouds and hence clear out all gas from the host galaxy. Further to this, stellar feedback could act to disrupt high density clouds and feed new material into the AGN driven outflow. While this would help in the removal of gas from the host, it may also affect the radiative cooling of the gas by introducing cold, enriched and or higher density material into the outflow.

The currently employed radiative cooling mechanism could also be improved. As mentioned in Section 5, the cooling function assumes that the gas is optically thin, however, this may not be the case for high density clumps. As such, the cooling/heating rate for these clumps is likely to be incorrect. With regard to heating against the AGN radiation field, a simple approach would be to have a density dependant heating function. A straight forward example has already been employed by Sijacki et al. (2015b), who have a fixed density threshold above which heating due to the AGN radiation field is neglected. A more sophisticated approach could include an estimate for the optical depth of the gas and a heating rate that is a decreasing function of the optical depth. Further to this, the current cooling functions employed (Sazonov et al., 2005; Mashchenko et al., 2008) assume all of the gas is enriched to have solar metallicity. While it is believed that AGN typically have super-solar abundances (e.g., Storch-Bergmann et al., 1998; Hamann et al., 2002; Groves et al., 2006), it is not necessarily uniformly distributed throughout the bulge ISM and can depend upon enrichment from a stellar component. Indeed the importance of chemical enrichment from supernova has already been shown when trying to form the fast cold molecular outflows discussed in section 1.6 (Costa et al., 2015).

Finally improvements with regard to the AGN feedback prescription may be necessary. The virtual particle scheme (Nayakshin et al., 2009a; Nayakshin & Power, 2010; Zubovas & Nayakshin, 2012) discussed in section 2.7 could provide a more realistic model of how the AGN feedback interacts with the host, at least in respect of a truly isotropic and spatially unrestrained outflow model. It would also be interesting to introduce self-consistent feedback i.e. link the feedback rate to the accretion rate. Although in order to do this further sub-grid models and assumptions will need to be made as it is not possible to simultaneously resolve the accretion onto the black hole on the scales at which the feedback is produced and also model the large scale outflow. Given the discussion in Section 4.5.2 regarding feeding black holes with high density clumps, such a self-consistent feedback loop could provide interesting insight into the feeding cycle of SMBHs. Perhaps allowing one to address the question of continuous feeding versus intermittent feeding in which feedback may completely shut off the SMBHs gas supply for a period of time. Finally this may also allow a detailed study of feedback induced feeding

as proposed by Dehnen & King (2013).

## 6.5 Final remarks

There are clearly still a number of open questions in the field of AGN feedback and in understanding how the observed scaling relations arise. An apparently fundamental question that still remains unanswered is how much time do the outflows spend in the momentum and energy driven regimes? This question is only likely to be answered through a strong collaborative effort between observers and theorists. However, what is already clear is that the properties of the  $M_{\text{BH}} - \sigma$  relation combined with the incredibly energetic large scale outflows suggest that a mix of momentum and energy driving is required.

Simulations also have an important role to play in trying to understand the AGN outflow - host galaxy interaction, however, they still rely heavily upon sub-grid physics, which often has to be tuned to match certain observations. This is a scenario that is unlikely to improve with any great gusto, although a combination of simulations performed across a range of resolutions can hopefully help to bridge the gap between the processes driving the feedback on small and large scales. Throughout such work it would, however, be important to ensure that one does not interpret numerical artefacts as physical processes!

In producing this thesis I hope that I have provided some new insights into the processes occurring in galaxies during AGN feedback episodes. I hope that the observational signatures described in Chapter 3 will aid observers in answering the question over momentum and energy driving. Finally the results in Chapters 4 and 5 indicate that AGN feedback is not necessarily purely negative. The multiphase nature of the ISM appears to provide some resilience against the feedback, allowing the galaxy to form stars and grow. This resilience may also explain the apparently weak coupling between AGN outflows and the host galaxy ISM. Therefore I suggest that the extent to which AGN feedback destroys galaxies is far less than originally thought.

---

# References

- Alexander, D. M. and Hickox, R. C.: 2012, *NewAR* **56**, 93
- Alexander, R. D., Armitage, P. J., Cuadra, J., and Begelman, M. C.: 2008, *The Astrophysical Journal* **674(2)**, 927
- Allen, L. R., Anderson, B., Conway, R. G., et al.: 1962, *Monthly Notices of the Royal Astronomical Society* **124(6)**, 477
- Anderson, R. W.: 2015, *The Cosmic Compendium: Black Holes*
- Anderson, W.: 1929, *Zeitschrift für Physik* **56(11-12)**, 851
- Angulo, R. E., Springel, V., White, S. D. M., et al.: 2012, *MNRAS* **426**, 2046
- Antonucci, R.: 1993, *ARA&A* **31**, 473
- Arav, N., Borguet, B., Chamberlain, C., Edmonds, D., and Danforth, C.: 2013, *MNRAS* **436**, 3286
- Arons, J., Kulsrud, R. M., and Ostriker, J. P.: 1975, *ApJ* **198**, 687
- Baade, W. and Minkowski, R.: 1954, *The Astrophysical Journal* **119**, 206
- Baes, M., Buyle, P., Hau, G. K. T., and Dejonghe, H.: 2003, *MNRAS* **341**, L44
- Baldry, I. K., Driver, S. P., Loveday, J., et al.: 2012, *MNRAS* **421**, 621
- Balick, B. and Brown, R. L.: 1974, *The Astrophysical Journal* **194**, 265
- Balsara, D. S.: 1989, *Ph.D. thesis*, , Univ. Illinois at Urbana-Champaign, (1989)
- Bardeen, J. M., Press, W. H., and Teukolsky, S. A.: 1972, *ApJ* **178**, 347
- Barnes, J. and Hut, P.: 1986, *Nature* **324**, 446
- Barth, A. J., Greene, J. E., and Ho, L. C.: 2005, *ApJ* **619**, L151
- Barthel, P. D.: 1989, *ApJ* **336**, 606

- 
- Batcheldor, D.: 2010, *ApJ* **711**, L108
- Bate, M. R.: 2009a, *MNRAS* **392**, 590
- Bate, M. R.: 2009b, *MNRAS* **392**, 590
- Bate, M. R.: 2012, *MNRAS* **419**, 3115
- Bate, M. R., Bonnell, I. A., and Bromm, V.: 2003, *MNRAS* **339**, 577
- Bate, M. R. and Burkert, A.: 1997, *MNRAS* **288**, 1060
- Bautista, M. A., Dunn, J. P., Arav, N., et al.: 2010, *ApJ* **713**, 25
- Beckmann, V. and Shrader, C.: 2012, in *Proceedings of "An INTEGRAL view of the high-energy sky (the first 10 years)" The AGN phenomenon: open issues 10*
- Begelman, M. C. and Rees, M. J.: 1978, *MNRAS* **185**, 847
- Begelman, M. C., Volonteri, M., and Rees, M. J.: 2006, *MNRAS* **370**, 289
- Beifiori, A., Courteau, S., Corsini, E. M., and Zhu, Y.: 2012, *MNRAS* **419**, 2497
- Belmonte, J. A.: 2009, in J. Rubiño-Martín, J. Belmonte, F. Prada, and A. Alberdi (eds.), *Cosmology Across Cultures*, Vol. 409 of *Astronomical Society of the Pacific Conference Series*, p. 116
- Benson, A. J., Bower, R. G., Frenk, C. S., et al.: 2003, *ApJ* **599**, 38
- Binney, J.: 2004, *MNRAS* **347**, 1093
- Binney, J. and Tremaine, S.: 2008, *Galactic Dynamics: Second Edition*, Princeton University Press
- Bisnovatyi-Kogan, G. S., Zel'dovich, Y. B., and Novikov, I. D.: 1967, *Soviet Ast.* **11**, 419
- Bogdán, Á., Forman, W. R., Zhuravleva, I., et al.: 2012, *ApJ* **753**, 140
- Böker, T., Falcón-Barroso, J., Schinnerer, E., Knapen, J. H., and Ryder, S.: 2008, *AJ* **135**, 479
- Bombaci, I.: 1996, *A&A* **305**, 871
- Bondi, H.: 1952, *MNRAS* **112**, 195
-

- 
- Bongiorno, A., Maiolino, R., Brusa, M., et al.: 2014, *MNRAS* **443**, 2077
- Booth, C. M. and Schaye, J.: 2009, *MNRAS* **398**, 53
- Booth, C. M. and Schaye, J.: 2010, *MNRAS* **405**, L1
- Bourne, M. A. and Nayakshin, S.: 2013, *MNRAS* **436**, 2346
- Bourne, M. A., Nayakshin, S., and Hobbs, A.: 2014, *MNRAS* **441**, 3055
- Bower, R. G., Benson, A. J., Malbon, R., et al.: 2006, *MNRAS* **370**, 645
- Bower, R. G., McLeish, T. C. B., Tanner, B. K., et al.: 2014, *Royal Society of London Proceedings Series A* **470**, 40025
- Bromm, V. and Loeb, A.: 2003, *ApJ* **596**, 34
- Burbidge, E. M. and Burbidge, G.: 1962
- Burbidge, G. R.: 1956, *ApJ* **124**, 416
- Burbidge, G. R.: 1959, *ApJ* **129**, 849
- Burbidge, G. R.: 1961, *Nature* **190**, 1053
- Burbidge, G. R., Burbidge, E. M., and Sandage, A. R.: 1963, *Reviews of Modern Physics* **35**, 947
- Cameron, A. G. W.: 1962, *Nature* **194**, 963
- Canalizo, G., Wold, M., Hiner, K. D., et al.: 2012, *ApJ* **760**, 38
- Cano-Díaz, M., Maiolino, R., Marconi, A., et al.: 2012, *A&A* **537**, L8
- Cappellari, M., Verolme, E. K., van der Marel, R. P., et al.: 2002, *ApJ* **578**, 787
- Carniani, S., Marconi, A., Maiolino, R., et al.: 2015, *A&A* **580**, A102
- Carter, B.: 1971, *Physical Review Letters* **26(6)**, 331
- Casares, J.: 2007, in V. Karas and G. Matt (eds.), *IAU Symposium*, Vol. 238 of *IAU Symposium*, pp 3–12
- Chadwick, J.: 1932a, in *Proceedings of the Royal Society of London A: Mathematical, Physical and Engineering Sciences*, Vol. 136, pp 692–708, The Royal Society
-

- 
- Chadwick, J.: 1932b, *Nature* **129(3252)**, 312
- Chandrasekhar, S.: 1931a, *Monthly Notices of the Royal Astronomical Society* **91**, 456
- Chandrasekhar, S.: 1931b, *The Astrophysical Journal* **74**, 81
- Chandrasekhar, S.: 1932, *Zeitschrift fur Astrophysik* **5**, 321
- Chandrasekhar, S.: 1935, *Monthly Notices of the Royal Astronomical Society* **95**, 207
- Churazov, E., Sazonov, S., Sunyaev, R., et al.: 2005, *MNRAS* **363**, L91
- Cicone, C., Feruglio, C., Maiolino, R., et al.: 2012, *A&A* **543**, A99
- Cicone, C., Maiolino, R., Gallerani, S., et al.: 2015, *A&A* **574**, A14
- Cicone, C., Maiolino, R., Sturm, E., et al.: 2014, *A&A* **562**, A21
- Ciotti, L. and Ostriker, J. P.: 1997, *ApJ* **487**, L105
- Ciotti, L. and Ostriker, J. P.: 2001, *ApJ* **551**, 131
- Ciotti, L. and Ostriker, J. P.: 2007, *ApJ* **665**, 1038
- Ciotti, L., Ostriker, J. P., and Proga, D.: 2009, *ApJ* **699**, 89
- Colless, M., Dalton, G., Maddox, S., et al.: 2001, *MNRAS* **328**, 1039
- Costa, T., Sijacki, D., and Haehnelt, M. G.: 2014, *MNRAS* **444**, 2355
- Costa, T., Sijacki, D., and Haehnelt, M. G.: 2015, *MNRAS* **448**, L30
- Courant, R., Friedrichs, K., and Lewy, H.: 1928, *Mathematische Annalen* **100**, 32
- Crain, R. A., Schaye, J., Bower, R. G., et al.: 2015, *MNRAS* **450**, 1937
- Cresci, G., Mainieri, V., Brusa, M., et al.: 2015, *ApJ* **799**, 82
- Cretton, N. and van den Bosch, F. C.: 1999, *ApJ* **514**, 704
- Croton, D. J., Springel, V., White, S. D. M., et al.: 2006, *MNRAS* **365**, 11
- Crummy, J., Fabian, A. C., Gallo, L., and Ross, R. R.: 2006, *MNRAS* **365**, 1067
- Cullen, L. and Dehnen, W.: 2010, *MNRAS* **408**, 669
-



- 
- Curtis, H. D.: 1917, *PASP* **29**, 206
- Dalla Vecchia, C. and Schaye, J.: 2012, *MNRAS* **426**, 140
- Davis, S. W. and Laor, A.: 2011, *ApJ* **728**, 98
- de Francesco, G., Capetti, A., and Marconi, A.: 2008, *A&A* **479**, 355
- Decarli, R., Falomo, R., Treves, A., et al.: 2010, *MNRAS* **402**, 2453
- Dehnen, W. and Aly, H.: 2012, *MNRAS* **425**, 1068
- Dehnen, W. and King, A.: 2013, *ApJ* **777**, L28
- Dehnen, W. and Read, J. I.: 2011, *European Physical Journal Plus* **126**, 55
- Di Matteo, T., Colberg, J., Springel, V., Hernquist, L., and Sijacki, D.: 2008, *ApJ* **676**, 33
- Di Matteo, T., Springel, V., and Hernquist, L.: 2005, *Nature* **433**, 604
- Dressler, A. and Richstone, D. O.: 1990, *ApJ* **348**, 120
- Dubinski, J., Narayan, R., and Phillips, T. G.: 1995, *ApJ* **448**, 226
- Dubois, Y., Devriendt, J., Slyz, A., and Teyssier, R.: 2012, *MNRAS* **420**, 2662
- Dunn, J. P., Bautista, M., Arav, N., et al.: 2010, *ApJ* **709**, 611
- Ebisuzaki, T., Makino, J., Tsuru, T. G., et al.: 2001, *ApJ* **562**, L19
- Eddington, A. S.: 1924, *Nature* **113**, 192
- Edge, D. O., Shakeshaft, J. R., McAdam, W. B., Baldwin, J. E., and Archer, S.: 1959, *MmRAS* **68**, 37
- Einstein, A.: 1915, *Sitzungsberichte der Königlich Preußischen Akademie der Wissenschaften (Berlin)*, Seite 844-847. pp 844–847
- Elbaz, D., Jahnke, K., Pantin, E., Le Borgne, D., and Letawe, G.: 2009, *A&A* **507**, 1359
- Fabian, A. C.: 1999, *MNRAS* **308**, L39
- Fabian, A. C.: 2012, *ARA&A* **50**, 455
- Fabjan, D., Borgani, S., Tornatore, L., et al.: 2010, *MNRAS* **401**, 1670
-

- 
- Falcke, H., Melia, F., and Agol, E.: 2000, *ApJ* **528**, L13
- Fan, X., Narayanan, V. K., Lupton, R. H., et al.: 2001, *AJ* **122**, 2833
- Fan, X., White, R. L., Davis, M., et al.: 2000, *AJ* **120**, 1167
- Fanaroff, B. L. and Riley, J. M.: 1974, *MNRAS* **167**, 31P
- Fanidakis, N., Baugh, C. M., Benson, A. J., et al.: 2012, *MNRAS* **419**, 2797
- Fath, E. A.: 1909, *Publications of the Astronomical Society of the Pacific* **21(126)**, 138
- Faucher-Giguère, C.-A. and Quataert, E.: 2012, *MNRAS* **425**, 605
- Faucher-Giguère, C.-A., Quataert, E., and Murray, N.: 2012, *MNRAS* **420**, 1347
- Federrath, C., Klessen, R. S., and Schmidt, W.: 2008, *ApJ* **688**, L79
- Federrath, C., Klessen, R. S., and Schmidt, W.: 2009, *ApJ* **692**, 364
- Federrath, C., Roman-Duval, J., Klessen, R. S., Schmidt, W., and Mac Low, M.-M.: 2010, *A&A* **512**, A81
- Ferrarese, L.: 2002, *ApJ* **578**, 90
- Ferrarese, L. and Ford, H.: 2005, *Space Sci. Rev.* **116**, 523
- Ferrarese, L., Ford, H. C., and Jaffe, W.: 1996, *ApJ* **470**, 444
- Ferrarese, L. and Merritt, D.: 2000, *ApJ* **539**, L9
- Ferré-Mateu, A., Mezcua, M., Trujillo, I., Balcells, M., and van den Bosch, R. C. E.: 2015, *ApJ* **808**, 79
- Feruglio, C., Maiolino, R., Piconcelli, E., et al.: 2010, *A&A* **518**, L155
- Field, G. B.: 1964, *The Astrophysical Journal* **140**, 1434
- Finkelstein, D.: 1958, *Phys. Rev.* **110**, 965
- Fish, V. L., Doeleman, S. S., Beaudoin, C., et al.: 2011, *ApJ* **727**, L36
- Fish, V. L., Johnson, M. D., Lu, R.-S., et al.: 2014, *ApJ* **795**, 134

- 
- Ford, H. C., Harms, R. J., Tsvetanov, Z. I., et al.: 1994, *The Astrophysical Journal* **435**, L27
- Freitag, M., Rasio, F. A., and Baumgardt, H.: 2006, *MNRAS* **368**, 121
- Frenkel, J.: 1928, *Zeitschrift für Physik* **50(3-4)**, 234
- Fukumura, K., Tombesi, F., Kazanas, D., et al.: 2015, *ApJ* **805**, 17
- Gabor, J. M. and Bournaud, F.: 2014, *MNRAS* **441**, 1615
- Gaibler, V., Khochfar, S., Krause, M., and Silk, J.: 2012, *MNRAS* **425**, 438
- Gallo, L. C., MacMackin, C., Vasudevan, R., et al.: 2013, *MNRAS* **433**, 421
- Gaskell, C. M.: 2011, in G. Alecian, K. Belkacem, R. Samadi, and D. Valls-Gabaud (eds.), *SF2A-2011: Proceedings of the Annual meeting of the French Society of Astronomy and Astrophysics*, pp 577–582
- Gebhardt, K., Bender, R., Bower, G., et al.: 2000, *ApJ* **539**, L13
- Geller, M. J. and Huchra, J. P.: 1989, *Science* **246**, 897
- Genzel, R., Förster Schreiber, N. M., Rosario, D., et al.: 2014, *ApJ* **796**, 7
- Ghez, A. M., Salim, S., Hornstein, S. D., et al.: 2005, *ApJ* **620**, 744
- Ghez, A. M., Salim, S., Weinberg, N. N., et al.: 2008, *ApJ* **689**, 1044
- Gibson, R. R., Jiang, L., Brandt, W. N., et al.: 2009, *ApJ* **692**, 758
- Gierliński, M. and Done, C.: 2004, *MNRAS* **349**, L7
- Gillessen, S., Eisenhauer, F., Trippe, S., et al.: 2009, *ApJ* **692**, 1075
- Gingold, R. A. and Monaghan, J. J.: 1977, *MNRAS* **181**, 375
- Gnedin, N. Y.: 1996, *ApJ* **456**, 1
- Graham, A. W.: 2016, *Galactic Bulges* **418**, 263
- Greenstein, J. L.: 1963, *Nature* **197**, 1041
- Groves, B. A., Heckman, T. M., and Kauffmann, G.: 2006, *MNRAS* **371**, 1559

- 
- Guilbert, P. W. and Rees, M. J.: 1988, *MNRAS* **233**, 475
- Gültekin, K., Richstone, D. O., Gebhardt, K., et al.: 2011, *ApJ* **741**, 38
- Gültekin, K., Richstone, D. O., Gebhardt, K., et al.: 2009, *ApJ* **698**, 198
- Gürkan, M. A., Fregeau, J. M., and Rasio, F. A.: 2006, *ApJ* **640**, L39
- Haardt, F. and Maraschi, L.: 1993, *ApJ* **413**, 507
- Haehnelt, M. G. and Rees, M. J.: 1993, *MNRAS* **263**, 168
- Hamann, F., Korista, K. T., Ferland, G. J., Warner, C., and Baldwin, J.: 2002, *ApJ* **564**, 592
- Häring, N. and Rix, H.-W.: 2004, *ApJ* **604**, L89
- Harms, R. J., Ford, H. C., Tsvetanov, Z. I., et al.: 1994, *The Astrophysical Journal* **435**, L35
- Harper-Clark, E. and Murray, N.: 2009, *ApJ* **693**, 1696
- Harrison, C. M., Alexander, D. M., Mullaney, J. R., and Swinbank, A. M.: 2014, *MNRAS* **441**, 3306
- Harrower, G.: 1960, *The Astrophysical Journal* **132**, 22
- Hazard, C., Mackey, M., and Shimmins, A.: 1963, *Nature* **197(487)**, 1037
- Hazard, C., Morton, D. C., Terlevich, R., and McMahon, R.: 1984, *ApJ* **282**, 33
- Heinz, S., Merloni, A., Di Matteo, T., and Sunyaev, R.: 2005, *Ap&SS* **300**, 15
- Hernquist, L.: 1990, *ApJ* **356**, 359
- Herrnstein, J. R., Moran, J. M., Greenhill, L. J., and Trotter, A. S.: 2005, *ApJ* **629**, 719
- Hewish, A., Bell, S. J., Pilkington, J., Scott, P., and Collins, R.: 1968, *Nature* **217(5130)**, 709
- Hirschmann, M., Khochfar, S., Burkert, A., et al.: 2010, *MNRAS* **407**, 1016
- Ho, L.: 1999a, in S. K. Chakrabarti (ed.), *Observational Evidence for the Black Holes in the Universe*, Vol. 234 of *Astrophysics and Space Science Library*, p. 157

- 
- Ho, L.: 1999b, in S. K. Chakrabarti (ed.), *Observational Evidence for the Black Holes in the Universe*, Vol. 234 of *Astrophysics and Space Science Library*, p. 157
- Hobbs, A., Nayakshin, S., Power, C., and King, A.: 2011, *MNRAS* **413**, 2633
- Hobbs, A., Read, J., Power, C., and Cole, D.: 2013, *MNRAS* **434**, 1849
- Holmberg, E.: 1941, *ApJ* **94**, 385
- Hopkins, P. F., Hernquist, L., Cox, T. J., Robertson, B., and Springel, V.: 2006, *ApJS* **163**, 50
- Hoyle, F. and Fowler, W. A.: 1962, *Monthly Notices of the Royal Astronomical Society* **125**(2), 169
- Hoyle, F. and Fowler, W. A.: 1963, *Nature* **197**, 533
- Hoyle, F. and Tayler, R. J.: 1964, *Nature* **203**, 1108
- Hubble, E.: 1929, *Proceedings of the National Academy of Science* **15**, 168
- Hubble, E. P.: 1925, *ApJ* **62**, 409
- Ishibashi, W., Auger, M. W., Zhang, D., and Fabian, A. C.: 2014, *MNRAS* **443**, 1339
- Israel, W.: 1967, *Physical review* **164**(5), 1776
- Jahnke, K. and Macciò, A. V.: 2011, *ApJ* **734**, 92
- Jüttner, F.: 1911, *Annalen der Physik* **339**(5), 856
- Katz, N.: 1992, *ApJ* **391**, 502
- Katz, N. and Gunn, J. E.: 1991, *ApJ* **377**, 365
- Katz, N., Weinberg, D. H., and Hernquist, L.: 1996, *ApJS* **105**, 19
- Kernighan, B. W. and Plauger, P. J.: 1978, *The elements of programming style*, by Kernighan, Brian W.; Plauger, P. J. New York: McGraw-Hill, c1978. 1
- Kerr, R.: 1963, *Physical review letters* (**11**), 237
- King, A.: 2003, *ApJ* **596**, L27
- King, A.: 2005, *ApJ* **635**, L121

- 
- King, A. and Pounds, K.: 2015, *Annual Review of Astronomy and Astrophysics* **53**(1), null
- King, A. R.: 2010, *MNRAS* **402**, 1516
- King, A. R. and Pounds, K. A.: 2003, *MNRAS* **345**, 657
- King, A. R. and Pringle, J. E.: 2006, *MNRAS* **373**, L90
- Knigge, C., Scaringi, S., Goad, M. R., and Cottis, C. E.: 2008, *MNRAS* **386**, 1426
- Kormendy, J.: 1993, in J. Beckman, L. Colina, and H. Netzer (eds.), *The Nearest Active Galaxies*, pp 197–218
- Kormendy, J. and Bender, R.: 2011, *Nature* **469**, 377
- Kormendy, J., Bender, R., and Cornell, M. E.: 2011, *Nature* **469**, 374
- Kormendy, J., Bender, R., Magorrian, J., et al.: 1997, *ApJ* **482**, L139
- Kormendy, J. and Gebhardt, K.: 2001, in J. C. Wheeler & H. Martel (ed.), *20th Texas Symposium on relativistic astrophysics*, Vol. 586 of *American Institute of Physics Conference Series*, pp 363–381
- Kormendy, J. and Ho, L. C.: 2013, *ARA&A* **51**, 511
- Kormendy, J. and Kennicutt, Jr., R. C.: 2004, *ARA&A* **42**, 603
- Kormendy, J. and Richstone, D.: 1995, *ARA&A* **33**, 581
- Koushiappas, S. M., Bullock, J. S., and Dekel, A.: 2004, *MNRAS* **354**, 292
- Kravtsov, A. V.: 2003, *ApJ* **590**, L1
- Landau, L. D.: 1932, *Phys. Z. Sowjetunion* **1**(285), 152
- Le Brun, A. M. C., McCarthy, I. G., Schaye, J., and Ponman, T. J.: 2014, *MNRAS* **441**, 1270
- Lemaître, G.: 1933, *Annales de la Société Scientifique de Bruxelles* **53**, 51
- Liu, G., Zakamska, N. L., Greene, J. E., Nesvadba, N. P. H., and Liu, X.: 2013, *MNRAS* **436**, 2576
-

- 
- Lodato, G. and Natarajan, P.: 2006, *MNRAS* **371**, 1813
- Longair, M. S. . S. .: 2006, *The cosmic century : a history of astrophysics and cosmology*, Cambridge University Press
- Lucy, L. B.: 1977, *AJ* **82**, 1013
- Lynden-Bell, D.: 1969, *Nature* **223(5207)**, 690
- Lynden-Bell, D. and Rees, M.: 1971, *Monthly Notices of the Royal Astronomical Society* **152(4)**, 461
- Madau, P. and Rees, M. J.: 2001, *ApJ* **551**, L27
- Magorrian, J., Tremaine, S., Richstone, D., et al.: 1998, *AJ* **115**, 2285
- Mahadevan, R.: 1997, *ApJ* **477**, 585
- Maiolino, R., Gallerani, S., Neri, R., et al.: 2012, *MNRAS* **425**, L66
- Makino, J.: 1991, *PASJ* **43**, 859
- Marconi, A. and Hunt, L. K.: 2003, *ApJ* **589**, L21
- Markarian, B. E.: 1967, *Astrofizika* **3**, 55
- Maron, J. L. and Howes, G. G.: 2003, *ApJ* **595**, 564
- Marquis de Laplace, P.-S.: 1798, *Exposition du systeme du monde*
- Mashchenko, S., Wadsley, J., and Couchman, H. M. P.: 2008, *Science* **319**, 174
- Matthews, T. A. and Sandage, A. R.: 1963, *The Astrophysical Journal* **138**, 30
- Maxwell, J. C.: 1860, *The London, Edinburgh, and Dublin Philosophical Magazine and Journal of Science* **20(130)**, 21
- McCarthy, I. G., Schaye, J., Bower, R. G., et al.: 2011, *MNRAS* **412**, 1965
- McCarthy, I. G., Schaye, J., Ponman, T. J., et al.: 2010, *MNRAS* **406**, 822
- McClintock, J. E. and Remillard, R. A.: 2006, *Black hole binaries*, pp 157–213
- McConnell, N. J. and Ma, C.-P.: 2013, *ApJ* **764**, 184
-

- 
- McCormmach, R.: 1968, *The British Journal for the history of Science* **4(02)**, 126
- McKee, C. F. and Cowie, L. L.: 1975, *ApJ* **195**, 715
- McKee, C. F. and Ostriker, J. P.: 1977, *ApJ* **218**, 148
- McLure, R. J. and Dunlop, J. S.: 2002, *MNRAS* **331**, 795
- McNamara, B. R. and Nulsen, P. E. J.: 2007, *ARA&A* **45**, 117
- McQuillin, R. C. and McLaughlin, D. E.: 2012, *MNRAS* **423**, 2162
- Merritt, D. and Ferrarese, L.: 2001, *MNRAS* **320**, L30
- Michell, J.: 1784, *Royal Society of London Philosophical Transactions Series I* **74**, 35
- Minkowski, R.: 1960, *ApJ* **132**, 908
- Miyoshi, M., Moran, J., Herrnstein, J., et al.: 1995, *Nature* **373**, 127
- Mo, H., van den Bosch, F. C., and White, S.: 2010, *Galaxy Formation and Evolution*
- Monaghan, J.: 1997, *Journal of Computational Physics* **136(2)**, 298
- Monaghan, J. J.: 2012, *Annual Review of Fluid Mechanics* **44**, 323
- Monaghan, J. J. and Lattanzio, J. C.: 1985, *A&A* **149**, 135
- Montgomery, C., Orchiston, W., and Whittingham, I.: 2009, *Journal of Astronomical History and Heritage* **12**, 90
- Mortlock, D. J., Warren, S. J., Venemans, B. P., et al.: 2011, *Nature* **474**, 616
- Murante, G., Monaco, P., Giovalli, M., Borgani, S., and Diaferio, A.: 2010, *MNRAS* **405**, 1491
- Murray, N., Quataert, E., and Thompson, T. A.: 2005, *ApJ* **618**, 569
- Mushotzky, R. F., Done, C., and Pounds, K. A.: 1993, *ARA&A* **31**, 717
- Nagirner, D. I. and Poutanen, J.: 1994, *Single Compton scattering*
- Nandra, K. and Pounds, K. A.: 1994, *MNRAS* **268**, 405
- Narayan, R. and Yi, I.: 1995, *ApJ* **452**, 710
-



- 
- Nayakshin, S.: 2014, *MNRAS* **437**, 2404
- Nayakshin, S., Cha, S.-H., and Hobbs, A.: 2009a, *MNRAS* **397**, 1314
- Nayakshin, S. and Melia, F.: 1998, *ApJS* **114**, 269
- Nayakshin, S. and Power, C.: 2010, *MNRAS* **402**, 789
- Nayakshin, S., Wilkinson, M. I., and King, A.: 2009b, *MNRAS* **398**, L54
- Nayakshin, S. and Zubovas, K.: 2012, *MNRAS* **427**, 372
- Ne’eman, Y.: 1965, *ApJ* **141**, 1303
- Newman, E. T., Couch, E., Chinnapared, K., et al.: 1965, *Journal of mathematical physics* **6(6)**, 918
- Nims, J., Quataert, E., and Faucher-Giguère, C.-A.: 2015, *MNRAS* **447**, 3612
- Novikov, I. D.: 1965, *Soviet Ast.* **8**, 857
- Nowak, N., Saglia, R. P., Thomas, J., et al.: 2008, *MNRAS* **391**, 1629
- Oke, J.: 1963, *Nature* **197**, 1040
- Oke, J. B.: 1967, *ApJ* **147**, 901
- Oppenheimer, B. D. and Davé, R.: 2006, *MNRAS* **373**, 1265
- Oppenheimer, B. D., Davé, R., Kereš, D., et al.: 2010, *MNRAS* **406**, 2325
- Oppenheimer, J. R. and Snyder, H.: 1939, *Physical Review* **56(5)**, 455
- Oppenheimer, J. R. and Volkoff, G. M.: 1939, *Physical Review* **55(4)**, 374
- Orosz, J. A., McClintock, J. E., Aufdenberg, J. P., et al.: 2011, *ApJ* **742**, 84
- Peng, C. Y.: 2007, *ApJ* **671**, 1098
- Peng, C. Y., Impey, C. D., Ho, L. C., Barton, E. J., and Rix, H.-W.: 2006a, *ApJ* **640**, 114
- Peng, C. Y., Impey, C. D., Rix, H.-W., et al.: 2006b, *ApJ* **649**, 616
- Penrose, R.: 1965, *Phys. Rev. Lett.* **14**, 57
-

- 
- Penzias, A. A. and Wilson, R. W.: 1965, *ApJ* **142**, 419
- Peterson, B. M.: 2014, *Space Sci. Rev.* **183**, 253
- Pilkington, J., Hewish, A., Bell, S., and Cole, T.: 1968, *Nature* **218**, 126
- Planck Collaboration, Adam, R., Ade, P. A. R., et al.: 2015, *ArXiv e-prints*
- Planelles, S., Borgani, S., Dolag, K., et al.: 2013, *MNRAS* **431**, 1487
- Porquet, D., Reeves, J. N., O'Brien, P., and Brinkmann, W.: 2004, *A&A* **422**, 85
- Portegies Zwart, S. F., Baumgardt, H., Hut, P., Makino, J., and McMillan, S. L. W.: 2004, *Nature* **428**, 724
- Pounds, K. A., King, A. R., Page, K. L., and O'Brien, P. T.: 2003a, *MNRAS* **346**, 1025
- Pounds, K. A., Nandra, K., Stewart, G. C., George, I. M., and Fabian, A. C.: 1990, *Nature* **344**, 132
- Pounds, K. A. and Reeves, J. N.: 2009, *MNRAS* **397**, 249
- Pounds, K. A., Reeves, J. N., King, A. R., et al.: 2003b, *MNRAS* **345**, 705
- Pounds, K. A. and Vaughan, S.: 2011, *MNRAS* **413**, 1251
- Power, C., Navarro, J. F., Jenkins, A., et al.: 2003, *MNRAS* **338**, 14
- Price, D. J.: 2008, *Journal of Computational Physics* **227**, 10040
- Price, D. J.: 2012, *Journal of Computational Physics* **231**, 759
- Proga, D., Stone, J. M., and Kallman, T. R.: 2000, *ApJ* **543**, 686
- Puccetti, S., Fiore, F., Risaliti, G., et al.: 2007, *MNRAS* **377**, 607
- Puchwein, E. and Springel, V.: 2013, *MNRAS* **428**, 2966
- Quataert, E.: 1998, *ApJ* **500**, 978
- Read, J. I. and Hayfield, T.: 2012, *MNRAS* **422**, 3037
- Read, J. I., Hayfield, T., and Agertz, O.: 2010, *MNRAS* **405**, 1513
- Rees, M. J.: 1984, *ARA&A* **22**, 471
-

- 
- Rees, M. J. and Ostriker, J. P.: 1977, *MNRAS* **179**, 541
- Reines, A. E. and Deller, A. T.: 2012, *ApJ* **750**, L24
- Reines, A. E., Greene, J. E., and Geha, M.: 2013, *ApJ* **775**, 116
- Reines, A. E., Sivakoff, G. R., Johnson, K. E., and Brogan, C. L.: 2011, *Nature* **470**, 66
- Rice, W., Armitage, P., Bate, M., and Bonnell, I.: 2003, *Monthly Notices of the Royal Astronomical Society* **339**(4), 1025
- Rice, W., Lodato, G., Pringle, J., Armitage, P., and Bonnell, I.: 2004, *Monthly Notices of the Royal Astronomical Society* **355**(2), 543
- Richstone, D., Ajhar, E. A., Bender, R., et al.: 1998, *Nature* **395**, A14
- Riquelme, M. A. and Spitkovsky, A.: 2011, *ApJ* **733**, 63
- Rivers, E., Markowitz, A., Duro, R., and Rothschild, R.: 2012, *ApJ* **759**, 63
- Robertson, B. E. and Kravtsov, A. V.: 2008, *ApJ* **680**, 1083
- Robinson, D. C.: 1975, *Physical Review Letters* **34**(14), 905
- Rogers, H. and Pittard, J. M.: 2013, *MNRAS* **431**, 1337
- Ross, R. R. and Fabian, A. C.: 2005, *MNRAS* **358**, 211
- Rupke, D. S. N. and Veilleux, S.: 2011a, *ApJ* **729**, L27
- Rupke, D. S. N. and Veilleux, S.: 2011b, *ApJ* **729**, L27
- Rupke, D. S. N. and Veilleux, S.: 2013a, *ApJ* **775**, L15
- Rupke, D. S. N. and Veilleux, S.: 2013b, *ApJ* **768**, 75
- Rusli, S. P., Erwin, P., Saglia, R. P., et al.: 2013a, *AJ* **146**, 160
- Rusli, S. P., Thomas, J., Erwin, P., et al.: 2011, *MNRAS* **410**, 1223
- Rusli, S. P., Thomas, J., Saglia, R. P., et al.: 2013b, *AJ* **146**, 45
- Rybicki, G. B. and Lightman, A. P.: 1986, *Radiative Processes in Astrophysics*, Radiative Processes in Astrophysics, by George B. Rybicki, Alan P. Lightman, pp. 400. ISBN 0-471-82759-2. Wiley-VCH, June 1986.
-

- 
- Sachs, A.: 1974, *Royal Society of London Philosophical Transactions Series A* **276**, 43
- Saitoh, T. R. and Makino, J.: 2009, *ApJ* **697**, L99
- Salpeter, E.: 1964, *The Astrophysical Journal* **140**, 796
- Sandage, A.: 1965, *ApJ* **141**, 1560
- Sani, E., Marconi, A., Hunt, L. K., and Risaliti, G.: 2011, *MNRAS* **413**, 1479
- Sargent, W. L., Young, P. J., Lynds, C., et al.: 1978, *The Astrophysical Journal* **221**, 731
- Sarria, J. E., Maiolino, R., La Franca, F., et al.: 2010, *A&A* **522**, L3
- Sarzi, M., Rix, H.-W., Shields, J. C., et al.: 2001, *ApJ* **550**, 65
- Sazonov, S. Y., Ostriker, J. P., Ciotti, L., and Sunyaev, R. A.: 2005, *MNRAS* **358**, 168
- Sazonov, S. Y., Ostriker, J. P., and Sunyaev, R. A.: 2004, *MNRAS* **347**, 144
- Schödel, R., Ott, T., Genzel, R., et al.: 2002, *Nature* **419**, 694
- Schaffer, S.: 1979, *Journal for the History of Astronomy* **10**, 42
- Scharwächter, J., Combes, F., Salomé, P., Sun, M., and Krips, M.: 2015, *ArXiv e-prints*
- Schaye, J., Crain, R. A., Bower, R. G., et al.: 2015, *MNRAS* **446**, 521
- Schaye, J. and Dalla Vecchia, C.: 2008, *MNRAS* **383**, 1210
- Schaye, J., Dalla Vecchia, C., Booth, C. M., et al.: 2010, *MNRAS* **402**, 1536
- Schechter, P.: 1976, *ApJ* **203**, 297
- Schmidt, M.: 1959, *ApJ* **129**, 243
- Schmidt, M.: 1963, *Nature* **197(4872)**, 1040
- Schmidt, M.: 1965, *ApJ* **141**, 1295
- Schmidt, M. and Matthews, T. A.: 1964, *ApJ* **139**, 781
- Schreier, E., Gursky, H., Kellogg, E., Tananbaum, H., and Giacconi, R.: 1971, *ApJ* **170**, L21
-

- 
- Schulze, A. and Gebhardt, K.: 2011, *ApJ* **729**, 21
- Schulze, A. and Wisotzki, L.: 2011, *A&A* **535**, A87
- Schulze, A. and Wisotzki, L.: 2014, *MNRAS* **438**, 3422
- Schwarzschild, K.: 1916, *Sitzungsberichte der Königlich Preußischen Akademie der Wissenschaften (Berlin), 1916, Seite 189-196* pp 189–196
- Scott, A. E., Stewart, G. C., and Mateos, S.: 2012, *MNRAS* **423**, 2633
- Seyfert, C. K.: 1943, *ApJ* **97**, 28
- Shakura, N. I. and Sunyaev, R. A.: 1973, *A&A* **24**, 337
- Shankar, F., Lapi, A., Salucci, P., De Zotti, G., and Danese, L.: 2006, *ApJ* **643**, 14
- Shen, J., Vanden Berk, D. E., Schneider, D. P., and Hall, P. B.: 2008, *AJ* **135**, 928
- Shen, Y., Greene, J. E., Ho, L. C., et al.: 2015, *ApJ* **805**, 96
- Shields, G. A.: 1999, *PASP* **111**, 661
- Shields, G. A., Menezes, K. L., Massart, C. A., and Vanden Bout, P.: 2006, *ApJ* **641**, 683
- Sijacki, D., Springel, V., Di Matteo, T., and Hernquist, L.: 2007, *MNRAS* **380**, 877
- Sijacki, D., Vogelsberger, M., Genel, S., et al.: 2015a, *MNRAS* **452**, 575
- Sijacki, D., Vogelsberger, M., Genel, S., et al.: 2015b, *MNRAS* **452**, 575
- Silk, J.: 1977, *ApJ* **214**, 152
- Silk, J.: 2013, *ApJ* **772**, 112
- Silk, J. and Norman, C.: 2009, *ApJ* **700**, 262
- Silk, J. and Rees, M. J.: 1998, *A&A* **331**, L1
- Slipher, V. M.: 1917, *Lowell Observatory Bulletin* **3**, 59
- Smith, H. J. and Hogg, D.: 1963, *Nature* **198**, 650
- Soltan, A.: 1982, *MNRAS* **200**, 115

- 
- Spitzer, Jr., L. and Saslaw, W. C.: 1966, *ApJ* **143**, 400
- Springel, V.: 2000, *MNRAS* **312**, 859
- Springel, V.: 2005, *MNRAS* **364**, 1105
- Springel, V.: 2010, *ARA&A* **48**, 391
- Springel, V., Di Matteo, T., and Hernquist, L.: 2005, *MNRAS* **361**, 776
- Springel, V. and Hernquist, L.: 2002, *MNRAS* **333**, 649
- Springel, V. and Hernquist, L.: 2003, *MNRAS* **339**, 289
- Springel, V., Yoshida, N., and White, S. D. M.: 2001, *New Astronomy* **6**, 79
- Stephenson, F. R., Yau, K. K. C., and Hunger, H.: 1985, *Nature* **314**, 587
- Stepney, S.: 1983, *MNRAS* **202**, 467
- Stoner, E. C.: 1929, *The London, Edinburgh, and Dublin Philosophical Magazine and Journal of Science* **7(41)**, 63
- Stoner, E. C.: 1930, *The London, Edinburgh, and Dublin Philosophical Magazine and Journal of Science* **9(60)**, 944
- Stoner, E. C.: 1932a, *Monthly Notices of the Royal Astronomical Society* **92**, 651
- Stoner, E. C.: 1932b, *Monthly Notices of the Royal Astronomical Society* **92**, 662
- Storchi-Bergmann, T., Schmitt, H. R., Calzetti, D., and Kinney, A. L.: 1998, *AJ* **115**, 909
- Sturm, E., González-Alfonso, E., Veilleux, S., et al.: 2011a, *ApJ* **733**, L16
- Sturm, E., González-Alfonso, E., Veilleux, S., et al.: 2011b, *ApJ* **733**, L16
- Sturm, E., González-Alfonso, E., Veilleux, S., et al.: 2011c, *ApJ* **733**, L16
- Targett, T. A., Dunlop, J. S., and McLure, R. J.: 2012, *MNRAS* **420**, 3621
- Tombesi, F., Cappi, M., Reeves, J. N., et al.: 2010a, *A&A* **521**, A57+
- Tombesi, F., Meléndez, M., Veilleux, S., et al.: 2015, *Nature* **519**, 436
- Tombesi, F., Sambruna, R. M., Reeves, J. N., et al.: 2010b, *ApJ* **719**, 700
-

- 
- Toomre, A.: 1977, in B. M. Tinsley and R. B. G. Larson, D. Campbell (eds.), *Evolution of Galaxies and Stellar Populations*, p. 401
- Trakhtenbrot, B., Urry, C. M., Civano, F., et al.: 2015, *Science* **349**, 168
- Tremaine, S., Gebhardt, K., Bender, R., et al.: 2002, *ApJ* **574**, 740
- Treu, T., Malkan, M. A., and Blandford, R. D.: 2004, *ApJ* **615**, L97
- Tristram, K. R. W., Raban, D., Meisenheimer, K., et al.: 2009, *A&A* **502**, 67
- Türler, M., Paltani, S., Courvoisier, T. J.-L., et al.: 1999, *A&AS* **134**, 89
- Turnshek, D. A.: 1988, in J. C. Blades, D. A. Turnshek, and C. A. Norman (eds.), *QSO Absorption Lines: Probing the Universe*, p. 17
- Ulrich, M.-H., Maraschi, L., and Urry, C. M.: 1997, *ARA&A* **35**, 445
- Uttley, P., Fruscione, A., McHardy, I., and Lamer, G.: 2003, *ApJ* **595**, 656
- van den Bosch, R. C. E., Gebhardt, K., Gültekin, K., et al.: 2012, *Nature* **491**, 729
- van der Marel, R. P. and van den Bosch, F. C.: 1998, *AJ* **116**, 2220
- van Loon, J. T. and Sansom, A. E.: 2015, *MNRAS* **453**, 2341
- Vaughan, S., Edelson, R., Warwick, R. S., and Uttley, P.: 2003, *MNRAS* **345**, 1271
- Vishniac, E. T.: 1983, *ApJ* **274**, 152
- Vogelsberger, M., Genel, S., Sijacki, D., et al.: 2013, *MNRAS* **436**, 3031
- Vogelsberger, M., Genel, S., Springel, V., et al.: 2014, *MNRAS* **444**, 1518
- Volonteri, M.: 2010, *A&A Rev.* **18**, 279
- Volonteri, M., Natarajan, P., and Gültekin, K.: 2011, *ApJ* **737**, 50
- Volonteri, M. and Rees, M. J.: 2005, *ApJ* **633**, 624
- Volonteri, M. and Stark, D. P.: 2011, *MNRAS* **417**, 2085
- von Hoerner, S.: 1960, *ZAp* **50**, 184
- Wagner, A. Y., Bicknell, G. V., and Umemura, M.: 2012, *ApJ* **757**, 136
-

- 
- Wagner, A. Y., Umemura, M., and Bicknell, G. V.: 2013, *ApJ* **763**, L18
- Walsh, J. L., Barth, A. J., and Sarzi, M.: 2010, *ApJ* **721**, 762
- Walter, R. and Fink, H. H.: 1993, *A&A* **274**, 105
- Weaver, R., McCray, R., Castor, J., Shapiro, P., and Moore, R.: 1977, *ApJ* **218**, 377
- Webster, B. L. and Murdin, P.: 1972, *Nature* **235**, 37
- Wendland, H.: 1995, *Advances in computational Mathematics* **4(1)**, 389
- Whitworth, A. P.: 1998, *MNRAS* **296**, 442
- Wiersma, R. P. C., Schaye, J., and Smith, B. D.: 2009, *MNRAS* **393**, 99
- Wolfe, A. and Burbidge, G.: 1970, *The Astrophysical Journal* **161**, 419
- Woo, J.-H., Treu, T., Malkan, M. A., and Blandford, R. D.: 2006, *ApJ* **645**, 900
- Woo, J.-H., Treu, T., Malkan, M. A., and Blandford, R. D.: 2008, *ApJ* **681**, 925
- Wright, T.: 1750, *An original theory or new hypothesis of the universe : founded upon general phaenomena of the visible creation; and particularly the Via the laws of nature, and solving by mathematical principles : the Lactea ...compris'd in nine familiar letters from the author to his friendand : illustrated with upward of thirty graven and mezzotinto plates ...*
- Yakovlev, D. G., Haensel, P., Baym, G., and Pethick, C.: 2013, *Physics-Uspekhi* **56(3)**, 289
- Young, P., Westphal, J., Kristian, J., Wilson, C. P., and Landauer, F.: 1978, *The Astrophysical Journal* **221**, 721
- Zeldovich, Y. B. and Novikov, I.: 1964, *DOKLADY AKADEMII NAUK SSSR* **158(4)**, 811
- Zubovas, K.: 2015, *MNRAS* **451**, 3627
- Zubovas, K., Bourne, M. A., and Nayakshin, S.: 2015, *ArXiv e-prints*
- Zubovas, K. and King, A.: 2012a, *ApJ* **745**, L34
- Zubovas, K. and King, A.: 2013, *ApJ* **769**, 51
-



- 
- Zubovas, K. and King, A. R.: 2012b, *MNRAS* **426**, 2751
- Zubovas, K. and Nayakshin, S.: 2012, *MNRAS* **424**, 666
- Zubovas, K. and Nayakshin, S.: 2014, *MNRAS* **440**, 2625
- Zubovas, K., Nayakshin, S., King, A., and Wilkinson, M.: 2013a, *MNRAS* **433**, 3079
- Zubovas, K., Nayakshin, S., Sazonov, S., and Sunyaev, R.: 2013b, *MNRAS* **431**, 793
- Zwicky, I. F.: 1964, *ApJ* **140**, 1467